# THE SIMULATION OF WATER UPTAKE BY VEGETATION AND ITS IMPACT ON SLOPE STABILITY USING AN IMAGE – BASED MODEL OF PLANT ROOT ARCHITECTURE

BY

KAI SHANG

Submitted for the degree of Doctor of Philosophy, Cardiff University

School of Engineering
Cardiff University

AUGUST 2016

# ABSTRACT

The overall aim of this research is to develop a new root-image based approach to modelling water uptake by plants. The approach developed employs a digitized image of the root zone to determine an 'effective root density ratio' that is subsequently used to yield a spatially variable sink term.

The moisture flow model chosen is based on Richards' Equation added a sink term to facilitate inclusion of a water uptake model (i.e. 1D, 2D and 2D axi-symmetric format). A numerical solution was achieved via the finite element method for spatial discretisation along with a finite difference time-marching scheme. The numerical evaluation of the root density ratio was coded in Matlab. The resulting values were then used to define the spatial variation of the sink term within the finite element code.

Initial applications of the new model operating in a one-dimensional mode provided some confidence with respect to the implementation of the new image-based root density approach to simulate moisture migration patterns beneath a uniform cover of vegetation. A new two-dimensional axi-symmetric form of the model was then developed and applied to simulate moisture migration near established trees. The model was validated by direct comparison to the field measurements recorded. The study provided an assessment of the significance of water content (and therefore suction) changes on the stability of unsaturated soil slopes. Two typical root architectures were considered to investigate the influence of root architecture on slope stability. In particular, effects of root architecture were emphasized.

In conclusion, a new root-image based approach to modelling water uptake by plants has been developed. In general, it is hoped that the current research has provided a useful further contribution on modelling water-uptake process and on the overall assessment of slope stability.

## ACKNOWLEDGEMENTS

This study was undertaken while I was a PhD student at the School of Engineering, Cardiff University. I would like to express my sincere thanks to Dr. Stephen William Rees and Dr. Peter John Cleall for their close supervision, guidance and encouragement at all stages of works. They supported me not only by providing a research tutorial over almost five years, but also academically and emotionally through the rough road to finish this thesis.

The completion of this thesis has been greatly helped by the support and understanding shown by my parents and friends. Their support has been unconditional all these years; they have given up many things for me to be at Cardiff University; they have cherished with me every great moment and supported me whenever I needed it. I am very grateful and fortunate.

# CONTENTS

# LIST OF FIGURES

# LIST OF TABLES

# LIST OF SYMBOLS

| | |
|---|---|
| $A_i$ | Area for a corresponding pixel (cm$^2$) |
| $C(\psi)$ | Specific moisture capacity (cm$^{-1}$) |
| $c'$ | Effective Cohesion (kPa) |
| $c_p$ | Specific heat at constant pressure (MJ kg$^{-1}$ °C$^{-1}$) |
| $d_r$ | Inverse relative distance Earth-Sun |
| $E$ | Evaporation (mm/day) |
| $ET$ | Evapotranspiration (mm/day) |
| $ET_o$ | Reference crop evapotranspiration (mm/day) |
| $E_{tree}$ | Transpiration rate for a whole tree (kg day$^{-1}$ or litre day$^{-1}$) |
| $e°(T)$ | Saturation vapour pressure at air temperature T (kPa) |
| $e_s$ | Saturation vapour pressure for a given time period (kPa) |
| $e_a$ | Actual vapour pressure (kPa) |
| $F$ | Factor of safety |
| $G_j, g_j$ | Prescribe known functions or operators |
| $i$ | Hydraulic gradient |
| $K, K_s$ | Saturated hydraulic conductivity (cm/s) |
| $K(\phi), K(\psi)$ | Unsaturated hydraulic conductivity (cm/s) |
| $L_i$ | Length of the corresponding pixel (cm) |
| $L$ | Total leaf area of the tree canopy (m$^2$) |

| | |
|---|---|
| LAI | Leaf area index ($m^2$ $m^{-2}$) |
| $N$ | Total normal force on the base of the slice (kN) |
| $N_i, N_r, N_s$ | Shape Function |
| $P$ | Atmospheric pressure (kPa) |
| $R, R_\Omega$ | The residual or error introduced by the approximation |
| $R_i$ | Root density ratio of a single pixel |
| $R_a$ | Extraterrestrial radiation (MJ $m^{-2}$ $day^{-1}$) |
| $R_l$ | Longwave radiation (MJ $m^{-2}$ $day^{-1}$) |
| $R_n$ | Net radiation (MJ $m^{-2}$ $day^{-1}$) |
| $R_{n,tree}$ | Net radiation absorbed per unit leaf area (MJ $m^{-2}$ $day^{-1}$) |
| $R_{nl}$ | Net longwave radiation (MJ $m^{-2}$ $day^{-1}$) |
| $R_{ns}$ | Net solar or shortwave radiation (MJ $m^{-2}$ $day^{-1}$) |
| $R_s$ | Solar or shortwave radiation (MJ $m^{-2}$ $day^{-1}$) |
| $R_{so}$ | Clear-sky solar or clear-sky shortwave radiation (MJ $m^{-2}$ $day^{-1}$) |
| $r_a$ | Aerodynamic resistance (s $m^{-1}$) |
| $r_l$ | Bulk stomatal resistance of well-illuminated leaf (s $m^{-1}$) |
| $r_s$ | (bulk) surface or canopy resistance (s $m^{-1}$) |
| $S_m$ | Shear force mobilized on the base of each slice (kN) |
| $S, S_{max}, S(\psi)$ | Sink term ($cm^3/cm^3/s$) |
| $T, T'$ | Potential transpiration rate (cm/s) corresponding the one-dimensional problem |
| $T''$ | Transpiration rate ($cm^2/s$) corresponding the two-dimensional problem |

| | |
|---|---|
| $T^r$ | Transpiration rate (cm³/s) corresponding the two-dimensional axi-symmetric problem |
| $t$ | Time (s) |
| $u$ | Functions in $\Omega$ |
| $u_a$ | The pore-air pressure (kPa) |
| $u_w$ | The pore-water pressures (kPa) |
| $\hat{u}$ | The approximation to the function $u$ |
| $V, V_w$ | Volume of water (cm³) |
| $V_i$ | Volume for a corresponding pixel (cm³) |
| $v_x, v_y, v_z$ | Velocity of water flow (cm/s) |
| $W$ | Total weight of a slice (kN) |
| $W_1$ | The weighting functions |
| $x, r, z$ | Cartesian co-ordinates (cm) |
| $\alpha(\psi)$ | Pressure head dependent reduction factor |
| $\alpha, l, m, n$ | Soil specific parameter |
| $\beta$ | Angle between the tangent to the centre of the base of each slice and the horizontal (degree) |
| $\gamma$ | Density (kN/m³) |
| $\theta$ | Volumetric moisture content (%) |
| $\theta_r$ | Residual water content (%) |
| $\theta_s$ | Saturated water content (%) |
| $\sigma_n$ | Normat stress (kPa) |
| $\psi$ | Capillary potential (cm) |
| $\hat{\psi}$ | The approximation to the $\psi$ (cm) |

| | |
|---|---|
| $\phi$ | Total potential for moisture flow |
| $\phi'$ | Angle of friction (degrees) |
| $\phi^b$ | Angle indicating the rate of increase in shear strength relative to matric suction (degrees) |
| $\hat{\phi}$ | The approximation to the $\phi$ |
| $\Omega$ | Domain |
| $\Gamma$ | Boundary |
| $\lambda$ | Water flux at the boundary (cm/s) |
| $\rho_a$ | Mean air density (kg m-3) |
| $\varepsilon$ | Ratio molecular weight of water vapour/dry air (0.622) |
| $\Delta$ | Slope of saturation vapour pressure curve (kPa $°C^{-1}$) |
| $\delta$ | Solar declination (rad) |
| $\varpi_s$ | Sunset hour angle (rad) |

**CHAPTER ONE**

**INTRODUCTION**

1.1     RESEARCH BACKGROUND

Vegetation is well-known to have a significant influence on pore water pressures and ground movements in soils. However, the processes involved are complex and driven by the inter-related dynamic factors of the atmosphere, vegetation and soil. As a result, modelling of water transport in the soil–root system can play an important role in attempts to predict a wide range of geotechnical, geo-environmental and soil science problems. Furthermore in-situ monitoring and measurement is inherently difficult and significant challenges arise in relation to the determination of the relevant physical properties of both the soil and the plant/root system.

In agricultural science, precise water-uptake models that can be used to evaluate water usage, and ultimately optimizing crop yield, are clearly of value with respect to the

internationally significant problem of crop security (food supply) and yield. In this context, agricultural production is becoming more critical in the future of significant challenges arises from climate change and population growth (Reynolds and Ortiz 2010). In addition, irrigation is a common activity during the production of crops. However, it may cause salinization and destruction of agricultural land. Soil salinization and contamination accumulation in the soil can be affected (remove saline and/or toxic ions from the soil) by plant root transpiration and uptake (Skaggs et al. 2006; Li et al. 2015). Although this aspect of the problem is beyond the scope of the current work, it is clear that the accurate estimation of the process of root water uptake is key component of this problem.

Failures of natural or man-made slopes which can give rise to serious loss of life and damage to assets are of significant concern in many countries. For example, a recent disaster in China demonstrated that removal of vegetation may result in significant slope failure. On 9th May 2016, a heavy rain triggered landslide in south-eastern China (a site in Fujian province's Taining County) where a hydropower project was being built, this accidence caused the death of 31 people and 7 others remain missing (Mckirdy 2016). The National Meteorological Centre reported the rainfall of this region had been 35% higher than average during this year and the precipitation in the area around the construction site was 215.7 mm for 24 hours before the landslide (BBC 2016). Investigation of the construction site and the surroundings at the disaster regions revealed that removal of trees from the adjacent slope resulted in the loss of suctions generally beneficial to stability. The presence of vegetation (specifically trees) on slopes have attracted continued attention in recent years because vegetation is considered a sustainable and environmentally friendly

alternative for reducing rainfall infiltration and stabilizing soil slopes (Rees and Ali 2012; Smethurst et al. 2015).

It is also becoming increasingly understood that as climate change occurs, behaviour of the UK's infrastructure slopes (more than 20,000 km of embankments and cuttings) may change, requiring a growth in maintenance cost and a refocussing of infrastructure renewal budgets on potential risk areas (Loveridge et al. 2010). Vegetated soil reduces pore-water pressure because of the process of root water uptake (Indraratna et al. 2006; Rees and Ali 2006; Nyambayo and Potts 2010; Ng et al. 2013). Recent research (Rees and Ali 2012; Zhu and Zhang 2015) indicates that progress is now being made to incorporate the influence of vegetation within the framework of slope stability analysis. Although good progress has been made with respect to the contribution of root-water uptake in slopes to the overall soil shear strength and slope stability, the direct influence of suction variations still appears to need further consideration.

Root water uptake by trees can cause seasonal shrinkage and swelling of clay soils, is the single most common cause of foundation movements which may damage domestic buildings or disturb the rail track geometry, resulting in train speed restrictions that disrupt normal operations (Biddle 1998, Smethurst et al. 2015). However, a reliable analysis method that enables the prediction of soil behaviour due to the presence of vegetation is yet to be established.

The broad objective of this study is to develop a numerical model capable of representing the extraction of water from the soil by the roots of various species of

vegetation – namely water-uptake process. At the centre of the research is the development of a model that is based on providing a realistic representation of the root-architecture involved. Initially, this research is assessed via relatively simple forms of root water-uptake scenarios, namely representing the moisture flow behaviour beneath a uniform crop cover. Then, the primary contribution of this work focuses on the consideration of applying the new model to predict water-uptake in the vicinity of established mature trees. It is suggested that the new approach can be extended and applied for to a wide range of geoengineering problems as indicated below.

This research begins by developing an existing finite element program for the use of Richards' equation for unsaturated moisture flow incorporating a sink term (Rees and Thomas 1990). It was coded in FORTRAN and built for a linear distribution of root water-uptake model for one-dimensional and two-dimensional axi-symmetric problems (Rees and Ali 2006). A significant development and extension of the code is required to meet the current research as indicated via the specific objectives listed below.

## 1.2     AIMS & OBJECTIVES

The overall aim of this research is to develop a new root-image based approach to modelling the water uptake process. The approach developed employs a digitized image of the root zone to determine an 'effective root density ratio' that is

subsequently used to yield a spatially variable sink term.  Detailed objectives of this investigation are to:

i.   Introduce a volumetric sink term, defined by a root-image based approach, into the governing equation for unsaturated moisture flow and the numerical finite element code (Rees and Thomas 1990; Rees and Ali 2006).

ii.  Develop a theoretical model of an image based water uptake for 1D, 2D, 2D-axisymetical applications.

iii. Implement a numerical solution of the chosen theoretical approach.

iv.  Incorporate an image based approach to define the root zone geometry and control routines related to the water uptake models within the finite element code.

v.   Validate the new 1D model beneath crops (a uniform crop cover) and compare a linear variation of water uptake model (Prasad 1988).

vi.  Validate the 2D axi-symmetric model by comparison with experimental data.

vii. Investigate water-uptake from an established tree over a seasonal time frame.

viii. Compare the performance of an image based water uptake model with established linear (with depth and radius) water extraction rate model (Rees and Ali 2006).

ix.  Implement a preliminary assessment of the role of a mature tree in slope stability analysis.

x.      Investigate the influence of tree locations and root architectures in slope

stability.

## 1.3      SCOPE AND LIMITATIONS

The current work aims to provide a tool for the simulation of moisture migration caused by vegetation that will be of significant value for a wide range of geotechnical engineering problems (as stated before).    Therefore, an essential principle of maintaining an approach that is as simple as possible to yield acceptable accuracy has been adopted.  Consequently, the resulting model will inevitably exclude or simplify some aspects of the problem – the main limitations are indicated below.

In the current work, a homogenous soil profile is assumed throughout.  Although the root water uptake model established is capable of development to include layered soils, this is not explicitly demonstrated in the current validation work.  Additionally, some soils may show deformation behaviour in relation to variations of soil moisture content.  However, deformation behaviour is considered to be beyond the scope of the current work and therefore this work is based on constant volume models.  Moreover, most roots significantly depend on oxygen for growth, but the required rates of diffusion of oxygen can be only reached in an unsaturated soil.  In addition, the scope of many practical problems of interest here is dominated by near-surface soil behaviour.   Therefore, this study is focussed on predicting moisture flow in the unsaturated zone.

Unsaturated moisture flow is described here by a partial differential equation that assumes isotropic conditions. Furthermore, the flow equation is solved by approximate numerical methods. In particular, the finite element method is used to achieve spatial discretisation and the finite difference method is used to achieve time discretisation. There are unavoidable approximations implicit in this approach. However, a significant effort has been made to ensure that discretisation errors are kept to a minimum.

Non-linearity of moisture transfer parameters is incorporated in this work. The flow parameters may also be recognized as temperature dependent; however, this effect is considered second order and is not included here (Milly 1989). Therefore, isothermal conditions are assumed to exist.

Root growth was excluded from the new model since the current work was focused on developing an approach for the simulation of crops for relatively short time periods and the behaviour of established a mature tree. It is clear that more broadly; the time dependent aspect of root growth and decay may be of interest for the analysis of some applications.

When considering the water uptake behaviour associated to a single (isolated) tree radial symmetry is assumed in the investigation. Although, it is clear that architecture of real root systems can be geometrically complex and affected by many environmental factors (Stokes et al. 2009). Nevertheless, the approach developed here is limited to a two-dimensional axi-symmetric formulation in the first instance.

Furthermore, more complex behaviour will occur when adjacent trees interact – this aspect of the problem is not considered here.

In this study, a new root density based approach to modelling the water uptake process is proposed. Although the new model is thought to provide a useful departure from previous models that impose artificial root geometry, it is recognized that the ultimate success of this approach is dependent on the quality of available root image data.

A first assessment of the influence of tree-location and tree-root-architectures on unsaturated soil slope stability is attempted here. However, in this context, the work is limited to the influence of pore-water pressure changes on shear strength only and the groundwater table is assumed to be at depth. Other factors that influence stability, for example, weight of vegetation, windthrow, and tensile strength of roots (Greenwood et al. 2004) are excluded from consideration. In addition, the assessment of slope analysis presented here was only considered in relation to a single tree present on a soil – no other vegetation (grass or more trees) were included in the current framework.

## 1.4    THESIS LAYOUT

An overview of related research work to the analysis of root water uptake and slope stability in unsaturated soils is presented in Chapter 2. The literature review presents an interpretation of the general significance of the water-uptake process. It then

provides a summary of the basic mechanisms involved and some background information that can be employed in following modelling work. The review also summarises developments in modelling the root-water-uptake process and the assessment of vegetated slope stability.

Chapter 3 describes the development of theoretical description of soil moisture flow in an unsaturated soil. Some of the fundamental concepts used to describe moisture flow due to water uptake plant by roots are also introduced. This chapter proposes a new root density based approach to modelling the water uptake process. The approach utilizes a digitized image of the root zone to determine an 'effective root density ratio' that is subsequently employed to yield a spatially variable sink term. This chapter also attempts to provide a reasonable and simple framework that will satisfy a preliminary assessment of the influence of pore-water pressure changes on soil shear strength and therefore changes on the stability of unsaturated soil slopes.

An approximate numerical solution of the theoretical model framework presented in Chapter 3 is detailed in Chapter 4. A numerical solution is developed via a finite-element spatial discretization procedure and a finite-difference time-stepping scheme.

Chapter 5 describes some preliminary applications of the new numerical model. This chapter presents application of the 1D form of the model, as described in Chapter 3. The applications considered generally relate to circumstances where a large surface area is covered by fairly uniform crop. The performance of the new model is verified against independent results of two case studies.

An exploration of the numerical simulation of moisture migration patterns in the vicinity of a mature tree is provided in Chapter 6. This chapter also attempts to provide an assessment of transpiration rate for a single tree calculated using the well-established Penman-Monteith equation. In the first case, the model is applied to simulate field measurements recorded (by others) for a mature lime tree located on a Boulder Clay sub-soil. It explores some of the issues that arise in relation to the seasonal climate variation of moisture migration patterns near a mature tree and considers a simple method of representing time dependent variations in boundary conditions based on daily rainfall patterns. To provide some confidence in the implementation of the approach, the model also has been validated by a second comparison to field measurements recorded for a mature almond tree located on a shallow gravely loam soil.

Chapter 7 considers how the new model may be employed to provide an assessment of the significance of pore water pressure (and therefore soil suction) changes on the stability of unsaturated soil slopes. It also explores the influence of root architectures on such variations within the context of slope stability assessment. Typical slope geometry, a range of tree root architectures (heart and taproot) and tree locations are considered. The corresponding variation of the lowest factor of safety (critical slip surface) against failure is examined.

The overall conclusions to be described from the current research are presented in Chapter 8. Suggested further research is also discussed at this stage.

1.5    REFERENCES

BBC. 2016. *China Fujian landslide: 41 missing under rubble*. [Online]. Available at: http://www.bbc.co.uk/news/world-asia-china-36240629 [Accessed: 01 June 2016].

Biddle, P. G. 1998. *Tree Root Damage to Buildings*. Swindon: Willowmead Publishing Ltd, Wantage.

Greenwood, J. R. Norris, J. E. and Wint, J. 2004. Assessing the contribution of vegetation to slope stability. *Geotechnical Engineering*. 157(GE4), pp. 199-207.

Indraratna, B. et al. 2006. Numerical analysis of matric suction effects of tree roots. *Geotechnical Engineering* 159, pp. 77-90.

Mckirdy, E. 2016. China landslide: More than 20 bodies recovered. [Online]. Available at: http://edition.cnn.com/2016/05/08/asia/china-fujian-landslide/ [Accessed: 1 June 2016].

Milly, P. C. D. 1989. Unsaturated Flow Induced by Evaporation and Transpiration. In: Morel-Seytoux, H. J. ed. *Unsaturated Flow in Hydrologic Modeling Theory and Practice*. London, Kluwer Acdemic Publishers, pp. 221-240.

Ng, C. W. W. Leung, A. K. Woon, K. X. 2013. Effects of soil density on grass-induced suction distribution in compacted soil subjected to rainfall. *Can Geotech J*. 51, pp. 311-321.

Nyambayo, V. P. and Potts, D. M. 2010. Numerical simulation of evapotranspiration using a root water uptake model. *Computers and Geotechnics*. 37, 175-186.

Prasad, R. 1988. A linear root water uptake model. *J. Hydrol*. 99, pp. 297-306.

Rees, S. W. and Ali, N. 2006. Seasonal water uptake near trees: a numerical and experimental study. *Geomechanics and Geoengineering*: An International Journal. 1(2), pp. 129-138.

Rees, S. W. and Ali, N. 2012. Tree induced soil suction and slope stability. *Geomechanics and Geoengineering*. 7 (2), pp. 103-113.

Rees, S. W. and Thomas, H. R. 1990. Modelling Field Infiltration into Unsaturated Clay. *Journal of Geotechnical Engineering*. 116(10), pp. 1483-1501.

Reynolds, M. P. and Ortiz, R. 2010. Adapting Crops to Climate Change: a Summary. In: Reynolds, M. P. eds. *Climate Change and Crop Production*. 1st ed. Oxford: CAB International, pp. 1-8.

Li, H. Yi, J. Zhang, J. Zhao, Y. Si, B. Hill, R. L. Cui, L. and Liu, X. 2015. Modeling of Soil Water and Salt Dynamics and Its Effects on Root Water Uptake in Heihe Arid Wetland, Gansu, China. *Water*. 7, pp. 2382-2401.

Loveridge, F. A. Spink, T. W. O'Brien, A. S. Briggs, K. M. and Butcher, D. 2010. The impact of climate and climate change on infrastructure slopes, with particular reference to southern England. *Quarterly Journal of Engineering Geology and Hydrogeology*. 43, pp. 461-472.

Skaggs, T. H. van Genuchten, M. T. Shouse, P. J. Poss, J. A. 2006. Macroscopic approaches to root water uptake as a function of water and salinity stress. *Agricultural Water Management*. 86, pp. 140-149.

Smethurst, J. A. Briggs, K. M. Powrie, W. Ridley, A. and Butcher, D. J. E. 2015. Mechanical and hydrological impacts of tree removal on a clay fill railway embankment. *Géotechnique*. 65, (11), 869-882.

Stokes, A. Atger, C. Bengough, A. Fourcaud, T. and Sidle, R. 2009. Desirable plant root traits for protecting natural and engineered slopes against landslides. *Plant Soil*. 324 (1), pp.1-30.

Zhu, L. and Zhang, L. M. 2015. Evaluating suction profile in a vegetated slope considering uncertainty in transpiration. *Computers and Geotechnics*. 63, pp. 112-120.

# CHAPTER TWO

# LITERATURE REVIEW

## 2.1    INTRODUCTION

This chapter presents a general overview of the literature relating to the movement and distribution of soil water in the presence of vegetation within the context of the analysis of a number of geotechnical and geo-environmental problems.  The chapter starts by describing an outline of the key behavioural mechanisms and the main approaches for estimating the rate of transpiration for uniform vegetation cover (e.g. crops) or individual trees.  The rooting habits of trees, the process of root water uptake, and a review of the numerical methods used to describe the process of water uptake by plant roots are then presented.  A summary of the historic development of theoretical/numerical models related to specific vegetation types and field conditions is also presented.  Finally, the role of vegetation in the assessment of soil slope stability is also provided.  This section considers how limiting equilibrium mechanics has been extended to incorporate the various effects of vegetation and also summarizes the

studies of the hydrological and mechanical effects from vegetation on the stability of soil slope.

## 2.2    FIELD MEASUREMENTS OF RELEVANT MATERIAL PROPERTIES

This study focuses on development of a numerical model to represent the water uptake process that is capable of predicting spatial variation in water content, without the need for detailed field measurement.  However, in order to apply the model in practice, some basic material properties are required.  Fundamental hydraulic properties of the soil are most commonly estimated from laboratory based data and/or some form of theoretical approximation.  However, to assess validity of the model there is a clear need for high quality full-scale (field) data.  Field data that reveals spatial and temporal variations in soil moisture content (ideally in the vicinity of vegetation) and field data representing root architecture for the vegetation of interest are of particular importance in this content.  A detailed description of field measurements on the unsaturated soil parameters and root system of plant available can be found elsewhere (Vereecken et al. 1990; Bohne et al. 1993; Jackson et al. 1995; Jadoon et al. 2012; Shi et al. 2015; Judd et al. 2015).  For completeness, a brief overview that summarises such research is presented below - no attempt is made at providing a full review of the subject at this point.

There are various methods available that can be used to determine (indirectly) in-situ soil water content.  These include: time-domain reflectometry (TDR) (Menziani et al. 1996; Noborio 2001), the neutron probe (Biddle 1998), frequency domain reflectometry (FDR) sensors (Lukanu and Savage 2006), capacitance sensors (Eller and Denoth 1996), amplitude

domain reflectometry (ADR) (Segundo et al. 2015), electrical resistivity tomography (ERT) (Brunet et al. 2010), ground penetrating radar (GPR) (Huisman et al. 2003). The advantages of using these methods are minimum disturbance of the soil, measured data are immediately available, the measurement can be repeated at the same spot or the measurement can be taken continuously and recorded by computer based data-loggers. However, such techniques often have complexities and limitations. They can be expensive and require highly trained operators who must be able to handle the frequent calibration procedures, the electronics, and the sampling equipment. The reference cited in each case can provide much more detail of these techniques.

Several of the available methods (e.g. psychrometer, pressure plate, tempe cell, tensiometer, hanging water column) for measuring soil matric potential have a limited range of measurement, and only some of them are amenable to in-situ investigations (Tuller and Or 2003). One of the most common field measurements methods for the soil-water retention curve is to install paired sensors such as tensiometers and time domain reflectometry waveguides to measure matric potential and soil water content and simultaneously and in the same soil volume (Werkhoven 1993). The saturated hydraulic conductivity of a soil in the field can be estimated using various approaches e.g. the auger-hole method, the piezometer method, well-pumping (slug) methods, shallow-well pump-in or dry auger-hole, double-tube, ring infiltrometer, air-entry permeameter, and constant-head test in a single drill hole, an extensive discussion on the measurement approaches for field experiments is presented in Amoozegar and Warrick (1986).

Briefly considering the field measurement of the properties of vegetation, there are a range of key technical papers that provide background on this (see for example: Stokes et al. 2002;

Crow 2004; Crow 2005; Gregory 2006; Hodge et al. 2009; Rood et al. 2011). In general, it is difficult to directly observe plant root architecture in the field without disturbing the soil profile in some manner to expose roots and this, of course, will often influence the properties under investigation. Some of the most commonly used techniques involve excavation of the entire root system with destructive, time-consuming and difficult techniques, such as washed soil cores (Gregory 2006), trench-profiling technique (Kücke et al. 1995; Luo et al. 2003), air spade excavation (Rizzo and Gross 2000), ground-penetrating radar (Hruska et al. 1999) and digitizing (Danjon et al. 1999). Root length density (the length of roots per unit volume of soil) is one of the most important parameters required to understand plant performance. It can be measured by some methods (e.g. trenches, photography, excavation, and 3D digitizing) with advantages and limitations (Böhm 1979; Kücke et al. 1995; Box 1996; Pierret et al. 2000; Reubens et al. 2007; Danjon et al. 2007; Gao 2010).

## 2.3    WATER UPTAKE BY ROOTS

### 2.3.1    The Evapotranspiration Process

The amount of water used by vegetation, as a subject of global research interest, has been studied for over one hundred years (Bosch and Hewlett 1982; McCulloch and Robinson 1993; Nisbet 2005). This process is of interest to many different fields of study such as: agriculture, geo-environmental engineering, ecology, hydraulic/hydro-environmental engineering and geotechnical engineering.

Nisbet (2005) suggests that vegetation uses water via two separate mechanisms (Figure 2.1):

i) Throughout periods of rainfall, water is intercepted initially by the leaves, branches and trunks and then is changed into a gas and released back to atmosphere. The term evaporation is used to describe this mechanism by which water is evaporated from the surface of vegetation. The rate of evaporation may be affected by the intensity of sunlight, air and water temperature, humidity and the speed of wind (Nisbet 2005).

ii) Transpiration - water is absorbed by plant roots from the soil and evaporated through the leaves of plant (Nisbet 2005). This physiological mechanism is strongly related to the soil water content and the ability of the soil to conduct water to the roots, the type of plant and the atmospheric environment (Allen et al. 1998).

The combination of the above two mechanisms is known as evapotranspiration (Nisbet 2005).
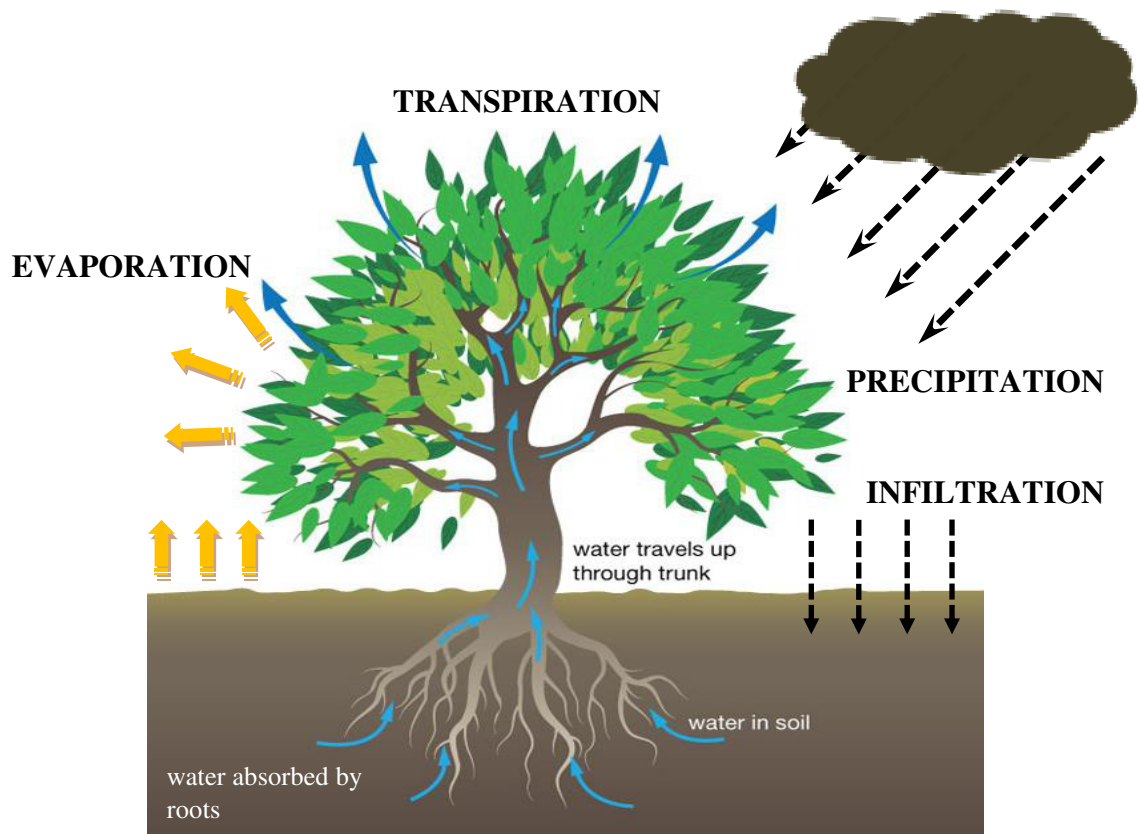
Figure 2. 1    Evapotranspiration process for an individual tree, image re-drafted after Story (2012)

2.3.2   Transpiration Rate

In this thesis, the focus of attention is on prediction of water uptake by roots from the soil and therefore transpiration is the key process of interest here.

Evaporation and transpiration take place simultaneously and it can be difficult to distinguish between the two processes (Allen et al. 1998). Hopkins (1999) reported that more than 90% of transpired water vapor escapes from leaves. Hence, the transpiration rate strongly relates to leaf characteristics. The partitioning of evapotranspiration into transpiration and

evaporation for an annual field crop is presented in Figure 2.2. It also plots the variation of leaf area index over the growing period. Initially, at 'sowing' nearly 100% of evapotranspiration comes from evaporation. Transpiration becomes the main process only when the crop is well developed and completely covers the soil.
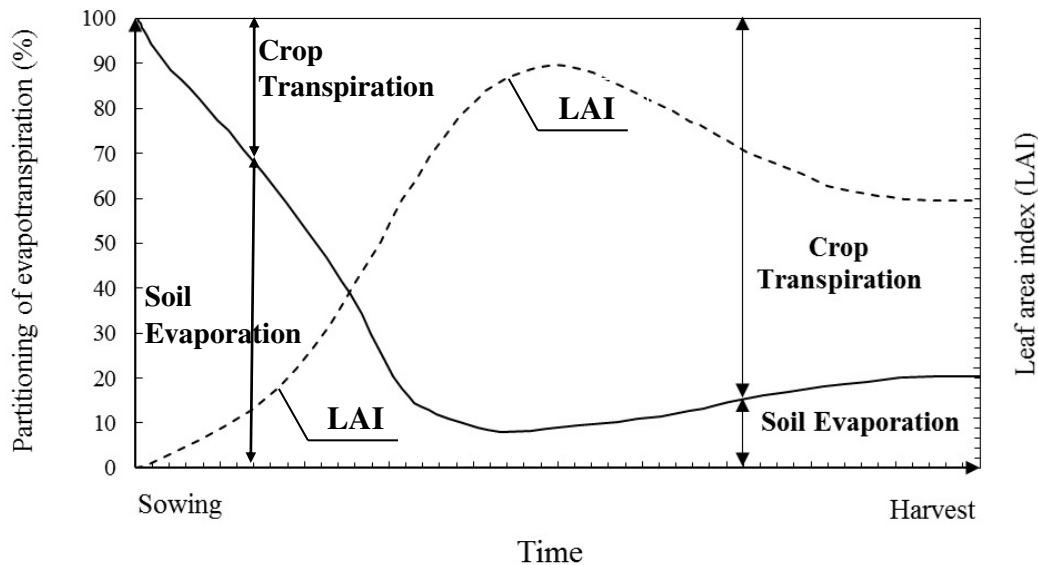


Figure 2. 2 The partitioning of evapotranspiration into evaporation and transpiration over the growing period for an annual field crop (reproduced from Allen et al. 1998).

The transpiration rates of a plant can be accelerated in response to rainfall (Zeppel et al. 2008; Mitchell et al. 2009; Macfarlane et al. 2010) and decreased throughout the seasons when there is a lack of soil water available (Luis et al. 2005; Gazal et al. 2006). If soil-water is in short supply during summer, trees may close their stomata on the surface of leaves, thus decreasing the water loss by transpiration (Nisbet 2005; Dye et al. 2013). In addition, low availability of soil water can cause the hydraulic resistance of the soil and root system to increase thus preventing soil water transfer to plant leaves (as well as triggering stomatal closure) hence decreasing the rate of transpiration (Meinzer et al. 1993; Sala and Tenhunen

1996; Tognetti et al. 2009). Furthermore, if this situation persists, it will cause the plant to wilt. As soil moisture is diminished and soil suction increases, the hydraulic conductivity may become too low to transmit soil water to the roots at the desired rate. As a result, the soil suction may exceed that of the root system and the soil will reach the wilting point moisture content. The water uptake by the roots may be assumed as zero, if the conditions wetter than "anaerobiosis point" and drier than "wilting point" (Feddes et al. 1976). If water in the soil is unlimited, the rate of transpiration will be dictated by the leaf area (Pereira et al. 2006).

The transpiration rate for trees is mainly determined by biological factors (e.g. leaf area index and the size of tree) and environmental factors (e.g. global radiation, wind speed, rainfall, vapour pressure deficit, temperature and soil water availability) (Granier et al. 1996; Wullschleger et al. 2000; Oren and Pataki 2001; David et al. 2004; Mellander et al. 2004; Oguntunde 2005; Komatsu et al. 2006; Burgess 2006; Tang et al. 2006; Ewers et al. 2008; Hernández-Santana et al. 2008; Tognetti et al. 2005, 2009). Furthermore, various species of vegetation may possess a wide range of transpiration rates. Some typical transpiration rates based on independent published data and are shown in Tables 2.1 and 2.2.

Table 2. 1        Transpiration rate for trees

| Source Reference | Type of Tree | Rate (mm/day) |
|---|---|---|
| Nisbet (2005) | Broadleaves | 2 |
| Indraratna et al. (2006) | Lime | 3 |
| Takagi et al. (2006) | Lotus | 7 |
| Dunin et al. (1985) | Gum | 9 |
| Vrught et al (2001b) | Almond | 4 |
| USGS (2005) | Oak | 5 |
| Biddle (1998) | Common | 5 |

Table 2. 2    Relevant water use for various crops (reproduced from Erie et al. 1965)

| Crop group | Crop | Seasonal crop water use (mm) | Maximum daily transpiration (mm/day) | Maximum root depth (m) | Time to attain the maximum transpiration (days) |
|---|---|---|---|---|---|
| Cash and oil crops | Caster beans | 1110 | 7.7 | 1.83 | 154 |
| | Cotton | 1030 | 8.8 | 1.83 | 128 |
| | Flax | 782.5 | 5.7 | 1.83 | 162 |
| | Safflower | 1135 | 11 | 1.83 | 138 |
| | Soybeans | 555 | 5.9 | 1.83 | 81 |
| Bermuda lawn and hay crops | Alfalfa | 1857.5 | 8.1 | 2.43 | 132 |
| | Bermuda lawn | 1087.5 | 6 | 1.83 | 88 |
| | Blue panic grass | 1307.5 | 7.4 | 1.83 | 110 |
| Small grain and forage crops | Barley | 632.5 | 9 | 1.83 | 114 |
| | Sorghum | 635 | 10.5 | 1.83 | 54 |
| | Wheat | 572.5 | 8.5 | 1.83 | 112 |
| Fruits | Grapefruit | 1197.5 | 4.8 | 1.83 | 202 |
| | Grapes | 490 | 6.1 | 1.83 | 71 |
| | Navel oranges | 977.5 | 2.1 | 1.83 | 221 |
| Vegetables | Broccoli | 492.5 | 3.2 | 1.23 | 68 |
| | Early cabbage | 430 | 4.3 | 1.23 | 65 |
| | Late cabbage | 612.5 | 2.1 | 1.23 | 69 |
| | Cantaloupe | 472.5 | 9.3 | 1.23 | 77 |
| | Carrots | 437.5 | 2 | 0.92 | 54 |
| | Cauliflower | 465 | 2.6 | 1.23 | 70 |
| | Lettuce | 212.5 | 2.4 | 0.92 | 84 |
| | Dry onion | 582.5 | 5.2 | 0.92 | 173 |
| | Green onion | 415 | 2.3 | 0.92 | 44 |
| | Potato | 607.5 | 7.4 | 1.23 | 84 |
| | Sweet corn | 490 | 10.2 | 1.23 | 70 |
| Green manure crops | Guar | 577.5 | 3.2 | 1.83 | 40 |
| | Papago peas | 487.5 | 3.6 | 1.83 | 93 |
| | Sesbania | 327.5 | 3.9 | 1.23 | 45 |

Nisbet (2005) indicates that the rate of transpiration through a single tree in the field tends to be more unpredictable than that from uniform land cover. Maximum daily transpiration rates of individual trees of varying species tend to range from 500-2000 litres per day which compares with 18 $l$ d$^{-1}$ for an individual tree (un-thinned Sitka spruce) at a density of 3300 stems ha$^{-1}$ (Nisbet 2005). The comparison of the annual water use for various land covers is presented in Table 2.3.

Table 2. 3     Typical range of annual evaporation losses (mm) for different land covers receiving 1000 mm annual rainfall, reproduced from Nisbet (2005)

| Land cover | Transpiration (mm) | Interception (mm) | Total evaporation (mm) |
|---|---|---|---|
| Conifers | 300-350 | 250-450 | 550-800 |
| Broadleaves | 300-390 | 100-250 | 400-640 |
| Grass | 400-600 | - | 400-600 |
| Heather | 200-420 | 160-190 | 360-610 |
| Bracken | 400-600 | 200 | 600-800 |
| Arable (no irrigation) | 370-430 | - | 370-430 |

The rate of transpiration is usually expressed in litres or millimetres per unit time. The length component expresses the quantity of water depletion through a vegetated surface as an equivalent depth of water. The time unit can be expressed in hours, days, decades, months or even a whole growing period or years, depending on context. For example, 1 ha is equal to an area of 10000 $m^2$ and 1 mm corresponds to 0.001 m, 1 mm of water lost from the area of 1 ha soil surface is corresponding to 10 $m^3$ of water per ha. Explicitly, 1 mm/day is equal to 10 $m^3$ $ha^{-1}$ $day^{-1}$. Allen et al. (1998) indicates that an equivalent depth of water can also be used to express energy (latent heat of vaporization) required to vaporize water per unit area. For instance, when the temperature is 20°C, this energy is approximately 2.45 MJ $kg^{-1}$. It can be found that vaporizing 1 kg (or 0.001 $m^3$) of water requires 2.45 MJ. Therefore, a loss of 1 mm of water corresponds to 2.45 MJ $m^{-2}$.

The rate of transpiration is one of the most significant values employed in modelling the water-uptake process. It can be determined using professional equipment or by measuring a range of physical parameters. By calculating the different parts of soil water balance, the plant transpiration can also be evaluated (see Figure 2.3). Unlike some other hydrological variables, such as runoff or precipitation, which can be measured directly, transpiration can

be generally estimated indirectly. Some methods have been used to determine transpiration for a single tree, such as the cut leaf method, chemical tracer measurements (Calder et al. 1992) or the heat-pulse method (Nicolas et al. 2005) for calculating sap flow, and Infra-red gas analysis (Stokes 2004) or porometer measurements of leaf transpiration (Schulze et al. 1985). However, those approaches are usually high-cost and difficult to operate in terms of accurate measurements (Allen et al. 1998). A number of the most commonly used evapotranspiration measurement methods summarised by Shuttleworth (2008) are shown in Table 2.4.
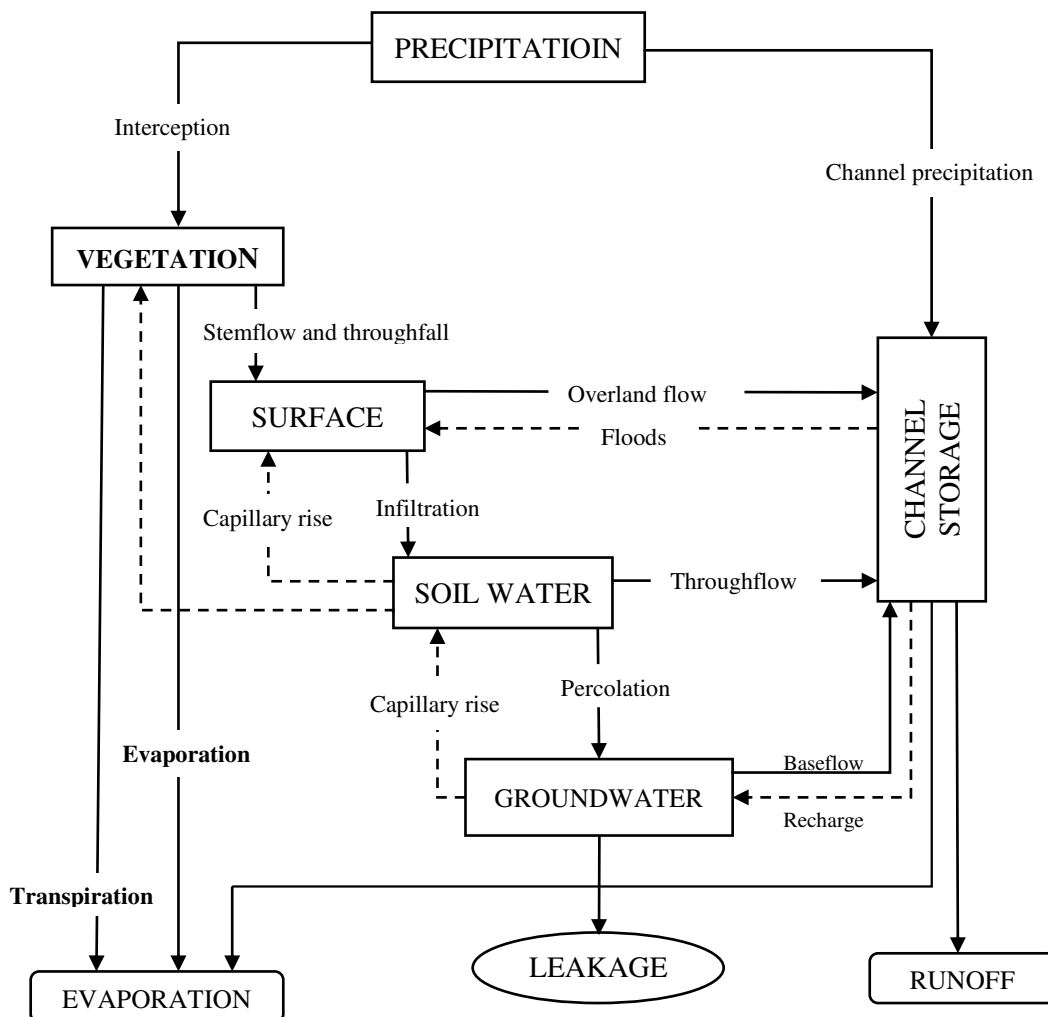
Figure 2. 3    The drainage basin hydrological system (adapted from Ward and Robinson 2000)

Table 2. 4    Evapotranspiration measurement methods (reproduced from Shuttleworth 2008)

| | Brief Description | Strengths and weaknesses |
|---|---|---|
| **Evaporation pan** | Directly measures change in water level over time for a sample of open water in a "pan". | A long-established method, simple and inexpensive; but because it relies on the validity of an extrapolated calibration factor, is primarily used for crop. |
| **Water balance of basin** | The unmeasured difference between other measured components of the basin water balance, including incoming precipitation, surface and groundwater outflow, and soil water storage. | Gives an area-average measurement for vegetation covers, however, area-average measurement of the other water balance terms can be expensive and difficult, especially |
| **Lysimetry** | Measures change in weight of an isolated undisturbed soil sample with overlying vegetation. | If the soil and vegetation sample is truly representative, the lysimeter is widely accepted. Modern high-precision lysimeters are expensive and require expert supervision. |
| **Soil moisture depletion** | Measures change in water content of a representative sample of undisturbed soil and vegetation while measuring precipitation and run-on/runoff and estimating deep drainage for the sample plot. | Measurement is reasonably inexpensive, but disturbance during installation of soil water sensors. Deep drainage is hard to estimate. |
| **Bowen Ratio - Energy Budget** | Calculates evaporation as latent heat from the surface energy budget using the ratio of sensible to latent heat (Bowen ratio) derived from the ratio between atmospheric temperature and humidity gradients measured a few meters above vegetation. | Well-established method. Relatively inexpensive proprietary systems can be purchased that work for both short crops. |
| **Eddy correlation (also called eddy covariance)** | Calculates evaporation as 20- to 60-minute time averages from the correlation coefficient between fluctuations in vertical windspeed and atmospheric humidity. | Currently preferred method for field-scale measurements in research applications. Implemented using relatively expensive proprietary logger and colocated sensors. |
| **Transpiration measurement by porometry or monitoring sap flow** | Porometry: measured from humidity increase in a chamber temporarily enclosing transpiring leaves/shoots. Sap Flow: measured from rate of sap flow in trunk, branches, or roots using heat as a tracer, with an estimate of the area of wood through which flow occurs. | Porometry: a manual measurement that allows determination of environmental influences on stomatal control at leaf level. Sap Flow: allows routine unsupervised measurement of transpiration from whole plants or plant components over extended periods. |

The quantification of water use by vegetation is complex and requires determination of environmental and biological variables. Some theoretical models have been established to predict evapotranspiration based on meteorological variables. Numerous researchers (Penman 1948; Monteith 1965; Rijtema 1965; Allen et al. 1998; Ward and Robinson 2000) developed and used a combination of energy (or thermodynamic) balance and mass transfer

(or aerodynamic) approaches to estimate transpiration rate. Such methods require accurate measurement of radiation, temperature, wind speed and humidity. Most approaches derive from the well-known Penman equation (Penman 1948) to determine evapotranspiration by a combined formulation considering of energy balance and aerodynamics. Monteith (1965) offered an approach with various derivations of the Penman equation including a bulk surface resistance term considering the energy exchanging leaf surface and the result is known as the Penman-Monteith equation. The Penman-Monteith method provides an equation that is useful for computing water evaporation from vegetated surfaces. Thorpe (1978) presented an application of a combination (energy balance-mass transfer) Penman-Monteith equation, derived for transpiration from a particular leaf of tree. Therefore, the rate of transpiration for an entire tree can be established by summing Thorpe's model (1980) over the numbers of tree leaves (Jones et al. 1988; Green 1993; Caspari et al. 1993; Zhang et al. 1997). However, the Penman-Monteith approach requires supporting sub-models or parameterizations for the aerodynamic and surface resistance (Landsberg and Powell 1973; Jarvis 1976; Thorpe et al. 1980; McNaughton 1994; Green and McNaughton 1997; Villalobos et al. 2000; Rana et al. 2005). An alternative approach for calculating transpiration rate of a whole tree, that has limited requirements in terms of site specific data and calibration is therefore attractive.

Table 2. 5    Typical values of aerodynamic resistance and stomatal resistance (s m$^{-1}$) (Szeicz et al. 1969; Miranda et al. 1984; Hall 1987; Oke 1987; Kelliher et al. 1995)

| Land cover | Aerodynamic resistance, $r_a$ | Stomatal resistance, $r_1$ | Canopy resistance, $r_c$ |
|---|---|---|---|
| open water | 125 | 0 | 0 |
| Grass | 50-70 | 100-400 | 40-70 |
| Arable | 30-60 | 100-500 | 50-100 |
| Heather | 20-80 | 200-600 | 60-100 |
| Forest | 5-10 | 200-700 | 80-150 |

On the other hand, the Food and Agricultural Organization (FAO) of the United Nations (Allen et al. 1998) recommended an updated procedure for calculating reference and crop evapotranspiration from climatic data and crop coefficients. In particular, the FAO Penman-Monteith method uses standard data for radiation, air temperature, humidity and wind speed or data derived from commonly measured records for daily, weekly, or monthly computations. Some researchers (Fernández et al. 2001; Nicolas et al. 2005) have utilized the evapotranspiration of grass as a reference value calculated by the FAO Penman-Monteith method (Allen et al. 1998) to determine transpiration rate of trees.

2.3.3   Tree Root System

The most important objectives of the current work focus on the role of below-ground vegetation (especially water-uptake near trees) and the importance of root zone effects on soil moisture. It is therefore important to understand the plant roots can have a significant influence on the water distribution and movement in the soil by the mechanism of transpiration. It is well recognised that roots play a significant role by transporting water and nutrients through soils for the survival of all plants and providing a connection between soil environment and atmosphere (Feddes et al. 2001).

The species of a particular tree influences its moisture demand and rooting configuration. Cutler and Richardson (1989) provide a guide of the maximum height and the horizontal root spread for common trees in Britain and this information is represented in Table 2.6. It appears that the average horizontal root spread is about 6 m for a tree and with an average height of 18 m. Therefore, the horizontal root spread may be roughly one third for the height

of a tree but some variation to this clearly occurs. Some investigations of the distance between trees and buildings in cases where building damage may have occurred due to the presence of a tree have been published (e.g. Cutler and Richardson 1989; Biddle 1998). However, these are generally not based on a direct measurement of root length in-situ.

Table 2. 6      Root spread of commonly planted trees in Britain, modified after Cutler and Richardson (1989)

| TREE SPECIES | | Max Tree Height (m) | Horizontal Root Spread (m) |
|---|---|---|---|
| APPLE | *Malus* | 10 | 4 |
| ASH | *Fraxinus* | 14 | 6 |
| BEECH | *Fagus* | 20 | 6 |
| BIRCH | *Betula* | 14 | 4 |
| CHERRIES | *Prunus* | 12 | 3 |
| DAMSONS | *Prunus* | 8 | 3 |
| ELM | *Ulmus* | 25 | 8 |
| FALSE ACACI | *Robinia* | 20 | 7 |
| HAWTHORN | *Crataegus* | 10 | 5 |
| HORSE CHESTNUT | *Aesculus* | 25 | 7.5 |
| LIME | *Tilia* | 24 | 6 |
| MAPLES | *Acer* | 24 | 6 |
| OAK | *Quercus* | 23 | 9.5 |
| PEAR | *Pyrus* | 12 | 4 |
| PLANE | *Platanus* | 30 | 5.5 |
| PLUMS | | 8 | 3 |
| POPLAR | *Populus* | 28 | 11 |
| ROWAN | *Sorbus* | 12 | 5 |
| SERVICE TREE | *Sorbus* | 12 | 5 |
| SYCAMORE | *Acer* | 24 | 6 |
| WHITE BEAM | *Sorbus* | 12 | 5 |
| WILLOW | *Salix* | 25 | 7 |

Root distribution and structure is determined by factors which include type of soil, species of plant, plant physical condition, planting density, environmental conditions and forest management. Dobson (1995) points out that a common misconception with regard to the architecture of tree root systems is that the roots volume and distribution is considered to reflect that of the trunk and branches as can be seen in the Figure 2.4a. A more realistic

image of tree roots is presented in Figure 2.4b. Commonly, the root system of trees is shallow and extensive (Dobson and Moffat 1993; Dobson 1995). Crow (2005) indicates that 80 – 90 % roots are detected within the top 0.6 m of the soil profile and suggest that it is rare for the plant roots reach at a depth deeper than 2 m.
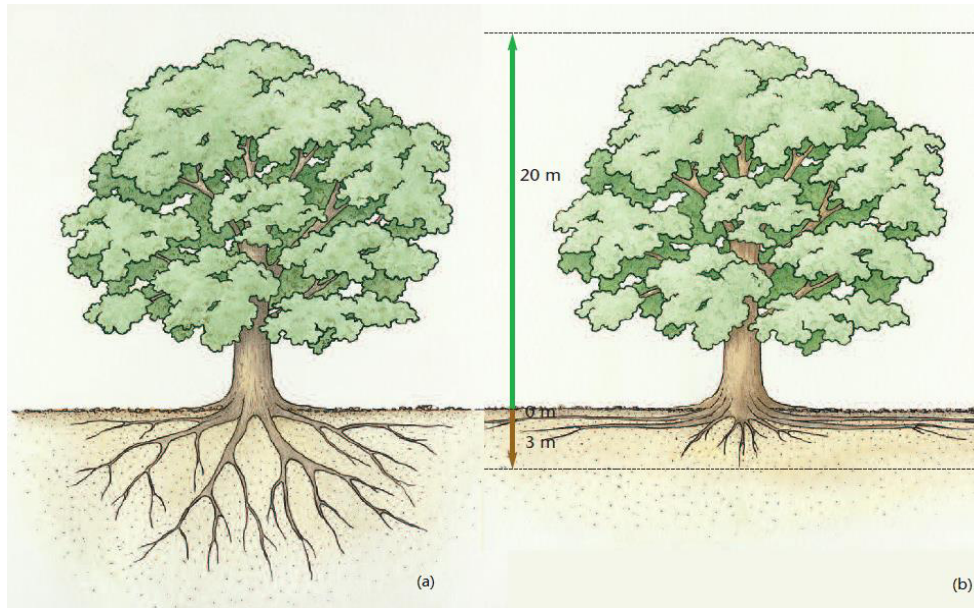


Figure 2. 4     The commonly held idea of root systems for a tree (a) and a more realistic representation (b), reproduced from Dobson (1995)

There are three primary types of root system architecture related to the characteristics of species (Büsgen et al. 1929). However, it is also noticed that the shape of the root system for a single species could be considerable variable. Figure 2.5 shows some examples of tree root system for three types of tree. The main categories of root systems are:

i.     Tap root systems – which have a strong main root that grows vertically downward as a dominant-root system. (e.g. English oak, Scots pine and sliver fir)

ii.    Surface root systems - which large horizontal lateral roots extend below the surface, from which smaller roots descend vertically. (e.g. birch, beech, larch and Norway maple)

iii.    Heart root systems - which have large and small roots that penetrate diagonally into the soil from the trunk. (e.g. ash, aspen, Norway spruce and white pine)



(a)  Tap roots                          (b)  Surface roots



(c)  Heart roots

Figure 2. 5     Typical root system types (reproduced from Mulrean 2000)

Trees are dependent on their roots as a food storage organ to obtain nutrients, water and support (Coutts 1987; Crow 2005). The growth of the tree root system is determined by both environmental conditions and the species of tree (Crow 2004; Crow 2005). Some generalisations about the rooting characteristics of common tree species on different soil conditions and grouped into three different types of root system are shown in Table 2.7. Certainly, although the outlined shapes of root systems here are beneficial to define the rooting characteristics, many exceptions may occur for a species in a different environment (Dobson and Moffat 1993).

Table 2. 7    Rooting information and relative water demands for some common tree species (modified after Dobson and Moffat 1993; Crow 2004; Crow 2005).

| Species | Regrowth (0=never, 1=rarely, 2=likely, 3=vigorus growth) | Typical root architecture [b] | Typical root depth (m) [b] | Mechanical root penetration | Water requirements 1=lowest 6=highest | Soil groups | | | | | | | |
|---|---|---|---|---|---|---|---|---|---|---|---|---|---|
| | | | | | | Loose, deep well-drained soils | Shallow soils over rock | Intermediate loamy soils | Impervious subsoils | Soils with moisture retaining upper horizons | Soils with wet lower horizons | Organic rich soils (drained) | Organic rich soils (waterlogged) |
| Ash | 3 | Surface | 1.1 | Medium | 2 - 4 | * | ** | | ** | * | * | ! | *** |
| Aspen [a] | 3 | Surface | 1.3 | High | 4 - 6 | * | ! | | | | | ! | * |
| Birch | 2 | Heart | 1.8 | Medium | 1 - 2 | | | | | | | | |
| Beech | 1 | Heart | 1.3 | Low | 2 - 3 | ** | ! | | ! | ! | ! | ** | *** |
| Common alder [a] | 3 | Heart/surface | 2 | High | 2 | ** | ! | | ! | | ! | ! | ! |
| Corsican pine | 0 | Tap | - | Medium | 1 | | | | | | | | |
| Douglas fir [a] | 0 | Heart | 2 | High | 1 - 2 | * | ** | | * | * | * | ! | *** |
| English oak [a] | 2 | Tap | 1.5 | High | 3 - 6 | * | | | ! | | | ! | *** |
| European larch | 0 | Heart | 2 | High | 1 | | ! | | | ** | ** | ! | ** |
| Hornbeam [a] | 2 | Heart | 1.6 | Medium | 2 | * | ! | | ! | | | ! | *** |
| Japanese larch [a] | 0 | Heart | - | Medium | 1 | ** | ! | ! | | ! | ! | ! | * |
| Lime | 2 | Heart | 1.3 | Low | 3 - 4 | ! | ! | | ! | ! | ! | ! | *** |
| Norway maple | 2 | Heart | 1 | - | 2 - 3 | ** | ** | | ** | ! | ! | ** | *** |
| Norway spruce | 0 | Surface | 2 | Low | 1 | * | | | ! | | ! | ! | * |
| Poplar [a] | 3 | - | - | - | 4 - 6 | ** | ** | | ! | | ! | ** | ** |
| Red oak [a] | 2 | Heart | 1.6 | Medium | 3 - 6 | * | | | ! | | | ! | *** |
| Scots pine | 0 | Tap | 2.1 | High | 1 | | | | | | | | |
| Sessile oak | 2 | Tap | 1.5 | High | 3 - 6 | | | | | | | | |
| Silver fir | 0 | Tap | 2 | High | 1 | | | | | | | | |
| Sycamore | 2 | Heart | 1.3 | Low | 2 - 3 | | | | | | | | |
| White pine | 0 | Surface | 1.7 | Low | 1 | | | | | | | | |

[a] Unlikely if soils are calcareous.
b When grown in well drained sandy soils.
*** Conditions not recommended for growth.** Not ideal and growth may be impeded(will vary from site to site).
* Not ideal for growth but some values published.
! Values are conjectural(all others values are from database).

Probable rooting depth range for mature trees

| | | | | | | | |
|---|---|---|---|---|---|---|---|
| | < 0.5 m | | < 1.5 m | | < 2.5 m | | < 4.0 m |
| | < 1.0 m | | < 2.0 m | | < 3.0 m | | |

Stokes (2002) also provided a summary of tree species (presented in scientific name) with three root system types as presented here in Table 2.8, however, it is only indicative, since many of the structures of root systems are extremely flexible. The architecture of root system may be complicated and it is significantly dependent on local environmental conditions.

Table 2. 8    Tree species for three root system types (Stokes 2002; Bűsgen et al. 1929; Kőstler et al. 1968; Eis 1978; Kutschera and Lichtenegger 1997, 2002; Wu 2007).

| Type of root system | | |
|---|---|---|
| **Plate or Surface** | **Heart** | **Tap** |
| *(Betula pendula Roth.)* | *Acer campestre* L. | *Abies alba* Mill. |
| *Fraxinus excelsior* L. | *Acer platanoides* L. | *Juniperus communis* L. |
| *Picea abies* L. | *Acer pseudoplatanus* L. | *(Quercus sp.)* |
| *Picea sitchensis* Bong. | *Alnus glutinosa* L. | *Pinus contorta* Dougl. |
| *Pinus cembra* L. | *Alnus incana* L. | *Pinus nigra* Arnold |
| *Pinus radiata* D. | *Betula verrucosa* Ehrh. | *Pinus pinaster* Ait. |
| *Pinus strobus* L. | *Carpinus betulus* L. | *Pinus syslvestrs* L. |
| *(Populus sp.)* | *Crateagus monogyna* Jacq. | *Pyrus pyraster* Burgsd. |
| *Populus tremula* L. | *Castanea sativa* Mill. | *(Robinia pseudoacacia* L.*)* |
| *(Robinia pseudoacacia* L.*)* | *(Fagus sylvatica* L.*)* | *Sorbus torminalis* L. |
| *(Sorbus aucuparia* L.*)* | *Larix decidua* Mill | |
| | *Larix leptolepis* Sieb. | |
| | *(Populus sp.)* | |
| | *Prunus avium* L. | |
| | *Pseudotsuga menziesii* Mirb. | |
| | *Pseudotsuga taxifolia* Britt. | |
| | *Quercus petraea* Liebl. | |
| | *Quercus robur* L. | |
| | *Quercus rubra* L. | |
| | *Taxus baccata* L. | |
| | *Tilia cordata* Mill | |
| | *Tilia platyphyllos* Scop. | |
| | *Ulmus effusa* Willd. | |
| | *Ulmus glabra* Huds. | |
| | *Ulmus montana* With. | |

Most of the studies of root architecture carried out in the Northern Hemisphere have revealed that the majority of tree roots are established within the first few metres below the soil surface (Shields and Gray 1992; Greenway 1987; Schenk and Jackson 2002a,b; Roering et al.

2003; Danjon et al. 2005; Reubens et al. 2007).  However, some researchers (Coatsworth and Evans 1984; Williams and Pidgeon 1983) indicated the roots of *Eucalyptus obliqua* in Australia have an average depth of 25m approximately.  Carbon et al. (1980) found that some plant roots (e.g. *Eucalyptus marginata*) may grow to depths of more than 20m in clay soils. Although the opportunities to explore the whole root systems of mature trees with varied species are uncommon, Cutler et al. (1989) conducted a survey for wind thrown trees and reports only 2.4 % were found to have deep roots or tap roots and no trees had roots deeper than 3m.  Two recent photos of storm blown tree are presented in Figure 2.6.  It is widely recognised that the rooting habit of a tree is significantly affected by the characteristics of various soil types (Crow 2005).



Figure 2. 6     Storm blown tree showing typical root plate (photos taken from Cardiff in 2014)

Although most researchers consider the morphology of root systems is an important factor, relatively few researchers have contributed on this aspect of plant root architecture until recently (Norris et al. 2008; Danjon et al. 2008; Hubble et al. 2010).  Coutts et al. (1999) indicate that the root architecture of a tree can be presented in a regular asymmetric system

and irregular arrangement, and the individual roots could have a significant variation of diameter (see Figure 2.7). Hubble et al. (2010) provide four representative geometry examples of the root systems for the common riparian species in terms of cross-sectional and plan views. The plan views show the root system with a radial distribution and the cross-sectional view presents the growth of near-surface lateral root and prominent tap root as shown in Figure 2.8. Danjon et al. (2008) presented two typical tree root architectures in slope stability context (see Figure 2.9).

This type of information, although limited, provides useful guidance for the modelling work presented in Chapter 6 and 7 of the thesis.



(a) Regular asymmetry

(b) Irregular asymmetry
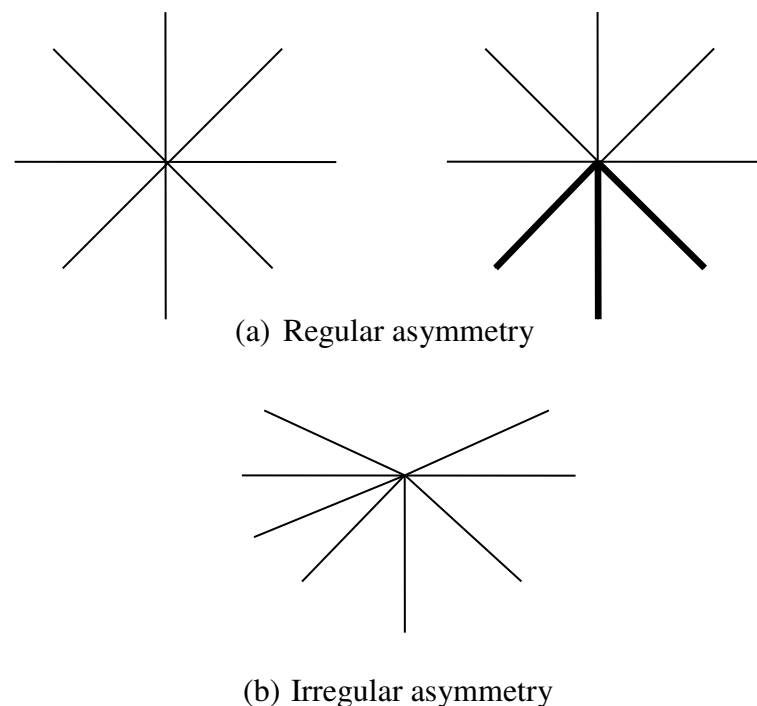
Figure 2. 7    Roots systems with different types of asymmetry: a) regular asymmetry and individual roots can be varied in diameter b) the arrangement of roots is irregular, figure reproduced from Coutts et al. (1999)
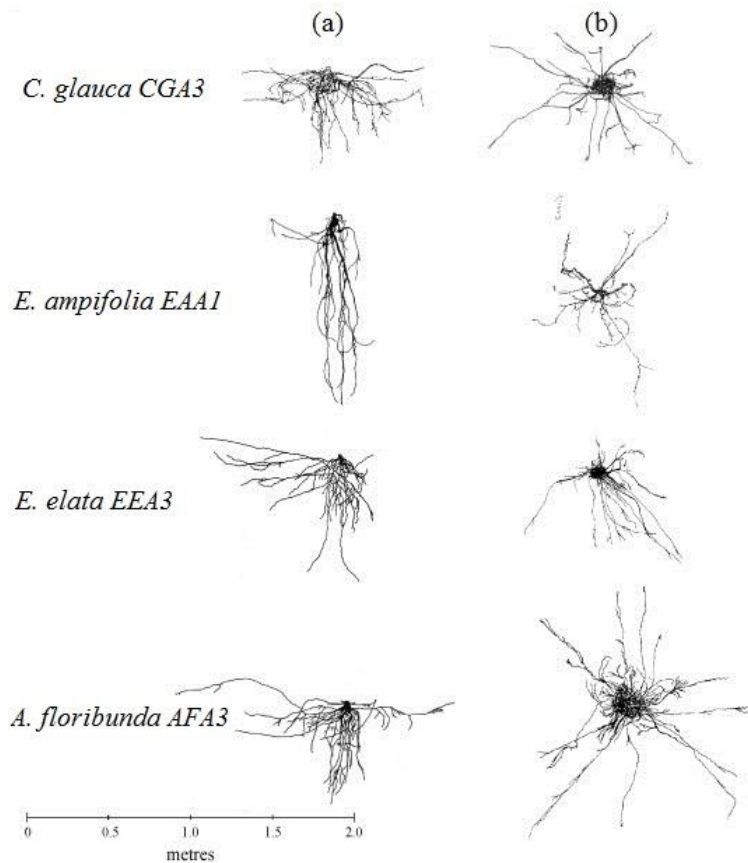
Figure 2. 8    Comparisons between typical root systems for some common east Australian riparian trees in (a) cross-sectional view, and (b) plan view, figure adapted from Hubble et al. (2010)



Figure 2. 9    Two typical tree root architectures in the slope, figure reproduced from Danjon et al. (2008)

## 2.4    WATER-UPTAKE MODELS

The influence of vegetation on pore-water pressures relates to the dynamic factors of the atmosphere, and the physical properties of the soil. Therefore, most root water-uptake models need to consider the influence of soil suction, root distribution and transpiration rate (Indraratna et al. 2006).

There are two major methods use to express the mechanism of water-uptake by plant roots (Feddes et al. 1976; Mathur and Rao 1999). The first approach is known as the 'microscopic' approach that typically follows radial flow of soil water to an individual root (Luo et al. 2003; Mu'azu and Ali 2011). Alternatively, a 'macroscopic' treatment of this problem can be developed to represent the whole root system acting as a single unit (Mu'azu and Ali 2011).

Phillip (1957) assumed radial flow of water towards a single root in one of the earlier investigations of the microscopic strategy. In this work, the plant roots were represented as a large number of infinitely long tubular roots planted into cylindrical soil volumes. Phillip (1957) also considered a constant rate of evaporation and the estimation of the hydraulic conductivity was independent of moisture content. Further developments based on the microscopic model and developed works of Philip (1957) have been published afterwards by many researchers (Gardner 1960; Cowen 1965; Passioura and Cowen 1968; Molz and Remson 1970; Hillel et al. 1975; Molz and Hornberber 1973; Pagès et al. 1989; Nobel and Alm 1993; Steudle 1994; Personne et al. 2003). However, the microscopic approach cannot be easily tested through experimentation and the boundary conditions required are not easily defined due to the experimental evaluation of root properties is not practical and the root

system is time dependent (Šimůnek et al. 1992; Wu et al. 1999; Vrugt et al. 2001b, Li et al. 2006).

Gardner (1964) firstly introduced a numerical model to represent a non-uniform root water-uptake based on the macroscopic approach which treats the root system as a single unit that does not take into account the effect of individual roots because of the difficultly in measuring the time-dependent geometry. A good correlation between the experimental and theoretical water-uptake was achieved. Therefore, most water uptake models tend to adopt the macroscopic approach rather than the microscopic model.

Based on the macroscopic approach, the root water uptake models can be further separated into two categories. One category considers the hydraulic parameters and water potential inside the roots of plant (Hillel et al. 1975; Molz 1981; Nimah and Hanks 1973; Kramer and Boyer 1995), although these are not easy to obtain. In the other category, the calculation of root water extraction rate is based on the transpiration rate of vegetation, soil water potential and the geometry of the plant roots (Feddes et al. 1976, 1978; Gardner 1983; Molz and Remson 1970; Prasad 1988; Raats 1974). It has been implemented in many mathematical models due to the fact that the parameters needed are not difficult to quantify (Šimůnek et al. 1992).

The macroscopic approach has been used quite widely (Whisler et al. 1968; Feddes et al. 1978; Molz 1981; Clausnitzer and Hopmans 1994; Green et al. 2003; Indraratna et al. 2006; Rees and Ali 2006; Fatahi et al. 2010), where the extraction of soil water caused by plant roots distributed in the soil is implemented by a sink term. The sink term is most often combined inside Richards equation to describe soil moisture flow. A macroscopic water

uptake model is then required to effectively distribute the volume of soil moisture extracted from the root zone in a pattern that mimics that observed in the field.

For the practical reasons stated above, the current study also employs a macroscopic approach. The precise approach developed here is described in Chapters 3 and 4. A targeted review of the development of water uptake models follows below.

2.4.1   One-Dimensional Water Uptake

Within the context of agricultural science and the assessment of the performance of crops, early models for water uptake, naturally focused on one-dimensional models that could be expected to yield 'typical' behaviour beneath an area of land that was uniformly covered by a crop. Feddes et al (1978) proposed one of the key models where the available transpiration was initially employed over the root zone and then decreased to actual root water-uptake through the use of a reduction function for soil water stress. This research formed the basis for a number of subsequent developments. Notably, Prasad (1988) developed a linear root distribution functions based on Feddes et al. (1978) and Hoogland et al. (1981) to represent water uptake. The linear extraction term varied with time and considered a zero rate of water extraction at the bottom of plant root (Prasad 1988). This approach provided an important development in water-uptake modelling. Prasad's model (1988) was conceptually simple and shown to be capable of representing real behaviour (Rees and Ali 2006; Nyambayo and Potts 2010).

In further developments, Gardner (1991) presented a sink term based on the depth of plant root and a parameter of water extraction. The model used a distributed sink moving downward through the soil profile, however, the moving sink was found not to explicitly explain the observed uptake patterns thoroughly (Gardner 1991).

Mathur and Rao (1999) proposed a numerical approach which considered root growth by implementing a sinusoidal 'root growth function'. However, the time dependent nature of root behaviour was not completely validated due to a relatively short time period simulated.

Li et al. (1999, 2001) examined the difference between Prasad's linear approach (Prasad 1988) and an alternative exponential model for non-uniform root distribution. The cumulative water uptake of both models was the same after 30 days, while the cumulative water uptake for the linear and exponential model differed by only 5 % after 60 days. This comparison suggested that a simple linear model may be adequate for some practical problems rather than an exponential model. However, non-linear models may provide the more exact geometry of the resulting moisture migration pattern in some circumstances.

Further contributions (e.g. Lai and Katul 2000; Nyambayo and Potts 2010) considering the behaviour of root water-uptake on the influence of potential and actual transpiration have been published. Zuo et al. (2006) also developed an approach to simulate water extraction rates at various depths by using the potential root water-uptake coefficient and the normalized root length density function. Dardanelli et al. (2004) proposed a simple model based on generalizations from the changes of measured soil moisture content to simulate water uptake by plant root. Braud et al. (2005) presented an appropriate evaluation of the water uptake while Li et al. (2006) developed a root water uptake model that explored recently presented

functions for asymptotic root distribution and water stress reduction.

Some researchers (Gardner 1964; Homaee 1999; Vrugt et al. 2001a; Hopmans and Bristow 2002) focus on transient simulation since the spatial distribution of actual root water uptake is determined not only by the distribution of root density but also on its transient response based on soil salinity and the availability of soil water. In irrigated soils, both salinity and water stress mainly affect the growth and development of plant. The efficiency in the utilization of water and nutrient uptake can be important in determining crop yield. Consequently, these models can be used to study the movement of both water and chemical substances in soils.

Recently, a model of root water-uptake considered the influence of soil temperature by employing irrigation operation was developed (Lv et al. 2013). The results indicate that root water-uptake was certainly affected directly or indirectly by the temperature of soil and that model taking the temperature of soil into account may enhance the accuracy of simulation. In addition, Kumar et al. (2013) developed and validated a non-linear root water-uptake model including an empirical relationship to present the nonlinear uptake parameter to mimic the depletion of soil water with non-uniform crop root systems.

All of the above studies have only considered water-uptake in one-dimension. This is an understandable hypothesis for the investigation of uniform crops/vegetation that covers a large surface of soil. However, for an individual tree or trees, this simplification may not present suitable. Therefore, the following section of the review considers developments that consider this aspect of the problem.

2.4.2   Multi – Dimensional Water Uptake

Neuman et al. (1975) was one of the earliest researchers to focus on multi-dimensional water-uptake by plants.  In this study, a numerical simulation was employed to deal with non-steady moisture flow of porous media in two-dimensions.  Warrick et al. (1980) proposed a mathematical model to simulate the process of water-uptake considering an unsaturated hydraulic conductivity as an exponential function of pressure head under steady state conditions but this model is limited only to uniform soil, negligible surface loss and is not time dependent.  Coelho and Or (1996) presented a parametric study of two-dimensional water-uptake by corn roots for drip irrigation management based on the experimental work without any numerical simulations.

Somma et al. (1998) presented a model to allow the simultaneous, transient three-dimensional simulation of the transport of water and solute, root water and nutrient uptake, and the root growth following the work of Clausnitzer and Hopmans (1994).  However, this model was only validated for short simulation periods and lacked consideration of root distribution.

Vrugt et al. (2001a) and Vrugt et al. (2001b) utilised Raats's model (1974) and developed it incorporating a radial component and a thickness term for solving two-dimensional and three-dimensional problems.  Limitations of this model include; a lack of consideration of root distribution, a short simulation time, and parameters that were found to be difficult to determine.

Gong et al. (2006) provided a 2D model for individual apple tree.  The simulation was verified by comparison with soil moisture content measurements from an orchard.  The

model included potential transpiration, a function of root density distribution, and a soil water stress modification factor. Although root growth was the main concern in this model, it was not applied to consider seasonal variations.

Indraratna et al. (2006) have developed a two-dimensional water-uptake model employing to the commercially available software, ABAQUS. Their simulation was compared to experimental data provided by Jaksa et al. (2002) for a Gum tree and data provided by Biddle (1998) for a Lime tree. However, a simplified root zone geometry (conical geometry) were included in this work.

Rees and Ali (2006) presented a numerical simulation of seasonal soil water movement in the vicinity of a mature lime tree located on boulder clay. The 2D axi-symmetric flow model was based on the application of Richards equation for unsaturated moisture flow combining a sink term. The study utilized radial symmetry and assumed water extraction rates by a linear distribution with both root depth and radial distance from the trunk of the tree. This mimics behaviour observed in field measurements (Biddle 1998).

It is also clear that simplifying assumptions regarding root geometry have been made in most attempts to model water-uptake in the vicinity of trees. Figure 2.10 shows some of the imposed root geometries that can be found in the literature. All of these models simplify the geometry of the root zone largely ignoring the complexities of the natural architecture of root system. It is recognised however that such approaches result in mathematical models that are readily amenable to implementation in both analytical and numerical solutions of boundary value problems. For reasons stated above, an alternative and new approach that aims to avoid some of this simplification is described in Chapters 3.
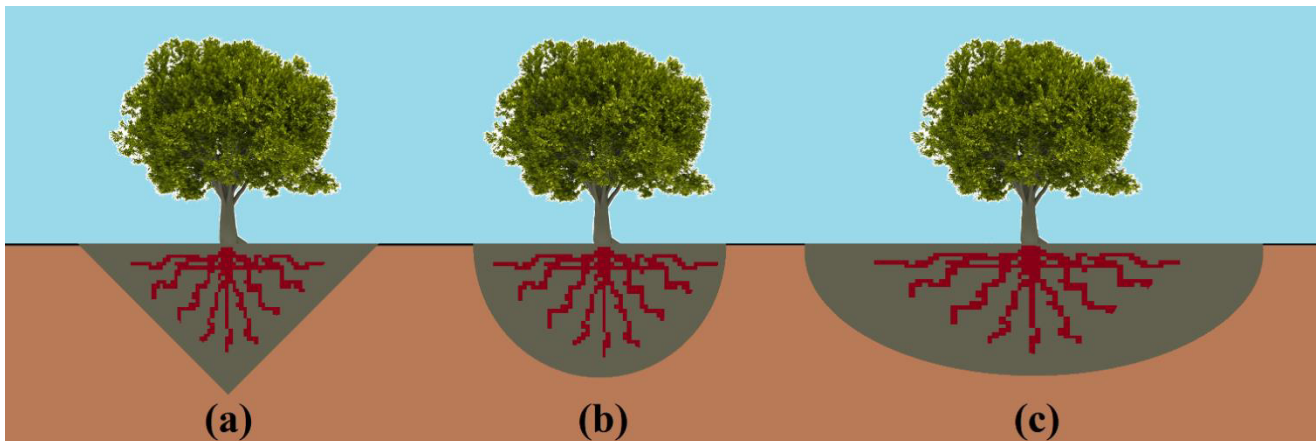
Figure 2. 10    Axisymmetric water uptake models for trees
(a) Conical Geometry (Indraratna et al. 2006); (b) Hemi-spherical Geometry (Vrugt et al. 2001a); (c) Elliptical Geometry (Rees and Ali 2006)

Recently, a three-dimensional model of the soil-plant scheme has been presented and applied to mimic soil moisture extraction by overlapping rooting systems of Loblolly pine trees (Manoli et al. 2014).    This approach utilises a numerical solution to solve the three-dimensional Richards equation developed to account for 3D transpiration and leaf photosynthesis (Manoli et al. 2014).

To date, water uptake models greatly simplify the complexities of the natural architecture of root system and often study behaviour over relatively short periods of time.  Therefore, this research aims to explore water-uptake simulation for an established tree with a new image based root-density approach.  The current work will also explore time dependent boundary conditions due to rainfall and surface effects.

2.5     SLOPE STABILITY& VEGETATION

Slope stability analysis is used to calculate a factor of safety against possible failure of a slope.   In general, it aims to determine the critical circular slip failure surface that corresponds to the lowest factor of safety.   A range of well-known methods have been established, e.g. Swedish or Fellenius's method (1936), Bishop's Simplified method (1955), Janbu's Simplified method (1956), Morgenstern and Price's method (1965), and Spencer's method (1967).   These methods differ with respect to how they handle the four inter-slice forces to satisfy all equations of statics.   The Swedish method of slices or Fellenius method (1936) ignores all inter-slice forces and satisfies moment equilibrium only.   It was the first method developed, in which a factor of safety can be calculated by hand.   Later, Bishop (1955) proposed a method which assumed the inter-slice normal forces to be horizontal but ignored the inter-slice shear forces, and satisfied only moment equilibrium condition. Consequently, the factor of safety occurred on both sides of equation and an iterative process is necessary for solution.   The Janbu's simplified method (1956) is the same as the Bishop's Simplified method in that both methods assume the normal inter-slice forces to be horizontal and neglect the inter-slice shear forces, but satisfy force equilibrium only.   Subsequently, computers have made it easier to manage the iterative process and to solve more comprehensive mathematical expressions that make the equations of equilibrium determinate and contain all inter-slice forces.   For example, the Morgenstern and Price method (1965), and Spencer's method (1967) were developed, which include all the inter-slice forces, and respects both moment and force equilibrium.   The details of the various limit equilibrium methods are summarised in Tables 2.9 and 2.10.

Table 2. 9    Conditions of static equilibrium satisfied by different limit equilibrium methods, modified after Krahn (2015)

| Method (circular slip surface) | Force Equilibrium | | Moment Equilibrium |
|---|---|---|---|
| | Vertical Direction | Horizontal Direction | |
| Swedish or Fellenius's method 1936 | Yes | No | Yes |
| Bishop's Simplified method 1955 | Yes | No | Yes |
| Janbu's Simplified method 1956 | Yes | Yes | No |
| Morgenstern and Price's method 1965 | Yes | Yes | Yes[*] |
| Spencer's method 1967 | Yes | Yes | Yes |
| [*]Moment equilibrium on individual slice is used to calculate interslice shear forces | | | |

Table 2. 10    Assumptions employed in different limit equilibrium methods, modified after Krahn (2015)

| Method (circular slip surface) | Interslice Normal Force | Interslice Shear Force | Assumption |
|---|---|---|---|
| Swedish or Fellenius's method 1936 | No | No | Interslice forces are neglected. |
| Bishop's Simplified method 1955 | Yes | No | Resultant interslice forces are horizontal (i.e., there are no interslice shear forces). |
| Janbu's Simplified method 1956 | Yes | No | Resultant interslice forces are horizontal. An empirical correction factor can be used to account for interslice shear forces. |
| Morgenstern and Price's method 1965 | Yes | Yes | Direction of the resultant interslice forces is determined using an arbitrary function. The percentage of the function required to satisfy moment and force equilibrium is computed with a rapid solver. |
| Spencer's method 1967 | Yes | Yes | Resultant interslice forces are of constant slope throughout the sliding mass. |

As indicated previously in the thesis (Chapter 1), the condition assessment of earth-works has been recognised to be significant for construction companies, since the removal and growth of vegetation are often encountered.    Therefore, an evaluation of slope strength in the

presence of trees, or other vegetation, is clearly of value in this context. Moreover, many researchers (Thorne 1990; Simon and Darby 1999; Simon et al. 2000; MacNeil et al. 2001; Greenwood et al. 2004, 2006; Pollen and Simon 2005; Norris et al. 2008; Stokes et al. 2009; Osman and Barakbah 2011; Rees and Ali 2012; Leung and Ng 2013; Ng et al. 2014; Leung et al. 2015; Kokutse et al. 2016) state that vegetation is commonly recognised to be an environmentally sympathetic/sustainable choice for improving the stability of a slope.

The influence of vegetation on slope stability can be categorised as either hydrological or mechanical. For example, the weight of vegetation and tensile strength of roots are known as 'mechanical effects' (Leung et al. 2015). In the past decades, mechanical reinforcement from the roots have been widely studied in slope stability (Greenwood et al. 2004; Hubble et al. 2010; Osiński et al. 2014; Leung et al. 2015; Kokutse et al. 2016). For stability analysis, an approach has been developed by Greenwood et al. (2004, 2006). This approach employed conventional limit equilibrium extended to include some of the most important effects of vegetation, such as; vegetation mass, groundwater conditions, effects of wind forces, increased cohesion and the anchoring effects caused by roots. Although this approach included changes of ground water table caused by vegetation, the research was based on piezometer records – there was no numerical modelling for this phenomenon considered in this research. Furthermore, it employed the effective stress analysis and hence it was only strictly applicable for saturated soils.

Docker and Hubble (2009) proposed mathematical relationships for both vertical and lateral root patterns beneath mature trees and employed them to study the effect of root cohesion and root area ratio based on spatial root distribution. This research presented an estimation of the increased soil shear strength due to the spatial root distribution beneath a full-sized mature

tree. Four tree species were investigated and the work concluded that the improvement of soil shear strength caused by the tree roots is extremely dependent on the geometric extent and the spatial density of roots.

The impact of plant variety on the stability of slope was explored at the early stages of succession in a diverse forest in the Sichuan province of China by Genet et al. (2010). In simulations with trees positioned at the top or in the middle of the slope, the factor of safety was found to decrease because the weight of the tree contributed a significant surcharge to the slope, while the factor of safety increased when the tree was located at the toe of the slope (Genet et al. 2010). Genet et al. (2010) also indicated that tree root density and size were more significant in affecting the stability of the slope than root tensile strength between different species. However, this study did not consider the influence of root architecture or the changes of pore-water pressure caused by the plant on slope stability.

A combined study of field and experimental investigations was carried out in Australia that estimated the role of local plants in mass failure of riverbanks (Hubble et al. 2010). This work demonstrated that the presence of vegetation on riverbanks significantly increases the stability of riverbank slopes as a result of soil reinforcement by plant roots.

Leung et al. (2011) estimated the mechanisms for triggering rainfall-induced landslides in Hong Kong. A comprehensive field monitoring programme for the measurement of the two stress-state variables (i.e. net normal stress and matric suction) was implemented in a saprolitic hillslope. The research revealed that the infiltration and deformation properties of unsaturated mixed soil slopes in Hong Kong under seasonal climatic variations were highly complicated.

Fan and Lai (2014) investigated the mechanical effects of vegetated slopes and the influence of the plant root spatial distribution on the slope stability by employing 3D numerical modelling. However, the influence of the distribution pattern of the root system architecture on assessment of the stability of vegetated slopes was not considered. Leung et al. (2015) considered the behaviour of four Hong Kong native shrubs and trees. Variation of root cohesion with depth and the contribution of roots to slope stability were assessed. Recently, a 2D numerical analysis of the influence of 'mechanical' parameters (additional root cohesion caused by plant roots) and slope geometry on stability was presented (Kokutse et al. 2016).

By contrast with mechanical effects, any potential benefit arising from the 'hydrological effects' of induced suction (changes in soil moisture content) due to plant transpiration has obtained relatively less attention. In addition, it has been recognized that hydrological effects can be as significant as mechanical effects and in some particular situations may provide a more important improvement on slope stability (Rees and Ali 2012). Therefore, a reasonably simple framework is sought that will allow assessment of the significance of soil suction changes on soil shear strength.

In order to link suction to shear strength, a linear equation for unsaturated soils shear strength was initially proposed by Fredlund et al. (1978). The unsaturated soil shear strength was defined by a linear form of the extended Mohr-Coulomb shear strength equation that employs a parameter $\phi^b$ to account for the rate of increase in shear strength with respect to matric suction. The corresponding failure surface of the extended Mohr-Coulomb criterion is shown in three-dimensional stress space in Figure 2.11.
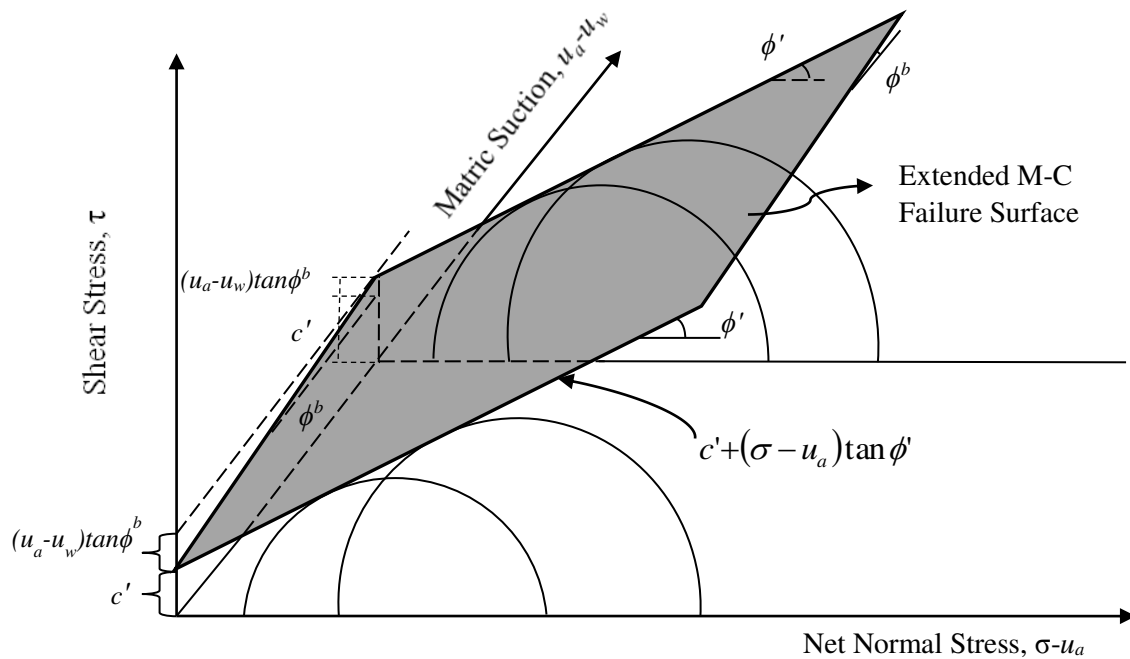
Figure 2. 11    Extended Mohr-Coulomb failure surface for unsaturated soil (modified from Lu and Likos 2004)

Although some other efforts (Escario and Juca 1989; Abramento and Carvalho 1989) have been conducted to calculate unsaturated soil shear strength with empirical procedures, these procedures may or may not be appropriate for a variety of soils.   Nevertheless, there is significant experimental evidence showing in literature (e.g. Donald 1956; Escario and Sáez 1986; Fredlund et al. 1987; Gan and Fredlund 1988) have proved a nonlinear relationship exists between the matric suction and unsaturated soil shear strength.  For analysis purposes, Fredlund et al. (1987) suggest that the nonlinear relationship between shear strength and matric suction can be dealt with by neglecting the nonlinearity and adopting a conservative envelope over the entire suction range with a slope equal to $\phi^b$ ( $\phi^b < \phi'$ ).   Fredlund and Rahardjo (1993) reported some experimental values of $\phi^b$ for various soils worldwide, as shown in Table 2.11.  This parameter is always smaller than or equal to $\phi'$, the saturated

effective angle of friction. For some situations, however, a $\phi^b$ value of zero is employed, indicating that the effect of matric suction is ignored. There are many studies of slope stability that use a constant value of $\phi^b$ to define the unsaturated shear strength (Ng and Shi 1998; Tsaparas et al. 2002; Blatz et al. 2004; Rahardjo et al. 2007; Litvin 2008; Cascini et al. 2010; Rees and Ali 2012).

Table 2. 11    Experimental Values of $\phi^b$ (modified after Fredlund and Rahardjo1993)

| Soil Type | $c'$ (kPa) | $\phi'$ (degrees) | $\phi^b$ (degrees) | References |
|---|---|---|---|---|
| Compacted shale | 15.8 | 24.8 | 18.1 | Bishop et al. (1960) |
| Boulder clay | 9.6 | 27.3 | 21.7 | Bishop et al. (1960) |
| Dhanauri clay | 37.3 | 28.5 | 16.2 | Satija (1978) |
| Madrid grey clay | 23.7 | 22.5 | 16.1 | Escario (1980) |
| Undisturbed decomposed granite | 28.9 | 33.4 | 15.3 | Ho and Fredlund (1982) |
| Tappen-Notch Hill silt | 0.0 | 35 | 16 | Krahn et al. (1989) |
| Compacted glacial till | 10.0 | 25.3 | 25 | Gan et al. (1988) |

Numerous nonlinear equations (Fredlund et al. 1996; Vanapalli et al. 1996; Khalili and Khabbaz 1998; Bao et al. 1998; Garven and Vanapalli 2006; Vilar 2006) were presented for the evaluation of the shear strength of an unsaturated soil. A nonlinear shear strength based on soil water characteristics curve between the saturated and residual soil conditions is suggested by Vanapalli et al. (1996). This model extends the theory proposed by Fredlund et al. (1978) and it is suitable for soils such as tills and clays (Vanapalli et al. 1996). The details of this model will be provided in the Chapter 3.

More supporting information about the significance of soil suction on shear strength is also presented in the literature. For example, Smith (2003) pointed out that a decrease of matric

suction led to a decrease of shear strength that could have been the reason for debris-flow initiation or shallow landslides with a failure surface.

Ridley et al. (2004) explained the roles of climate, soil water loss, and the resulting seasonal pore-water pressure variations caused by the presence of trees in the evaluation of infrastructure embankments. This research suggested that the majority embankment failures in the London region were caused by an enhancement of soil moisture content as there was no transpiration from deciduous trees for the period of winter season. These findings indicate the significance of water uptake by trees in improving the slope stability.

It is clear that vegetation in soil may reduce pore-water pressure as the result of root water uptake (Biddle 1998; Rees and Ali 2006; Indraratna et al. 2006; Nyambayo and Potts 2010; Ng et al. 2013; Ng et al. 2015). The decrease of pore-water pressure generates adequate matric suction to increase the shear strength, thus affecting slope stability. These results further clarify that the water uptake by plant root has a significant influence on slope stability.

As explored and outlined by Indraratna et al. (2006) water uptake by trees has been shown to improve the shear strength of the soil by increasing the matric suction. Limitations of this study include that the role of the root zone on slope stability has not been implemented in the model and the shape of the root zone is of a conical geometry. Rees and Ali (2012) provided a study of water movement patterns around a mature lime tree at three locations of slope and the effects on the stability of slope. However, the calculations of slope stability were based on the same critical slip surface for each case study. The impact of vegetation induced suction on the stability of slope has also been investigated using the centrifuge (Ng et al. 2014). An idealization and simplification of plant transpiration is developed and verified

during a centrifuge model test that can consider both mechanical and hydrological effects of plant roots. Nevertheless, it should be noted that the design of tap-shaped simplified root model is only one of the many types of root architectures.

Recently Ng et al. (2015) considered analytical solutions for predicting pore-water pressure within an infinite unsaturated vegetated slope by utilising four different types of root morphologies (i.e. uniform, triangular, exponential, and parabolic root morphologies). Employing the various solutions, the results showed that the highest negative pore-water pressure in the soil was caused by the exponential root morphology during the dry period, followed by the root architectures with triangular, uniform, and parabolic geometries. In contrast, four different root morphologies present similar distributions of pore-water pressure during a wet period of the simulation. However, the impact of various root morphologies on water uptake by plant root and therefore the influence of pore-water pressure distributions on slope stability are not considered. Zhu and Zhang (2015) estimated the profile of suction for grass covered slope represented by three simplified root geometries (uniform, triangular and parabolic root distribution) and the slope stability in the wet season. The above two studies still ignore the complexities of the natural architecture of root system.

## 2.6   CONCLUSIONS

A general overview of the literature related to modelling water-uptake by plant root in soils has been presented. This revealed the complexity of the problem in hand and described the interactions between the soil, water and plant. This chapter has been targeted to address the specific aspects of the particular problem in hand.

The review shows that trees have rather shallow but widespread root systems. The results from a number of studies show that the maximum root water uptake occurs near the soil surface. This chapter also provided useful guidance of the rooting characteristics of different tree species provides for the subsequent modelling work. However, it was clear that detailed measurement of root architecture for many vegetation types is somewhat sparse. There is also only limited measurement of transpiration and time-dependent processes (growth, decay, climatic conditions etc.). It is reasonably well established that the rate of transpiration for a single tree can be estimated. For example, this can be based on the Penman-Monteith model that includes a range of climatology.

The various approaches found in the literature ranged from simple one-dimensional models to more complex multi-dimensional models suggested by other researchers were discussed. The review indicates that most root water-uptake models have been applied for relatively short time periods. There appears to be a gap in the literature related to the simulation of longer-term seasonal behaviour as may be of interest for a number of engineering problems. More importantly, it was found that the representation of root zone geometry has been significantly simplified in all previous models. Many models assume an 'artificial' geometry employing, for example, linear root density variation, conical geometries or even elliptical root zones. In practical applications, where only the bulk response of the system is of interest, such simplification would appear appropriate. However, where a more precise representation of the zone of influence is required then further refinement may be desirable. Therefore, a simple approach which is capable to represent the complexity of real root systems and more closely mimic the natural root morphology is developed in Chapter 3.

Furthermore, a summary of the historic development of theoretical/numerical models related to the role of vegetation in an estimation of the slope stability has also been provided. This revealed a number of significant steps have already been taken to provide models of slope stability that can account for the main contributions that arise from vegetation. Therefore, a preliminary assessment combined with water-uptake model and slope stability analysis to investigate how suctions generated by a tree may contribute to the overall stability of unsaturated soil slopes is explored in Chapter 7.

## 2.7    REFERENCES

Abramento, M. and Carvalho, C. S. 1989. Geotechnical parameters for the study of natural slopes instabilzation at Serra do Mar-Brazilian Southeast. *Proceedings of the 12th International Conference on Soil Mechanics and Foundation Engineering*, *Rio de Janeiro*. 3, pp. 1599-1602.

Allen, R. G. Pereira, L. S. Raes, D. Smith, M. 1998. Crop Evapotranspiration (guidelines for computing crop water requirements). *FAO Irrigation and Drainage Paper No. 56.*

Amoozegar, A. and Warrick, A. W. 1986. Hydraulic conductivity of saturated soils: field methods. In Klute, A. (ed.) *Methods of soil analysis*. No. 9 Agronomy, American Society of Agronomy, Madison, Wisconsin.

Bao, C. Gong, B. and Zhan, L. 1998. Properties of unsaturated soils and slope stability of expansive soils. *In Proceedings of the Second International Conference on*

*Unsaturated Soils (UNSAT 98), Beijing*. 1, pp. 71-98.

Biddle, P. G. 1998. *Tree Root Damage to Buildings*. Swindon: Willowmead Publishing Ltd, Wantage.

Bishop, A. W. 1955. The use of the slip circle in the stability analysis of earth slopes. *Geotechnique* 5(1), 7- 17.

Bishop, A. W. 1959. The principle of effective stress. *Teknisk Ukeblad I S amarbeide Med Teknikk*, Oslo, Norway. 106(39), pp. 859-863.

Blatz, J. A. Ferreira, N. J. and Graham, J. 2004. Effects of near-surface environmental conditions on instability of an unsaturated soil slope. *Canadian Geotechnical Journal*. 41(6), pp. 1111-1126.

Böhm, W. 1979. *Methods of studying root systems*. New York: Springer.

Bohne, K. Roth, C. Leij, F. J. and van Genuchten, M. Th. 1993. Rapid Method for Estimating the Unsaturated Hydraulic Conductivity from Infiltration Measurements. *Soil Science*. 155(4), pp. 237-244.

Bosch, J. M. and Hewlett, J. D. 1982. A review of catchment experiments to determine the effects of vegetation changes on water yield and evapotranspiration. *Journal of Hydrology*. 55, pp. 3-23.

Box, J. E. 1996. Modern methods for root investigations. pp. 193-237. In: Waisel, Y. Eshel, A. Kafkafi, U. eds. Plant roots the hidden half. New York:Dekker YM.

Braud, I. Bariac, T. Vauclin, M. Boujamlaoui, Z. Gaudet, J. P. Biron, Ph. Richard, P. 2005. Comparison of root water uptake modules using either the surface energy balance or potential transpiration. *Journal of Hydrology* 301, pp. 267-286.

Brunet, P. Clément, R. and Bouvier, C. 2010. Monitoring soil water content and deficit using Electrical Resistivity Tomography (ERT) – A case study in the Cevennes area, France. Journal of Hydrology. 380(1-2), pp. 146-153.

Burgess, S. S. O. 2006. Measuring transpiration responses to summer precipitation in a Mediterranean climate: a simple screening tool for identifying plant water-use strategies. *Physiologia Plantarum* 127(3), pp. 404-412.

Büsgen, M. Münch, E. and Thomsom, T. 1929. *The structure and life of forest trees*. Chapman and Hall, London.

Calder, I. R. Kariyappa, G. S. Srinivasalu, N. V. Srinivasa Murty, K. V. 1992. Deuterium tracing for the estimation of transpiration from trees Part 1. Field calibration. *J. Hydrol*. 130, pp. 17-25.

Carbon, B. A. Bartle, G. A. Murray, A. M. McPherson, D. K. 1980. The distribution of root length, and limits to flow of soil water to roots in a dry sclerophyll forest. *For Sci* 4, pp. 656-664.

Cascini, L. Cuomo, S. Pastor, M. and Sorbin, G. 2010. Modelling of rainfall induced shallow landslides of the flow-type. *Journal of Geotechnical and Geoenvironmental Engineering*. 136(1), pp. 85-98.

Caspari, H. Green, S. and Edwards, W. R. N. 1993. Transpiration of well-watered and water-stressed Asian pear trees as determined by lysimetry, heat-pulse, and estimated by a Penman-Monteith model. *Agricultural and Forest Meteorology* 67, pp. 13-27.

Clausnitzer, V. and Hopmans, J. W. 1994. Simultaneous modeling of transient three dimensional root growth and soil water flow. *Plant and Soil* 164, pp. 299-314.

Coatsworth, A. and Evans, J. 1984. Discussion on influence of vegetation on shrinking and swelling of clays. *Gèotechnique*. 34, pp. 154-155.

Coelho, F. E. and Or, D. 1996. A parametric model for two-dimensional water uptake intensity by corn roots under drip irrigation. *Soil Sci. Am. J.* 60, pp. 1039-1049.

Coutts, M. P. 1987. Developmental processes in tree root systems. *Canadian Journal of Forest Research*. 17, pp. 761-767.

Coutts, M. P. Nielsen, C. C. N. Nicoll, B. C. 1999. The development of symmetry, rigidity and anchorage in the structural root system of conifers. *Plant and Soil*. 217, pp. 1-15.

Cowen, I. R. 1965. Transport of water in the soil-plant-atmosphere system. *J. Appl. Ecology*. 2, pp. 221-239.

Crow, P. 2004. *Trees and Forestry on Archaeological sites in the UK: A review document*. Edinburgh: Forest Commission.

Crow, P. 2005. *The Influence of Soils and Species on Tree Root Depth*. Edinburgh: Forest Commission.

Cutler, D. F. and Richardson, I. B. K. 1989. *Tree roots and buildings*. Singapore: Longman Scientific and Technical.

Danjon, F. Bert, D. Godin, C. Trichet, P. 1999. Structural root architecture of 5-year-old Pinuspinaster measured by 3D digitising and analysed with AMAPmod. *Plant Soil.* 217, 49-63.

Danjon, F. Fourcaud, T. and Bert, D. 2005. Root architecture and wind-firmness of mature Pinuspinaster. *New Phytol*. 168(2), pp. 387-400.

Danjon, F. Barker, D. H. Drexhage, M. Stokes, A. 2007. Analysis of 3D structural root architecture data of trees grown on slopes. *In the 2nd International Symposium on Plant Growth Modeling, Simulation, Visualization and Applications*, Beijing, CHN. IEEE Computer Society, pp. 74-77.

Danjon, F. Barker, D. H. Drexhage, M. and Stokes, A. 2008. Using Three-dimensional Plant Root Architecture in Models of Shallow-slope Stability. *Annals of Botany.* 101, pp. 1281-1293.

Dardanelli, J. L. Ritchie, J. T. Calmon, M. Andriani, J. M. and Collino, D. J. 2004. An empirical model for root water uptake. *Field Crops Research* 87, pp. 59- 71.

David, T. S. Ferreira, M. I. Cohen, S. Pereira, J. S. David, J. S. 2004. Constraints on transpiration from an evergreen oak tree in southern Portugal. *Agric. For. Meteorol.* 122, pp. 193-205.

Dobson, M. C. and Moffat, A. J. 1993. *The potential for woodland establishment on landfill sites*. London: HMSO.

Dobson, M. 1995. *Tree root systems*. Arboriculture Research and Information Note 130. Arboricultural Advisory and Information Service, Farnham.

Docker, B. B. and Hubble, T. C. T. 2009. Modelling the distribution of enhanced soil shear strength beneath riparian trees of south-eastern Australia. *Ecological Engineering* 35, pp. 921–934.

Donald, I. B. 1956. Shear strength measurements in unsaturated non-cohesive soils with negative pore pressures. *Proceedings of the 2nd Australia - New Zealand Conference on Soil Mechanics and Foundation Engineering*. pp. 200-204.

Dunin, F. X., Mcilroy, I. C. and Oloughlin, E. M. 1985. A lysimeter characterization of evaporation by eucalypt forest and its representativeness for the local environment. *Forest–Atmosphere Interaction*, pp. 271-291.

Dye, P. J. Olbrich, B. W. and Everson, C. S. 2013. The water use of plantation forests and montane grassland in summer-rainfall forestry regions of South Africa. *7th SA National Hydrology Symposium*. South Africa. June 13.

Eis, S. 1978. Natural root forms of western conifers. In: *Symposium on Root Form of Planted Trees*. Victoria. BC. Canda. Pp. 23-27.

Eller, H. and Denoth, A. 1996. A capacitivesoilmoisture sensor. *Journal of Hydrology.* 185(1), pp. 137-146.

Erie, L. J. French, O. F. and Harris, K. 1965. Consumptive use of water by crops in Arizona. Technical Bulletin, No. 169, Agricultural Experiment Station, Univ. of Arizona, Tucson, AZ.

Escario, V. 1980. Suction-controlled penetration and shear tests. *In Proceedings of the 4th International Conference on Expansive Soils*, Denver, CO, pp. 781-787.

Escario, V. and Juca, J. 1989. Strength and deformation of party saturated soils. *Proceedings of the 12th International Conference on Soil Mechanics and Foundation Engineering, Rio de Janeiro*. 3, pp. 43-46.

Escario, V. and Sáez, J. 1986. The shear strength of partly saturated soils. *Géotechnique*. 36 (3), pp. 453-456.

Ewers, B. E. Mackay, D. S. Tang, J. Bolstad, P. V. Samanta, S. 2008. Intercomparison of sugar maple (Acer saccharum Marsh.) stand transpiration responses to environmental conditions from the Western Great Lakes Region of the United States. *Agric. For. Meteorol* 148, pp. 231-246.

Fan, C. C. and Lai, Y, F. 2014. Influence of the spatial layout of vegetation on the stability of slopes. *Plant Soil*. 377, pp. 83-95.

Fatahi, B. Khabbaz, H. Indraratna, B. 2010. Bioengineering ground improvement considering root water uptake model. *Ecological Engineering* 36, pp. 222-229.

Feddes, R. A. Kowalik, P. Kolinska-Malinka, K. Zaradny, H. 1976. Simulation of field water uptake by plants using a soil water dependent root extraction function. *J. Hydro*. 31, pp. 13-26.

Feddes, R. A. Kowalik, P. I. and Zaradny, H. 1978. Simulation of field water use and crop yield. *Wageningen Center for Agriculture and Documentation*. Wageningen, 189.

Feddes, R. A. Hoff, H. Bruen, M. Dawson, T. de Rosnay, P. Dirmeyer, P. Jackson, R. B. Kabat, P. Kleidon, A. Lilly, A. and Pitman, A. 2001. Modeling Root Water Uptake in Hydrological and Climate Models. *Bulletin of the American Meteorological Society*. 82(12), pp. 2797-2809.

Fellenius, W. 1936. *Calculation of the Stability of Earth Dams*. Washington: Trans. 2nd Int. Cong. Large Dams, pp. 445- 459.

Fernández, J. E. Palomo, M. J. Díaz-Espejo, A. Clothier, B. E. Green, S. R. Girón, I. F. Moreno, F. 2001. Heat-pulse measurements of sap flow in olives for automating irrigation: tests, root flow and diagnostics of water stress. *Agricultural Water Management*. 51(2), pp. 99-123.

Fredlund, D. G. Morgenstern, N. R. and Widger, R. A. 1978. The shear strength of unsaturated soils. *Canadian Geotechnical Journal*. 15(3), pp. 313-321.

Fredlund, D. G. Rahardjo, H. and Gan, J. K.M. 1987. Nonlinearity of strength envelope for unsaturated soils. In: *Proceedings of the Sixth International Conference on Expansive Soils, New Delhi*. 1, pp. 49-54.

Fredlund, D. G. and Rahardjo, H. 1993. *Soil Mechanics of Unsaturated Soils*. New York: John Wiley & Sons.

Fredlund, D. G. Xing, A. Fredlund, M. D. and Barbour, S. L. 1996. The relationship of the unsaturated soil shear strength to the soil water characteristic curve. *Canadian Geotechnical Journal*. 32(3), pp. 440-448.

Gan, J. K. M. and Fredlund, D. G. 1988. Multistage direct shear testing of unsaturated soils. *Geotechnical Testing Journal*. 11(2), pp. 132-138.

Gan, J. K. Fredlund, D. G. and Rahardjo, H. 1988. Determination of the shear strength parameters of an unsaturated soil using the direct shear test. *Canadian Geotechnical Journal*. 25(3), pp. 500-510.

Gao, Y. Duan, A. Qiu, X. Liu, Z. Sun, J. Zhang, J. Wang, H. 2010. Distribution of roots and root length density in a maize/soybean strip intercropping system. *Agricultural Water Management*. 98, pp. 199-212.

Garven, E. A. and Vanapalli, S. K. 2006. Evaluation of empirical procedures for predicting the shear strength of unsaturated soils. In: Miller, G. A. Zapata, C. E. Houston, S. L. and Fredlund, D. G. eds. *Proceedings of the Fourth International Conference on Unsaturated Soils*. GSP 147. American Society of Civil Engineers, Reston, *Va*. 2, pp. 2570-2581.

Gardner, W. R. 1960. Dynamic aspects of water availability to plants. *Soil Sci*. 89, pp. 63-73.

Gardner, W. R. 1964. Relation of root distribution to water uptake and availability. *Agronomy J*. 56, pp. 41-45.

Gardner, W. R. 1983. Soil properties and efficient water use: A review. In: Taylor, H. Jordan, W. R. and Sinclair, T. R. eds. *Limitations to Efficient Water Use in Crop Production*, pp. 45-64.

Gardner, W. R. 1991. Modelling water uptake by roots. *Irrig. Sci*. 12, pp. 109-114.

Gazal, R. M. Scott, R. L. Goodrich, D. C. Williams, D. G. 2006. Controls on transpiration in a semiarid riparian cottonwood forest. *Agric. For. Meteorol*. 137, pp. 56-67.

Genet, M. Stokes A. Fourcaud, T. Norris J. E. 2010. The influence of plant diversity on slope stability in a moist evergreen deciduous forest. *Ecological Engineering* 36, pp. 265-275.

Gong, D. Kang, S. Zhang, L. Du, T. and Yao, L. 2006. A two-dimensional model of root water uptake for single apple trees and its verification with sap flow and soil water content measurements. *Agricultural Water Management* 83, pp. 119-129.

Granier, A. Huc, R. Barigah, S. T. 1996. Transpiration of natural rain forest and its dependence on climatic factors. *Agricultural and Forest Meteorology*. 78, pp. 16-29.

Green, S. R. 1993. Radiation balance, transpiration and photosynthesis of an isolated tree. *Agric. For. Meteorol*. 64, pp. 201-221.

Green, S. R. McNaughton, K. G. 1997. Modelling effective stomatal resistance for calculating transpiration from an apple tree. *Agric. For. Meteorol*. 83, pp. 1–26.

Green, S. R. Vogeler, I. Clothier, B. E. Mills, T. M. and Dijssel, C. 2003. Modelling water uptake by a mature apple tree. *Aust. J. Soil Res*. 41 (3), pp. 365–380.

Greenway, D. R. 1987. Vegetation and slope stability. In: Anderson, M. G. and Richards, K. S. (eds.). *Slope Stability*. John Wiley and Sons.

Greenwood, J. R. Norris, J. E. and Wint, J. 2004. Assessing the contribution of vegetation to slope stability. *Geotechnical Engineering*. 157(GE4), pp. 199-207.

Greenwood, J. R. 2006. SLIP4EX – A program for routine slope stability analysis to include the effects of vegetation, reinforcement and hydrological changes. *Geotechnical and Geological Engineering* 24, pp. 449-465.

Gregory, P. 2006. Plant Roots Growth, Activity and Interaction with Soils. Oxford: Blackwell Publishing Ltd.

Hall, R. L. 1987. Processes of evaporation from vegetation of the uplands of Scotland. *Trans. Roy. Soc. Edinburgh: Earth Sciences*. 81, pp. 193-210.

Hernández-Santana, V. David, T. S. Martínez-Fernández, J. 2008. Environmental and plant-based controls of water use in a Mediterranean oak stand. *For. Ecol. Manage*. 255, pp. 3707-3715.

Hillel, D. Beek, V. Talpaz, H. 1975. A microscopic scale model of soil water uptake and salt movement to plant roots. *Soil Sci*. 120, pp. 385-399.

Ho, D. Y. F. and Fredlund, D. G. 1982. Increase in shear strength due to suction for two Hong Kong soils. *In Proceedings of the ASCE Geotechnical Conference Engineering and Construction in Tropical and Residual Soils*. Honolulu, HI, pp. 263-295.

Hodge, A. Berta, G. Doussan, C. Nerchan, F. Crespi, M. 2009. Plant root growth, architecture and function. *Plant Soil*. 321, pp. 153-187.

Homaee, M. 1999. Root Water Uptake under Non-Uniform Transient Salinity and Water Stress. PhD Thesis, van de LandbouwuniversiteitWageningen.

Hoogland, J. C. Feddes, R. A. and Belmans, C. 1981. Root water uptake model depending on soil water pressure head and maximum extraction rate. *Acta Hort*. 119, pp. 123-131.

Hopkins, W. G. 1999. *Introduction to Plant Physiology*. USA: John Wiley & Sons, Inc.

Hopmans, J. W. and Bristow, K. L. 2002. Current capabilities and future needs of root water and nutrient uptake modelling. *Advances in Agronomy*. 77, pp. 103-183.

Hruska, J. Cermák, J. and Sustek, S. 1999. Mapping tree root systems with ground-penetrating radar. *Tree Physiology*. 19, pp. 125-130.

Hubble, T. C. T. Docker, B. B. Rutherfurd, I. D. 2010. The role of riparian trees in maintaining riverbank stability: A review of Australian experience and practice. *Ecological Engineering*. 36, pp. 292-304.

Huisman, J. A. Hubbard, S. S. Redman, J. D. and Annan,A. P. 2003. Measuring Soil Water Content with Ground Penetrating Radar: A Review. Vadose Zone Journal. 2, pp. 476-491.

Indraratna, B. et al. 2006. Numerical analysis of matric suction effects of tree roots. *Geotechnical Engineering* 159, pp. 77-90.

Jackson, T. J. Levine, D. M. Swift, C. T. Schmugge, T. J. Schiebe, F. R. 1995. Large-area mapping of soil moisture using the ESTAR passive microwave radiometer in Washita92. *Remote Sens. Environ*. 54, pp. 27-37.

Jadoon, K. Z. Weihermüller, L. Scharnagl, B. Kowalsky, M.B. Bechtold, M. Hubbard, S.S. Vereecken, H. Lambot, S. 2012. Estimation of soil hydraulic parameters in the field by integrated hydrogeophysical inversion of time-lapse ground-penetrating radar data. *Vadose Zone J*. 11(4).

Jaksa, M. B. Kaggwa, W. S. and Woodburn, J. A. 2002. Influence of large gum trees on the soil suction profile in expansive soils. *Australian Geomechanics Journal* 37(1), 23-33.

Janbu, N. Bjerrum, L. and Kjaernsli, B. 1956. Soil mechanics applied to some engineering problems. *Norwegian Geotechnical Institute Publication* 16.

Jarvis, P. G. 1976. The interpretation of the variation in the leaf water potential and stomatal conductance found in canopies in the field. Philos. *Trans. R. Soc*. 273, pp. 293-310.

Jones, H. G. Hamer, P. J. C. Higgs, K. H. 1988. Evaluation of various heat-pulse methods for estimation of sap flow in orchard trees: comparison with micrometeorological estimates of evaporation. *Trees: Structure and Function* 2, pp. 250-260.

Judd, L. A. Jackson, B. E. and Fonteno, W. C. 2015. Advancements in Root Growth Measurement Technologies and Observation Capabilities for Container-Grown Plants. *Plants*. 4, pp. 369-392.

Kelliher, F. M. Leuning, R. Raupach, M. R. and Schulze, E. D. 1995. Maximum conductances for evaporation from global vegetation types. *Agricultural and Forest Meteorology* 73, pp. 1-16.

Khalili, N. and Khabbaz, M. H. 1998. A unique relationship for χ for the determination of the shear strength of unsaturated soils. *Géotechnique*. 48(5), pp. 681-687.

Kokutse, N. K. Temgouaa, A. G. T. and Kavazović, Z. 2016. Slope stability and vegetation: Conceptual and numerical investigation of mechanical effects. *Ecological Engineering*. 86, pp. 146-153.

Komatsu, H. Kang, Y. Kume, T. Yoshifuji, N. Hotta, N. 2006. Transpiration from a Cryptomeria japonica plantation, part 2: responses of canopy conductance to meteorological factors. *Hydrol. Process*. 20, pp. 1321-1334.

Köstler, J. N. Bruckner, E. Bibelriether, H. 1968. *Die Wurzeln der Waldbäume*. Verlag Paul Parey. Hamburg & Berlin.

Krahn, J. Fredlund, D. G. and Klassen, M. J. 1989. Effect of soil suction on slope stability at Notch Hill. *Canadian Geotechnical Journal*. 26(2), pp. 269-278.

Krahn, J. 2015. *Stability modelling with SLOPE/W-An Engineering Methodology*. 11th ed. Canada: GEO-SLOPE/W International Ltd.

Kramer, P. J. and Boyer, J. S. 1995. The absorption of water and root and stem pressures. In *Water Relations of Plants and Soils*. Kramer, P. J. and Boyer, J. S. eds. San Diego: Academic Press, Inc., pp 167-200.

Kücke, M. Schmid, H. Spiess, A. 1995. A comparison of four methods for measuring roots of field crops in three contrasting soils. *Plant andSoil*. 172(1), pp. 63-71.

Kutschera, L. and Lichtenegger, E. 1997. Wurzeln. Bewurzelung von Pflanzen in verschiedenen Lebensraumen. Stapfia 49. *Land Oberosterreich*. OO. Landesmuseum, Linz.

Kutschera, L. Lichtenegger, E. 2002. *Wurzelatlas mitteleuropaischer Waldbaume und Straucher*. Leopold Stocker Verlag, Graz-Stuttgart.

Kumar, R. Shankar, V. and Jat, M. K. 2013. Efficacy of Nonlinear Root Water Uptake Model for a Multilayer Crop Root Zone. *J. Irrig. Drain Eng*. 139, pp. 898-910.

Landsberg, J. J. and Powell, D. B. B. 1973. Surface exchange characteristics of leaves subject to mutual interference. *Agric. Meteorol*. 13, pp. 169-184.

Lai, C. T. and Katul, G. 2000. The dynamic role of root-water uptake in coupling potential to actual transpiration. *Advances in Water Resources* 23(4), pp. 427-439.

Leung, A. K. Sun, H. W. Millis, S. W. Pappin, J. W. Ng, C. W. W. and Wong, H. N. 2011. Field monitoring of an unsaturated saprolitic hillslope. *Can. Geotech. J*. 48, pp. 339-353.

Leung, A. K. and Ng, C. W. W. 2013. Analyses of groundwater flow and plant evapotranspiration in a vegetated soil slope. *Can. Geotech. J*. 50, pp. 363-365.

Leung, F. T. Y. Yan, W. M. Hau, B. C. H. Tham, L. G. 2015. Root systems of native shrubs and trees in Hong Kong and their effects on enhancing slope stability. *Catena*. 125, pp. 102-110.

Li, K. Y. Boisvert, J. B. and Jong, R. D. 1999. An exponential root-water-uptake model. *Can. J. Soil Sci*. 79, pp. 333-343.

Li, K. Y. Jong, R. D. and Boisvert, J. B. 2001. An exponential root water uptake model with water stress compensation. *Journal of Hydrology* 252, pp. 189-204.

Li, K. Y. Jong, R. De. Coe, M. T. and Ramankutty, N. 2006. Root-Water-Uptake Based upon a New Water Stress Reduction and an Asymptotic Root Distribution Function. *Earth Interactions*. 10(14), pp. 1-22.

Litvin, E. 2008. Numerical analysis of the effect of rainfall infiltration on slope stability. *GROUND ENGINEERING*. May, pp. 38-41.

Lu, N. and Likos, W. J. 2004. *Unsaturated Soil Mechanics*. New Jersey: John Wiley & Sons. Inc.

Lukanu, G. and Savage,M. J. 2006. Calibration of a frequency-domain reflectometer fordetermining soil-water content in a clay loam soil. *Water SA*. 32(1), pp. 37.

Luis, V. C. Jiménez, M. S. Morales, D. Kucera, J. Wieser, G. 2005. Canopy transpiration of a Canary Islands pine forest. *Agric. For. Meteorol*. 135, pp. 117-123.

Luo, Y. OuYang, Z. Yuan, G. Tang, D. Xie, X. 2003. Evaluation of Macroscopic Root Water Uptake Models Using Lysimeter Data. *American Society of Agricultural Engineers*. 46(3), pp. 1-10.

Lv, G. Hu, W. Kang, Y. Liu, B. Li, L. and Song, J. 2013. Root Water Uptake Model Considering Soil Temperature. *J. Hydrol. Eng*. 18, pp. 394-400.

Macfarlane, C. Bond, C. White, D. A. Grigg, A. H. Ogden, G. N. Silberstein, R. 2010. Transpiration and hydraulic traits of old and regrowth eucalypt forest in Southwestern Australia. *For. Ecol. Manage*. 260, pp. 96-105.

MacNeil, D. J. Steele, D. P. McMahoii, W. and Carder, D. R. 2001. *Vegetation for slope stability*. Prepared for Quality Services, Civil Engineering, Highways Agency, 48.

Manoli, G. Bonetti, S. Domec, J. C. Putti, M. Katul, G. 2014. Tree root systems competing for soil moisture in a 3D soil–plant model. *Advances in Water Resources* 66, pp. 32-

42.

Mathur, S. and Rao, S. 1999. Modelling water uptake by plant roots. *Journal of Irrigation and Drainage Engineering* 125(3), pp. 159-165.

McCulloch, J. S. G. and Robinson, M. 1993. History of forest hydrology. *Journal of Hydrology*. 150, pp. 189–216.

McNaughton, K. G. 1994. Effective stomatal and boundary-layer resistances of heterogeneous surfaces. *Plant Cell Environ*. 17, pp. 1061-1068.

Meinzer, F. C. Goldstein, G. Holbrook, N. M. Jackson, P. Cavelier, J. 1993. Stomatal and environmental control of transpiration in a lowland tropical forest tree. *Plant Cell Environ*. 16, pp. 429-436.

Mellander, P. E. Bishop, K. Lundmark, T. 2004. The influence of soil temperature on transpiration: a plot scale manipulation in a young Scots pine stand. *Forest Ecology and Management* 195(1-2), pp. 15-28.

Menziani, M. Rivasi, M. R. Pugnaghi, S. Santangelo, R. and Vinenzi, S. 1996. SoilVolumetricWater Content MeasurementsUsing TDR Technique. *ANNALI DI GEOFISICA*. XXXIX(1), pp. 91-96.

Miranda, A. C. Jarvis, P. G. and Grace, J. 1984. Transpiration and evaporation from heather moorland. *Boundary-Layer Met*. 28, pp. 227-243.

Mitchell, P. J. Veneklaas, E. Lambers, H. Burgess, S. S. O. 2009. Partitioning of evapotranspiration in a semi-arid eucalypt woodland in South-western Australia. *Agric. For. Meteorol*. 149, pp. 25-37.

Molz, F. J. and Hornberger, G. M. 1973. Water transport through plant tissue in the presence of a diffusible solute. *Soil Sci. Soc. Am. Proc*. 37, pp. 383-387.

Molz, F. J. and Remson, I. 1970. Extraction term models of soil moisture use by transpiring plants. *Water Resour. Res*. 6(5), pp. 1346-1356.

Molz, F. J. 1981. Models of water transport in the soil-plant system: A review. *Water Res. Res*. 17, pp. 1245-1260.

Monteith, J. L. 1965. Evaporation and environment. *In The State and Movement of Water in Living Organisms*. In: FOGG G. E. eds. New York: Academic Press pp. 204–234.

Morgenstern, N. R. and Price, V. E. 1965. The analysis of the Stability of General Slip Surfaces. *Geotechnique* 15, pp. 79- 93.

Mu'azu, M. A. and Ali, N. B. 2011. Parametric evaluation of tree root water-uptake effect on ground movement. *International Journal of the Physical Sciences.* 6(14), pp. 3468–3474.

Mulrean, E. 2000. *Arid Zone Trees*. [Online]. Available at:
http://www.aridzonetrees.com/AZTimes%20Horticultural/Quality%20Control_%20

Principles%20and%20Practices.htm

Neuman, S. P. Feddes, R. A. and Bresler, E. 1975. Finite Element analysis of two-dimensional flow in soil considering water uptake by roots: I. Theory. *Soil Sci. Am. J.* 35, pp. 224-230.

Ng, C. W. W. and Shi, Q. 1998. A numerical investigation of the stability of unsaturated soil slopes subjected to transient seepage. *Computers and Geotechnics.* 22(1), pp. 1-28.

Ng, C. W. W. Leung, A. K. and Woon, K. X. 2013. Effects of Soil Density on Grass-Induced Suction Distributions in Compacted Soil Subjected to Rainfall. *Can. Geotech. J.* 51 (3), pp. 311-321.

Ng, C. W. W. Leung, A. K. Kamchoom, V. and Garg, A. 2014. A Novel Root System for Simulating Transpiration-Induced Soil Suction in Centrifuge. *Geotechnical Testing Journal.* 37(5), pp. 1-15.

Ng, C. W. Liu, H. W. and Feng, S. 2015. Analytical solutions for calculating pore-water pressure in an infinite unsaturated slope with different root architectures. *Can. Geotech. J.* 52, pp. 1981-1992.

Nicolas, E. Torrecillas, A. Ortuño, M. F. Domingo, R. Alarcón, J. J. 2005. Evaluation of transpiration in adult apricot trees from sap flow measurements. *Agricultural Water Management.* 72, pp. 131-145.

Nimah, M. N. and Hanks, R. J. 1973. Model for estimating soil water, plant and atmospheric interrelations: I. Description and Sensitivity. *Soil Sci. Soc. Am. Proc*. 37, pp. 522-532.

Nisbet, T. R. 2005. *Water Use by Trees*. Edinburgh: Forestry Commission.

Nobel, P. S. and Alm, D. M. 1993. Root orientation vs. water uptake simulated for monocotyledonous and dicotyledonous desert succulents by root-segment model. *Funct. Ecol*. 7, pp. 600-609.

Noborio, K. 2001. Measurement of soil water content and electrical conductivity by time domain reflectometry: a review. *Computers and Electronics in Agriculture*. 31(3), pp. 213-237.

Norris, J. E. Stokes, A. Mickovski, S. B. Cameraat, E. van Beek, R. Nicoll, B. C. Achim, A. Eds. 2008. *Slope Stability and Erosion Control: Ecotechnological Solutions*. Springer, pp, 100-106.

Nyambayo, V. P. and Potts, D. M. 2010. Numerical simulation of evapotranspiration using a root water uptake model. *Computers and Geotechnics* 37, 175-186.

Oguntunde, P. G. 2005. Whole-plant water use and canopy conductance of cassava under limited available soil water and varying evaporative demand. *Plant and Soil*. 278(1-2), 371-383.

Oke, T. R. 1987. Boundary layer climates. 2e, Routledge, London, pp. 435.

Oren, R. and Pataki, D. 2001. Transpiration in response to variation in microclimate and soil moisture in southeastern deciduous forests. *Oecologia* 127, pp. 549-559.

Osman, N. and Barakbah, S. S. 2011. The effect of plant succession on slope stability. *Ecological Engineering*. 37, pp. 139-147.

Osińsiki, P. Rickson, R. J. Hann, M. J. Koda, E. 2014. Assessment of slope stability influenced by vegetation cover and additional loads applied. *Ann. Warsaw Univ. of Life Sci. – SGGW, Land Reclam*. 46 (2), pp. 81-91.

Pagès, L. Jordan, M. O. Picard, D. 1989. A simulation of the three dimensional architecture of the maize root system. *Plant Soil* 119, pp. 147-154.

Passioura, J. B. and Cowen, I. R. 1968. On solving the nonlinear diffusion equation for the radial flow of water to roots. *Agr. Meteorology*. 5, pp. 129-134.

Penman, H. L. 1948. Natural evaporation from open water, bare soil and grass. *Proceedings of the Royal Society of London, Series A* 193, pp. 120–146.

Pereira, A. Green, S. Nova, N. A. V. 2006. Penman–Monteith reference evapotranspiration adapted to estimate irrigated tree transpiration. *Agricultural water management* 83, pp. 153-161.

Personne, E. Perrier, A. Tuzet, A. 2003. Simulating water uptake in the root zone with a microscopic-scale model of root extraction. *Agronomie*. 23, pp. 153-168.

Philip, J. R. 1957. The physical principles of water movement during the irrigation cycle. *Proc. Int. congress on Irrig. Drain* 8, pp. 124-154.

Pierret, A. Moran, C. J. Mclachlan, C. B. Kirby,J. M. 2000. MEASUREMENT OF ROOT LENGTH DENSITY IN INTACT SAMPLES USING X-RADIOGRAPHY AND IMAGE ANALYSIS. *Image Analysis & Stereology.* 19(2), pp. 145-149.

Pollen, N. and Simon, A. 2005. Estimating the mechanical effects of riparian vegetation on streambank stability using a fiber bundle model. *Water Resources Research.* 41, pp. 1-11.

Prasad, R. 1988. A linear root water uptake model. *J. Hydrology* 99, pp. 297-306.

Raats, P. A. C. 1974. Steady flows of water and salt in uniform soil profiles with plant roots. *Soil Sci. Am. Proc.* 38, pp. 717-722.

Rahardjo, H. Ong, T. H., Rezaur, R. B., and Leong, E. C. 2007. Factors controlling instability of homogeneous soil slopes under rainfall. *Journal of Geotechnical and Geoenvironmental Engineering.* 133(12), pp. 1532-1543.

Rana, G. Katerji, N. Lorenzi, F. 2005. Measurement and modeling of evapotranspiration of irrigated citrus orchard under Mediterranean conditions. *Agric. For. Meteorol.* 128, pp. 199-209.

Rees, S. W. and Ali, N. 2006. Seasonal water uptake near trees: a numerical and

experimental study. *Geomechanics and Geoengineering: An International Journal*. 1(2), pp. 129-138.

Rees, S. W. and Ali, N. 2012. Tree induced soil suction and slope stability. *Geomechanics and Geoengineering*. 7 (2), pp. 103-113.

Reubens, B. Poesen, J. Danjon, F. Geudens, G. Muys, B. 2007. The role of fine and coarse roots in shallow slope stability and erosion control with a focus of root system architecture: a review. *Trees* 21, pp. 285-402.

Ridley, A. Ginnity, M. and Vaughan, P. 2004. Role of pore water pressures in embankment stability. *Geotechnical Engineering* 157, pp. 193-198.

Rijtema, P. E. 1965. An analysis of actual evapotranspiration. *Agricultural Research Report*, pp. 659-766.

Rizzo, D. Gross, R. 2000. Distribution of Armillaria on pear root systems and a comparison of root excavation techniques. In: Stokes, A. (ed.). *The Supporting Roots of Trees and Woody Plants: Form, Function and Physiology*. Kluwer Academic Publishers, Dordrecht, pp. 305-311.

Roering, J. J. Schmidt, K. M. Stock, J. D. Dietrich, W. E. Montgomery, D. R. 2003. Shallow landsliding, root reinforcement and the spatial distribution of trees in the Oregon Coast Range. *Can. Geotech. J*. 40, pp. 237-253.

Rood, S. B. Bigelow, S. G. and Hall, A. A. 2011. Root architecture of riparian trees: river cut-banks provide natural hydraulic excavation, revealing that cottonwoods are facultative phreatophytes. *Trees*. 25, pp. 907-917.

Sala, A. and Tenhunen, J. D. 1996. Simulations of canopy net photosynthesis and transpiration in Quercus ilex L. Under the influence of seasonal drought. *Agric. For. Meteorol.* 78, pp. 203-222.

Satija, B. S. 1978. *Shear Behavior of Partially Saturated Soils*. PhD Thesis. Indian Institute of Technology, Delhi.

Schenk, H. J. and Jackson, R. B. 2002a. The global biogeography of roots. *Ecol. Monogr.* 72, pp. 311-328.

Schenk, H. J. and Jackson, R. B. 2002b. Rooting depths, lateral root spreads and below-ground/above-ground allometries of plants in water-limited ecosystems. *J. Ecol.* 90, pp. 480-494.

Schulze, E. D. Cermák, J. Matyssek, R. Penka, M. Zimmermann, R. Vasicek, F. Gries, W. Kucera, J. 1985. Canopy transpiration and water fluxes in the xylem of the trunk of *Larix* and *Picea* trees. A comparison of xylem flow, porometer and cuvette measurements. *Oecologia*. 66, 475-483.

Segundo, A. K. Martins, J. H. Monteiro, P. M. de Oliveira, R. A. and Freitas, G. M. 2015. A Novel Low-Cost Instrumentation System for Measuring the Water Content and

Apparent Electrical Conductivity of Soils. Sensors (Basel). 15(10), pp. 25546-25563.

Shi, L. Song, X. Tong, J. Zhu, Y. Zhang, Q. 2015. Impacts of different types of measurements on estimating unsaturated flow parameters. *Journal of Hydrology*. 524, pp. 549-561.

Shields, F. D. and Gray, D. H. 1992. Effects of woody vegetation on sandy levee integrity. *Water Res*.28, pp. 917-931.

Shuttleworth, W. J. 2008. Evapotranspiration Measurement Methods. *Southwest Hydrology*, pp. 22-23.

Simon, A. and Darby, S. E. 1999. The nature and significance of incised river channels. In: *Incised River Channels: Processes, Forms, Engineering and Management*. John Wiley and Sons, pp. 3-18.

Simon, A. Curini, A. Darby, S. E. and Langendoen, E. J. 2000. Bank and near-bank processes in an incised channel. *Geomorphology*, 35, pp. 193-217.

Smith, P. G. C. 2003. *Numerical analysis of infiltration into partially saturated soil slopes*. PhD Thesis, Imperial College of Science, London.

Šimůnek, J. Huang, K. and van Genuchten, M. Th. 1992. *The SWMS 2D code for simulating water flow and solute transport in two dimensional variably saturated media*. Research Report No. 126, U.S. Salinity Lab, ARS USDA, Riverside.

Somma, F. Hopmans, J. W. and Clausnitzer, V. 1998. Transient three-dimensional modeling of soil water and solute transport with simultaneous root growth, root water and nutrient uptake. *Plant Soil* 202, pp. 281-293.

Spencer, E. 1967. A Method of Analysis of the Stability of Embankments Assuming Parallel Interslice Forces. *Geotechnique* 17, pp. 11-26.

Steudle, E. 1994. Water transport across roots. *Plant Soil*. 167, pp. 79-90.

Stokes, A. 2002. The biomechanics of tree root anchorage. In: Waisel, Y. Eshel, A. Kafkaki, U. eds. *Plant Roots – The Hidden Half*. New York: Plenum Publishing, pp. 175-186.

Stokes, V. 2004. Assessing water use in plants: an introduction and guide to methods of measurement. *Scottish Forestry*. 58(2), pp. 13-19.

Stokes, A. Atger, C. Bengough, A. Fourcaud, T. and Sidle, R. 2009. Desirable plant root traits for protecting natural and engineered slopes against landslides. *Plant Soil*. 324 (1), pp.1-30.

Story, T. 2012. *Terran's Tree Tips – Beating the Heat*. [Online] Available at: http://tips.woodlandtree.com/terrantip2012_4.html. [Accessed: 29 April 2016].

Szeicz, G. Endrodi, G. and Tajchman, S. 1969. Aerodynamic and surface factors in evaporation. *WRR* 5, pp. 380-394.

Takagi, K. Harazono, Y. Noguchi, S. Miyata, A. Mano, M. and Komine, M. 2006. Evaluation of the transpiration rate of lotus using the stem heat-balance method. *Aquatic Botany* 85(2), pp. 129-136.

Tang, J. Bolstad, P. Ewers, B. Desai, A. Davis, K. Carey, E. 2006. Sap flux−upscaled canopy transpiration, stomatal conductance, and water use efficiency in an old growth forest in the Great Lakes region of the United States. *J. Geophys. Res*. 111, pp. 1-12.

Thorne, C. R. 1990. Effects of vegetation on riverbank erosion and stability. In: Thomas, J. B. eds. *Vegetation and Erosion: Processes and Environments*. John Wiley and Sons, pp. 125-144.

Thorpe, M. R. 1978. Net radiation and transpiration of apple trees in rows. *Agricultural Meteorology*. 19, pp. 41-57.

Thorpe, M. R. Warrit, B. Landsberg, J. J. 1980. Responses of apple leaf stomata: a model for single leaves and a whole canopy. *Plant Cell Environ*. 3, pp. 23-27.

Tognetti, R. d'Andria, R. Morelli, G. Alvino, A. 2005. The effect of deficit irrigation on seasonal variations of plant water use in Olea europaea L. *Plant Soil* 273, 139-155.

Tognetti, R. Giovannelli, A. Lavini, A. Morelli, G. Fragnito, F. d'Andria, R. 2009. Assessing environmental controls over conductances through the soil−plant

atmosphere continuum in an experimental olive tree plantation of southern Italy. *Agric. For. Meteorol*. 149, 1229-1243.

Tsaparas, I. Rahardjo, H. Toll, D. G. and Leong, E. C. 2002. Controlling parameters for rainfall-induced landslides. *Computers and Geotechnics*. 29(1), pp. 1-27.

Tuller, M. and Or, D. 2003. *RETENTION OF WATER IN SOIL AND THE SOIL WATERCHARACTERISTIC CURVE.* [Online] Available at: http://www.engr.uconn.edu/environ/envphys/pdf/vadose_pdf/SWC_revised01.pdf [Accessed: 20May 2016].

USGS. 2005. *The water cycle: Evapotranspiration*. United State Geological Survey.

Vanapalli, S. K. Fredlund, D. G. Pufahl, D. E. and Clifton, A. W. 1996. Model for the prediction of shear strength with respect to soil suction. *Canadian Geotechnical Journal*. 33(3), pp. 379-392.

Vereecken, H. 1990. Estimating Unsaturated Hydraulic Conductivity from Easily Measured Soil Properties. *Soil Science*. 149(1), pp. 1-12.

Vilar, O. M. 2006. A simplified procedure to estimate the shear strength envelope of unsaturated soils. *Canadian Geotechnical Journal*. 43(10), pp. 1088-1095.

Villalobos, F. J. Orgaz, F. Testi, L. Fereres, E. 2000. Measurement and modeling of evapotranspiration of olive (Olea europaea L.) orchards. *Eur. J. Agron*. 13, pp. 155-

163.

Vrugt, J. A. Hopmans, J. W. and Šimunek, J. 2001a. Calibration of Two-Dimensional Root Water Uptake Model. *Soil Sci. Am. J*. 65(4), 1027-1037.

Vrugt, J. A. van Wijk, M. T. Hopmans, J. W. and Šimunek, J. 2001b. One, two and three-dimensional root water uptake functions for transient modelling. *Water Resour. Res*. 37(10), 2457-2470.

Ward, R. C. and Robinson, M. 2000. *PRINCIPLES OF HYDROLOGY*. 4th ed. London: McGraw-Hill Publishing Company.

Warrick, A. W. Lomen, D. O. and Fard, A. A. 1980. Linearized moisture flow with root extraction for three dimensional, steady conditions. *Soil Sci. Am. J*. 44, 911-914.

Werkhoven, C. 1993. TIME-DOMAIN REFLECTOMETRY AND TENSIOMETERS FOR DETECTING SOIL MOISTURE CONTENT. *Acta Hort*. 335(60), pp. 491-496.

Whisler, F. D. Klute, A. and Millington, R. J. 1968. Analysis of steady state evapotranspiration from a soil column. *Soil Sci. Soc. Am. Proc*. 32, pp. 167-174.

Williams, A. A. B. and Pidgeon, J. T. 1983. Evapotranspiration and heaving clays in South Africa. *Gèotechnique*. 33, pp. 141-150.

Wu, J. Zhang, R. and Gui, S. 1999. Modeling soil water movement with water uptake by

roots. *Plant and Soil* 215, pp. 7-17.

Wu, T. 2007. Root reinforcement analyses and experiments. In: Stokes, A. Spanos, I. Norris, J. E. Cammeraat, L. H. (eds) *Eco- and Ground Bio-Engineering: The Use of vegetation to Improve Slope Stability*. Developments in Plant and Soil Sciences, Dordrecht, Netherlands, pp 21-30.

Wullschleger, S. D. Wilson, K. B. Hanson, P. J. 2000. Environmental control of wholeplant transpiration, canopy conductance and estimates of the decoupling coefficient for large red maple trees. *Agric. For. Meteorol*. 104, 157-168.

Zeppel, M. J. B. Macinnis-Ng, C. M. O. Yunusa, I. A. M. Whitley, R. J. Eamus, D. 2008. Long term trends of stand transpiration in a remnant forest during wet and dry years. *J. Hydrol*. 349, pp. 200-213.

Zhang, H. P. Simmonds, L. P. Morison, J. I. L. Payne, D. 1997. Estimation of transpiration by single trees: comparison of sap flow measurements with a combination equation. *Agricultural and Forest Meteorology* 87, pp. 155-169.

Zhu, H. and Zhang, L. M. 2015. Evaluating suction profile in a vegetated slope considering uncertainty in transpiration. *Computers and Geotechnics*. 63, pp. 112-120.

Zuo, Q. Shi, J. Li, Y. Zhang, R. 2006. Root length density and water uptake distributions of winter wheat under sub-irrigation. *Plant and Soil* 285, pp. 45-55.

# CHAPTER THREE

# THEORETICAL APPROACH

## 3.1    INTRODUCTION

The theoretical basis for describing moisture flow in an unsaturated soil is presented in this chapter.   The chapter includes some assumptions on the main types of unsaturated soil flow and the key parameters involved.   The fundamental concepts used to describe water-uptake by plant roots and an image-based root density approach is also introduced.   These are developed to provide the theoretical basis of the model used throughout the remainder of the thesis.

In the approach developed, a sink term is included within the moisture transfer equation.   This term is then used to facilitate implementation of the chosen water-uptake model.   In general, a sink term can be used for one-dimensional, two-dimensional, two-dimensional axi-symmetric and three-dimensional unsaturated flow.

The new approach to modelling the water uptake process requires a digitized image of the root zone to determine an 'effective root density ratio' that is subsequently employed to yield a spatially variable sink term. The four basic steps needed to accomplish this are described. This chapter also attempts to provide a reasonably simple framework that can be used for a preliminary assessment of the influence of pore-water pressure changes (from the water-uptake process) on soil shear strength, and therefore changes on the stability of unsaturated soil slopes. A summary of the necessary stability theory is therefore also presented in this chapter.

## 3.2    UNSATURATED MOISTURE FLOW

In an unsaturated soil, the flow of water is a problem of clear significance to geotechnical engineers and soil scientists. This fact is substantiated by the abundance of literature that has appeared on the subject (Fredlund 1979; Justo and Saertersdal 1979; Schreiner 1986; Nielsen et al. 1986; Alonso et al. 1987; Fredlund and Rahardjo 1993). The brief explanations provided below aim only to provide a context for the particular theoretical approach used here - no attempt is made at providing a full review of the subject at this point.

### 3.2.1   Type of Unsaturated Moisture Flow

There are generally three types of approaches to represent unsaturated flow behaviour in soils (Yong et al. 2012).

i.   As assumption of no change in soil volume and soil fabric during and as a result of unsaturated flow (ie. little or no change in porosity or where no volume change in pore geometry), corresponding to a rigid porous block.

ii.  No change in soil volume but change in soil fabric, i.e. change in pore geometry.  This is the most likely case for nonswelling soils.

iii. Change in soil volume and soil fabric, i.e. a significant change in pore geometry and porosity.

The assumption of no change in soil volume and little-to-no change in pore geometry and porosity is typically taken.  In the current work, unsaturated moisture flow in such soils can be generally determined in terms of changes in the volumetric water content at a point by the mass conservation law.

There are also two different theoretical approaches presented to describe moisture flow in a non-deformable soil.  Most commonly, moisture flow models utilize either a diffusivity based formulation with volumetric moisture content as the independent variable (Philip 1957) or are proposed in terms of capillary potential (or pressure head).  The latter form is usually referred to as Richards' theoretical formulation (Richards 1931).  Both approaches have advantages and disadvantages.

An approach related to volumetric moisture content can be attractive since moisture content is a parameter of direct interest in some areas – in particular for soil science and agricultural practices.  However, Alonso et al (1987) state that a formulation based on volumetric moisture content would not be of use in an analysis if the analysis of containing both saturated and unsaturated zones.  Discontinuities in

moisture content may also arise due to differing saturated values of volumetric moisture content at the material interfaces when modelling layered soils. This can be accommodated easily in a pressure-based model. In addition, pressure-based results may be more practical if the results are related to stress analysis.

It is recognised that most of models for the simulation of water flow in unsaturated soils with considering root zone behaviour, use Richards' equation coupled with some model to represent water extraction by the root system (Chang and Corapcioglu 1997; Luo et al. 2003; Rees and Ali 2006; Shankar et al. 2013; Manoli et al. 2014).

3.2.2   Hydraulic Properties of Unsaturated Soil

In view of the above, the pressure head $(\psi)$ based Richards' formulation was chosen for this work. The two soil properties to be determined for application of Richards' equation are: the unsaturated hydraulic conductivity $K(\psi)$, and the specific moisture capacity $C(\psi)$. The unsaturated hydraulic conductivity is recognised to be strongly related to the soil moisture content. In a fine grained soil, the hydraulic conductivity may typically decrease by several orders of magnitude from saturated to dry conditions. The specific moisture capacity is a storage term which come from the formulation of the moisture flow in unsaturated soil. It is defined directly from the slope of the capillary potential – volumetric moisture content relationship or soil water characteristic curve.

It is well known that estimating the unsaturated hydraulic conductivity is hard to accomplish in practice (Klute 1972; van Genunchten 1980). Therefore, many methods estimate unsaturated hydraulic conductivity based on the form of the soil-water retention curve, which can be more easily measured. The most common method is to install paired sensors such as tensiometers and time domain reflectometry waveguides to measure matric potential and soil water content and simultaneously and in the same soil volume. Although the soil water characteristic is easier to determine than the hydraulic conductivity, the necessary work usually involves special equipment and can be time consuming and expensive. In addition, the measured data is often fragmentary, and usually constitute relatively few measurements over the range of interest. For these reasons and modelling purposes, a considerable effort has been made to develop techniques of representing this relationship in a continuous and parametric form from a limited amount of data. One such fitting parametric model was provided by van Genunchten (1980). This model employs an equation contains few parameters to describe the behaviour of the soil water characteristic and it has been shown closely fitting the nonlinear shape of soil-water retention curve (Mathur and Rao 1999; Feddes at al. 2001; Vrugt et al. 2001; Li et al. 2006; Gong et al. 2006). For this reason this approach is also adopted in the current work.

The water retention curve is described using van Genuchten's (1980) method:

$$\theta(\psi) = \theta_r + \frac{\theta_s - \theta_r}{\left(1 + |\alpha\psi|^n\right)^m} \qquad (3.1)$$

where, $\theta_r$ and $\theta_s$ are the residual and saturated water contents, respectively; $\psi$ is the pressure head; $\alpha$ is the inverse of the air-entry pressure, $n$ is a dimensionless parameter reflecting the pore size distribution of a soil. In most applications, $m = 1 - 1/n$.

An estimate of the hydraulic conductivity function for the soil is determined utilizing the water retention curve obtained from equation (3.1) and the pore size distribution model provided by Mualem (1976):

$$K(\psi) = K_s \frac{\left[ \left( 1 + |\alpha\psi|^n \right)^m - |\alpha\psi|^{n-1} \right]^2}{\left( 1 + |\alpha\psi|^n \right)^{m(l+2)}} \qquad (3.2)$$

where, $K_s$ is the saturated hydraulic conductivity, $l$ is an empirical pore tortuosity parameter that is normally assumed to be 0.5 (Mualem 1976) and $n$ and $m$ are as defined in equation (3.1).

## 3.3    MOISTURE TRANSFER IN UNSATURATED SOILS

### 3.3.1   Governing Differential Equation Describing Isothermal Moisture Flow

The governing differential equation describing unsaturated moisture flow may be derived from considering conservation of mass in a reference element of soil. Figure 3.1 illustrates a typical control element, in x, y and z co-ordinates.
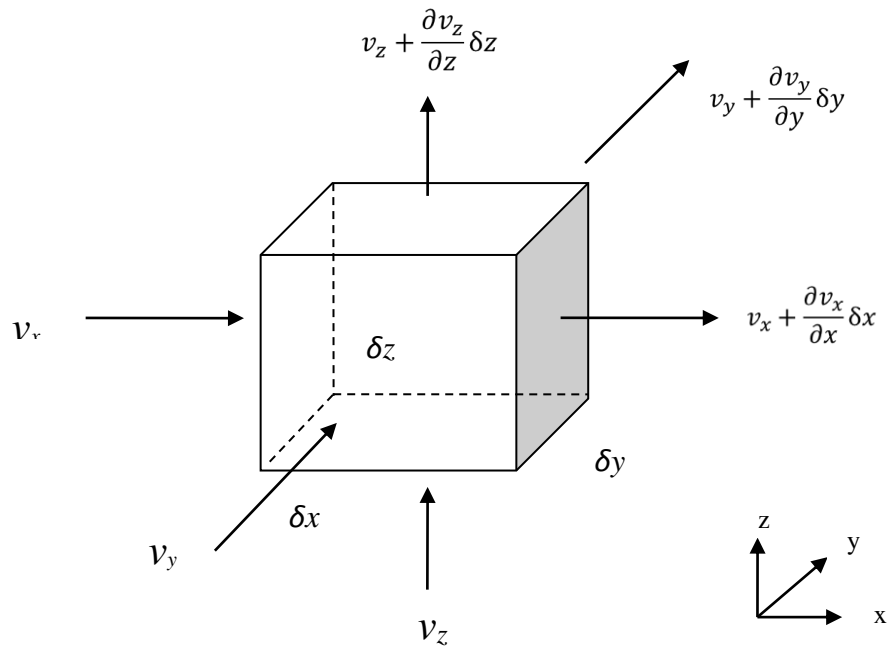
Figure 3. 1    3D Flow through a typical control element, in x, y and z co-ordinates

In the first instance, for a one-dimensional formulation, inflow and outflow are considered in the vertical ($z$) only.  The volume of water entering the system per unit time in the $z$ direction ($V_{Input}$) is given by:

$$V_{Input} = v_z \cdot \delta x \cdot \delta y \tag{3.3}$$

where $v_z$ is the velocity of water flow in the $z$ direction.  Similarly, the volume of water leaving the system per unit time is ($V_{Output}$) given by:

$$V_{Output} = \left( v_z + \frac{\partial v_z}{\partial z} \delta z \right) \cdot \delta x \cdot \delta y \tag{3.4}$$

The change in the volume of water stored in the control element per unit time is therefore given by the difference between inflow and outflow i.e.:

$$V_{Input} - V_{Output} = -\frac{\partial v_z}{\partial z} \cdot \delta x \cdot \delta y \cdot \delta z \qquad (3.5)$$

For the case of flow through a saturated soil, assuming steady conditions exist, the change in storage of water in the control element must be equal to zero i.e.:

$$\frac{\partial v_z}{\partial z} \delta x \cdot \delta y \cdot \delta z = 0 \qquad (3.6)$$

and since $\delta x \cdot \delta y \cdot \delta z = 0$ then:

$$\frac{\partial v_z}{z} = 0 \qquad (3.7)$$

Alternatively, for an unsaturated soil the net excess flow is equated to the change in the volume of water in the control element per unit time, thus:

$$\frac{\partial v_z}{\partial z} = -\frac{\partial \theta}{\partial t} \qquad (3.8)$$

where, $\theta$ is the volumetric moisture content. Equation (3.8) may be abbreviated to:

$$\nabla \cdot v = -\frac{\partial \theta}{\partial t} \qquad (3.9)$$

Equation (3.9) can be expressed as follows for one dimensional flow only:

$$-\frac{\partial \theta}{\partial t} = \frac{\partial v_z}{\partial z}$$ 

(3.10)

For the axi-symmetric formulation required here, inflow and outflow are shown to occur in both the vertical ($z$) and radial ($r$) directions. Figure 3.2 illustrates a typical control element, in r z co-ordinates.
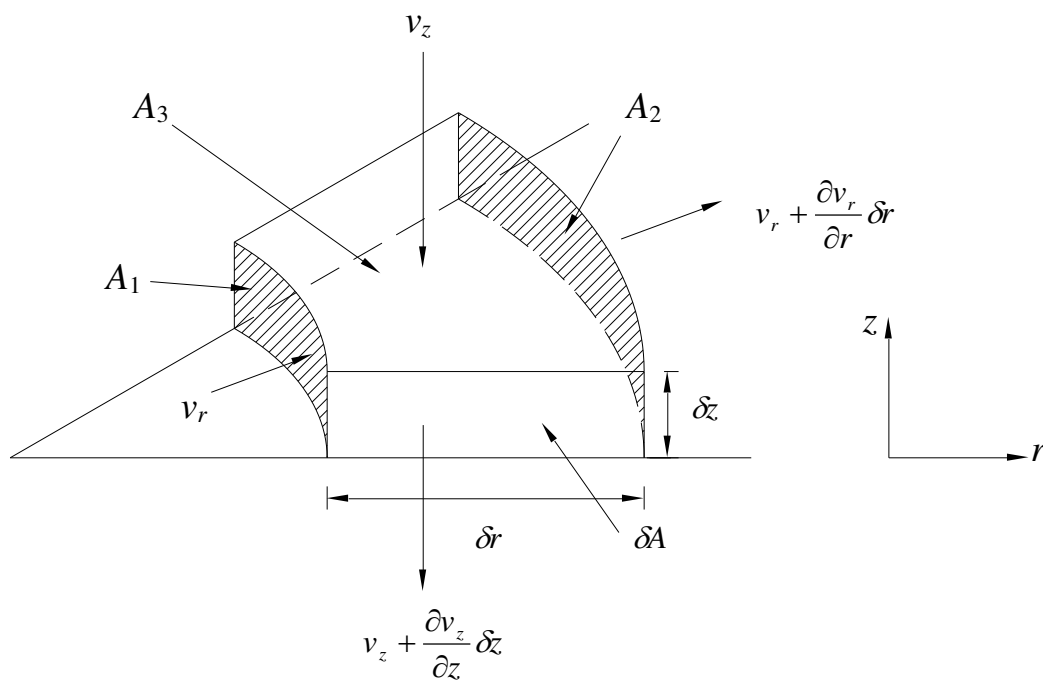


Figure 3. 2    3D Flow through a typical control element

Considering the flow of the moisture in the $r$ direction only, the volume of water entering the system per unit time is given by:

$$V_{Input} = v_r A_1 \tag{3.11}$$

where, $v_r$ is the velocity of water flow in the $r$ direction and $A_1$ is the area over which this flow occurs. Noting that, $A_1 = 2\pi r \delta z$ equation (3.11) becomes:

$$V_{Input} = v_r 2\pi r \delta z \tag{3.12}$$

Similarly, the volume of water leaving the system per unit time is given by:

$$V_{Output} = \left( v_r + \frac{\partial v_r}{\partial r} \delta r \right) A_2 \tag{3.13}$$

Again, noting that $A_2 = 2\pi(r + \delta r)\delta z$ equation (3.13) becomes:

$$V_{Output} = v_r 2\pi(r + \delta r)\delta z + \frac{\partial v_r}{\partial r} \delta r 2\pi(r + \delta r)\delta z \tag{3.14}$$

Expanding equation (3.14) yields:

$$V_{Output} = v_r 2\pi r \delta z + v_r 2\pi \delta r \delta z + \frac{\partial v_r}{\partial r} \delta r 2\pi r \delta z + \frac{\partial v_r}{\partial r} \delta r 2\pi \delta r \delta z \tag{3.15}$$

Letting $\delta A = \delta r \delta z$ and substituting into equation (3.15) gives:

$$V_{Output} = v_r 2\pi r \delta z + v_r 2\pi \delta A + \frac{\partial v_r}{\partial r} 2\pi r \delta A + \frac{\partial v_r}{\partial r} 2\pi \delta r^2 \delta z \tag{3.16}$$

The fourth term is relatively small and is therefore eliminated from further consideration. The change in the volume of water stored in the control element is therefore given by difference between inflow and outflow i.e.

$$V_{input} - V_{Output} = -\left( v_r \, 2\pi\delta A + \frac{\partial v_r}{\partial r} \, 2\pi r\delta A \right)$$  (3.17)

The net excess flow in $r$ direction can be equated to the change in the volume of water, $V_w$ in the control element per unit time, $t$ thus:

$$-\frac{\partial V_w}{\partial t} = v_r \, 2\pi\delta A + \frac{\partial v_r}{\partial r} \, 2\pi r\delta A$$  (3.18)

Next flow in the $z$ direction can be considered, using a similar approach as above, the net outflow in $z$ direction can be written as:

$$-\frac{\partial V_w}{\partial t} = \frac{\partial v_z}{\partial z} \, 2\pi r\delta A$$  (3.19)

Now, combining flow from both the $r$ and $z$ directions yields:

$$-\frac{\partial V_w}{\partial t} = v_r \, 2\pi\delta A + \frac{\partial v_r}{\partial r} \, 2\pi r\delta A + \frac{\partial v_z}{\partial z} \, 2\pi r\delta A$$  (3.20)

Multiplying through by $r$ gives:

$$-r\frac{\partial V_w}{\partial t} = rv_r 2\pi\delta A + r\frac{\partial v_r}{\partial r} 2\pi r\delta A + r\frac{\partial v_z}{\partial z} 2\pi r\delta A \qquad (3.21)$$

Noting from figure 3.2, that the total volume of the element, $V_T = 2\pi r\delta A$ and substituting this into equation (3.21) yields:

$$-r\frac{\partial V_w}{\partial t} = v_r V_T + r\frac{\partial v_r}{\partial r} V_T + r\frac{\partial v_z}{\partial z} V_T \qquad (3.22)$$

Re-arranging equation (3.22) gives:

$$-\frac{1}{V_T}\frac{\partial V_w}{\partial t} = \frac{1}{r}\left(v_r + r\frac{\partial v_r}{\partial r} + r\frac{\partial v_z}{\partial z}\right) \qquad (3.23)$$

For constant $V_T$ and volumetric moisture content, $\theta = \partial V_w/V_T$ , equation (3.23) may be abbreviated to:

$$-\frac{\partial \theta}{\partial t} = \frac{v_r}{r} + \frac{\partial v_r}{\partial r} + \frac{\partial v_z}{\partial z} \qquad (3.24)$$

Equation (3.10) and (3.24) are the fundamental governing differential equation describing flow of moisture. The both equations provided moisture flow under isothermal conditions in non-deformable unsaturated soil. These two equations can be further developed by introducing an expression for flow velocity (e.g. Darcy's Law) which presented in section 3.3.2 below.

3.3.2    Application of Darcy's Law

In order to develop a model for predicting moisture transfer through unsaturated soils, a relationship between flow and the appropriate driving force or potential for moisture flow must be established.  In practice, Darcy's Law is normally applied to give an average flow velocity through a given cross section of the porous medium.

For a saturated soil, Darcy's linear flow law presents the following equation for flow velocity:

$$v = -K\nabla i \tag{3.25}$$

where, $K$ is the hydraulic conductivity (cm/s) and $i$ is the hydraulic gradient.  The negative sign indicates that flow takes place in the direction of decreasing total head or potential.

For dealing with the analysis of saturated flow, a constant saturated value of $K$ may be reasonable.  However, the magnitude of the hydraulic conductivity is recognised to be reliant on the soil water density and viscosity, the flow turbulence, the soil porosity, the shape and arrangement of soil particles and the thickness of adsorbed layers in the case of fine grained soils (Rees 1990).

For the unsaturated soil moisture flow, Darcy's Law may be used under the following conditions (Swatzendruber 1968):

i.      That a relatively large sample that at least a few hundred grains in width is employed, and

ii.     That flow is quite slow with a Reynolds number is less than unity.

These conditions are commonly accepted in practice.

When applying Darcy's Law to moisture flow in unsaturated soil, the driving force (or hydraulic gradient) is known as the 'total potential' for moisture flow. Although soil water may have kinetic and potential energy, the kinetic energy is proportional to the square of the velocity. Since the velocity of flow in many soils is usually small, therefore, the kinetic energy may assume to be negligible.

Total potential may be considered as the sum of various component potentials that could contribute to the overall driving force for moisture transfer are pressure potential, gravitational potential, osmotic potential and pneumatic potential (Yong and Warkentin 1974). Osmotic potential may be considered when chemical (e.g. salt) gradients exist and pneumatic potential relates to the variations of gas pressure. However, both these contributions are considered to be negligible for the problems in hand. As a result, in this study the only components to total potential that are considered here are the pressure potential and the gravitational potential.

The term capillary potential is taken to have broadly the same meaning as the negative pressure and it is used in the current study. Capillary potential can be directly converted to equivalent negative pore water pressure or soil suction (a positive quantity).

Gravitational potential is also considered in this study.  This is important for achieving correct equilibrium moisture content distributions.  In addition, the soil's hydraulic conductivity is considered to be dependent on the degree of saturation (and therefore total potential).  Therefore, describing Darcy's Law for practice in the analysis of unsaturated soil yields,

$$v = -K(\phi)\nabla\phi \tag{3.26}$$

where, $K(\phi)$ is the unsaturated hydraulic conductivity (cm/s) and $\phi$ is the total potential for moisture flow.  $K(\phi)$ is written here in this manner to indicate a general dependence of $K$ on total potential.

Introducing Darcy's Law expressed for fluid flow in a partially saturated can be used to expand equation (3.10) and (3.24) yielding:

$$\frac{\partial\theta}{\partial t} = \frac{\partial}{\partial z}\left[K_z(\phi)\frac{\partial\phi}{\partial z}\right] \tag{3.27}$$

$$\frac{\partial\theta}{\partial t} = K_r(\phi)\frac{1}{r}\left(\frac{\partial\phi}{\partial r}\right) + K_r(\phi)\frac{\partial}{\partial r}\left(\frac{\partial\phi}{\partial r}\right) + K_z(\phi)\frac{\partial}{\partial z}\left(\frac{\partial\phi}{\partial z}\right) \tag{3.28}$$

As discussed above, the total potential for moisture flow is taken as the sum of the pressure or capillary potential and gravitational potential i.e.

$$\phi = \psi + z \tag{3.29}$$

Therefore, substituting equation (3.29) into equation (3.27) and (3.28) gives:

$$\frac{\partial \theta}{\partial t} = \frac{\partial}{\partial z}\left[ K_z(\psi)\frac{\partial(\psi + z)}{\partial z} \right] \qquad (3.30)$$

$$\frac{\partial \theta}{\partial t} = K_r(\psi)\frac{1}{r}\left( \frac{\partial(\psi + z)}{\partial r} \right) + K_r(\psi)\frac{\partial}{\partial r}\left( \frac{\partial(\psi + z)}{\partial r} \right) + K_z(\psi)\frac{\partial}{\partial z}\left( \frac{\partial(\psi + z)}{\partial z} \right) \qquad (3.31)$$

But $\partial z/\partial r = 0$, therefore equation (3.31) becomes:

$$\frac{\partial \theta}{\partial t} = K_r(\psi)\frac{1}{r}\left( \frac{\partial(\psi)}{\partial r} \right) + K_r(\psi)\frac{\partial}{\partial r}\left( \frac{\partial(\psi)}{\partial r} \right) + K_z(\psi)\frac{\partial}{\partial z}\left( \frac{\partial(\psi)}{\partial z} \right) + \frac{\partial K_z(\psi)}{\partial z} \qquad (3.32)$$

It can be noted that a solution is sought for the variation of capillary potential with time and that the unsaturated hydraulic conductivity is known to be dependent on capillary potential. Therefore assuming further that the soil is isotropic and restating the left hand side of equations (3.30) and (3.32) in terms of capillary potential yields:

$$\frac{\partial \theta}{\partial \psi}\frac{\partial \psi}{\partial t} = \frac{\partial}{\partial z}\left[ K(\psi)\frac{\partial \psi}{\partial z} \right] + \frac{\partial K(\psi)}{\partial z} \qquad (3.33)$$

$$\frac{\partial \theta}{\partial \psi}\frac{\partial \psi}{\partial t} = \frac{\partial}{\partial r}\left[ K(\psi)\frac{\partial \psi}{\partial r} \right] + \frac{\partial}{\partial z}\left[ K(\psi)\frac{\partial \psi}{\partial z} \right] + \frac{\partial K(\psi)}{\partial z} + \frac{1}{r}K(\psi)\frac{\partial \psi}{\partial r} \qquad (3.34)$$

The term $\partial\theta/\partial\psi$ is called the specific moisture capacity of the soil and is often denoted as $C(\psi)$ (Carslaw and Jaeger 1959).

$$C(\psi)\frac{\partial\psi}{\partial t} = \frac{\partial}{\partial z}\left[K(\psi)\frac{\partial\psi}{\partial z}\right] + \frac{\partial K(\psi)}{\partial z}$$

(3.35)

$$C(\psi)\frac{\partial\psi}{\partial t} = \frac{\partial}{\partial r}\left[K(\psi)\frac{\partial\psi}{\partial r}\right] + \frac{\partial}{\partial z}\left[K(\psi)\frac{\partial\psi}{\partial z}\right] + \frac{\partial K(\psi)}{\partial z} + \frac{1}{r}K(\psi)\frac{\partial\psi}{\partial r}$$

(3.36)

Equation (3.35) and (3.36) are referred to as one-dimensional and two-dimensional axi-symmetric Richards' equation (Richards 1931).

## 3.4    THE WATER-UPTAKE MODEL

As discussed in Chapter 2, the current work will be based on the development of a macroscopic model for water uptake by vegetation.  In this approach, a pre-defined root-zone is assumed to be active.  Within this zone moisture will be extracted at a rate determined by root density and the overall transpiration demand.  This type of behaviour can be conveniently representing by the use of a volumetric sink term included in the unsaturated flow equation.  The sink term can simply be included into equation (3.35) and (3.36) to yield the 1D and 2D axi-symmetric equations to yield:

$$C(\psi)\frac{\partial\psi}{\partial t} = \frac{\partial}{\partial z}\left[K(\psi)\frac{\partial\psi}{\partial z}\right] + \frac{\partial K(\psi)}{\partial z} - S$$

(3.37)

$$C(\psi)\frac{\partial \psi}{\partial t} = \frac{\partial}{\partial r}\left[K(\psi)\frac{\partial \psi}{\partial r}\right] + \frac{\partial}{\partial z}\left[K(\psi)\frac{\partial \psi}{\partial z}\right] + \frac{\partial K(\psi)}{\partial z} + \frac{1}{r}K(\psi)\frac{\partial \psi}{\partial r} - S \qquad (3.38)$$

The sink term, *S*, is expressed as the volume of water per unit volume of soil per unit time (cm$^3$ water. cm$^{-3}$ soil. sec$^{-1}$).

However, in order to be able to make use of equation (3.37) and (3.38) to simulate water uptake by roots, this sink term has to be defined in a manner that will adequately reflect the water extraction process throughout the root-zone. The development of a spatially variable sink term, based on a photographic (or pictorial) representation of the root zone, is presented below.

### 3.4.1   Development of an Image-Based Root Density Approach

The current work is aimed at applications for a range of geo-engineering problems mentioned previously. With this in mind, an effort is made to maintain as simple an approach as possible that may yield acceptable accuracy for application to the class of problems envisaged.

There are a number of different approaches available in the literature that may be used to 'distribute' the transpired water through the soil profile. In most cases, this is based on an assumed geometry of the root zone. Figure 3.3 shows some of the methods that have been used elsewhere for this purpose. Figure 3.3a shows a constant rate of extraction assumed for the entire depth of the root zone (Feddes et al. 1978). Field observation has, in many cases, revealed the main shortfall of Figure 3.3a – namely

that root density and water uptake clearly vary with depth at least to some extent. Figure 3.3b is a further development to accommodate this observation in a simple manner. Here a linear variation of extraction rate with depth is assumed. Figure 3.3c represents a further simplification, where the rate of extraction at the very tip of the root system is assumed to be zero, while that near the surface indicates where root densities are at a maximum. Figure 3.3d shows an alternative model where an exponential form can be employed.
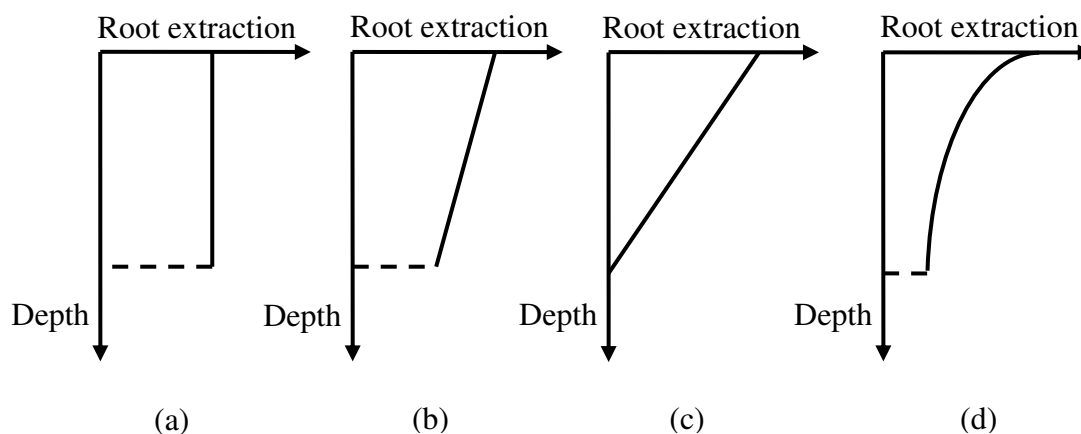


Figure 3. 3     One-dimensional water uptake model

(a) One-dimensional linear model by Feddes et al. 1978; (b) One-dimensional linear model by Hoogland et al. 1981; (c) One-dimensional linear model by Prasad 1988; (d) Exponential model by Dwyer et al. 1988.

Some of the models shown in Figure 3.3 have been applied with varying degree of success. Perrochet (1987) presents a review of the performance of these methods. Simplicity may be an attractive characteristic for modelling purposes. However, it is fairly self-evident that most real root systems (see Figure 3.4 for examples) will

exhibit more complex root morphologies that are quite different from those implied in the above models.



Figure 3. 4    The diversity of root architecture in prairie plants, figure reproduced from Illinois EPA (2005)

It is also realised that similar assumptions have been made in attempts to model water uptake in the vicinity of trees (see Chapter 2). Some common forms of imposed root geometries can be found in the literature (Indraratna et al. 2006; Vrugt et al. 2001; Rees and Ali 2006). All of these models simplify the geometry of the root zone largely ignoring the complexities of the natural architecture of the root system.
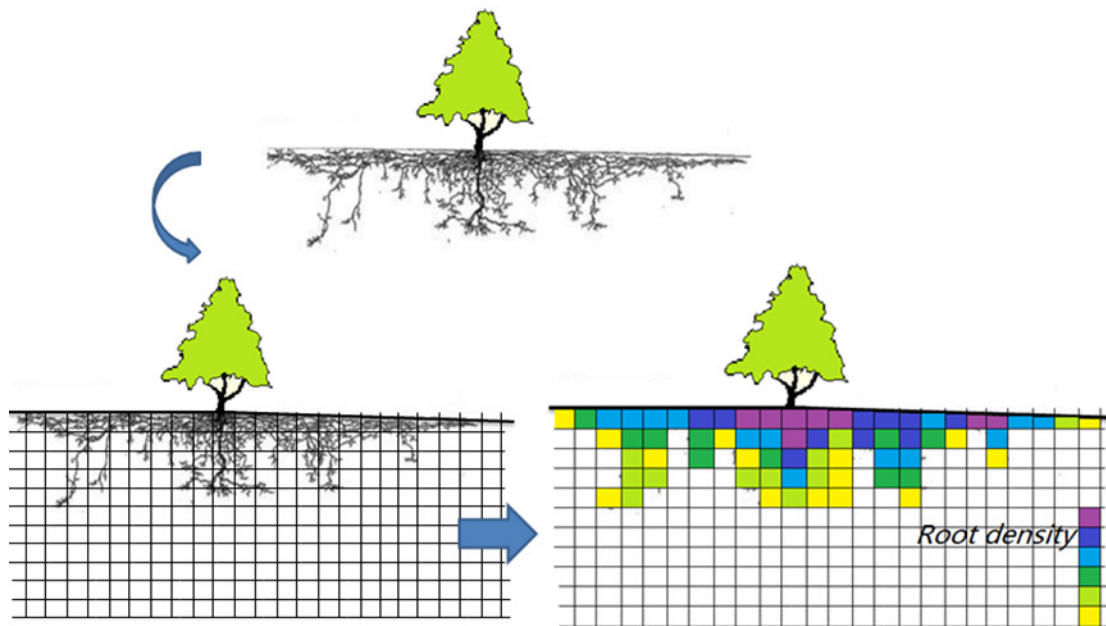
Figure 3. 5     Image-based Root density ratio approach

In view of the above, a new approach is proposed here that aims to both avoid such simplification in geometry, and hence more closely mimic natural root morphology, and to allow efficient implementation within numerical solutions. The method suggested is conceptually outlined in Figure 3.5 and essentially comprises four basic steps:

(1)     Obtain the most representative available data to define the root system architecture; this could be for example an image, as illustrated in Figure 3.5, or measured root length density data;

(2)     Define a grid system that will be used to discretise the domain containing the root system into a number of pixels - this can be chosen at convenience perhaps matching a finite element mesh for example;

(3)     Calculate an equivalent root density ratio for each pixel.  For the image example this is defined as proportion of the pixel occupied by root material, (resulting in a pixilation of the image as illustrated in Figure 3.5), or if root length density data is available this can be averaged across a particular pixel normalised by a unit length per volume (m/m$^3$) and then used directly to define the root density ratio;

(4)     Determine the sink term for each pixel – the sum of which will amount to the overall transpiration.

The calculation of the sink term for each pixel will depend upon the assumed geometry.  For example, for a one-dimensional case it can be defined as:

$$S_i = T' \cdot \frac{R_i L_i}{\displaystyle\sum_{i=1}^{M} R_i L_i} \frac{1}{L_i} \left(i = 1,2,3\ldots M\right) \tag{3.39}$$

where, $R_i$ is the root density ratio of a single pixel, $L_i$ is the length of the corresponding pixel, the subscript $i$ denotes the pixel number and $M$ is the number of pixels in the domain, the total transpiration, $T'$, is expressed in centimetres per unit time (cm. sec$^{-1}$) corresponding the one-dimensional problem.

Equations (3.39) permit a 'natural' root density distribution of the total transpiration $T'$ with depth.  Similar equations can be readily developed for 2D, 2D-axisymetical and 3D applications.  For a two-dimensional plane geometry, the sink term can be given as:

$$S_i = T'' \cdot \frac{R_i A_i}{\sum\limits_{i=1}^{M} R_i A_i} \frac{1}{A_i} \left(i = 1,2,3...M\right) \tag{3.40}$$

In Equation (3.40), $A_i$ is the area for a corresponding pixel; $T''$ is the total transpiration which is expressed in square centimetres per unit time ($cm^2 \cdot sec^{-1}$).

For a two-dimensional axi-symmetric form, the sink term can be written as:

$$S_i = T^r \cdot \frac{R_i V_i}{\sum\limits_{i=1}^{M} R_i V_i} \frac{1}{V_i} \left(i = 1,2,3...M\right) \tag{3.41}$$

where, $V_i$ is the volume for a corresponding pixel in a 2D axi-symmetric form; $T^r$ is the total transpiration which is expressed as the volume of water per unit time ($cm^3 \cdot sec^{-1}$).

Implementation within a finite element analysis, when the defined grid matches the finite element mesh, is then achieved via sink term in equation (3.39), (3.40) or (3.41) for a one-dimensional, two-dimensional or two-axisymmetric problem.

3.4.2   Water Uptake Reduction Factor

Soil suction resists water movement and affects the transpiration rate: the greater the soil suction, the more difficult it becomes for the soil water to be discharged by the

roots. Soil suction is a reduction factor for the potential transpiration rate, and as a model proposed by Feddes et al. (1978) describes the sink term for actual transpiration is as follows:

$$S(\psi) = \alpha(\psi) S_{max} \qquad (3.42)$$

where, $S_{max}$ is water uptake by plant root with the potential transpiration rate; $\alpha(\psi)$ (dimensionless) is a prescribed function of the capillary potential referred to as a water-stress function (Figure 3.6). The root water uptake is zero above the anaerobiosis point ($h_1$) as well as below the wilting point ($h_4$), and it is constant at its maximum value between $h_2$ and $h_3$. A linear variation of $\alpha(\psi)$ with $\psi$ is assumed when $\psi$ is less than $h_2$ and greater than $h_1$ or greater than $h_3$ and less than $h_4$.
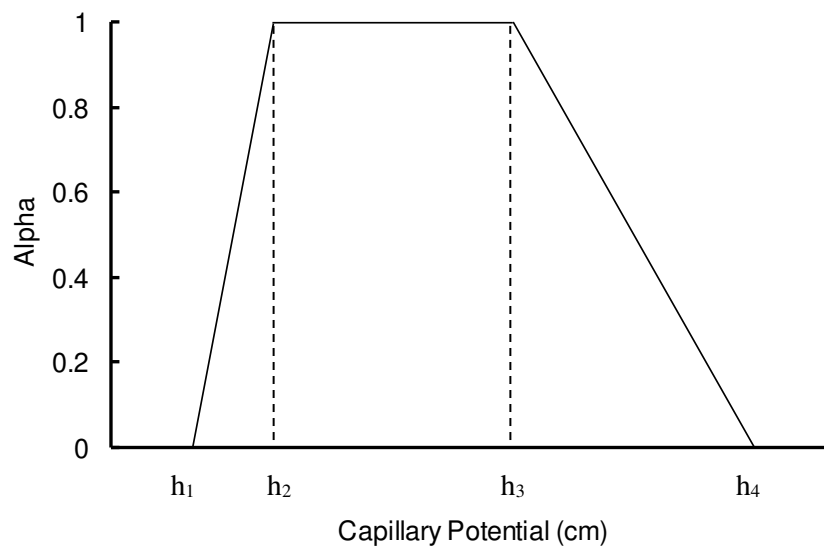


Figure 3. 6    General shape of the alpha as a function of the absolute value of the capillary potential, figure modified after Feddes et al (1978)

The water uptake by roots may be assumed to zero for conditions drier than wilting

point and wetter than a certain anaerobiosis point. It is recognized that there is no exact wilting point exists since it varies from -10000 cm to -20000 cm, but for many practical purposes a mean value of about -15000 cm can be considered as a reasonable estimate (Feddes et al. 1976).

There are two assumptions also provided by Feddes et al. (1976): i) no water uptake by the roots appear above anaerobiosis point which corresponds a pressure head of -50 cm, and ii) if the pressure head is less than -50 cm, a linear variation of water uptake with $\psi$ is assumed. From an evaluation of moisture needs and the effects of pressure head on production and quality of various crops, Feddes et al. (1976) stated that in general for these crops the pressure head at which soil water begins to limit plant growth is about -400 cm. Therefore, the water uptake by roots is constant and at a maximum rate for -400 cm ($h_2$) < $\psi$ < -50 cm ($h_1$). The water uptake for the plant, is assumed to decrease linearly between $h_3$ = -400 cm and $h_4$ = -15000 cm. Therefore, if soil moisture is limiting, Equation (3.43), (3.44) and (3.45) become:

$$S_i = \alpha(\psi) \cdot T' \cdot \frac{R_i}{\sum_{i=1}^{M} R_i} \frac{1}{L_i} \left(i = 1,2,3\ldots M\right) \qquad (3.43)$$

$$S_i = \alpha(\psi) \cdot T'' \cdot \frac{R_i}{\sum_{i=1}^{M} R_i} \frac{1}{A_i} \left(i = 1,2,3\ldots M\right) \qquad (3.44)$$

$$S_i = \alpha(\psi) \cdot T^r \cdot \frac{R_i}{\sum_{i=1}^{M} R_i} \frac{1}{V_i} \left(i = 1,2,3\ldots M\right) \qquad (3.45)$$

In this section, a numerical model has been presented for unsaturated moisture flow incorporating a sink term, *S,* to represent water uptake by root extraction. The development of a spatially variable sink term, based on a photographic (or pictorial) representation of the root zone, enables the representation of the water extraction process throughout the entire root-zone.

As detailed in Chapter 1 one of the objectives of this study is to implement a preliminary assessment of the role of a mature tree in slope stability analysis and another is to investigate the influence of tree locations and root architectures in slope stability. To enable these objectives to be addressed utilization of a multidisciplinary approach in the areas of mass transfer (soil moisture flow), soil science (plant water uptake processes) and geotechnical engineering (slope stability) is required. The new water uptake model developed here is aimed at the prediction of the soil suction patterns spatially generated by the plant through the whole simulated domain and has been achieved by considering aspects of both mass transfer and soil science. The next step, considered in the following section, is to link this model of water uptake to geotechnical models of slope stability. Vegetation can clearly influence slope stability not only through mechanical soil reinforcement (Wu 2013) but also via root water uptake (Rees and Ali 2012). The resulting variation in soil moisture content (or suction) is included, in the following section, within an extended slope stability analysis that employs a method of estimating shear strength as a function of suction that can be linked the influence of pore-water pressure changes (from the water-uptake process) on soil shear strength, and therefore changes on the stability of unsaturated soil slopes.

## 3.5     UNSATURATED SOIL SLOPE STABILITY

The stability of natural or man-made soil slopes still remains a significant matter of worldwide interest.  Slope stability analysis has become a common analytical process which generally aims to identify the lowest factor of safety through a possible failure surface.

Traditionally, for a saturated soil, there are two main types of stability analysis considered which are total stress analysis and effective stress analysis (Lambe and Whitman 1969).  Total stress analysis is generally used to analyse a recently cut or constructed slope (i.e. short-term period) and it is assumed that the water pressure in the slope has had no time to dissipate.  The strength parameters of that analysis are defined using Mohr-Coulomb failure envelope in terms of total stresses and pore-water pressures are not required.  On the other hand, effective stress analysis is normally applied for a long term slope stability analysis.  The strength parameters are described by Mohr-Coulomb failure envelope and the effective shear strength concept provided by Terzaghi (1936).  However, such analyses focus on saturated conditions and therefore, by definition, do not need to include any contribution to shear strength from negative pore water pressures (suctions).

Sometimes, it may be a reasonable assumption to ignore negative pore water pressures in situations where the major portion of possible slip surfaces is below the groundwater table and the saturated state (the most dangerous condition) is of major concern.  However, the effect of negative pore water pressure may become more significant, for example, when the groundwater table is far away from soil surface and perhaps where plant root activity is involved.  As indicated earlier in the thesis, an

evaluation of slope stability in the presence of vegetation is clearly of value in this context. Therefore, the stability of an unsaturated soil slope is considered in relation to soil suction created by the plant water-uptake process in this study. With regards to this, the approach adopted here is to implement slope stability analysis which includes the contributions of vegetation to shear strength.

3.5.1  Shear Strength of Unsaturated Soils

In the current work, a reasonably simple framework is sought that will satisfy a preliminary assessment of the influence of soil suction changes on soil shear strength. A detailed description of research on unsaturated shear strength, stress path analysis and the variety strength experiments available can be found elsewhere (Fredlund et al. 1978; Escario and Juca 1989; Abramento and Carvalho 1989; Fredlund and Rahardjo 1993; Fredlund et al. 1996; Vanapalli et al. 1996; Khailili and Khabbaz 1998; Bao et al. 1998; Vilar 2006; Sheng et al. 2008; Zhang et al. 2014). Many researchers (Litvin 2008; Cascini et al. 2010; Zhu and Zhang 2015) refer to a linear equation for the shear strength of an unsaturated soil that expressed as an extended Mohr-Coulomb shear strength equation as proposed by Fredlund et al. (1978).

Fredlund et al. (1978) considered a constant angle value ($\phi^b$) for indicating the rate of increase in shear strength relative to matric suction. The use of $\phi^b$ is simple and gives a rough estimation as the increase of shear strength as a function of soil suction.

$$\tau = c' + \tau_\sigma + \tau_{s1} \qquad (3.46)$$

where, $\tau_\sigma = (\sigma_n - u_a)\tan\phi'$ and $\tau_{s1} = (u_a - u_w)\tan\phi^b$. $c'$ is the effective cohesion, $(\sigma_n - u_a)$ is the net normal stress, and $\phi'$ is angle of friction. $(u_a - u_w)$ is the matric suction and $\phi^b$ is the angle indicating the rate of increase in shear strength relative to matric suction.

However, some published experimental results on shear strength of unsaturated soil show significant nonlinearity in the shape of the shear strength envelope with respect to soil suction (Donald 1956; Escario and Sáez 1986; Fredlund et al. 1987; Gan and Fredlund 1988). As the unsaturated soil shear strength is strongly related to the amount of water in the voids of the soil that causes matric suction (Vanapalli et al. 1996). Therefore, it is clear that a general relationship between the unsaturated shear strength of a soil and soil-water characteristic curve should be established (Fredlund et al. 1996; Vanapalli et al. 1996).

There is a direct correspondence between the nonlinear nature of the shear strength envelope with respect to increasing matric suction and the behaviour of the soil-water characteristic curve for a typical soil is presented in Figure 3.7. The shear strength envelope for all soil types behaves as a saturated soil when the matric suction is less than the air-entry value of the soil. The shear strength function starts to curve once the air-entry value is exceeded. In most cases, there is an increase in shear strength with an increase in soil suction beyond the air-entry value. The unsaturated shear strength envelope turns to a near horizontal line at the residual suction for soils with considerable silt or clay. Sandy soils generally tend to decrease in strength at higher soil suction. The drawback of the use of linear forms of the unsaturated shear strength equation is that the unsaturated strength envelop is assumed to be linearly increasing

with soil suction which tends to overestimate the unsaturated shear strength particularly when the soil suction is very high.
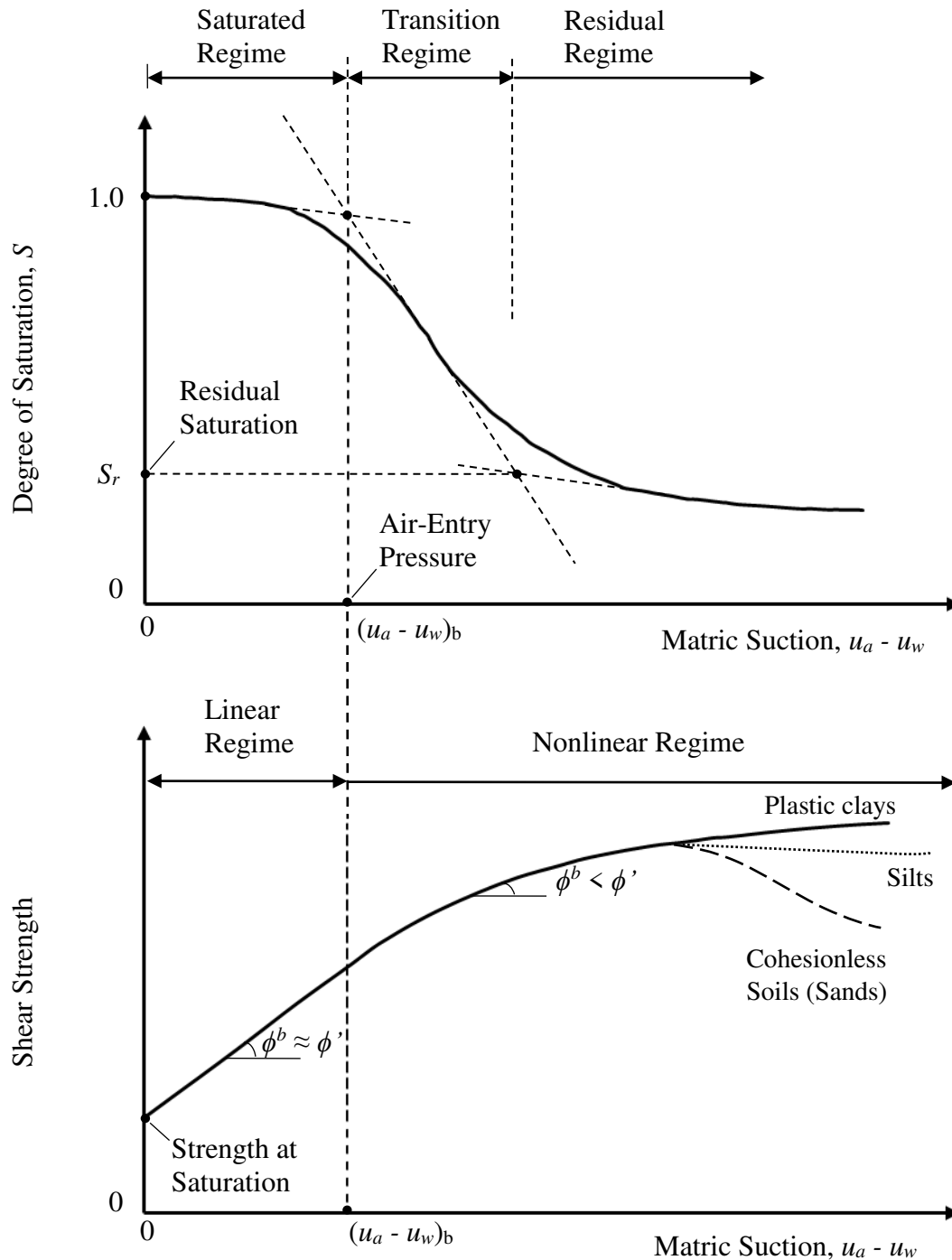


Figure 3. 7    Conceptual relationship between soil water characteristic curve and unsaturated shear strength envelope (modified from Vanapalli et al. 1996)

Therefore, the following nonlinear relationship for quantifying the unsaturated shear strength of a soil provided by Vanapalli et al. (1996) based on soil-water characteristics curve is utilized appears suitable in this study. The performance of this approach and Fredlund's approach are explored in Chapter 7.

$$\tau = c' + \tau_\sigma + \tau_{s2}$$
(3.47)

In Equation (3.47), $\tau_\sigma = (\sigma_n - u_a) \tan \phi'$ and $\tau_{s2} = (u_a - u_w) \left[ \left( \dfrac{\theta_w - \theta_r}{\theta_s - \theta_r} \right) \tan \phi' \right]$. Where, $\theta_w$ is the volumetric water content, $\theta_s$ is the saturated volumetric water content and $\theta_r$ is the residual volumetric water content.

The total suction of soil is defined as two components, specifically, matric and osmotic suction (Fredlund and Rahardjo 1993). The matric suction component is commonly related to the capillary phenomenon arising from the surface tension of water. Osmotic suction is associated with the dissolved salt content in the pore water. Since osmotic suction changes are generally less significant in this study, it is therefore assumed that the soil has the same chemical properties throughout the profile. Hence only matric suction is considered. The matric suction as the difference between the pore-air and the pore-water pressures $(u_a - u_w)$ and in this work the pore air pressure is assumed to be constant at its atmospheric value. Therefore, only changes in pore-water pressure are considered.

### 3.5.2    Stability of Unsaturated Slopes

In order to evaluate the factor of safety ($F$) against rotational shear failure in a soil slope a traditional method of slices approach (Bishop's Simplified method) is utilised in this study.  It is of interest to note that with this method, by including the normal interslice forces, the factor of safety equation becomes nonlinear and an iterative procedure is required.  This approach is capable of providing more accurate and realistic factors of safety than Fellenius's method and it is possible to easily handle the shear strength of an unsaturated soil equation in calculations.  Numerous more complete descriptions of Bishop's Simplified method available can be found elsewhere (e.g. Fredlund and Rahardjo 1993; Craig 2004; Krahn 2015).

The mobilized shear force, $S_m$, at the base of a slice can then be written as (Fredlund and Rahardjo 1993; Craig 2004):

$$S_m = \frac{\tau l}{F} \tag{3.48}$$

where, $\tau$ is shear strength of unsaturated soil as defined previously in Equation (3.47) and $l$ is the length of slice.  Thus, the influence of soil suction arising from water-uptake by roots can be accommodated by combining Equation (3.47) and (3.48), gives

$$S_m = \frac{l\left[c' + (\sigma_n - u_a)\tan\phi' + (u_a - u_w)(\frac{\theta_w - \theta_r}{\theta_s - \theta_r})\tan\phi'\right]}{F} \tag{3.49}$$

Considering equilibrium in the traditional manner then yields:

$$F = \frac{\sum \left[ c'l + N \tan\phi' - u_w l \left( \dfrac{\theta_w - \theta_r}{\theta_s - \theta_r} \right) \tan\phi' \right]}{\sum W \sin\beta} \tag{3.50}$$

where, $W$ is the total weight of a slice (kN), $N = \sigma_n l$ is the total normal force on the base of the slice (kN), $\beta$ is the angle between the tangent to the centre of the base of each slice and the horizontal (*degrees*).

In summary, the Bishop's Simplified method (1955): i) considers normal inter-slice forces, but ignores inter-slice shear forces, and ii) satisfies over all moment equilibrium, but not overall horizontal force equilibrium. The normal force at the base of a slice is derived from the summation of forces in a vertical direction on each slice, and the equation can be written as:

$$N = \frac{W - \dfrac{c'l\sin\beta}{F} + \dfrac{u_w \left[ \left( \dfrac{\theta_w - \theta_r}{\theta_s - \theta_r} \right) \tan\phi' \right] l\sin\beta}{F}}{\cos\beta + \dfrac{\tan\phi'\sin\beta}{F}} \tag{3.51}$$

Inserting the above normal force expression into equation (3.50) and gives the factor of safety for the unsaturated soil slope:

$$F = \frac{\sum\left[\dfrac{c'l + \dfrac{W\tan\phi'}{\cos\beta} - u_w\left(\dfrac{\theta_w - \theta_r}{\theta_s - \theta_r}\right)\tan\phi'l}{1 + \dfrac{\tan\phi'\sin\beta}{F}}\right]}{\sum W\sin\beta} \qquad (3.52)$$

Therefore, a factor of safety for a partially saturated slope can be evaluated in this manner. If the suction becomes zero (and the soil is saturated) Equation (3.52) defaults to the standard Bishop's Simplified method (1955).

As the result, Equation (3.52) forms the basis for the following exploration of the influence of vegetation induced suction changes on slope strength. Since the value of $F$ occurs on both sides of the expression, a trial value for $F$ must be chosen on the right-hand side to obtain of $F$ on the left-hand side. By successive iteration, convergence on the true value of $F$ is obtained. The method is obviously better solved by using a computer program which can obtain the factor of safety of a trial circle in a matter of seconds compared to hours when done manually.

3.6    CONCLUSIONS

The theoretical basis for describing moisture flow in an unsaturated soil is presented in this chapter. Some general aspects of the behaviour of unsaturated soils were discussed in the first section of the chapter. Included were brief descriptions of the types of unsaturated moisture flow and introduction of the key hydraulic properties.

The governing differential equation for moisture flow has been derived. The chosen approach is based on Richards' Equation. In this work, a sink term has been added to Richards' equation to facilitate inclusion of a water uptake model and it was presented in 1D and 2D axi-symmetric format. The application of Darcy's Law to unsaturated flow and various components of total potentials also have been presented.

The theoretical development of an image based root-density approach has been presented. The approach can be applied to 1D, 2D, 2D axi-symmetric and 3D problems. This new approach will be employed for a range of the finite element simulations which are presented later chapters of the thesis.

The theoretical development of slope stability model to provide a preliminary assessment of the significance of water content (and therefore suction) changes on the stability of unsaturated soil slopes. The new model will be employed and presented in later chapters of the thesis.

## 3.7    REFERENCES

Abramento, M. and Carvalho, C. S. 1989. Geotechnical parameters for the study of natural slopes instabilzation at Serra do Mar-Brazilian Southeast. *Proceedings of the 12$^{th}$ International Conference on Soil Mechanics and Foudation Engineering*, *Rio de Janeiro*. 3, pp. 1599-1602.

Alonso, E. E., Gens, A. and Hight, D. W. 1987. Special problem soils. *Ninth*

*European Conf. on Soil Mechanics and Foundation Engineering*. 1087-1146.

Bao, C. Gong, B. and Zhan, L. 1998. Properties of unsaturated soils and slope stability of expansive soils. *In Proceedings of the Second International Conference on Unsaturated Soils (UNSAT 98), Beijing*. 1, pp. 71-98.

Cascini, L., Cuomo, S., Pastor, M., and Sorbin, G. 2010. Modelling of rainfallinduced shallow landslides of the flow-type. *Journal of Geotechnical and Geoenvironmental Engineering*. 136(1), pp. 85-98.

Carslaw, H. S. and Jaeger, J. C. 1959. *Conduction of Heat in Solids*. Oxford: Oxford University Press.

Chang, Y. Y. and Corapcioglu, M. Y. 1997. Effect of Roots on Water Flow in Unsaturated Soils. *Journal of Irrigation and Drainage Engineering*, pp. 202-209.

Craig, R. F. 2004. *CRAIG'S SOIL MECHANICS*. 7th ed. London and New York: Spon Press.

Donald, I. B. 1956. Shear strength measurements in unsaturated non-cohesive soils with negative pore pressures. *Proceedings of the 2nd Australia - New Zealand Conference on Soil Mechanics and Foundation Engineering*. pp. 200-204.

Dwyer, L. M. Stewart, D. W. and Balchin, D. 1988. Rooting characteristics of corn, soybeans, and barley as a function of available water and soil physical characteristics. *Can. J. Soil Sci*. 68, pp. 121-132.

Escario, V. and Juca, J. 1989. Strength and deformation of party saturated soils. *Proceedings of the 12<sup>th</sup> International Conference on Soil Mechanics and Foundation Engineering, Rio de Janeiro*. 3, pp. 43-46.

Escario, V. and Sáez, J. 1986. The shear strength of partly saturated soils. *Géotechnique*. 36 (3), pp. 453-456.

Feddes, R. A. Kowalik, P. J. Malink, K. K. and Zaradny, H. 1976. Simulation of field water uptake by plants using a soil water dependent root extraction function. *J. Hydro* 31, 13-26.

Feddes, R. A. Kowalik, P. J. and Zaradny, H. 1978. *Simulation of field water use and crop yield*. Wiley.

Feddes, R. A. Hoff, H. Bruen, M. Dawson, T. Rosnay, P. Dirmeyer, P. Jackson, R. B. Kabat, P. Kleidon, A. Lilly, A. and Pitmank, A. J. 2001. Modeling Root Water Uptake in Hydrological and Climate Models. *American Meteorological Society* 82(12), pp. 2797-2809.

Fredlund, D. G. Morgenstern, N. R. and Widger, R. A. 1978. The shear strength of unsaturated soils. *Canadian Geotechnical Journal*. 15(3), pp. 313-321.

Fredlund, D. G. 1979. Appropriate concepts and technology for unsaturated soils. *Can. Geotech. J*. 16, pp. 121-139.

Fredlund, D. G. Rahardjo, H. and Gan, J. K.M. 1987. Nonlinearity of strength envelope for unsaturated soils. In: *Proceedings of the Sixth International Conference on Expansive Soils, New Delhi*. 1, pp. 49-54.

Fredlund, D. G. and Rahardjo, H. 1993. *Soil Mechanics of Unsaturated Soils*. New York: John Wiley & Sons.

Fredlund, D. G. Xing, A. Fredlund, M. D. and Barbour, S. L. 1996. The relationship of the unsaturated soil shear strength to the soil water characteristic curve. *Canadian Geotechnical Journal*. 32(3), pp. 440-448.

Gan, J. K. M. and Fredlund, D. G. 1988. Multistage direct shear testing of unsaturated soils. *Geotechnical Testing Journal*. 11(2), pp. 132-138.

Gong, D. Kang, S. Zhang, L. Du, T. and Yao, L. 2006. A two-dimensional model of root water uptake for single apple trees and its verification with sap flow and soil water content measurements. *Agricultural Water Management* 83, pp. 119-129.

Hoogland, J. C. Feddes, R. A. and Belmans, C. 1981. Root water uptake model depending on soil water pressure head and maximum extraction rate. *Acta Hort*. 119, 276-280.

Illinois Environmental Protection Agency. 2005. Landfill to Prairie Hill. *Environmental Progress*. Available at:

http://www.epa.state.il.us/environmental-progress/v30/n4/landfill.html

Indraratna, B. Fatahi, B. Khabbaz, H. 2006. Numerical analysis of matric suction effects of tree roots. *Geotechnical Engineering* 159, pp. 77-90.

Justo, J. L. and Saertersdal R. 1979. Design parameters for special soil conditions. *General Report, Proc. 7$^{th}$ Eor. Conf. SMFE* 4, pp. 181-208.

Khalili, N. and Khabbaz, M. H. 1998. A unique relationship for $\chi$ for the determination of the shear strength of unsaturated soils. *Géotechnique*. 48(5), pp. 681-687.

Klute, A. 1972. The determination of the hydraulic conductivity and diffusivity of unsaturated soils. *Soil Sci. J*. 113 (4), pp. 264-276.

Krahn, J. 2015. *Stability modelling with SLOPE/W-An Engineering Methodology*. 11$^{th}$ ed. Canada: GEO-SLOPE/W International Ltd.

Lambe, T. W. and Whitman, R. V. 1969. *Soil Mechanics*. New York: Wiley.

Luo, Y. QuYan, Z. Yuan, G. Tang, G. and Xie, X. 2003.Evaluation of macroscopic root water uptake models using lysimeter data. *American Society of Agricultural Engineers*. 46, 3.

Li, K. Y. Jong, R. D. Coe, M. T. and Ramankutty, N. 2006. Root-Water-Uptake Based upon a New Water Stress Reduction and an Asymptotic Root Distribution Function. *Earth Interactions* 10(14), pp. 1-22.

Litvin, E. 2008. Numerical analysis of the effect of rainfall infiltration on slope stability. *GROUND ENGINEERING*. pp. 38-41.

Manoli, G. Bonetti, S. Domec, J-C. Putti, M. Katul, G. Marani, M. 2014. Tree root systems competing for soil moisture in a 3D soil–plant model. *Advances in Water Resources.* 66, pp. 32-42.

Mathur, S. and Rao, S. 1999. Modelling water uptake by plant roots. *Journal of Irrigation and Drainage Engineering* 125(3), pp. 159-165.

Mualem, Y. 1976. A new model for predicting the hydraulic conductivity of unsaturated porous media. *Water Resour. Res*. 12, pp. 513-522.

Nielsen, D. R. Genuchten, M. T. V. and Biggar, J. W.  1986. Water flow and solute transport processes in the unsaturated zone. *Water Resour. Res*. 22(9), pp. 89-108.

Perrochet, P. 1987. Water uptake by plant roots: a simulation model. I: Conceptual model. *Journal of Hydrology*. 95, pp. 1-2, 55-61.

Philip, J. R. 1957. The theory of infiltration: 1. The infiltration equation and its

solution. *Soil Sci*. 83, pp. 345-357.

Prasad, R. 1988. A linear root water uptake model. *J. Hydrology*. 99, pp. 297-306.

Rees, S. W. 1990. *Seasonal Ground Movement Effects on Buried Services*. PhD thesis. University of Wales, Cardiff.

Rees, S. W. and Ali, N. 2006. Seasonal water uptake near trees: a numerical and experimental study. *Geomechanics and Geoengineering: An International Journal.* 1(2), pp. 129-138.

Rees, S. W. and Ali, N. 2012. Tree induced soil suction and slope stability. *Geomechanics and Geoengineering: An International Journal*. 7(2), pp. 103-113

Richards, L. A. 1931. Capillary conduction of liquids in porous media. *Physics* 1, pp. 318-333.

Schreiner, H. D. 1986. *State of the art review of expansive soils for TRRL*. London: Imperial College.

Shankar, V. Prasad, K. S. H. Ojha, C. S. P. and Govindaraju, R. S. 2013. Model for Nonlinear Root Water Uptake Parameter. *Journal of Irrigation and Drainage Engineering*. 138 (10), pp. 905-917.

Sheng, D. Fredlund, D. G. and Gens, A. 2008. A new modelling approach for unsaturated soils using independent stress variables. *Canadian Geotechnical Journal*. 45(4), pp. 511-534.

Swatzendruber, D. 1968. The applicability of Dracy's Law. *Proc. SSSA* 32, pp. 11-18.

Terzaghi, K. 1936. The Shear Resistence of Saturated Soils. *Proc. Conf. Soil Mech. Found. Eng., Cambridge*, pp. 54-56.

van Genuchten, M. T. V. 1980. A closed form equation for predicting the hydraulic conductivity of unsaturated soils. *Soil Sci. Am. J*. 44, pp. 892-898.

Vanapalli, S. K. Fredlund, D. G. Pufahl, D. E. and Clifton, A. W. 1996. Model for the prediction of shear strength with respect to soil suction. *Canadian Geotechnical Journal*. 33(3), pp. 379-392.

Vilar, O. M. 2006. A simplified procedure to estimate the shear strength envelope of unsaturated soils. *Canadian Geotechnical Journal*. 43(10), pp. 1088-1095.

Vrugt, J. A. Hopmans, J. W. and Simunek, J. 2001. Calibration of Two-Dimensional Root Water Uptake Model. *Soil Sci. Am. J*. 65(4), pp. 1027-1037.

Wu, T. H. 2013. Root reinforcement of soil: review of analytical models, test results, and applications to design. *Canadian Geotechnical Journal.* 50(3), pp. 259-274.

Yong, R. N. Nakano, M. and Pusch, R. 2012. *Environmental Soil Properties and Behaviour.* London: CRC Press.

Zhang, L. L. Fredlund, D. G. Fredlund, M. D. and Wilson, G. W. 2014. Modeling the unsaturated soil zone in slope stability analysis. *Can. Geotech. J.* 51, pp. 1384-1398.

Zhu, H. and Zhang, L. M. 2015. Evaluating suction profile in a vegetated slope considering uncertainty in transpiration. *Computers and Geotechnics.* 63, pp. 112-120.

**CHAPTER FOUR**

**THE NUMERICAL SOLUTION**

4.1    INTRODUCTION

An approximate numerical solution of the moisture transfer model presented in Chapter 3 is now developed in this chapter.  The numerical solution is presented for the more general 2D axi-symmetric form.  However, it can easily be reduced to operate in 1D mode.  The problem addressed is one in which both spatial and time variations of the unknown variable, capillary potential in this case, are required.

Spatial discretisation of the governing partial differential equation is achieved by an application of the finite element method.  In particular the Galerkin weighted residual approach is adopted.  Whilst a full explanation of the finite element method is not presented here a complete description is provided in Zienkiewicz (1977) and

Zienkiewicz and Taylor (1989). Nevertheless, for the clarity of presentation, an introduction to the concepts relevant to the particular finite element formulation adopted is provided.

The discretisation of the time domain is achieved by the application of a finite difference time marching algorithm. A fully implicit mid-interval backward difference algorithm is employed to the spatially discretised equations. The technique required to achieve a solution is described along with the chosen convergence criterion.

The numerical evaluation of the root density ratio was coded in Matlab (see Appendix 1). The resulting values were then used to define the spatial variation of the sink term within the finite element code.

## 4.2    SPATIAL DISCRETISATION

### 4.2.1    Finite Element Concepts

Numerous practical engineering problems such as heat conduction, distribution of electrical potential, and water flow in soil that give rise to systems of ordinary or partial differential equations. The mathematical models derived thereof require solutions – but often only simple forms of the governing equations with geometrically simple boundaries can be solved exactly by available mathematical methods. The solution of multiple sets of simultaneous equations can be solved by a computer

program. Therefore, methods of obtaining solutions of problems cast in an algebraic form were developed.

Discretisation of the continuum problem is usually necessary and to achieve this end some form of approximation is normally introduced. The particular form of discretisation of the space domain adopted here is known as a trial function approximation. The process of approximating a given function by using trial functions provides a useful introduction to the finite element approach (Rockey et al. 1983). Zienkiewicz and Taylor (1989) clearly illustrate approximation by trial functions and provide the following description.
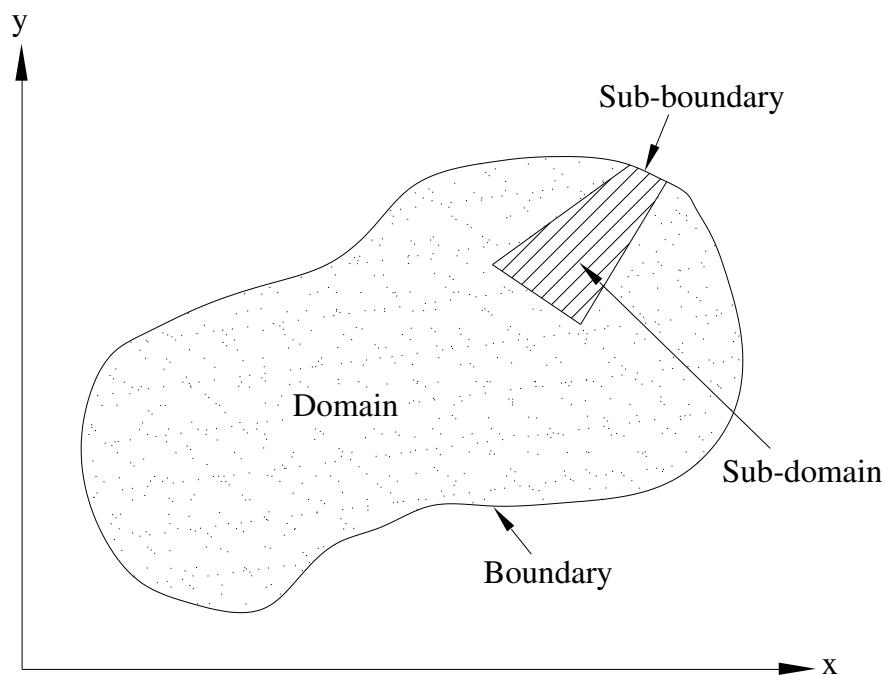


Figure 4. 1    Problem domain $\Omega$ and boundary $\Gamma$ , figure reproduced from Zienkiewicz and Taylor (1989)

A given function $u$ in some region $\Omega$ bounded by closed curve $\Gamma$ is to be approximated as shown in Figure 4.1. All functions $u$ in $\Omega$ may be approximated by:

$$u \approx \hat{u} = \sum_{i=1}^{n} N_i a_i = Na \qquad (4.1)$$

where $N_i$ are shape functions prescribed in terms of independent variables (such as coordinates $x$, $y$, etc.), $\hat{u}$ are the approximation to the function $u$ , $i$ is a point associated with that element, $n$ is the maximum number of points associated with that element and $a_i$ mostly are unknown. This equation can then be cast in an integral form from which the unknown parameters $a_i$ are to be obtained.

$$\int_{\Omega} G_j(\hat{u}) d\Omega + \int_{\Gamma} g_j(\hat{u}) d\Gamma = 0 \qquad j = 1 \text{ to } n \qquad (4.2)$$

where $G_j$ and $g_j$ prescribe known functions or operators. These integral forms will permit the approximation to be obtained element by element and an assembly to be achieved:

$$\int_{\Omega} G_j d\Omega + \int_{\Gamma} g_j d\Gamma = \sum_{e=1}^{m} \left( \int_{\Omega^e} G_j d\Omega + \int_{\Gamma^e} g_j d\Gamma \right) = 0 \qquad (4.3)$$

where $\Omega^e$ is the domain of each element, $\Gamma^e$ is the boundary, $e$ is the element number and $m$ is the maximum number of elements in the domain.

Two distinct procedures are available for obtaining an approximate solution. These are (Zienkiewicz and Taylor 1989):

     i.       The method of weighted residuals (known alternatively as the Galerkin procedure) and,

     ii.      The determination of variational functionals.

In this study, the method of weighted residuals is used for spatial discretisation. This method is widely recognised as a useful numerical approach for the solution of partial differential equation systems subject to appropriate boundary and initial conditions (Taylor and Hughes 1981, Hinton and Owen 1989).

## 4.2.2   The Weighted Residual Approach

The residual or error introduced by the approximation is given by

$$\boldsymbol{R} = \boldsymbol{u} - \hat{\boldsymbol{u}} \tag{4.4}$$

The weighted residual approach attempts to reduce this residual over the entire domain by requiring the integral of the error over the domain, weighted in various ways is equal to zero, i.e.

$$\int_{\Omega} \boldsymbol{W}_1 \boldsymbol{R}_{\Omega} \partial \Omega = 0 \tag{4.5}$$

where $W_l$ are the weighting functions required to minimise the error.

This statement leads to a set of simultaneous linear equations for the unknown coefficients $a_i$ (Equation 4.1). Thus when a function is to be approximated in this way, the resulting system of equations may be solved to obtain the unknown coefficients, by using suitable shape and weighting functions.

The type of weighting functions chosen gives rise to different forms of approximation, for example Galerkin, point collocation or least square approximation (Hinton and Owen 1989). When the chosen weighting functions are the same as the shape functions, $N_i$ then the resulting approximation is known as the Galerkin method. Application of the Galerkin method to the solution of partial differential equations is common in practice. In such cases, the residual $R_\Omega$ is produced by the insertion of the trial function approximation of the unknown variables into the governing equations. The resulting residual is minimised as described above.

The application of this process to achieve spatial discretisation of the governing moisture transfer equation defined in Chapter 3 is presented in the section below.

4.2.3    Spatial Discretisation of the Moisture Transfer

The two-dimensional axi-symmetric form of the governing differential equation (equation 3.38) may be re-arranged to give:

$$\frac{\partial}{\partial r}\left[K(\psi)\frac{\partial \psi}{\partial r}\right]+\frac{\partial}{\partial z}\left[K(\psi)\frac{\partial \psi}{\partial z}\right]+\frac{\partial K(\psi)}{\partial z}+\frac{1}{r}K(\psi)\frac{\partial \psi}{\partial r}$$

$$-S-C(\psi)\frac{\partial \psi}{\partial t}=0$$

(4.6)

Multiplying through by $r$, yields:

$$r\frac{\partial}{\partial r}\left[K(\psi)\frac{\partial \psi}{\partial r}\right]+r\frac{\partial}{\partial z}\left[K(\psi)\frac{\partial \psi}{\partial z}\right]+r\frac{\partial K(\psi)}{\partial z}+K(\psi)\frac{\partial \psi}{\partial r}$$

$$-rS-rC(\psi)\frac{\partial \psi}{\partial t}=0$$

(4.7)

The unknown variable, capillary potential may be approximated using the trial function approach, for an eight node element, to give:

$$\psi \approx \hat{\psi}=\sum_{s=1}^{8}N_s(r,z)\psi_s(t)=N_s\psi_s$$

(4.8)

where, $\hat{\psi}$ provides an approximation to the function, $N_s$ is the shape functions. Replacing $\psi$ by $\hat{\psi}$ in equation (4.7) yields:

$$r\frac{\partial}{\partial r}\left[K(\hat{\psi})\frac{\partial \hat{\psi}}{\partial r}\right]+r\frac{\partial}{\partial z}\left[K(\hat{\psi})\frac{\partial \hat{\psi}}{\partial z}\right]+r\frac{\partial K(\hat{\psi})}{\partial z}+K(\hat{\psi})\frac{\partial \hat{\psi}}{\partial r}$$

$$-rS-rC(\hat{\psi})\frac{\partial \hat{\psi}}{\partial t}=R_\Omega$$

(4.9)

where $R_\Omega$ is the residual obtained by introducing the approximation in equation 4.9.

Application of the Galerkin weighted residual approach described in section 4.2.2, and making use of the specific moisture capacity, yields:

$$\int_{\Omega^e} N_r \left[ \begin{array}{c} r\dfrac{\partial}{\partial r}\left[ K(\hat{\psi})\dfrac{\partial \hat{\psi}}{\partial r} \right] + r\dfrac{\partial}{\partial z}\left[ K(\hat{\psi})\dfrac{\partial \hat{\psi}}{\partial z} \right] \\[3mm] + r\dfrac{\partial K(\hat{\psi})}{\partial z} + K(\hat{\psi})\dfrac{\partial \hat{\psi}}{\partial r} - rS - rC(\hat{\psi})\dfrac{\partial \hat{\psi}}{\partial t} \end{array} \right] \partial\Omega = 0 \qquad (4.10)$$

Hereafter, for the clarity of presentation, the dependency of the unsaturated hydraulic conductivity, the sink term and the specific moisture capacity on capillary potential will be assumed recognised and the notation abbreviated accordingly. Therefore, expanding equation (4.10) and abbreviating the notation yields:

$$\int_{\Omega^e} N_r r\frac{\partial}{\partial r} K\frac{\partial \hat{\psi}}{\partial r}\partial\Omega^e + \int_{\Omega^e} N_r r\frac{\partial}{\partial z} K\frac{\partial \hat{\psi}}{\partial z}\partial\Omega^e + \int_{\Omega^e} N_r r\frac{\partial K}{\partial z}\partial\Omega^e$$

$$(4.11)$$

$$+ \int_{\Omega^e} N_r K\frac{\partial \hat{\psi}}{\partial r}\partial\Omega^e - \int_{\Omega^e} N_r rS\partial\Omega^e - \int_{\Omega^e} N_r rC\frac{\partial \hat{\psi}}{\partial t}\partial\Omega^e = 0$$

Using integration by parts, the weak form of equation may be obtained. Considering the first term of equation (4.11) and integrating by parts gives:

$$\int_{\Omega^e} N_r r\frac{\partial}{\partial r} K\frac{\partial \hat{\psi}}{\partial r}\partial\Omega^e = \int_{\Omega^e} \frac{\partial}{\partial r} N_r rK\frac{\partial \hat{\psi}}{\partial r}\partial\Omega^e - \int_{\Omega^e} K\frac{\partial \hat{\psi}}{\partial r}\frac{\partial N_r r}{\partial r}\partial\Omega^e \qquad (4.12)$$

Similarly, for the second term of equation (4.11), repeating the above process yields:

$$\int_{\Omega^e} N_r r \frac{\partial}{\partial z} K \frac{\partial \hat{\psi}}{\partial z} \partial \Omega^e = \int_{\Omega^e} \frac{\partial}{\partial z} N_r r K \frac{\partial \hat{\psi}}{\partial z} \partial \Omega^e - \int_{\Omega^e} K \frac{\partial \hat{\psi}}{\partial z} \frac{\partial N_r r}{\partial z} \partial \Omega^e \qquad (4.13)$$

Substituting equations (4.12) and (4.13) into equation (4.11) yields the weak equation:

$$\int_{\Omega^e} \frac{\partial}{\partial r} N_r r K \frac{\partial \hat{\psi}}{\partial r} \partial \Omega^e - \int_{\Omega^e} K \frac{\partial \hat{\psi}}{\partial r} \frac{\partial N_r r}{\partial r} \partial \Omega^e + \int_{\Omega^e} \frac{\partial}{\partial z} N_r r K \frac{\partial \hat{\psi}}{\partial z} \partial \Omega^e$$

$$- \int_{\Omega^e} K \frac{\partial \hat{\psi}}{\partial z} \frac{\partial N_r r}{\partial z} \partial \Omega^e + \int_{\Omega^e} N_r r \frac{\partial K}{\partial z} \partial \Omega^e + \int_{\Omega^e} N_r K \frac{\partial \hat{\psi}}{\partial r} \partial \Omega^e \qquad (4.14)$$

$$- \int_{\Omega^e} N_r r S \partial \Omega^e - \int_{\Omega^e} N_r r C \frac{\partial \hat{\psi}}{\partial t} \partial \Omega^e = 0$$

Noting that:

$$\frac{\partial}{\partial r} N_r r = r \frac{\partial N_r}{\partial r} + N_r \qquad (4.15)$$

and

$$\frac{\partial}{\partial z} N_r r = r \frac{\partial N_r}{\partial z} \qquad (4.16)$$

Substituting equations (4.15) and (4.16) into equation (4.14), gives:

$$\int_{\Omega^e} \frac{\partial}{\partial r} N_r r K \frac{\partial \hat{\psi}}{\partial r} \partial \Omega^e - \int_{\Omega^e} K \frac{\partial \hat{\psi}}{\partial r} \left( r \frac{\partial N_r}{\partial r} + N_r \right) \partial \Omega^e + \int_{\Omega^e} \frac{\partial}{\partial z} N_r r K \frac{\partial \hat{\psi}}{\partial z} \partial \Omega^e$$

$$- \int_{\Omega^e} K \frac{\partial \hat{\psi}}{\partial z} \left( r \frac{\partial N_r}{\partial z} \right) \partial \Omega^e + \int_{\Omega^e} N_r r \frac{\partial K}{\partial z} \partial \Omega^e + \int_{\Omega^e} N_r K \frac{\partial \hat{\psi}}{\partial r} \partial \Omega^e \qquad (4.17)$$

$$- \int_{\Omega^e} N_r r S \partial \Omega^e - \int_{\Omega^e} N_r r C \frac{\partial \hat{\psi}}{\partial t} \partial \Omega^e = 0$$

Expanding equation (4.17) yields:

$$\int_{\Omega^e} \frac{\partial}{\partial r} N_r rK \frac{\partial \hat{\psi}}{\partial r} \partial \Omega^e - \int_{\Omega^e} rK \frac{\partial \hat{\psi}}{\partial r} \frac{\partial N_r}{\partial r} \partial \Omega^e - \int_{\Omega^e} N_r K \frac{\partial \hat{\psi}}{\partial r} \partial \Omega^e$$

$$+ \int_{\Omega^e} \frac{\partial}{\partial z} N_r rK \frac{\partial \hat{\psi}}{\partial z} \partial \Omega^e - \int_{\Omega^e} rK \frac{\partial N_r}{\partial z} \frac{\partial \hat{\psi}}{\partial z} \partial \Omega^e + \int_{\Omega^e} N_r r \frac{\partial K}{\partial z} \partial \Omega^e \qquad (4.18)$$

$$+ \int_{\Omega^e} N_r K \frac{\partial \hat{\psi}}{\partial r} \partial \Omega^e - \int_{\Omega^e} N_r rS \partial \Omega^e - \int_{\Omega^e} N_r rC \frac{\partial \hat{\psi}}{\partial t} \partial \Omega^e = 0$$

By eliminating third and seventh terms equation (4.18) becomes:

$$\int_{\Omega^e} \frac{\partial}{\partial r} N_r rK \frac{\partial \hat{\psi}}{\partial r} \partial \Omega^e - \int_{\Omega^e} rK \frac{\partial \hat{\psi}}{\partial r} \frac{\partial N_r}{\partial r} \partial \Omega^e + \int_{\Omega^e} \frac{\partial}{\partial z} N_r rK \frac{\partial \hat{\psi}}{\partial z} \partial \Omega^e$$

$$- \int_{\Omega^e} rK \frac{\partial N_r}{\partial z} \frac{\partial \hat{\psi}}{\partial z} \partial \Omega^e + \int_{\Omega^e} N_r r \frac{\partial K}{\partial z} \partial \Omega^e - \int_{\Omega^e} N_r rS \partial \Omega^e \qquad (4.19)$$

$$- \int_{\Omega^e} N_r rC \frac{\partial \hat{\psi}}{\partial t} \partial \Omega^e = 0$$

Expressing the first and third terms of equation (4.19) in terms of an approximate total potential $\hat{\phi}$ yield:

$$\int_{\Omega^e} \frac{\partial}{\partial r} N_r rK \frac{\partial \hat{\phi}}{\partial r} \partial \Omega^e - \int_{\Omega^e} rK \frac{\partial \hat{\psi}}{\partial r} \frac{\partial N_r}{\partial r} \partial \Omega^e + \int_{\Omega^e} \frac{\partial}{\partial z} N_r rK \frac{\partial \hat{\phi}}{\partial z} \partial \Omega^e - \int_{\Omega^e} \frac{\partial}{\partial z} N_r rK \partial \Omega^e$$

$$(4.20)$$

$$- \int_{\Omega^e} rK \frac{\partial N_r}{\partial z} \frac{\partial \hat{\psi}}{\partial z} \partial \Omega^e + \int_{\Omega^e} N_r r \frac{\partial K}{\partial z} \partial \Omega^e - \int_{\Omega^e} N_r rS \partial \Omega^e - \int_{\Omega^e} N_r rC \frac{\partial \hat{\psi}}{\partial t} \partial \Omega^e = 0$$

Since $\dfrac{\partial}{\partial z}(N_r K) = N_r \dfrac{\partial K}{\partial z} + K \dfrac{\partial N_r}{\partial z}$ , this equation may be simplified:

$$\int_{\Omega^e} \frac{\partial}{\partial r} N_r rK \frac{\partial \hat{\phi}}{\partial r} \partial \Omega^e - \int_{\Omega^e} rK \frac{\partial \hat{\psi}}{\partial r} \frac{\partial N_r}{\partial r} \partial \Omega^e + \int_{\Omega^e} \frac{\partial}{\partial z} N_r rK \frac{\partial \hat{\phi}}{\partial z} \partial \Omega^e$$

$$- \int_{\Omega^e} rK \frac{\partial N_r}{\partial z} \frac{\partial \hat{\psi}}{\partial z} \partial \Omega^e - \int_{\Omega^e} rK \frac{\partial N_r}{\partial z} \partial \Omega^e - \int_{\Omega^e} N_r rS \partial \Omega^e \qquad (4.21)$$

$$- \int_{\Omega^e} N_r rC \frac{\partial \hat{\psi}}{\partial t} \partial \Omega^e = 0$$

Gauss-Green divergence theorem (Zienkiewicz 1977) may be used to relate surface integrals to boundary integrals.  Application of the divergence formula to the first and third terms in equation (4.21) yields;

$$\int_{\Omega^e} \frac{\partial}{\partial r} N_r rK \frac{\partial \hat{\phi}}{\partial r} \partial \Omega^e = \oint_{\Gamma} N_r rK \frac{\partial \hat{\phi}}{\partial r} n_x \partial \Gamma \qquad (4.22)$$

and

$$\int_{\Omega^e} \frac{\partial}{\partial z} N_r rK \frac{\partial \hat{\phi}}{\partial z} \partial \Omega^e = \oint_{\Gamma} N_r rK \frac{\partial \hat{\phi}}{\partial z} n_z \partial \Gamma \qquad (4.23)$$

Therefore, noting that;

$$\frac{\partial \hat{\phi}}{\partial n} = n_x \frac{\partial \hat{\phi}}{\partial x} + n_z \frac{\partial \hat{\phi}}{\partial z} \qquad (4.24)$$

and also incorporating equations (4.22) and (4.23), equation (4.21) may be re-cast as:

$$\int_{\Gamma} N_r rK \frac{\partial \hat{\phi}}{\partial n} \partial\Gamma - \int_{\Omega^e} rK \frac{\partial \hat{\psi}}{\partial r} \frac{\partial N_r}{\partial r} \partial\Omega^e - \int_{\Omega^e} rK \frac{\partial N_r}{\partial z} \partial\Omega^e$$

$$-\int_{\Omega^e} rK \frac{\partial N_r}{\partial z} \frac{\partial \hat{\psi}}{\partial z} \partial\Omega^e - \int_{\Omega^e} N_r rS \partial\Omega^e - \int_{\Omega^e} N_r rC \frac{\partial \hat{\psi}}{\partial t} \partial\Omega^e = 0$$

(4.25)

Letting $\lambda = K \dfrac{\partial \hat{\phi}}{\partial n}$ and noting that;

$$\frac{\partial \hat{\psi}}{\partial r} = \sum_{s=1}^{8} \frac{\partial N_s}{\partial r} \cdot \psi_s \qquad \text{and} \qquad \frac{\partial \hat{\psi}}{\partial z} = \sum_{s=1}^{8} \frac{\partial N_s}{\partial z} \cdot \psi_s \qquad (4.26)$$

Equation (4.25) may be recast as follows:

$$\int_{\Gamma} N_r r\lambda \partial\Gamma - \int_{\Omega^e} rK \frac{\partial N_s}{\partial r} \frac{\partial N_r}{\partial r} \psi_s \partial\Omega^e - \int_{\Omega^e} rK \frac{\partial N_r}{\partial z} \frac{\partial N_s}{\partial z} \psi_s \partial\Omega^e$$

$$-\int_{\Omega^e} rK \frac{\partial N_r}{\partial z} \partial\Omega^e - \int_{\Omega^e} N_r rS \partial\Omega^e - \int_{\Omega^e} N_r N_s rC \frac{\partial \psi_s}{\partial t} \partial\Omega^e = 0$$

(4.27)

Summing for all elements and re-casting equation (4.27) into concise matrix notation yields;

$$\mathbf{K}\boldsymbol{\psi}_s + \mathbf{C}\frac{\partial \boldsymbol{\psi}_s}{\partial t} + \mathbf{J} + \mathbf{S} = 0 \qquad (4.28)$$

where,

$$\mathbf{K} = \sum_{e=1}^{m} \int_{\Omega^e} r \left[ K \frac{\partial N_s}{\partial r} \cdot \frac{\partial N_r}{\partial r} + K \frac{\partial N_s}{\partial z} \cdot \frac{\partial N_r}{\partial z} \right] \partial \Omega^e \qquad (4.29)$$

$$\mathbf{C} = \sum_{e=1}^{m} \int_{\Omega^e} r [N_r N_s C] \partial \Omega^e \qquad (4.30)$$

$$\mathbf{J} = \sum_{e=1}^{m} \int_{\Omega^e} r \left[ K \frac{\partial N_r}{\partial z} \right] \partial \Omega^e - \sum_{e=1}^{m} \int_{\Gamma^e} r [N_r \lambda] \partial \Gamma^e \qquad (4.31)$$

$$\mathbf{S} = \sum_{e=1}^{m} \int_{\Omega^e} r [N_r S] \partial \Omega^e \qquad (4.32)$$

The matrix representation of the discretised equations is further used in section 4.3.

4.2.4   Boundary Conditions

The above formulation permits the specification of two types of boundary conditions (Feddes et al. 1976).  The first, known as Dirichlet type boundary conditions, take the form of prescribed values of capillary potential (in cm of water) at the boundary nodes.  The second, known as Neumann or flux type boundary conditions take the form of a moisture flux (specified in cm / sec) set at the boundary nodes.  The flux term is represented in the above formulation by the term $\lambda$ defined after equation (4.25) above.

## 4.3    TIME DISCRETISATION

The spatially discretised matrix equation (4.28) is time discretised by the application of a fully implicit mid-interval backward difference algorithm.  The chosen scheme is known to be particularly suitable for application to highly non-linear problems such as the one in hand (Neuman 1973).  This scheme has been illustrated by Thomas and Rees (1991) who provided the following description.  Equation (4.28) may be approximated by:

$$\mathbf{K}^{n+1/2}\boldsymbol{\psi}^{n+1} + \mathbf{C}^{n+1/2}\left[\frac{\boldsymbol{\psi}^{n+1} - \boldsymbol{\psi}^{n}}{\Delta t}\right] + \mathbf{J}^{n+1/2} + \mathbf{S}^{n+1/2} = 0 \tag{4.33}$$

Re-arranging yields

$$\boldsymbol{\psi}^{n+1} = \left[\mathbf{K}^{n+1/2} + \frac{\mathbf{C}^{n+1/2}}{\Delta t}\right]^{-1} \times \left[\frac{\mathbf{C}^{n+1/2}\psi^{n}}{\Delta t} - \mathbf{J}^{n+1/2} - \mathbf{S}^{n+1/2}\right] \tag{4.34}$$

Clearly equation (4.34) cannot be solved directly as each calculation of $\boldsymbol{\psi}^{n+1}$ requires the determination of the coefficients at the mid-interval.  Therefore, an iterative solution procedure is necessary.  In the current work a predictor-corrector approach is used.  The method is described as follows.

For a given time interval, a first estimate of $\boldsymbol{\psi}^{n+1}$ is made, this is called the predictor, where the matrices are evaluated using the values of $\boldsymbol{\psi}$ at the start of the time interval.  For the first time step these values of $\boldsymbol{\psi}$ clearly represent the initial

conditions of the problem under consideration. Mathematically the predictor is expressed as,

$$\psi_p^{n+1} = \left[ \mathbf{K}_0^n + \frac{\mathbf{C}_0^n}{\Delta t} \right]^{-1} \times \left[ \frac{\mathbf{C}_0^n \psi_0^n}{\Delta t} - \mathbf{J}_0^n - \mathbf{S}_0^n \right] \tag{4.35}$$

The mid-interval values of $\psi$ are calculated next such that,

$$\psi_1^{n+1/2} = \left( \psi_o^n + \psi_p^{n+1} \right)/2 \tag{4.36}$$

And the first correction is made as:

$$\psi_{1c}^{n+1} = \left[ \mathbf{K}_1^{n+1/2} + \frac{\mathbf{C}_1^{n+1/2}}{\Delta t} \right]^{-1} \times \left[ \frac{\mathbf{C}_1^{n+1/2} \psi_o^n}{\Delta t} - \mathbf{J}_1^{n+1/2} - \mathbf{S}_1^{n+1/2} \right] \tag{4.37}$$

In equation (4.37) the matrices $\mathbf{K}$, $\mathbf{C}$, $\mathbf{J}$ and $\mathbf{S}$ are evaluated corresponding to the values of $\psi$ given in equation (4.36). The next correction is made based on a new set of values of $\psi^{n+1/2}$ i.e.,

$$\psi_2^{n+1/2} = \left( \psi_o^n + \psi_{1c}^{n+1} \right)/2 \tag{4.38}$$

and therefore,

$$\psi_{2c}^{n+1} = \left[ \mathbf{K}_2^{n+1/2} + \frac{\mathbf{C}_2^{n+1/2}}{\Delta t} \right]^{-1} \times \left[ \frac{\mathbf{C}_2^{n+1/2} \psi_o^n}{\Delta t} - \mathbf{J}_2^{n+1/2} - \mathbf{S}_2^{n+1/2} \right] \tag{4.39}$$

As the process continues the matrices are evaluated at the last mid-interval estimate. Convergence is monitored between successive correctors and is deemed to have been achieved when,

$$\left| \psi_{ic}^{n+1} - \psi_{(i+1)c}^{n+1} \right| < \text{TOLERANCE} \qquad \text{for all } \psi \qquad (4.40)$$

The value of *TOLERANCE* is judged for the case in hand, throughout the current work the value adopted is a capillary potential of -l cm of water. The value of *i* at which the convergence criterion is satisfied, for every node in the flow domain, represents the number of iterations required to obtain solution for the current time step. The iterative process takes place within each time interval. The higher the degree of non-linearity involved, the higher the number of iterations required and consequently the larger the computing cost.

The resulting numerical solution has been coded using FORTRAN. An original code was available at the start of this research programme as developed by Thomas, Rees and Ali (1991, 1993 and 2006). The new image based root-density approach has been introduced as a result of the current work.

## 4.4    MATERIAL PROPERTY NON-LINEARITY

The numerical solution algorithm presented in the previous incorporates material property non-linearity. In the code, this is achieved by adopting an average calculation based on the models of van Genuchten (1980) and Mualem (1976).

Therefore, during the numerical integration process the values of $K(\psi)$ and $C(\psi)$ are always related to the current sampling point by using the appropriate values (of capillary potential) and reading the corresponding values (of the hydraulic properties) of from the moisture retention curves (Appendix 2 provides an example). Proceeding in this manner for each guass point yields an element stiffness matrix evaluated using material properties current to the appropriate values of capillary potential. Hence the non-linear nature of the material properties used in the current work is incorporated.

4.5     CONCLUSIONS

An introduction to the relevant concepts of the finite element method has been presented in this chapter. The moisture flow equation for two-dimensional axi-symmetric flow with image based root-density approach has been discretised to achieve an approximate numerical solution.

In particular, spatial discretisation has been achieved by application of using a Galerkin weighted residual approach to the finite element method. In the study presented here, parabolic shape functions and eight-node isoparametric elements are employed (Zienkiewicz and Taylor 1989). The water uptake model is applied through the sink term in the governing moisture flow equation. The transient nature of the problem has been solved by application of a finite difference method. The procedure of a fully implicit mid-interval backward difference algorithm has been described. Material property non-linearity is achieved by adopting an average calculation based on the models of van Genuchten (1980) and Mualem (1976). The numerical

evaluation of root density ratio has been coded in Matlab (Appendix 1 provides the full code). Then, the equation of sink term with the input root density data is achieved by the finite element code.

Application of the algorithm may yield an approximate solution of the governing differential equation thus permitting numerical predictions of water uptake by plant roots to be achieved. The numerical solutions are subject to errors from both the spatial and time discretisation procedures. In particular, an attempt should be made to minimize the spatially derived errors by avoiding the acutely irregular element shapes or unduly coarse finite element meshes. The derived errors from timestepping should also be kept to a minimum by using suiteable timestep sizes. The image based root-density approach are subject to the quality of image.

Therefore, that an appropriate algorithm has been developed for the solution of image based water uptake model.

## 4.6    REFERENCES

Feddes, R. A. Kowalik, P. J. Malink, K. K. and Zaradny, H. 1976. Simulation of field water uptake by plants using a soil water dependent root extraction function. *J. Hydro.* 31, pp. 13-26.

Hinton, E. and Owen, D. R. J. 1989. *Finite Element Programming*. London: Academic Press.

Neuman, S. P. 1973. Saturated-Unsaturated Seepage by Finite Elements. *J.Hydro.* 99, pp. 2233-2249.

Rees, S. W. and Ali, N. 2006. Seasonal water uptake near trees: a numerical and experimental study. *Geomechanics and Geoengineering: An International Journal* 1(2), pp. 129-138.

Rockey, K. C. Evans, H. R. Griffiths, D. W. and Nethercot, D. A. 1983. *The Finite Element Method*. London: Collins.

Taylor, C. and Hughes, T. G. 1981. *Finite Element Programming of the Navier-Stokes Equations*. Swansea: Pineridge.

Thomas, H. R. and Rees, S. W. 1991. A comparison of field monitored and numerically predicted moisture movement in unsaturated soil. *Int. J. for Num. and Anal. Meth. in Geomechanics.* 15, pp. 417-431.

Thomas, H. R. and Rees, S. W. 1993. The numerical simulation of seasonal soil drying in an unsaturated clay soil. *Int. J. for Num. and Anal. Meth. in Geomechanics* 17(1), pp. 119-132.

Zienkiewicz, O. C. 1977. *The Finite Element Methods*. London: McGraw-Hill.

Zienkiewicz, O. C. and Taylor, R. L. 1989. *The Finite Element Method*. London: McGraw-Hill Book Company.

**CHAPTER FIVE**

**SIMULATION OF ONE-DIMENSIONAL**

**WATER UPTAKE**

5.1     INTRODUCTION

As indicated previously (Chapter 1), one of the main objectives of this research is the development of a two-dimensional axi-symmetric water-uptake model for application to the simulation of water uptake near trees.  However, the development of this model has been approached in a step-by-step manner, starting with 1D application.  Therefore, this chapter presents application of the 1D form of the model, as described in Chapter 3.  The applications considered generally relate to circumstances where a large surface area is (or will be) covered by fairly uniform vegetation.  Typically, for example, this is the situation that arises within the middle of a field of an agricultural crop.  The importance of

modelling this problem is highlighted in Chapter 1 – it clearly relates to the internationally significant problem of crop security (food supply) and yield. In particular, two test cases are considered:

- Case 1 – One-dimensional simulation of water uptake by winter wheat – based on the work of Luo et al. (2003).

- Case 2 – One-dimensional simulation of water uptake by Indian mustard – based on the work of Shankar et al. (2013).

5.2    CASE 1 - One-dimensional simulation of water uptake by winter wheat

5.2.1   Problem Description

The experiment chosen for initial validation of the model is based on the field measurements undertaken at the Yucheng Agro-ecosystem Experimental Station (37℃ 10′N, 116℃25′E) of the Chinese Academy of Sciences, which is located in northwest of Shandong Province, China (Luo et al, 2003). The particular case considered here relates to data recorded in the vicinity of a wheat field located on a sandy loam soil. Field observations of the soil moisture content profile were available for 24th April 1999 and 6th May 1999 (a 12 day period). The specific crop used was winter wheat (*Triticum*

*aestivum L.*).  China's winter wheat crop is planted from late September through October and harvested in May or June the following year.

China produces wheat about 120 million metric tons (265 million pounds) each year (see Figure 5.1) – on approximately 24 million hectares (59 million acres) of land (He et al. 2014).  China is one of the world's most important wheat-producing countries, China's wheat area is ranked at the third place after Indian and the European Union in 2014/15 (United States Department of Agriculture 2014).  However, China's wheat yield (Winter wheat accounts for about 95 % of China's total wheat output) is the highest in the world, and its estimated production is second only to the European Union (United States Department of Agriculture 2014).
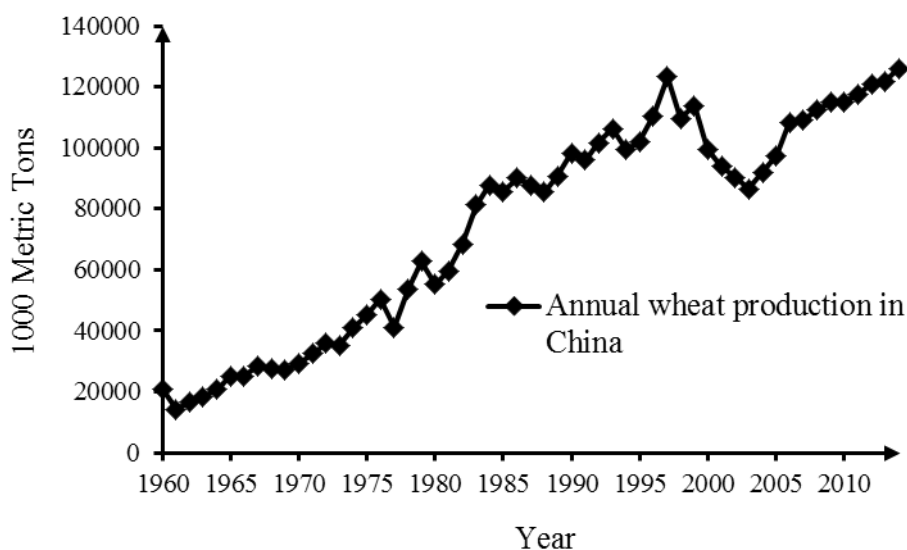


Figure 5. 1    Annual wheat production for China (data from United States Department of Agriculture 2014)

Figure 5.2 shows the weighing lysimeter used to provide an estimate of evapotranspiration, soil water content, drainage, and groundwater level. The root length density profile was determined in a nearby wheat field. Root sampling and density profile were measured at an excavated trench (2 m deep). Along the wall of the trench, soil sampled cores were taken for each 0.10 m soil layer at a depth of 1.40 m. Then, the sampled cores were rinsed with water and manually picked free of soil and other debris. Root length was measured with the CI201 Area Meter (CID Corporation) and root length density (root length in unit volume of soil, $m/m^3$) was calculated from the length and volume of the sample (Luo et al. 2003). For brevity, the experimental soil water content results are presented later in comparison with the results from the numerical simulation.
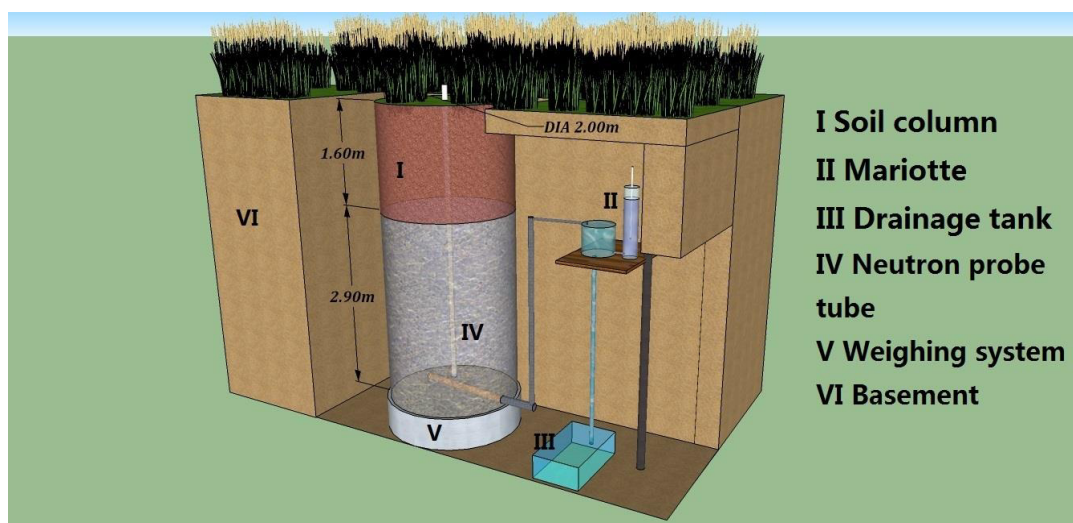


Figure 5. 2    Diagram of the weighing lysimeter system, image re-drafted after Luo et al. (2003)

The weighing lysimeter was constructed and located in the middle of a cultivated field. The basic components of the lysimeter are illustrated in Figure 5.2. The soil column is

contained within a steel soil cylinder of 4.5 m in depth and 2 m in diameter. The steel cylinder was cut into the soil at the time the lysimeter was constructed. Therefore, the lysimeter was filled with relatively undisturbed soil. The Mariotte system (II) is connected to the soil column to control and record the water table inside and measure the amount of water that is supplied to the soil column and/or leaks out of it. Gravity drainage is collected by a drainage tank (III). A neutron probe access tube (IV) was installed in the column. The soil column rests on a sensitive weighing system (V).

## 5.2.2   Material Properties

The proposed model requires specification of the specific moisture capacity (determined from the water retention curve) and the hydraulic conductivity relationship for sandy loam soil. In the absence of directly measured data, approximate relationships have been determined in the following manner. The water retention curve for sandy loam is defined using van Genuchten's (1980) method by equation (3.1), and equation (3.2) described in Chapter 3 has been used to estimate the hydraulic conductivity for the soil.

The saturated water content of sandy loam soil was measured as part of the field experiment yielding a value of $\theta_s = 0.44$. The remaining hydraulic parameters required have been obtained from the dataset reported in the Rosetta Model (United States Department of Agriculture 1999). The residual water content was estimated based on the measured soil water content profile at the soil surface on 6th May 1999 (Luo et al. 2003).

All the hydraulic parameters used to define the water retention curve for the sandy loam soil are summarised in Table 5.1. The resulting relationships for the water retention curve and hydraulic conductivity are shown in Figures 5.3 and 5.4 respectively.

Table 5. 1    Parameters defining the water retention curve and hydraulic conductivity for sandy loam soil (United States Department of Agriculture 1999)

| $\theta_r$ | $\theta_s$ | $K_s$ (cm/s) | $\alpha$ (cm$^{-1}$) | $n$ | $l$ | $m$ |
|---|---|---|---|---|---|---|
| 0.075 | 0.440 | 0.000096936260 | 0.027 | 1.449 | -0.861 | 0.310 |
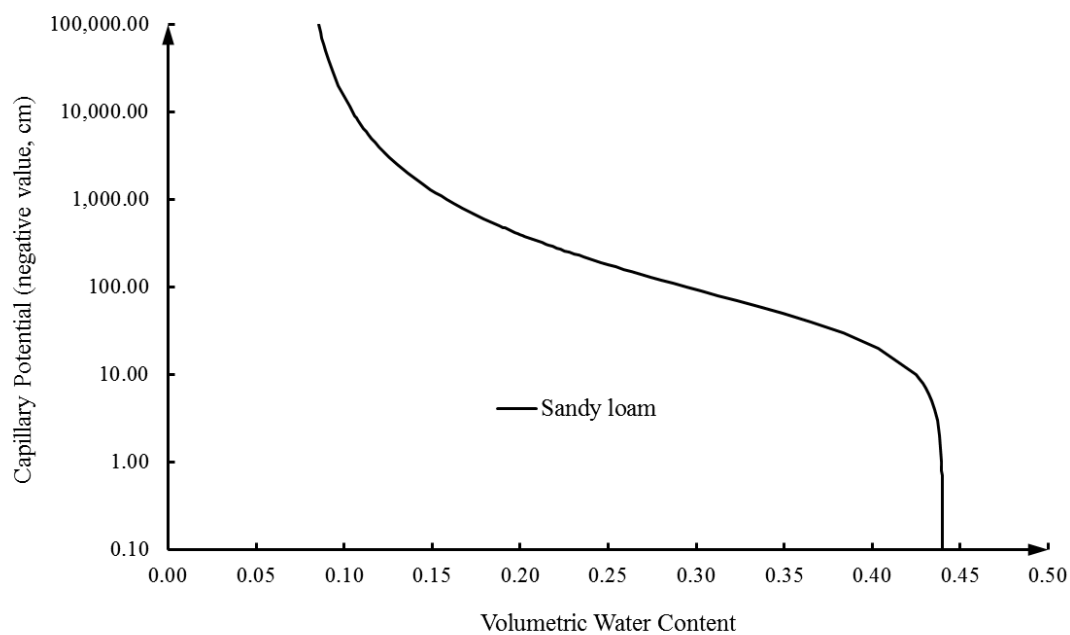


Figure 5. 3    Soil water retention curve for sandy loam (plotted on a log scale of capillary potential)
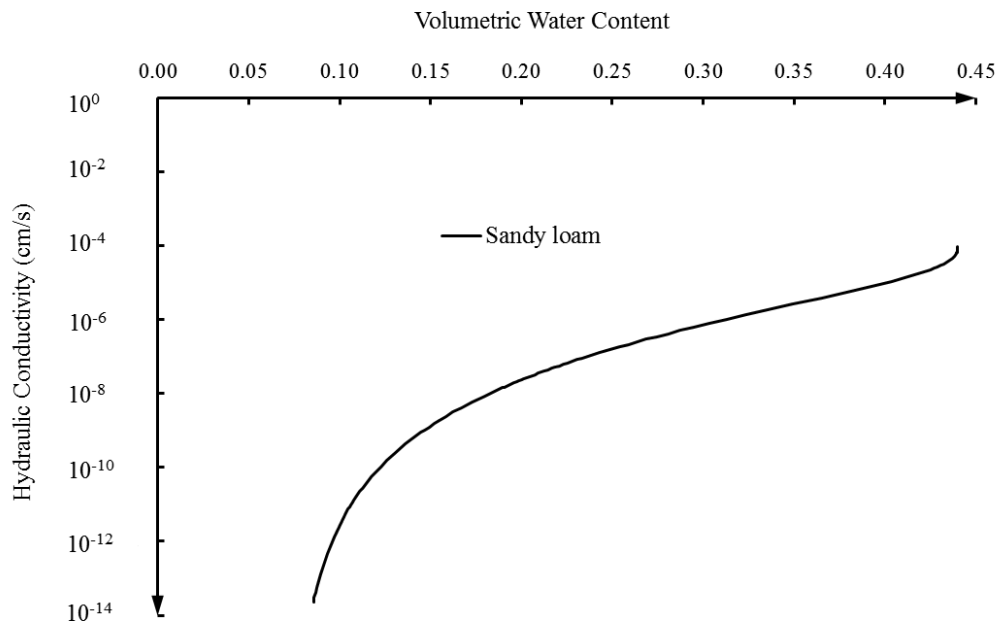
Figure 5. 4    Hydraulic conductivity curve for sandy loam soil (plotted on a log scale of hydraulic conductivity)

### 5.2.3    Numerical Simulation

Figure 5.5 shows a diagrammatic representation of the wheat, the extent of the root zone, and the domain size employed.  Based on the field observations, the overall size of the finite-element domain is 2 m $\times$ 4.5 m.  Spatial discretization was achieved using the finite-element mesh also shown in Figure 5.5.  The mesh consists of 53 eight-node isoparametric elements with 268 nodes.  A constant time-step size of 600 seconds is used throughout.  A trial and error check was made to ensure that the solution is both spatially and time-step converged.
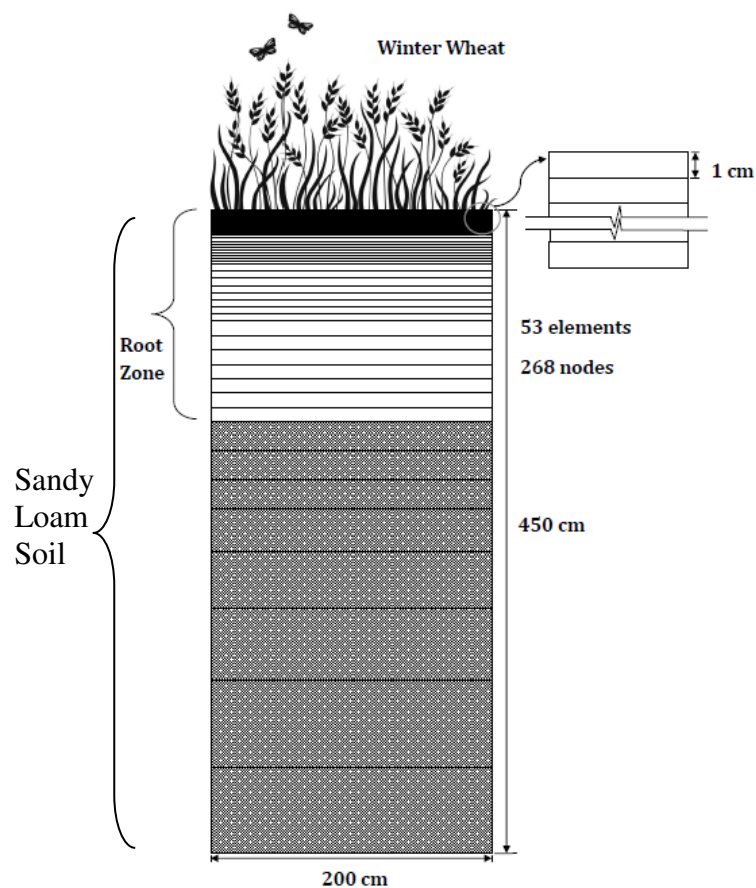
Figure 5. 5      Simulation Domain and Finite Element Mesh

For this case study, four simulations have been undertaken to explore the implementation of the new approach and to compare the alternative representations of root morphology shown in Figure 5.6.  The four simulations can be summarized as follows:

- Simulation 1:  Utilizes the measured root length density data provided by Luo et al. (2003) to define the distribution of water uptake with depth.

- Simulation 2:  Employs a graphical representation of the winter wheat root morphology to define the distribution of water uptake with depth.  In this case the

root zone is assumed to extend to the maximum depth of the active zone indicated by the experimental data (1.5 m).

- Simulation 3: As Simulation 2, but in this case a shallower active zone is assumed and the root morphology employed is of a more compressed form.

- Simulation 4: Applies a linear variation of the water uptake using after Prasad (1988).

It is recognized that root growth will occur over the lifecycle of winter wheat. However, the full life cycle from planting to harvest can be expected to be of the order of 5.5 months (approximately 170 days) (Xu et al. 2008). In the current application, experimental data is only available for 12 days. Therefore, the simulations undertaken here assume a maximum root depth and the transpiration rate that are constant with respect to time.

Figure 5.6 (a) shows the measured winter wheat root length density profile which was applied in Simulation 1 using the proposed approach. Figure 5.6 (b) and (c) show two simple graphical representations of a typical winter wheat root system reported by Marschner (1995) with maximum root depths of 1.5 m and 0.72 m below ground respectively. These were considered in Simulation 2 and Simulation 3 respectively – utilizing the proposed graphically based root density distribution approach. Figure 5.6 (d)

shows a linear approach (Prasad 1988) that has been employed in Simulation 4 to provide

the distribution of the total transpiration with depth.

**Root length density ($10^4$ m/m$^3$)**



(a) Simulation 1

(b) Simulation 2 (c) Simulation 3
(b) and (c) reproduced from
Marschner (1995)
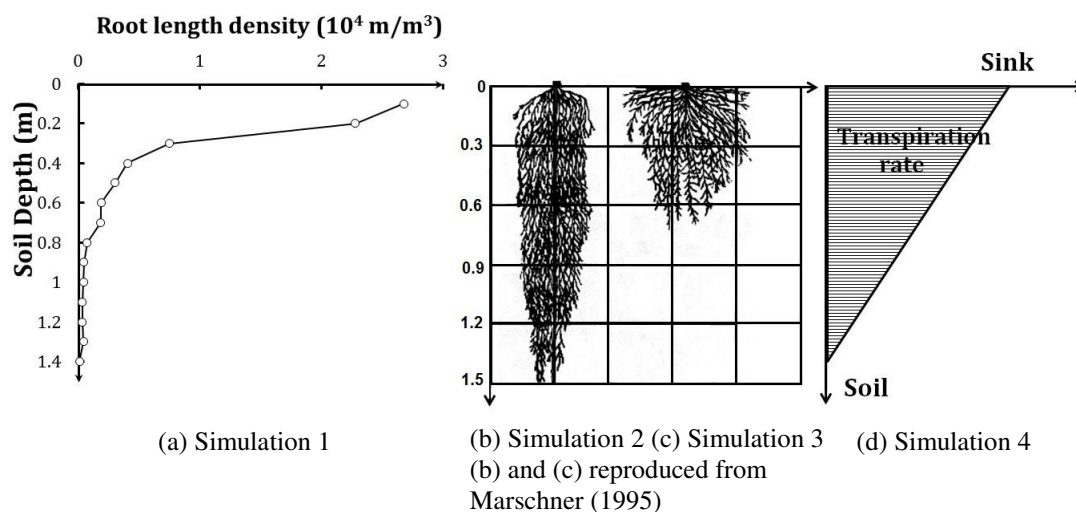
(d) Simulation 4

Figure 5. 6      Root density profiles employed

The simulated period covers 12 days from 24th April to 6th May.  The initial conditions

employed for the simulation are based on the experimental moisture profile at the start of

the period considered, as shown in Figure 5.7 alongside the measured soil water content

profile on 24th April.  The transpiration rate for winter wheat was estimated from the

experiment to be 0.4089 cm/day.  Luo et al. (2003) reported that the measured total

evapotranspiration from the system over the period considered was 54.52 mm (i.e.  4.54

mm/day) and estimated that the soil evaporation rate was approximately 10% of the

measured evapotranspiration. Since no irrigation or rainfall was observed during the

experimental period a flux of 0.45 mm/day is applied at the surface as a boundary

condition to represent soil evaporation.  An average leakage rate of 0.18 mm/day from

the lysimeter was measured.  Therefore a flux boundary of this magnitude was applied in

the simulation at the lower boundary of the domain. The numerical results are presented in the section below.

5.2.4    Interpretation of Results

The numerical solution of equation (3.38) yields raw output in terms of the primary variable of capillary potential (with respect to space and time). For ease of discussion and to facilitate direct comparison between simulated and field measured data, the results of the simulation have been converted to volumetric moisture content. This has been done using of the water retention curve (for sandy loam soil) shown in Figure 5.3.

A comparison of simulated and measured moisture content profiles is provided in Figure 5.8. The figure shows that the majority of water is extracted from within the root zone itself. The figure also indicates the depth over which the sink terms are active for each (i.e. 1.4 m, 1.5 m, 0.72 m and 1.4 m for simulations 1 to 4 respectively). Below a depth of 1.6 m, the soil is saturated (i.e. at a volumetric water content of 0.44) which relates to the observed depth of the groundwater table. In each case, the majority of the moisture extraction has occurred near the surface – corresponding to the region of highest root density.

In Simulation 1 for example, the soil moisture content reduces to 0.076 at a depth of approximately 0.05 m. Figure 5.8 also indicates that Simulation 1 provides reasonable

agreement with the measured data. It was found that the difference between the two sets of results was generally less than 5%. However, this is to be expected since this simulation directly employs the measured root length density data. The results for Simulation 2 provide a relatively poor match with the measured data - in this approach the sink term (root density) is underestimated at the surface of the domain. The results of simulation 3 provide some improvement when compared to the measured data at 12 days. Although the results from Simulation 3 are not always closer to the measured data than Simulation 1, the match between measured and simulated results at the end of the full period is reasonable. By contrast, it can be seen that the simulated results from the new image-based root density approach achieve better quality than the results by Prasad's linear approach (Simulation 4). In general, good agreement between simulated and measured profiles is achieved for Simulation 3 indicating that this root pattern is closer to the real field condition.

Figures 5.9 presents the results plotted in terms of moisture content versus time, at depths 0.05 m, 0.35 m and 0.55 m. The measured data are simply plotted as discrete data points at the times when measurements were recorded on site. It can be seen that relatively little moisture variation occurred at (and below) a depth of 0.55 m. The plot again indicates that Simulation 1 is in reasonable agreement with measured data and Simulation 3 is in better agreement than simulation 2. However, it is also clear that this comparison would benefit from more exhaustive measured data to support the conclusions. Moreover, some hydraulic parameters obtained from other published sources due to a lack of field experimental data may affect the accuracy of the results. Whilst the hydraulic parameters

used are considered reasonable, the simulated results generated are in part determined by the shape of the soil-water-retention curve (Figure 5.3) and therefore further work should be undertaken to validate the approach.

An image based root density approach has been employed to modelling water uptake by plants. The new model includes natural root morphology within the modelling process and avoids imposition of an artificial root zone geometry that is common in alternative methods. The prediction of soil water variation beneath a field of winter wheat was represented by the proposed model. In the present study, the new model is also shown to be capable of representing the processes that govern the upper and lower boundary conditions, namely evaporation and gravity drainage. However, this work was limited to a period of 12 days, during which root density was treated as static and the transpiration rate was assumed to be constant. In addition, the infiltration (rainfall and irrigation) is excluded in this study. Further work should be done to consider root growth during the crop season, irrigation management on the field, the impact of weather variations and changed transpiration rates.
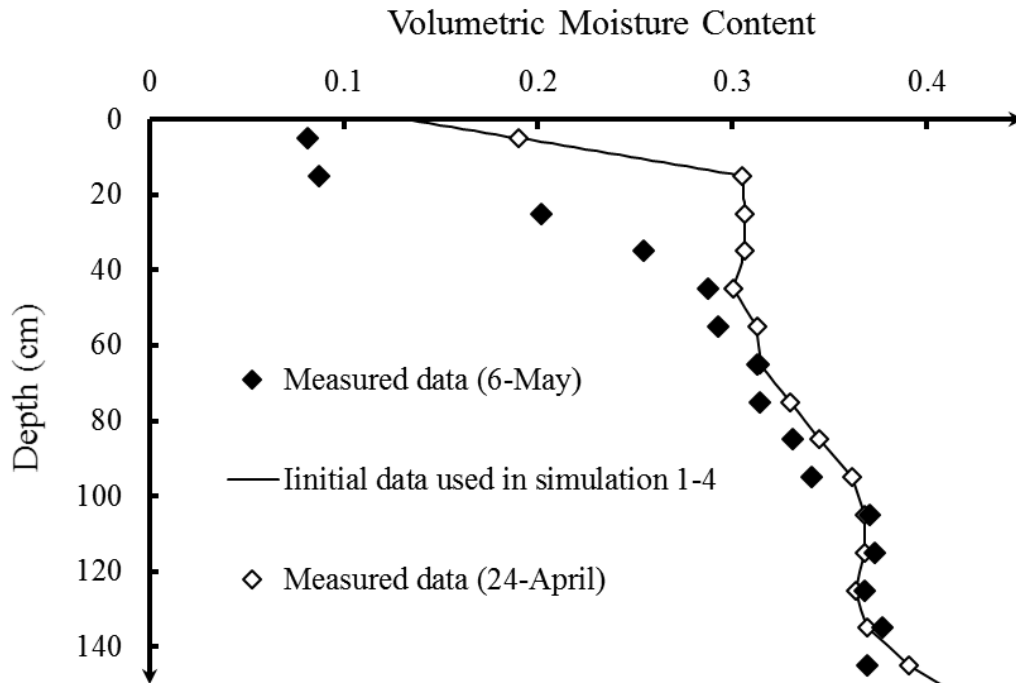
Figure 5. 7    Measured and initial moisture content profiles
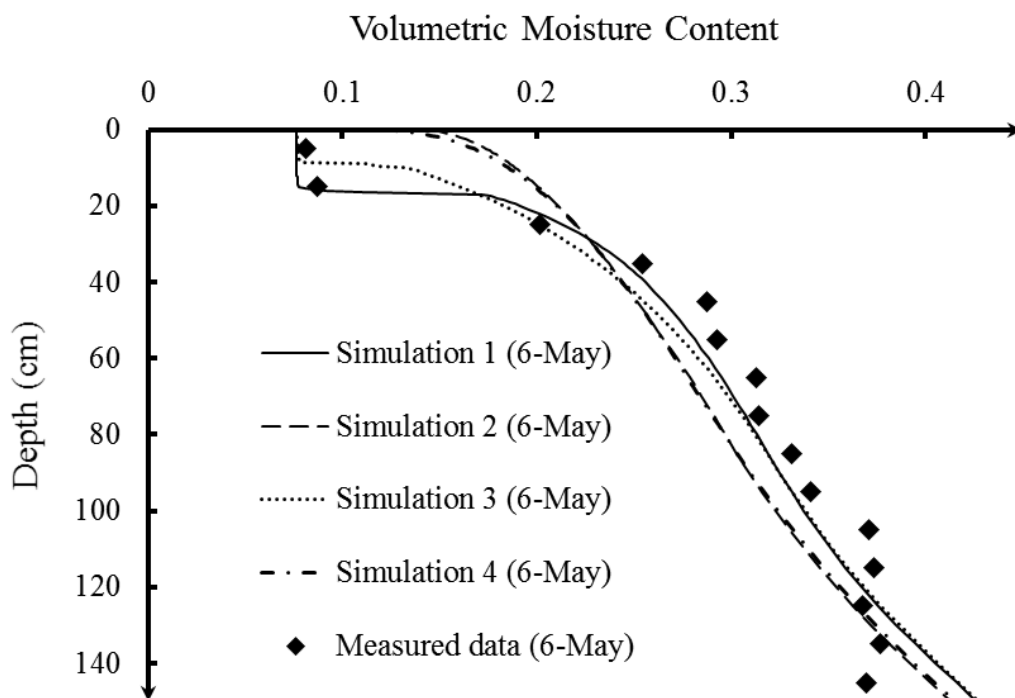


Figure 5. 8    Simulated and measured moisture content profiles
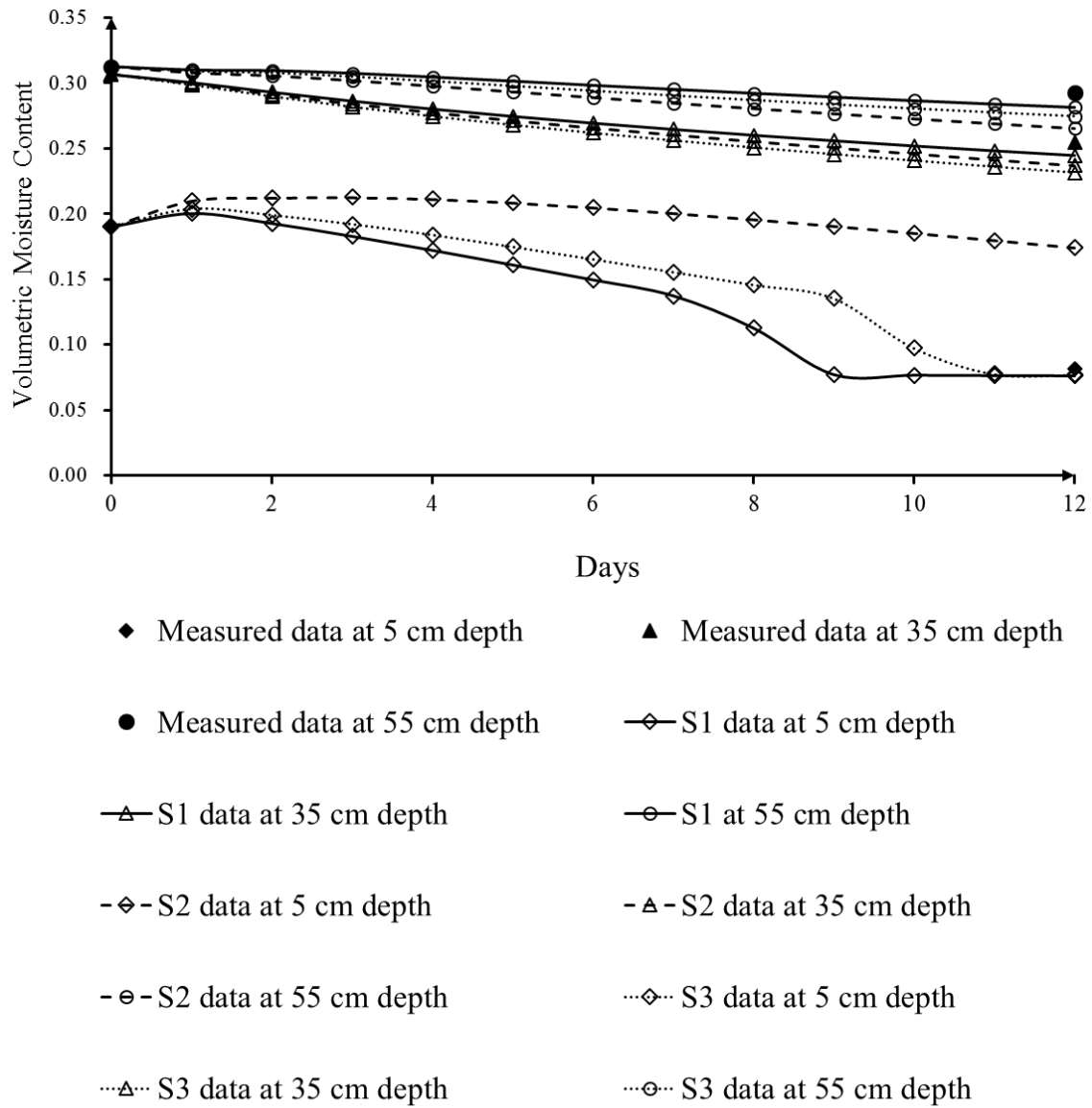
Figure 5. 9    Simulated and measured moisture content variation

## 5.3 CASE 2 - One-dimensional simulation of water uptake by Indian Mustard

### 5.3.1 Case 2 – Problem Description

The lysimeter and field crop experiments were carried out at the field experimental station of the Civil Engineering Department, Indian Institute of Technology Roorkee, from May 2006 to April 2007 (Ojha et al. 2009; Shankar et al. 2013). The experimental site was located remote from big trees and tall buildings to avoid boundary effects and to be near the water source that was selected for the field crop experiments.
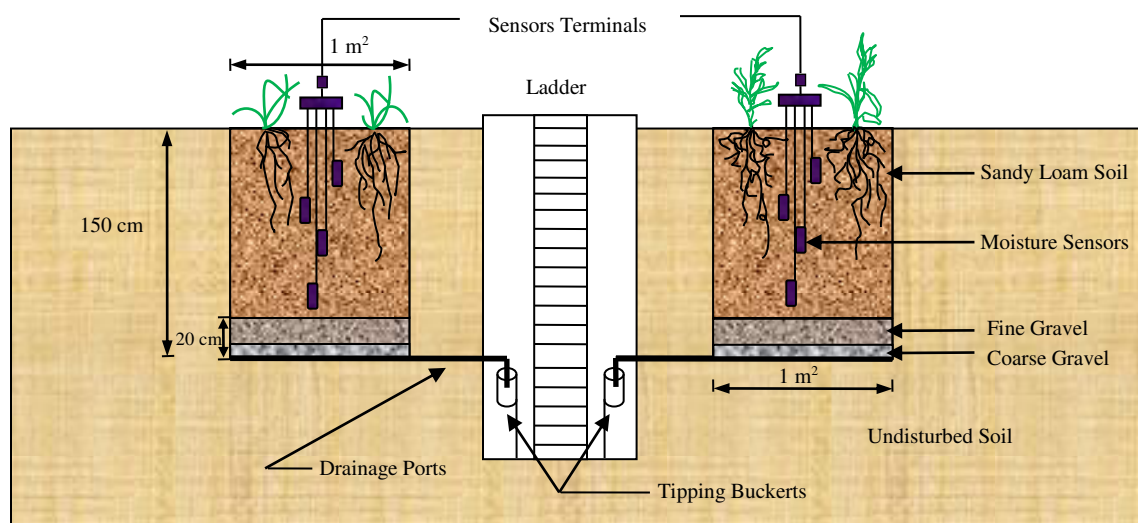


Figure 5. 10    A line diagram of the lysimeter Setup, image re-drafted after Ojha et al. (2009)

Figure 5.10 shows two cylindrical drainage lysimeters (a surface area of 1 m$^2$) used to estimate soil moisture throughout the crop season. The height of the lysimeter rim was

maintained near ground level to minimize the boundary layer effect. Similar height and plant densities from the inside and outside of the lysimeter were maintained by sowing the Indian mustard on the same date and following similar agronomic practices (Shankar et al. 2013). The lysimeter was filled with a sandy-loam textured soil, homogeneous throughout the profile and the bottom 0.2 m was filled with fine and coarse gravel to allow drainage towards the pipe. An arrangement was provided to collect water from the bottom of the lysimeter. Soil moisture sensors (Watermark, Irrometer Company, Riverside, CA, range 0–199 centibars) were embedded at 0.05, 0.15, 0.30, 0.45, 0.60, 0.75, 0.90, 1.05, 1.20 and 1.35 m depth. The amount of precipitation/irrigation applied, the percolated water from the lysimeter, and the soil suction profile at different times were recorded. Field observations were available for the period 25$^{th}$ September 2006 to 22$^{nd}$ October 2006 (a 27 day period). One locally important crop (Indian mustard) was grown during the appropriate crop season in the experimental field. The crops were sown uniformly in the lysimeters and the surrounding field so that the natural field conditions could be best represented in and around the lysimeters. Table 5.2 gives the details of crop duration, crop growth stages, spacing, and timing of irrigation in the field (i.e. covering the full cycle from sowing the crop to harvest).

Table 5. 2     Details of crop duration, growth stages, and irrigation days pertaining to crops grown in the field (Shankar et al. 2013)

| Crop | Date of sowing | Date of harvesting | Duration | Growth stages (days) | | | | Irrigation provided (day after sowing) | Spacing (cm) |
|---|---|---|---|---|---|---|---|---|---|
| | | | | I | II | III | IV | | |
| Indian mustard (Brassica juncea) | 12 September 2006 | 10 December 2006 | 90 days | 15 | 25 | 30 | 20 | 13  26  57  74 | 40 × 15 |

Note: I-initial, II-development, III-mid season, IV-late season

5.3.2    Material Properties

The United State epartment of Agriculture soil textural class for the experimental field soil is a sandy loam (Ojha et al. 2009; Shankar et al. 2013).  The bulk density, particle density, and porosity were 1.62 g/cm$^3$, 2.61 g/cm$^3$, and 0.38, respectively.  The saturated moisture content was assumed to be equal to the measured soil porosity (Ojha et al. 2009).  In addition, a residual moisture content value equal to 0.065 cm$^3$ cm$^{-3}$ for sandy loam soil was considered to be reasonable (Carsel and Parrish 1988).  In the absence of directly measured data, approximate relationships have been determined in the following manner.  Equation (3.1) has been again used to determine the water retention curve and equation (3.2) has been used to estimate the hydraulic conductivity.  All the hydraulic parameters used to define the water retention curve for the sandy loam soil are shown in Table 5.3; these are based upon the relationships adopted by Ojha et al. 2009 for the same soil.  The resulting water retention and hydraulic conductivity relationships for sandy loam soil, as adopted for this study, are shown in Figures 5.11 and 5.12 respectively.

Table 5. 3    Parameters defining the water retention curve and hydraulic conductivity (Ojha et al. 2009)

| $\theta_r$ (cm$^3$/cm$^3$) | $\theta_s$ (cm$^3$/cm$^3$) | $\alpha$ (cm$^{-1}$) | $n$ | $K_s$ (cm/s) | $l$ | $m$ |
|---|---|---|---|---|---|---|
| 0.065 | 0.38 | 0.062 | 1.68 | 1.08E-03 | 0.5 | 0.4048 |
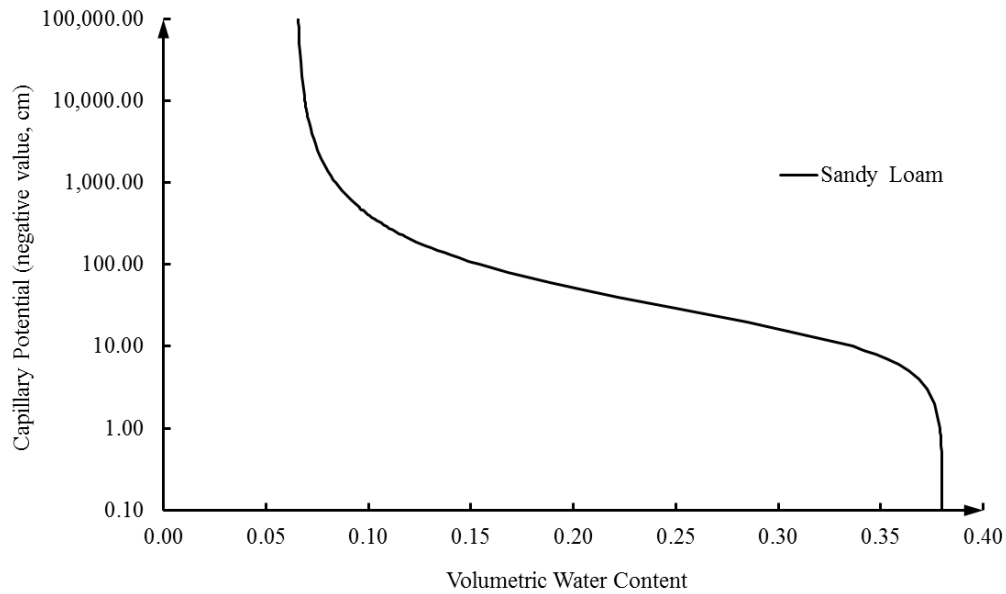
Figure 5. 11    Soil water retention curve for sandy loam soil (plotted on a log scale of capillary potential)
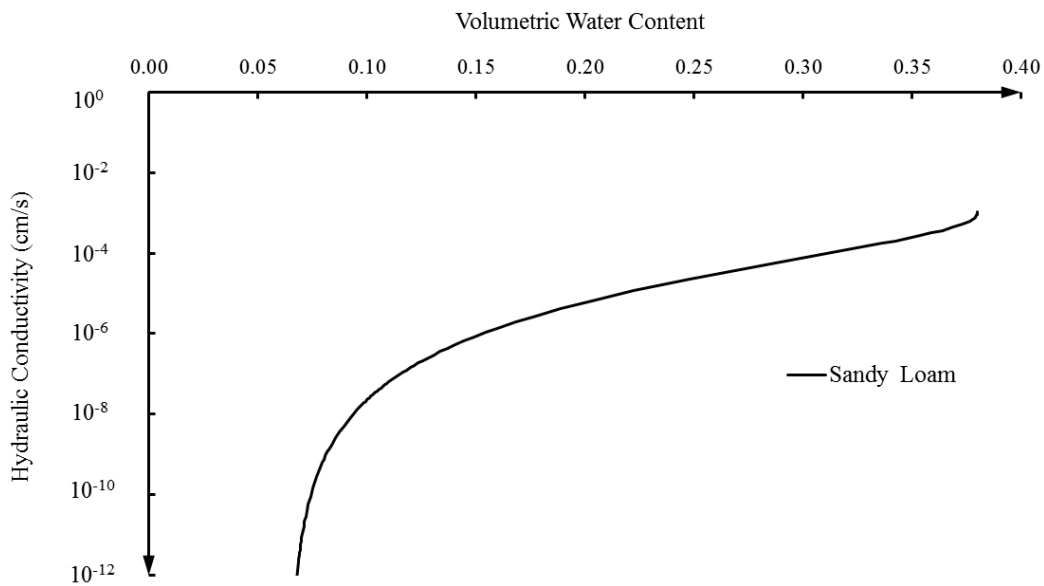


Figure 5. 12    Hydraulic Conductivity for sandy loam soil (plotted on a log scale of hydraulic conductivity)

5.3.3    Numerical Simulation

The current simulation employs a total of 61 eight noded quadratic elements – constrained to 1D behaviour – the element width is essentially arbitrary and has no influence on this problem.  The domain size employed and finite element mesh is shown in Figure 5.13.  In the present study, the simulated period covers 27 days from $25^{th}$ September 2006 to $22^{nd}$ October 2006.    The initial conditions employed for the simulation are based on the experimental moisture profile with various depths in the soil at the start of the period considered ($25^{th}$ September 2006) – for the sake of brevity this variation is shown later with the results of the simulation.
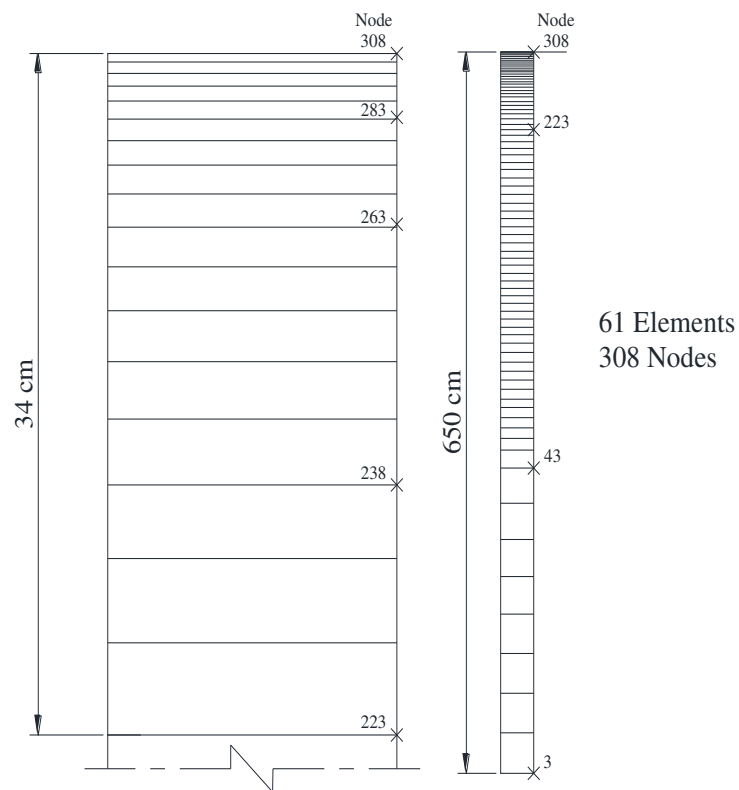
Figure 5. 13    1-D Finite Element Mesh

The processes that govern the upper boundary condition are evaporation and infiltration (attributable to rainfall or irrigation). These processes are determined by the ability of the soil matrix to transport water, crop cover, and the infiltration capacity of the soil. In the present work, the upper boundary condition comprises a prescribed flux to represent evaporation that takes place from the surface of the soil, and a Dirichlet type (fixed) boundary condition to represent a saturated surface during irrigation. The saturated boundary condition was only applied to the surface for 12 hours on the reported date of irrigation (7th October 2006). Therefore, the simulation is based on an alternating surface boundary that is either fixed at saturation or is unconstrained (free state) depending on this criterion.

The simulation employs a time-step size of 3600 seconds, which was held constant throughout the entire period considered. Numerical tests indicated that the numerical solution obtained for this domain size and a time-step size of 3600 seconds (constant for the entire period considered) is converged.

Roorkee is located near the river Ganges at 77°53"53' E longitude, 29°52"00' N latitude and 274.0 m altitude above mean sea level. All the meteorological data required for the estimation of reference evapotranspiration was obtained from an automatic weather station located within 500 m aerial distance from the experimental site. The average annual sunshine duration is 2,800 hours (Ojha et al. 2009). The average annual rainfall is 1,032 mm, of which about 75% is usually received from July to September (Ojha et al. 2009). Indian mustard evapotranspiration was determined as the product of daily crop

coefficient and reference evapotranspiration. The reference evapotranspiration is a complex phenomenon and depends on several climatological factors, such as temperature, humidity, wind speed, radiation, and type and growth stage of crop. During the study period, reference evapotranspiration was computed by the Penman-Monteith method (Allen et al. 2006).
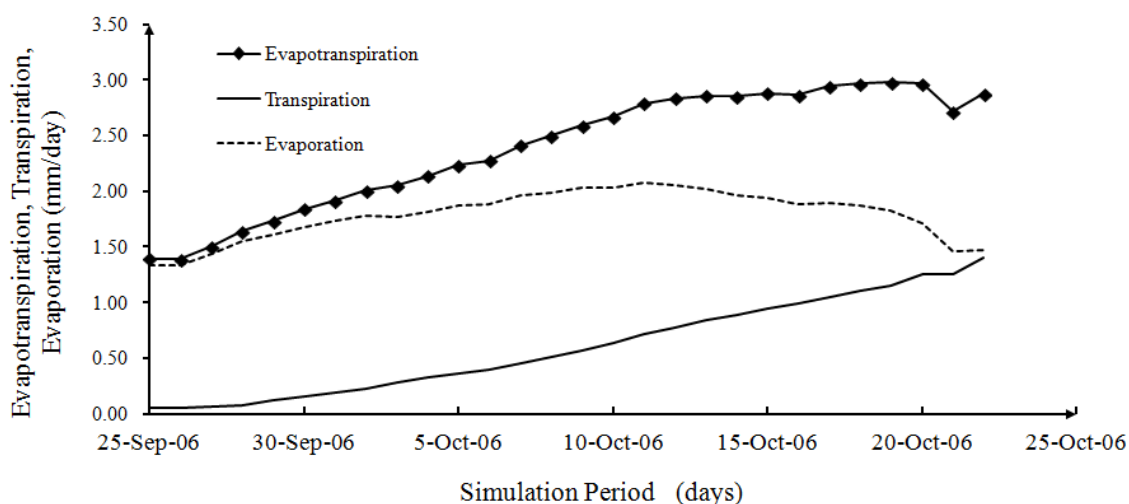


Figure 5. 14    Daily evapotranspiration, evaporation and transpiration for Indian mustard (re-drafted from Shankar et al. 2013)

Figure 5.14 shows the variation of evapotranspiration and its components, evaporation and transpiration for Indian mustard throughout the simulated period (from 25th September 2006 to 22nd October 2006) as reported by Shankar et al. (2013, p.912). The plant transpiration is used as the sink term in the numerical model and the soil evaporation is used as the boundary condition at the ground surface. In this study, the simulation employed time dependent varying boundary conditions and transpiration rate throughout the entire simulated period.
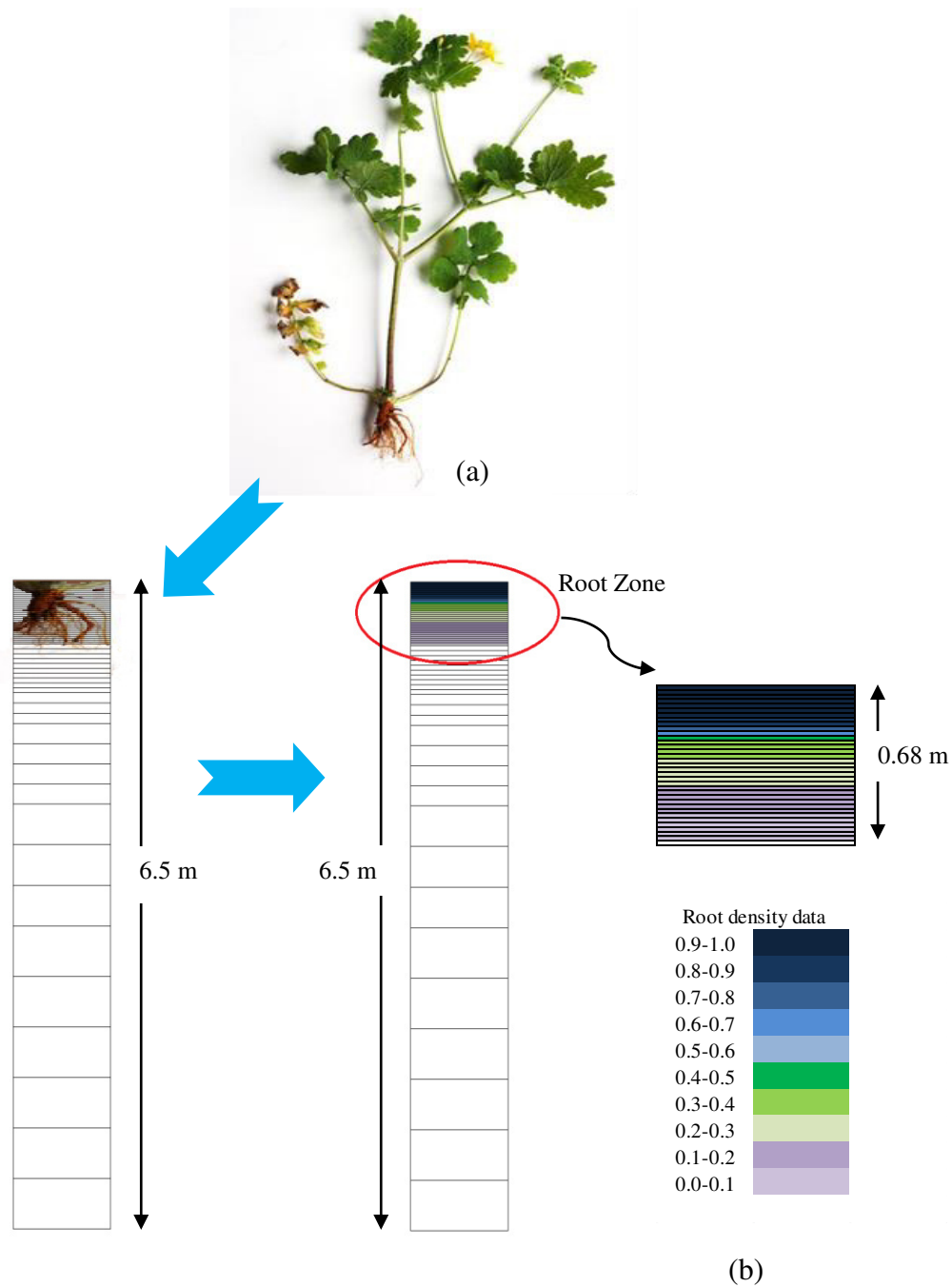
Figure 5. 15    Root system of Indian mustard (*Brassica juncea*): (a) is the root system of Indian mustard (*Brassica juncea*) in reality (Piovan 2012), (b) is a process diagram of root density based on a graphical (or photographic) representation of the actual root morphology

In the current application, experimental data was only available for 27 days. Therefore the simulation undertaken here assumes that maximum root depth of Indian mustard is constant with respect to time. Based on Shankar's study (Shankar et al. 2013) the maximum root depth of Indian mustard (*Brassica juncea*) is approximately 68 cm. Figure 5.15 shows the real root system of Indian mustard and a process diagram of root density based on a graphical (or photographic) representation of the actual root morphology.

Two simulations have been undertaken to explore the behaviour of the new approach and to compare the linear root distribution approach. The two approaches are:

- Simulation 1: Employs a graphical representation of the root morphology (see figure 5.15). The depth of the root zone is taken from the experimental data to be 0.68 m.

- Simulation 2: Applies a linear variation of the water uptake by roots using after Prasad (1988).

5.3.4    Interpretation of Results

The comparisons of simulated and field measured soil moisture content profiles are provided in Figure 5.16 and 5.17 respectively. The figures show that the majority of water is extracted from within the root zone itself. The figures also indicate that the depth over which the sink term is active. Below a depth of 2 m, the volumetric soil

moisture content is at 0.208 which relates to the field capacity of soil. In this case, the majority of the moisture extraction has occurred near the surface – corresponding to the region of highest root density and the soil surface due to the higher rate of evaporation than transpiration rate. The results show that moisture content in the root zone progressively decreases with time and depth. These two figures also show that the simulated soil moisture profiles at different times in the root zone compare well with experimental observations.

In Figure 5.16, it is clear that the majority of the moisture extraction has occurred near the surface with the volumetric moisture content reducing to 0.11 on 06th October 2006. According to the irrigation event had been undertaken for about 12 hours on the 7th October 2006. Therefore, the saturated boundary condition was applied to the surface for 12 hours at the date of irrigation (7th October 2006). In Figure 5.17, it is clear to see that although the results from simulation are not always closer to the measured data, the match between measured and simulated results after irrigation event is reasonable. It can be seen that the simulated results from the new image-based root density approach achieve a good quality. In general, good agreement between simulated and measured profiles is achieved indicating that this simulation with time dependent varying evapotranspiration and boundary condition is closer to the real field condition.

Figure 5.18 to 5.22 present the results plotted in terms of moisture content versus time, at depths 5 cm, 15 cm, 30 cm, 6 cm and 90 cm. The measured data are simply plotted as discrete data points at the times when measurements were recorded on site. It can be

seen that relatively little moisture variation occurred at (and below) a depth of 90 cm. The plots again indicate that the simulation is in good agreement with measured data.

According to Figure 5.23 to 5.25, the results for Simulation 2 provide a relatively poor match with the measured data - in this approach the sink term (root density) is underestimated at the surface of the domain. Although the results from Simulation 1 are not always closer to the measured data than Simulation 2, the match between measured and simulated results at the end of the full period is more reasonable. By contrast, it can be seen that the results of Simulation 1 from the new image-based root density approach achieve better quality than the results of Simulation 2 from Prasad's linear approach. In general, good agreement between simulated and measured profiles is achieved for Simulation 1 indicating that this approach is more representative of the real field condition.

In this study, the new approach has been employed to predict soil water variation in relation to a field of Indian mustard. The new model includes natural root morphology within the modelling process and avoids imposition of artificial root zone geometry. Time dependent varying boundary conditions to represent the irrigation during the simulated period and various daily evapotranspiration rates were represented by the proposed model. However, as this study assumed the soil moisture was not limiting, the problem of actual transpiration was excluded in this study. Due to lack of information on the amount of irrigation water used, this study only applied a saturated surface for 12 hours to represent the irrigation during the simulated period. The present study only

explored the water uptake by crops for a short period (27 days) and employed a constant root depth.  Further work should be done to consider the development of roots during the entire crop season.
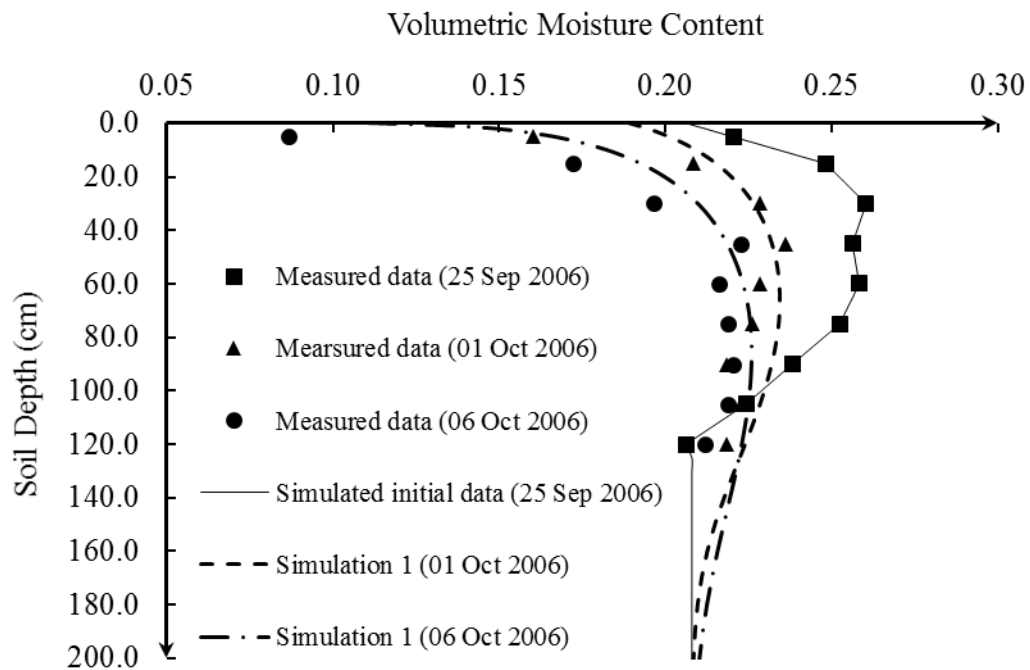


Figure 5. 16    Comparison of simulated and field measured soil moisture profiles for Indian mustard on 25th September 2006, 01st October 2006 and 06th October 2006.

Volumetric Moisture Content
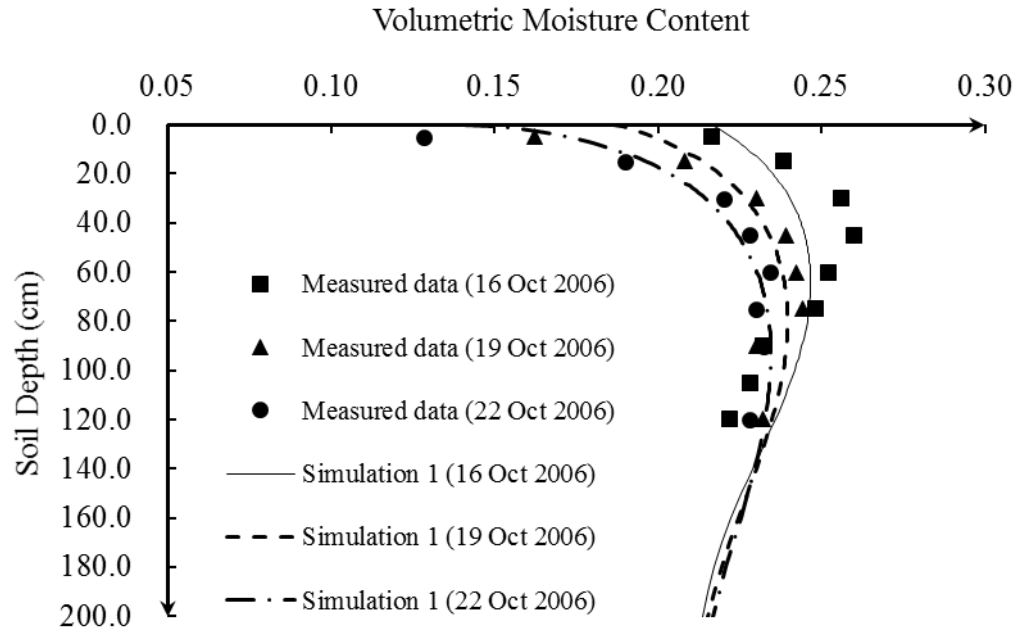


Figure 5. 17    Comparison of simulated and field measured soil moisture profiles for Indian mustard on 16th October 2006, 19th October 2006 and 22nd October 2006.
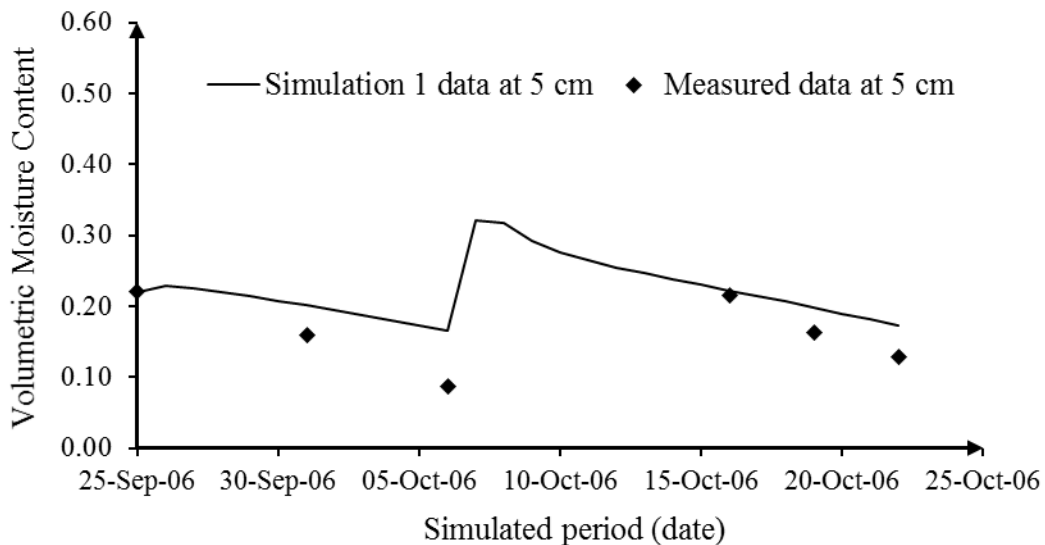


Figure 5. 18    Comparison of simulated and field measured soil moisture status for the entire simulated period for Indian mustard at depths of 5 cm.
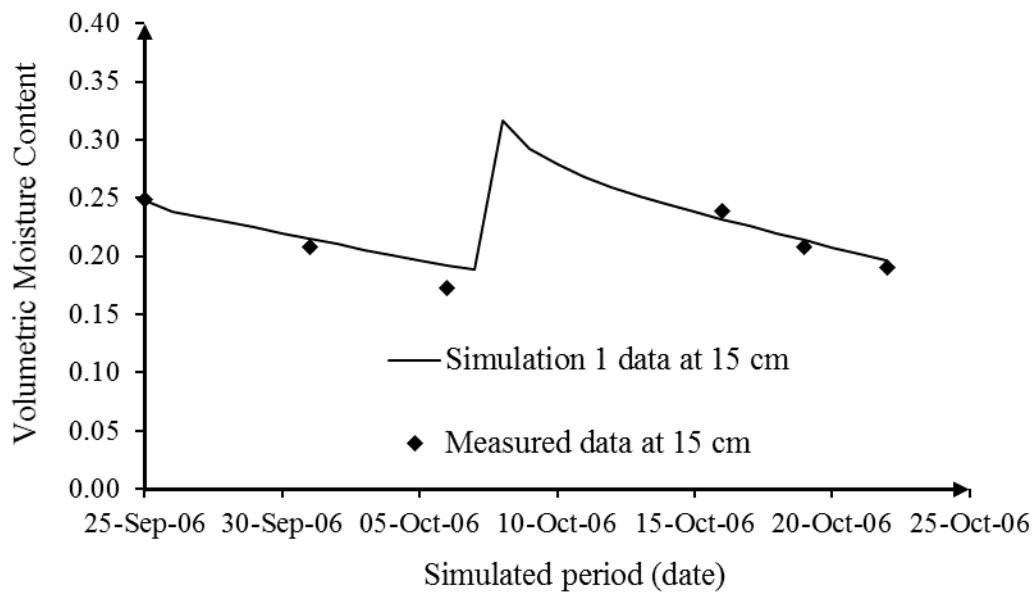
Figure 5. 19　Comparison of simulated and field measured soil moisture status for the

entire simulated period for Indian mustard at depths of 15 cm.
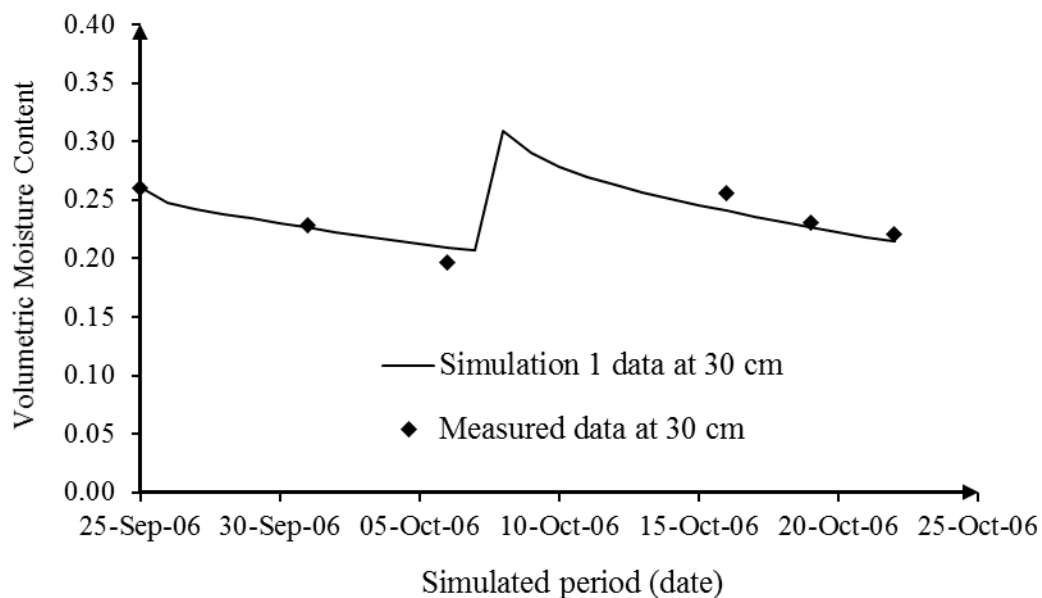


Figure 5. 20　Comparison of simulated and field measured soil moisture status for the

entire simulated period for Indian mustard at depths of 30 cm.
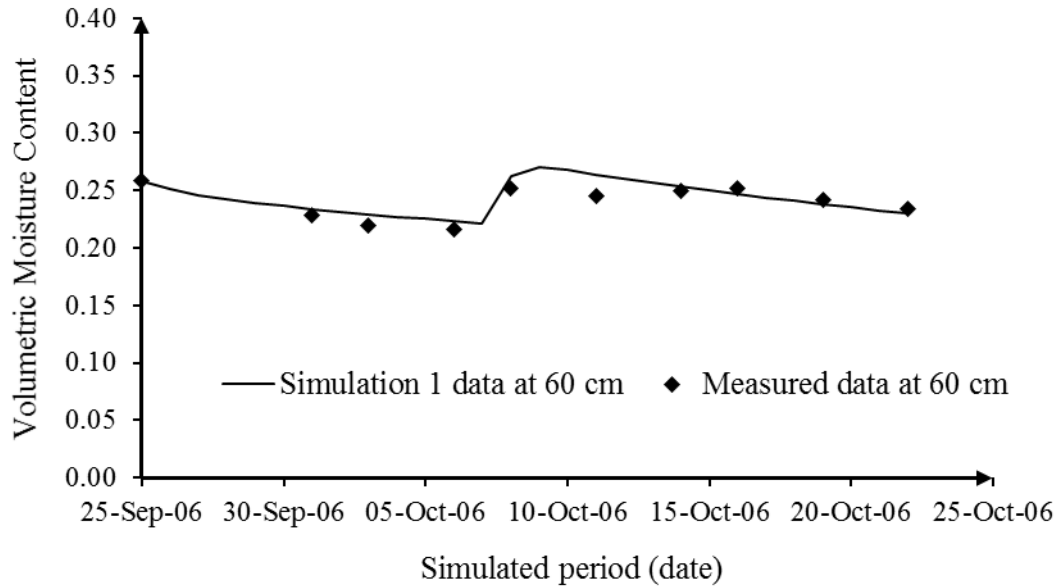
Figure 5. 21  Comparison of simulated and field measured soil moisture status for the entire simulated period for Indian mustard at depths of 60 cm.
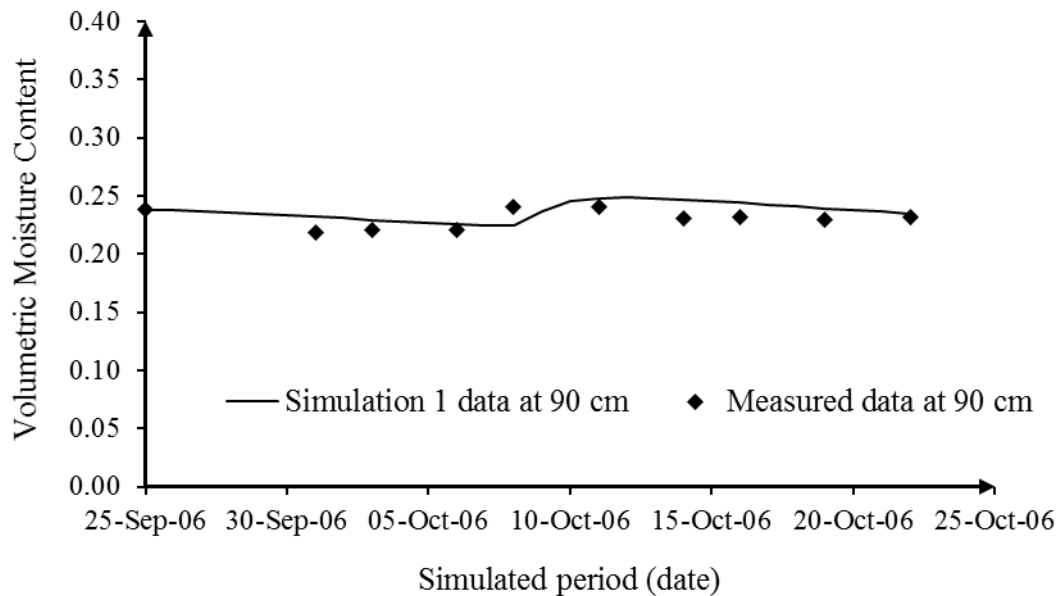


Figure 5. 22  Comparison of simulated and field measured soil moisture status for the entire simulated period for Indian mustard at depths of 90 cm.
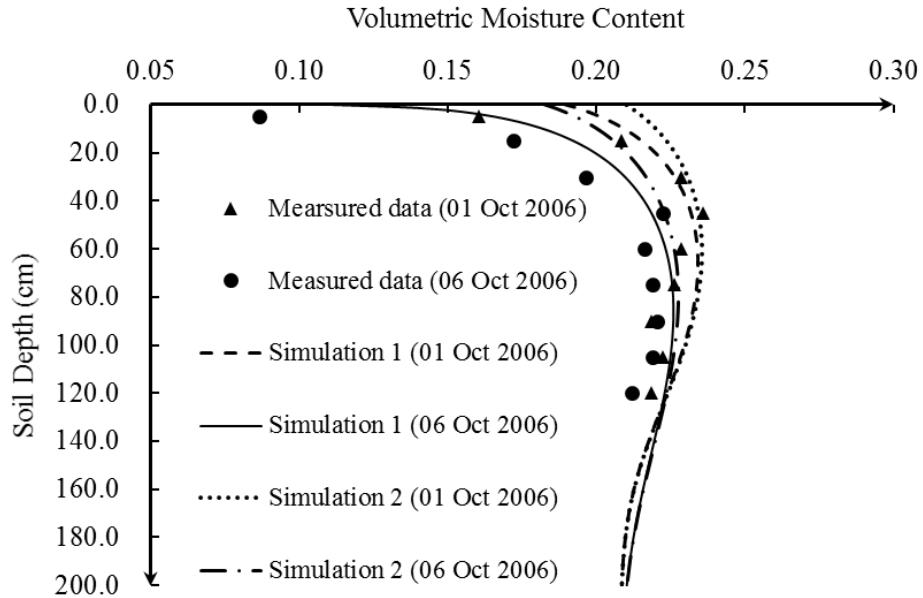
Figure 5. 23    Comparison of Simulation 1 and Simulation 2 soil moisture profiles for Indian mustard on 01st October 2006 and 06th October 2006.
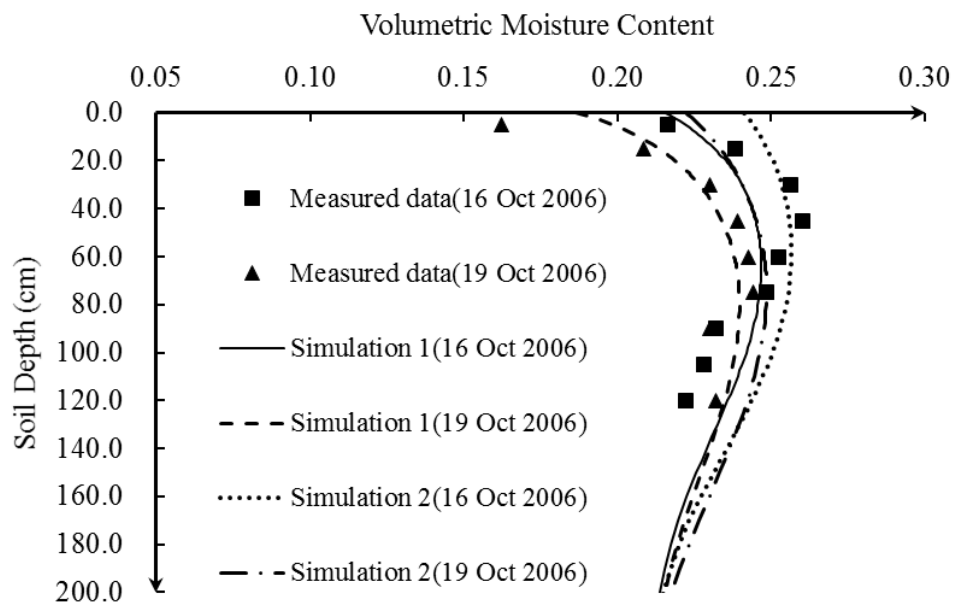


Figure 5. 24    Comparison of Simulation 1 and Simulation 2 soil moisture profiles for Indian mustard on 16th October 2006 and19th October 2006.

Volumetric Moisture Content
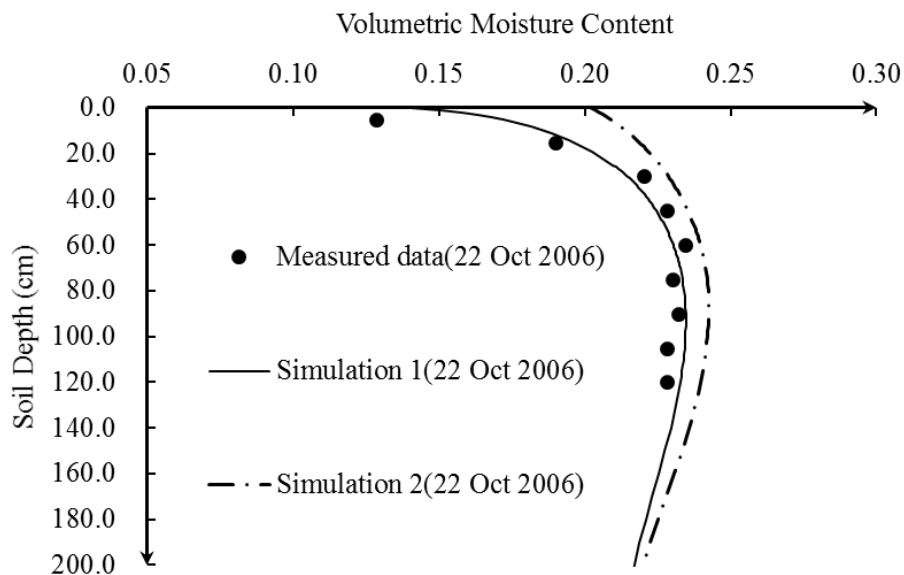


Figure 5. 25    Comparison of Simulation 1 and Simulation 2 soil moisture profiles for Indian mustard on 22nd October 2006.

5.4    CONCLUSIONS

This chapter has presented some initial applications of the new model operating in a one-dimensional mode.  The main aim of this work was to provide some confidence with respect to both the implementation of the volumetric sink term with the new image-based root density approach and the basic formulation of the water-uptake model.  Two specific case studies have been presented for this purpose.

The first case illustrated that in contrast to many established water uptake models that impose an artificial geometry of the root zone on the solution routine, the current model evaluates root density based on a graphical (or photographic) representation of the actual

root morphology. The new model produced results that were generally within 5.0 % of independently simulated results. The model was validated by direct comparison with field measurements recorded for winter wheat growing in a sandy loam soil. A good overall correlation between field data and simulated results was achieved. The second study explored a problem involving time dependent varying evapotranspiration and boundary condition. The new image-based root density approach model performed adequately for this type of problem. The model was validated by direct comparison with field measurements observation and a good overall correlation between field data and simulated results was achieved. In both cases the new model performed better than the often used linear water uptake model of Prasad (1988).

Overall, the new model has been shown to be capable of producing results that are physically meaningful and give a better correlation than traditional linear water uptake models when compared to experimental behaviour. The development and application of a numerical model for the simulation of moisture migration patterns beneath a uniform cover of vegetation has been presented. The implementation of the water-uptake model and the associated sink term with new image-based root density approach therefore appear to have been successfully undertaken. The approach can be extended for application to a wide range of geotechnical problems.

5.5    REFERENCES

Allen, R. G. Pereira, L. S. Raes, D. and Simth, M. 2006. Crop Evapotranspiration (guidelines for computing crop water requirements). *FAO Irrigation and Drainage Paper* No. 56.

Carsel, R. F., and Parrish, R. S. 1988. Developing joint probability distributions of soil water retention characteristics. *Water Resour. Res*. 24, pp. 755-759.

He, Z. Xia, X. Peng, S. Lumpkin, T. A. 2014. Meeting demands for increased cereal production in China. *Journal of Cereal Science*. 59, pp. 235-244.

Luo, Y. QuYang, Z. Yuan, G. Tang, D. and Xie, X. 2003. Evaluation of macroscopic root water uptake models using lysimeter data. *American Society of Agricultural Engineers*. 46(3), pp. 1-10.

Marschner, H. 1995. *Mineral Nutrition of Higher Plants*. 2nd ed. London: Elsevier, pp. 508-536.

Ojha, C. S. P. Prasad, K. S. H. Shankar, V. and Madramootoo, C. A. 2009. Evaluation of a nonlinear root-water uptake model. *Journal of irrigation and drainage engineering*. 135 (3), pp. 303-312.

Piovan, G. 2012. Farming the pollution. *Domus*. Available at:

http://www.domusweb.it/en/news/2012/11/21/giacomo-piovan-farming-the-

pollution.html


Prasad, R.1988. A linear root water uptake model. *J. Hydrol*. 99, pp. 297-306.


Shankar, V. Prasad, K. S. H. Ojha, C. S. P. and Govindaraju, R. S. 2013. Model for

Nonlinear Root Water Uptake Parameter. *Journal of Irrigation and Drainage

Engineering*. 138 (10), pp. 905-917.


United States Department of Agriculture. 1999. Rosetta Model. Class average values of

hydraulic parameters. Available at:

http://www.ussl.ars.usda.gov/MODELS/rosetta/rosetta.htm


United States Department of Agriculture. 2014. Commodity Intelligence Report. *Foreign

Agricultural Service*. Available at:

http://pecad.fas.usda.gov/highlights/2014/12/China/index.htm


van Genuchten, M. Th. 1980. A closed-form equation for predict-ing the hydraulic

conductivity of unsaturated soils. *Soil Sci. Am. J*. 44:892-898.


Xu, L. Yang, J. Zhang, Q. and Niu, H. 2008. Modelling water and salt transport in a soil–

water–plant system under different ground-water tables. *Water and Environment*

*Journal*. 22, pp. 265-273.

**CHAPTER SIX**

**TWO-DIMENSIONAL WATER UPTAKE NEAR TREES**

6.1    INTRODUCTION

This chapter explores the issues related to the numerical simulation of moisture migration patterns in the unsaturated zone and in the vicinity of mature trees. The research is based on the application of the new image based root-density approach presented in Chapters 3 and 4. The problem solved lends itself to a solution that exploits radial symmetry. The distribution of water extraction rates includes both depth and radial variation based on the root pattern of a particular tree. This chapter also provides an assessment of the transpiration rate for a single tree calculated using the well-established Penman-Monteith equation.

The model is validated by direct comparison to field measurements recorded by others.  In particular, numerical simulations of two field experiment are presented, namely:

- Case 1 – Mature Lime tree located on Boulder Clay, UK (Biddle 1998).

- Case 2 – Mature Almond tree located on Shallow Gravely Loam, USA (Koumanov et al. 1997).

The simulation of a Lime tree situated on Boulder Clay explores some of the issues that arise in relation to the seasonal climate variation of moisture migration patterns near mature trees and considers a simple method of representing time dependent variations in boundary conditions based on daily rainfall patterns.

To provide some confidence in the implementation of the approach, the model also has been validated by a second comparison to field measurements recorded for a mature almond tree located on a shallow gravely loam soil.  Since there is considerable similarity in the approach adopted and the results generated for both case studies, Case 2 is presented in relatively less detail than Case one.

## 6.2    CASE 1: MATURE LIME TREE ON BOULDER CLAY

### 6.2.1    Field Experiment

Ideally, in order to fully assess the performance of the new model, extensive field data are required.  To this end, Biddle (1998) presented a comprehensive treatise on how the interaction of trees, soils and water can cause foundation movement and damage to buildings.  Amongst other matters, Biddle's work included the measurement of patterns of soil moisture variation in the region of established trees.  A total of sixty trees were observed, covering a range of tree species and soil types.  All of the studies were undertaken in simple open field sites, thus avoiding some of the potential complications which occur in the urban situation (i.e. the effects of building foundations, water supply, trenches for underground services, drainage systems and hard surfaces).  Soil moisture content was measured using a Neutron Probe or a Neutron Soil Moisture Gauge.  The probes were based on designs developed at the Institute of Hydrology (Bell 1987) and are known as Wallingford Neutron Probes. Typically, Biddle measured soil moisture content using around five neutron probe access tubes positioned at various distances from the trees.  The work resulted in what is probably the most comprehensive data set (of this kind) to appear in the literature. It therefore provides an invaluable source of measured data that is used here to help assess the performance of the new modelling approach presented in chapters 3 and 4. A brief summary of the relevant experimental data and site conditions follows.

## 6.2.2   Site Description

The particular experimental data set chosen for analysis is based on the field measurements undertaken (by Biddle) at a site located at Stacey Hall, Wolverton, UK. The case considered relates to a single mature lime tree 15 m in height, located on a Boulder Clay sub-soil.  Field observations were available for the period July 1979 to October 1979.   The Neutron Probe access points for the moisture content measurements were placed in a line to the South West of the tree. Measurements were taken at distances of 1.4 m, 3.0 m, 4.9 m, 10.0 m and 30.0 m from the tree.  An aerial view of the site is shown in Figure 6.1.  The current work will consider the readings taken at distances of 1.4 m and 4.9 m from the tree since these measurements were thought to provide reasonable detail for an assessment of the new model. Unfortunately, Biddle's published work does not provide all of the data acquired in his research – therefore some selectivity for this study was unavoidable.



Figure 6. 1    Aerial view of study site at Stacey Hall, Wolverton. (Figure reproduced from the UK Grid Reference Finder)

Distance
from tree

| | 1.4 m | 3.0 m | 4.9 m | 10.0 m | 30.0 m | |
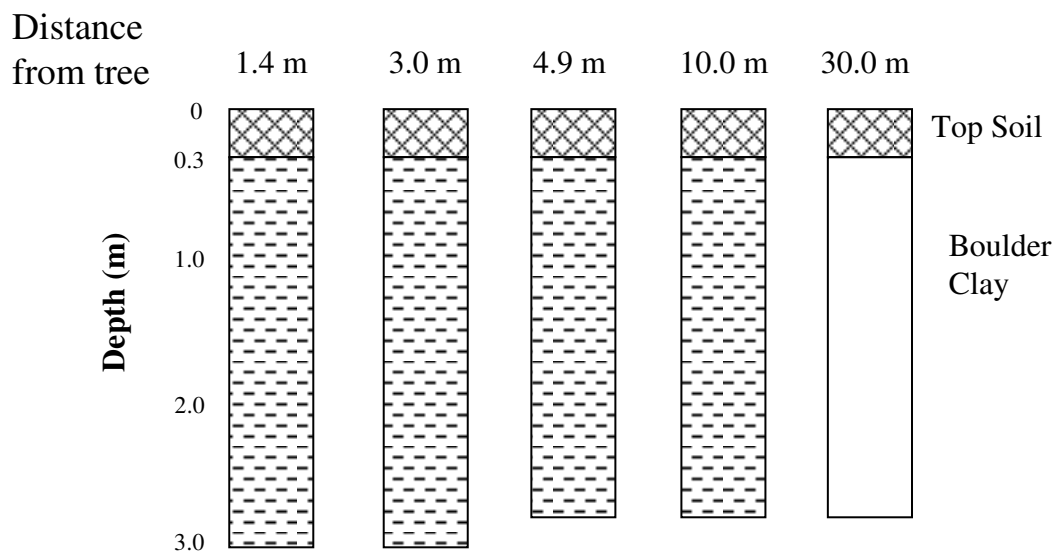


Figure 6. 2    Soil Profile at the site, figure modified after Biddle (1998)

Table 6. 1    Soil profile detail at 1.4m and 3.0m from tree, table modified after Biddle (1998)

| Index Properties of Soil: | | | | |
|---|---|---|---|---|
| Distance from tree (m) | 1.4 | 3.0 | 3.0 | 3.0 |
| Depth (m) | 2.0 | 1.0 | 1.5 | 2.0 |
| Liquid Limit | 45 | 36 | 36 | 34 |
| Plastic Limit | 29 | 18 | 17 | 17 |
| Plasticity Index | 16 | 18 | 19 | 17 |
| % linear shrinkage | - | - | - | 8.9 |

Figure 6.2 and Table 6.1 provide some detail of the ground conditions at the site. These consist of a layer of topsoil, approximately 0.3 m thick, underlain by a 3 m

thick layer of Boulder Clay. Biddle (1998) indicates that in all cases the shallowest reading of soil moisture content was taken at a depth of 0.3 m. Readings at shallower depths than this were not practicable given the dimensions of the probes and disturbance related to inserting the access tubes. No information was available on the soil profile below 3 m depth. However, the field measured data indicate that all of the seasonal variation in moisture content of interest occurred above a depth of 3m.

6.2.3    Lime Trees

The Lime Tree under consideration is 15 m tall with the diameter at breast height of 0.68 m and was located close to edge of a field grazed by horses. The tree can be considered as a single tree, as the neighbouring trees are sufficiently far away to have negligible effect on local soil moisture patterns. To provide some further background, a local photographical survey of Lime trees (*Tilia x europaea*) was carried out at Pontcanna Fields, Cardiff from March to November in 2014 for establishing a full leave lifecycle (Appendix 3 provides the photos for the other selected trees). Figure 6.3 provides some photographic images of typical common Lime trees (*Tilia x europaea*). The figure also shows the seasonal variation in leaf density.

The common Lime Tree or "*Tilia x europaea*" is a broadleaved tree which can be found in the United Kingdom. This tree has been selected for consideration here since it has been widely planted in avenues on estates, in streets, parks and large gardens, therefore it can be found throughout much of the United Kingdom (SAPS 2007).

Figure 6. 3     Lime tree - *Tilia x europaea* (photos taken at Cardiff, from March to November in 2014)

*Tilia x europaea* is a large deciduous tree (losing its leaves in autumn) up to 24 m tall with a trunk diameter up to 5.0 m (Cutler and Richardson 1989). It is a hybrid between small-leaved and large-leaved lime and exhibits characteristics from both species. The old bark (outermost layer of stems and roots) is grey and fissured and punctuated by irregular bosses. The leaves, which are heart-shaped with a drawn-out pointed tip, are typically 6–15 cm long and 6–12 cm broad. They are dark green and hairless above, but have tufts of white hairs at the junctions of the veins below. The margins have small, sharp teeth, whilst the leaf-stalks are 3-5 cm long. Some typical photographs of the leaves are shown in Figure 6.4.
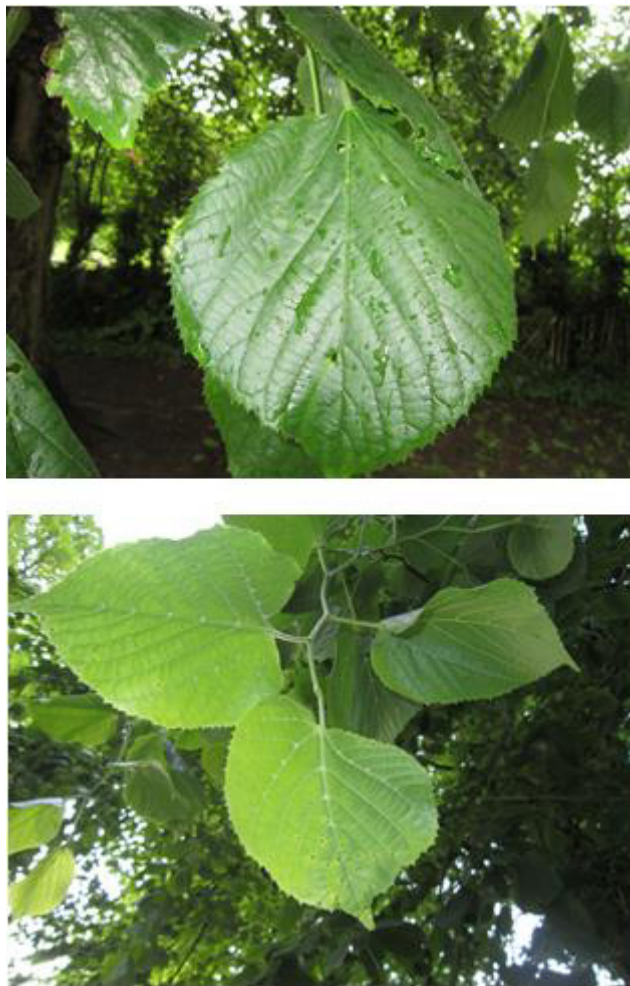


Figure 6. 4    Lime Tree Leaves (*Tilia x europaea*)

6.2.4   Hydraulic Properties of Boulder Clay

Due to a lack of definitive field data the soil profile is assumed to be a homogenous layer of boulder clay.  Although the moisture flow model is capable of representing more than one soil type, this is recognised as a limitation of the following simulation. Besides, it is noted that extension of the work will be attempted later (Chapter 7) to link this type of simulation with slope stability analysis.  Therefore, simplification of the soil profile, where acceptable, offers significant advantages at this stage of the research.

Application of the proposed model requires specification of the water retention curve (hence specific moisture capacity) and the hydraulic conductivity relationship for the boulder clay.  A similar approach has been adopted here for the boulder clay as that described in Chapter 5.  In fact, equation (3.1) has been again used to determine the water retention curve and equation (3.2) has been used to estimate the hydraulic conductivity.  To apply these for boulder clay, reference has been made to the available published data for this material.  A summary of the relevant properties is shown in Table 6.2.

Table 6. 2      Assumed soil properties for boulder clay

| $\theta_r$ | $\theta_s$ | $K_s$ (cm/s) | $\alpha$ (cm$^{-1}$) | $l$ | $m$ | $n$ |
|------------|------------|--------------|----------------------|-----|-----|-----|
| 0.1 | 0.44 | 0.00000006 | 0.028 | -1.561 | 0.285714 | 1.4 |

The values of $\theta_r$ and $\theta_s$ have been taken directly from the measured moisture profiles provided by Biddle (1998). The remaining parameters (except for $K_s$ – see below) are based on the typical shape of a water retention curve for clay provided by Rees (1990). Based on this information, Figure 6.5 shows the assumed water retention curve for boulder clay. For comparison, the figure also shows measured data for three other soil types: a typical sand, Kimmeridge clay and typical loam (Rees 1990). The overall set of results would appear to suggest that the assumed relationship for boulder clay is within the range of previously published data for this soil type.
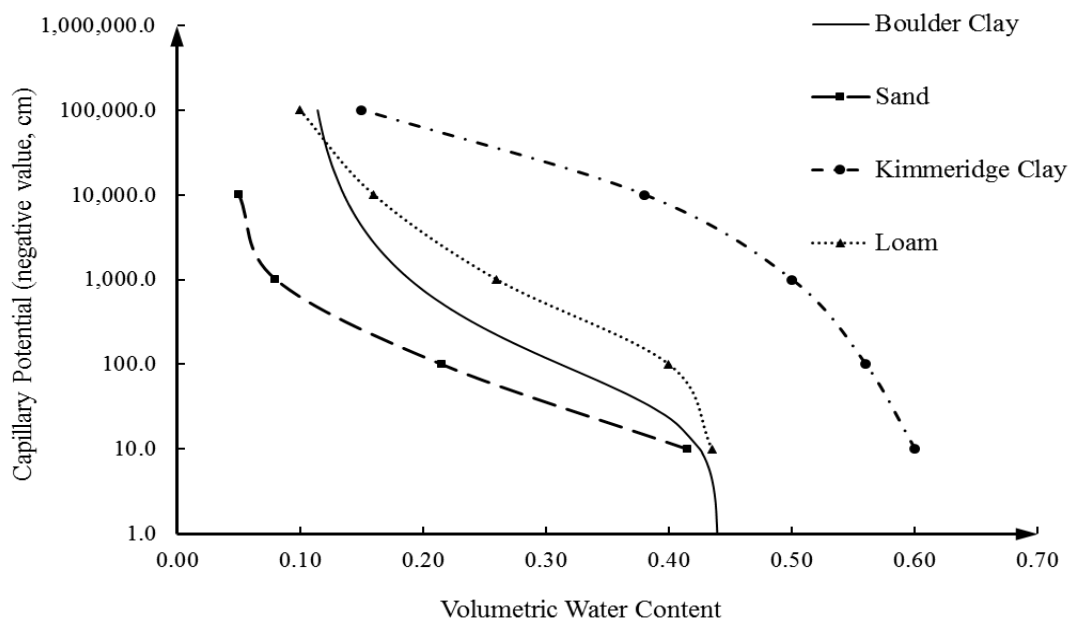


Figure 6. 5    Soil Water Retention Curve for Boulder Clay (plotted on a log scale of capillary potential)

Figure 6.6 shows that a similar approach has been adopted to approximate the hydraulic conductivity of boulder clay. The saturated hydraulic conductivity, $K_s$ for boulder clay can range from 1 x $10^{-8}$ cm/s to 1 x $10^{-7}$ cm/s based on independent data published in the literature as shown in Table 6.3.
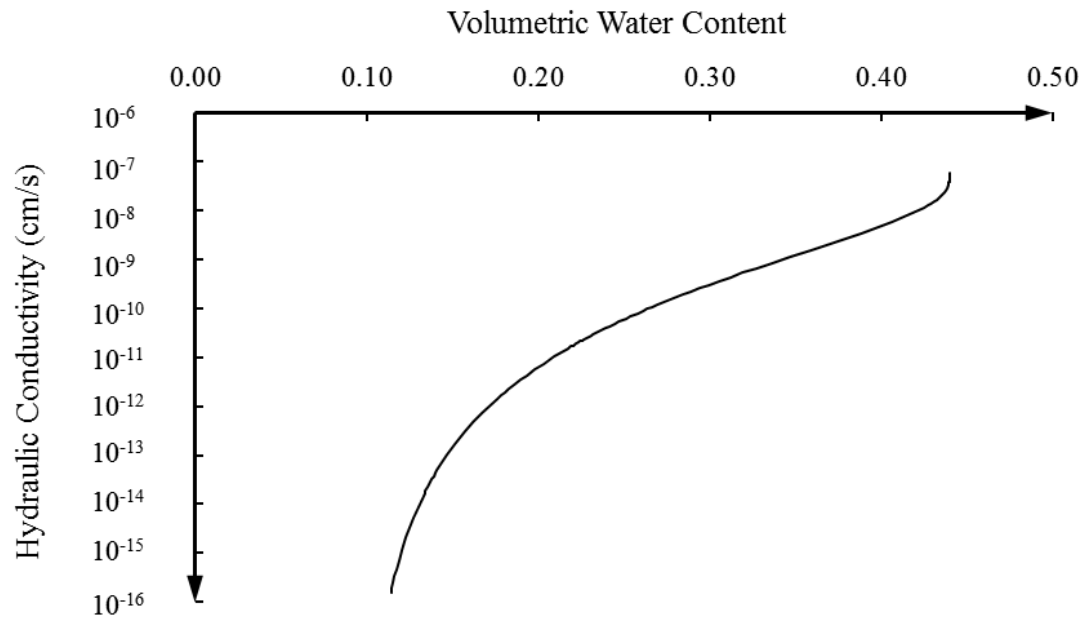
Figure 6. 6    Hydraulic Conductivity Curve for Boulder Clay (plotted on a log scale of hydraulic conductivity)

Table 6. 3    Saturated Hydraulic Conductivity for Boulder Clay

| Authors | Soil types | Hydraulic conductivity, $K_s$ (cm/s) |
|---|---|---|
| Anderson and Sivakumar (2008) | Belfast Upper Boulder Clay | $2.10 \times 10^{-8} \sim 5.31 \times 10^{-8}$ |
| Aplin et al. (1999) | Welsh Boulder Clay | $7.282 \times 10^{-8}$ |
| Price (2009) | Clay | $< 10^{-7}$ |

6.2.5   Numerical Simulation

Figure 6.7 shows a diagrammatic representation of the tree, the extent of the root zone and the domain size employed.  Based on the field observations of Biddle (1998), the root zone is assumed to extend to a depth of 1.3 m and a radial distance of 5 m.  The overall size of the axisymmetric finite element domain considered is 10 m × 10 m.
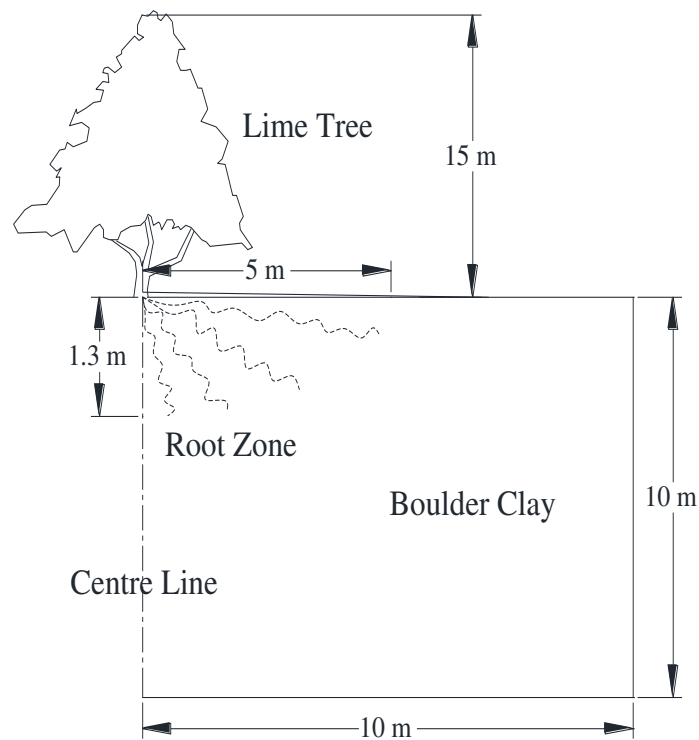


Figure 6. 7        Axi-symmetric Domain

Spatial discretisation has been achieved via the finite element mesh shown in Figure 6.8.  The mesh consists of four hundred, eight-node isoparametric elements with 1281 nodes.  The mesh was configured to offer some refinement within the root zone area since this is the region where the most significant moisture content variations were

expected to occur.  Preliminary numerical tests were conducted to ensure for this domain size, the outer boundaries do not significantly influence the simulated results within the region of interest.  The simulation employs a time-step size of 86400 seconds, which was held constant for the entire period considered.  Preliminary checks were made to ensure that the solution is both time-step and spatially converged.  The pressure head dependent reduction factor $\alpha(\psi)$ was assumed to be constant at a value of 1.0.  This value ensures that optimal water extraction was possible throughout the simulation period.
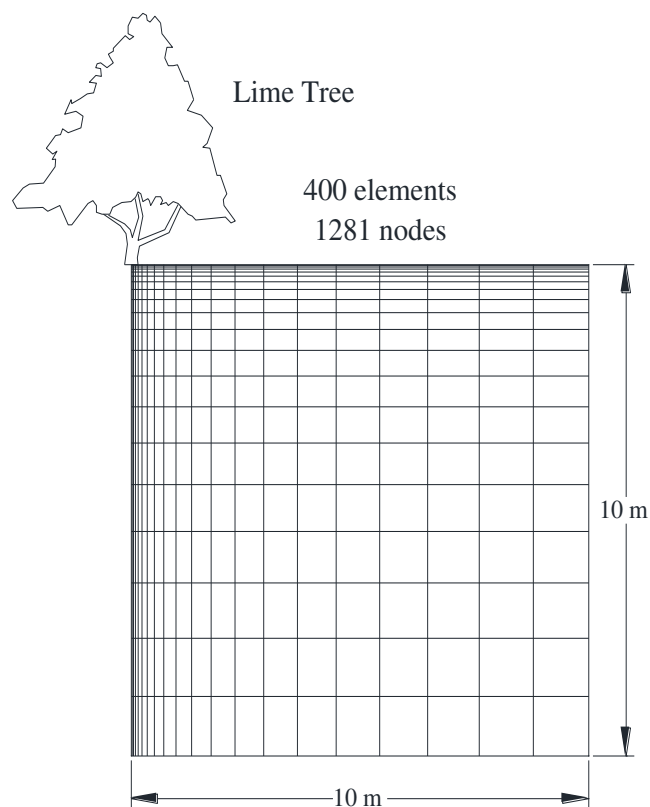


Figure 6. 8      Finite Element Mesh

In the present study, where initial moisture content is not available, a uniform pressure head corresponding to the field capacity has been assumed.  The initial

conditions employed for the simulation were based on the measured moisture content profile for the start date of the period considered. In fact, the profile indicated the soil was near field capacity at this time. Therefore, a uniform initial value of capillary potential of -34 cm was applied throughout the domain, representing an initial volumetric water content of 38.2 % - this corresponds to a degree of saturation of approximately 86.8 %. The simulated period covered a full range of leaf growth (from early appearance of leaves through to the time where most leaves drop off the tree) of 7 months (16th April 1979 to 24th October 1979).

Four simulations have been undertaken to explore the performance of the new modelling approach and can be summarized as follows:

- Simulation 6-1: Utilizes a graphical representation of the lime tree root morphology (see Figure 6.9 a-c) to define the distribution of water uptake with depth and radius and a transpiration rate based on field data (Biddle 1998) with free surface boundary conditions.

- Simulation 6-2: As Simulation 6-1, but with the addition of representing time dependent variations in boundary conditions based on daily rainfall patterns.

- Simulation 6-3: Considers transpiration rate sensitivity study based on Penman-Monteith equation.

- Simulation 6-4: Assumes a linear distribution of water extraction rates with both depth and radius after Rees and Ali (2006), to allow comparison with the new image based method.
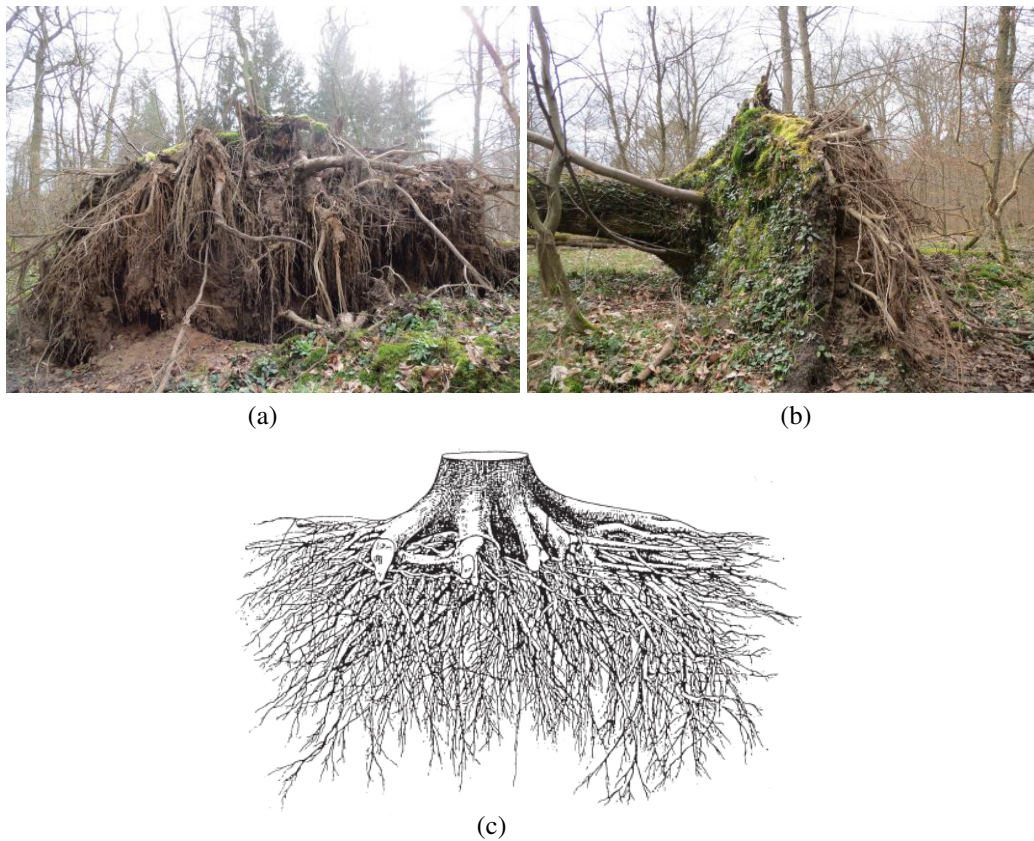
Figure 6. 9    The Root System of Lime tree: (a) and (b) are the root systems of Lime tree (*Tilia cordata*) in reality, (c) is a drawing of root system of *Tilia cordata* (Köstler et al. 1968)

Figure 6.9 (c) shows a simple graphical representation of a typical lime tree root system at depth of 1.3 m below ground and a radial distance of 5 m.   These were considered in Simulation 1 to 3 respectively utilizing the new graphically based root density distribution approach.   The real root system of Lime tree and a process diagram of root density based on a graphical (or photographic) representation of the actual root morphology are provided in Figure 6.10.
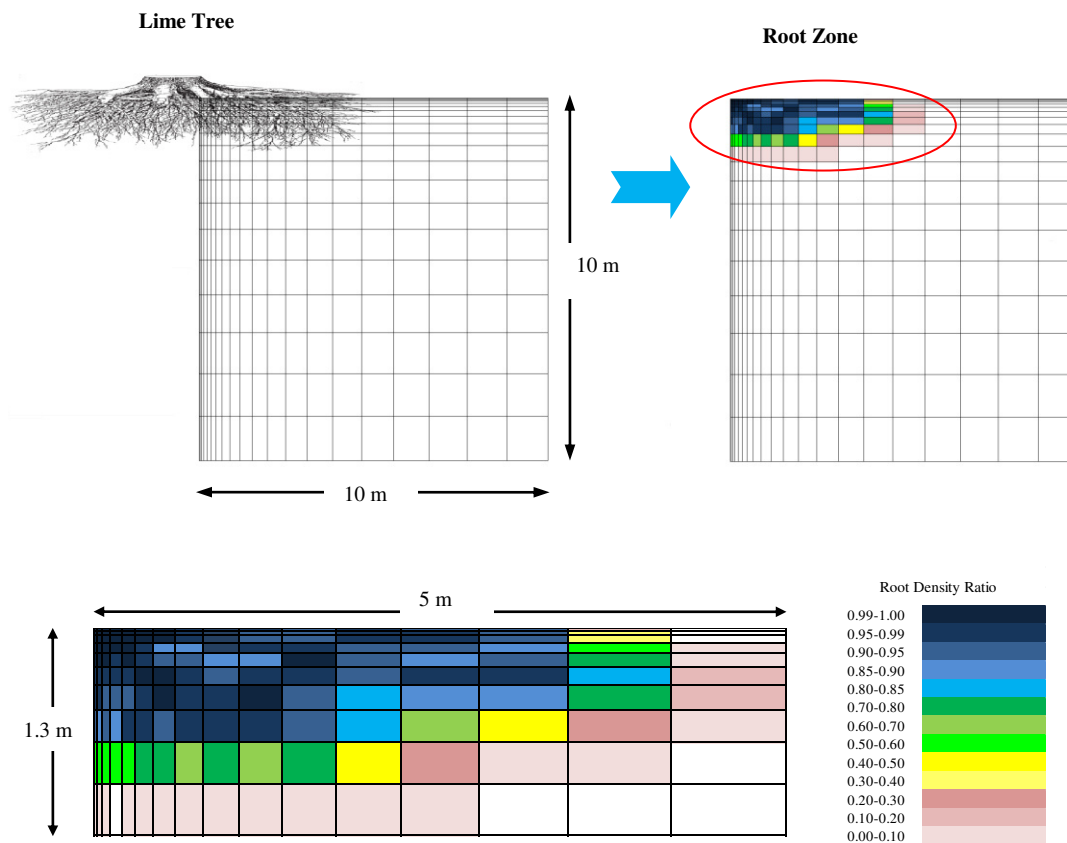
Figure 6. 10    A process diagram of root density based on a graphical (or photographic) representation of the actual root morphology.

These SMD values were calculated by Biddle (1998) based on a spring average profile.  The development of a deficit during the season is shown to occur at depths of 0.3 m, 1.0 m and 2.0 m below ground level.  In Figure 6.11, the soil moisture deficit at 0.3 m below ground level indicated that there was wetting period in the soil between July 1979 and August 1979. This profile indicates some seasonality in the soil profile.  This aspect of behaviour is considered in more detail in Simulation 6-2.
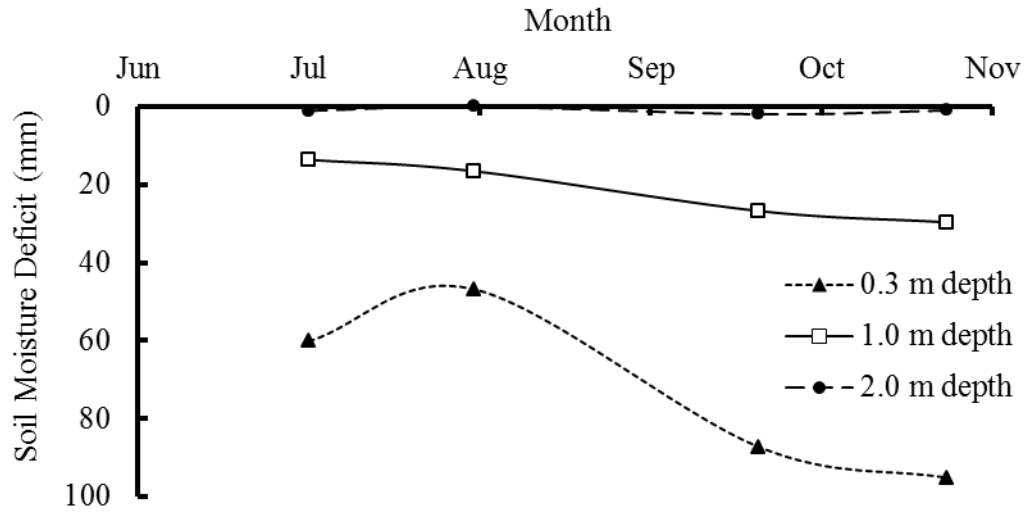
Figure 6. 11     Soil Moisture Deficit at 1.4 m distance from tree
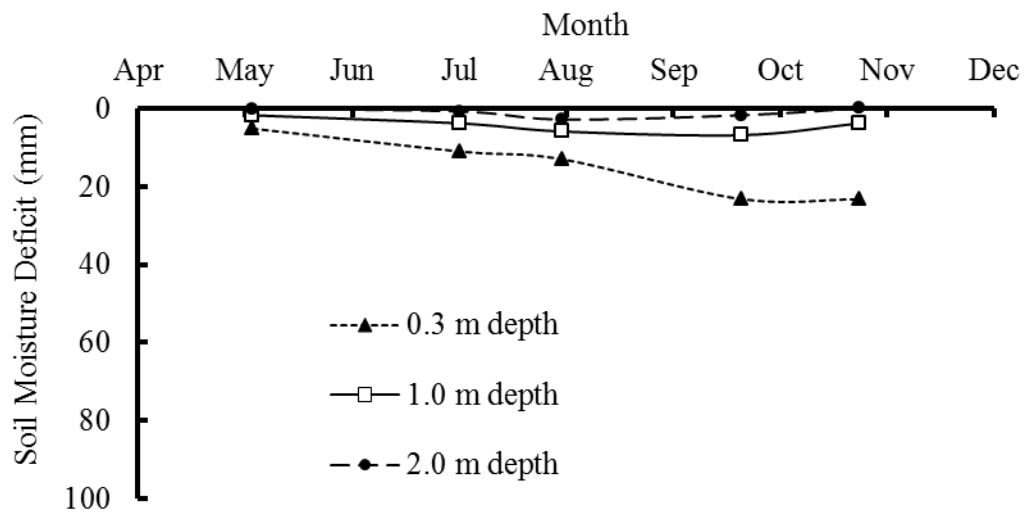
Figure 6. 12     Soil Moisture Deficit at 4.9 m distance from tree

6.2.6   Estimating Transpiration Rate

Detailed calculations of estimating transpiration rate for an individual tree problem, modification of the Penman-Monteith equation are provided in Appendix 4.
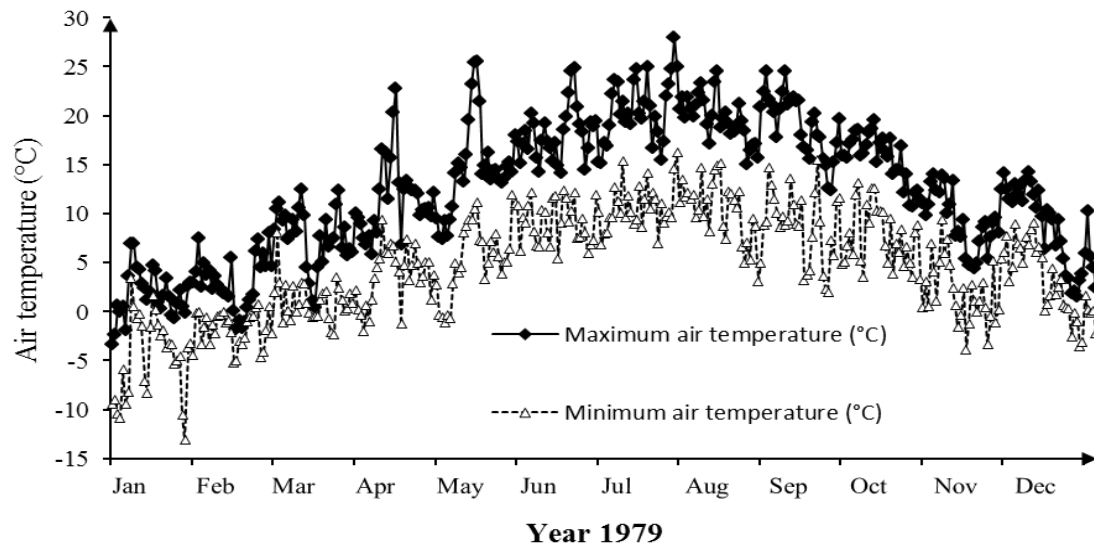


Figure 6. 13   Measured maximum and minimum air temperature of the weather station (British Atmospheric Data Centre).

The proposed method requires specification of meteorological data.  Some of the data are measured directly in weather stations.  Others are related to commonly measured data and can be derived with the support of a direct or empirical relationship.  The measured maximum and minimum air temperature provided by the British Atmospheric Data Centre has been acquired for the nearest weather station to the site (Grendon Underwood, Buckinghamshire, UK).  Figure 6.13 shows the temperature data recorded at Grendon Underwood for the year of 1979 under consideration here.
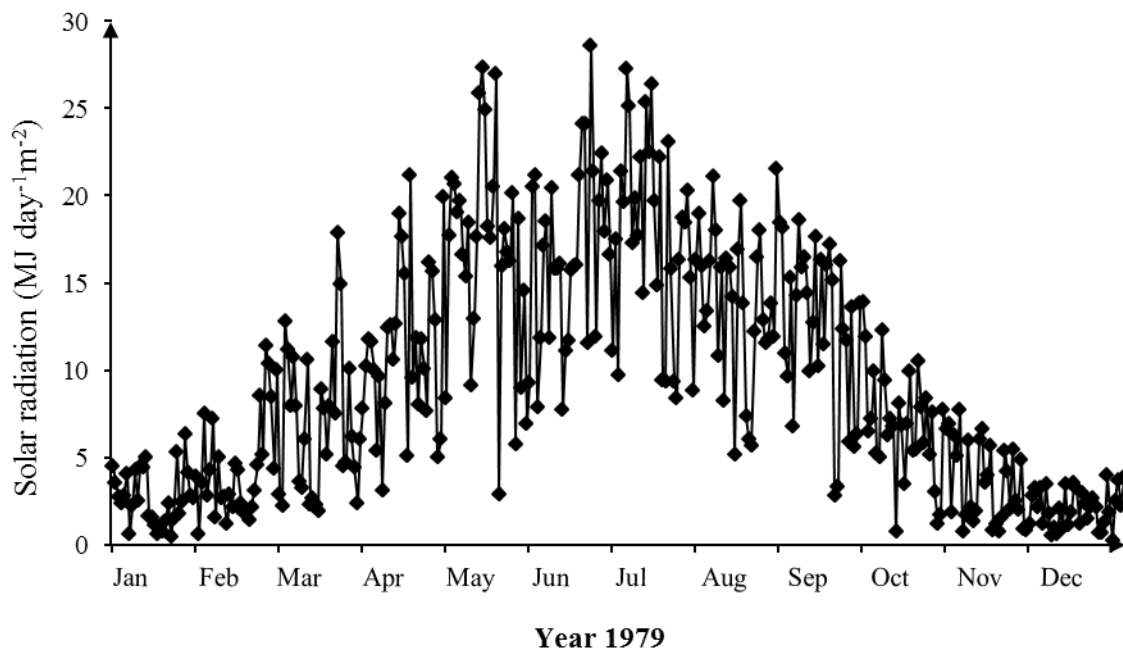
Figure 6. 14    The measured solar radiation at the nearest weather station (British

Atmospheric Data Centre)
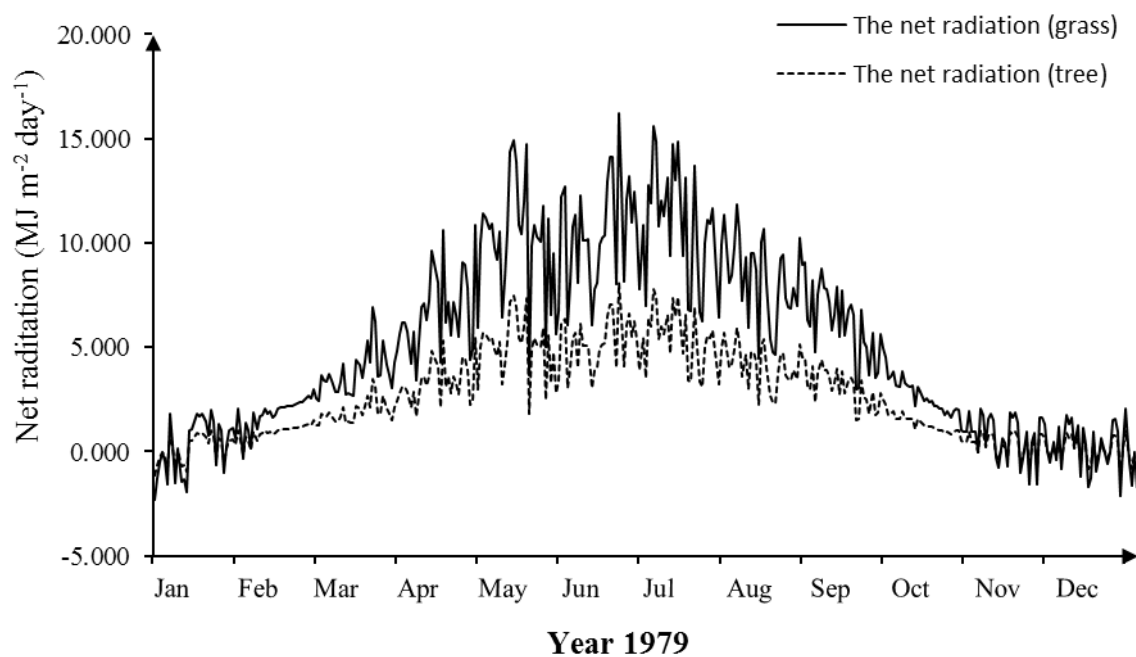


Figure 6. 15    The net radiation data

The data of solar radiation provided by the British Atmospheric Data Centre has been

acquired for the nearest weather station to the site (Rothamsted, Hertfordshire).

Figure 6.14 shows the solar radiation data recorded at Rothamsted for the year of 1979 under consideration here. The net radiation for a tree can be calculated (Appendix 4 provides the full calculation) and the results are shown in Figure 6.15.

The average daily measured mean stomatal resistance ($r_s$) within the tree canopy is from 500 s m$^{-1}$ to 2000 s m$^{-1}$ (Tang et al. 2006; Martin et al. 1999; Jarvis 1976; Kelliher and Blacek 1986). According to the calculations and parameters data shown in Appendix 4 the transpiration rate for a whole tree can be estimated. Figure 6.16 shows the variation of calculated maximum and minimum transpiration, for the entire leaf period of a deciduous tree at this experimental site.
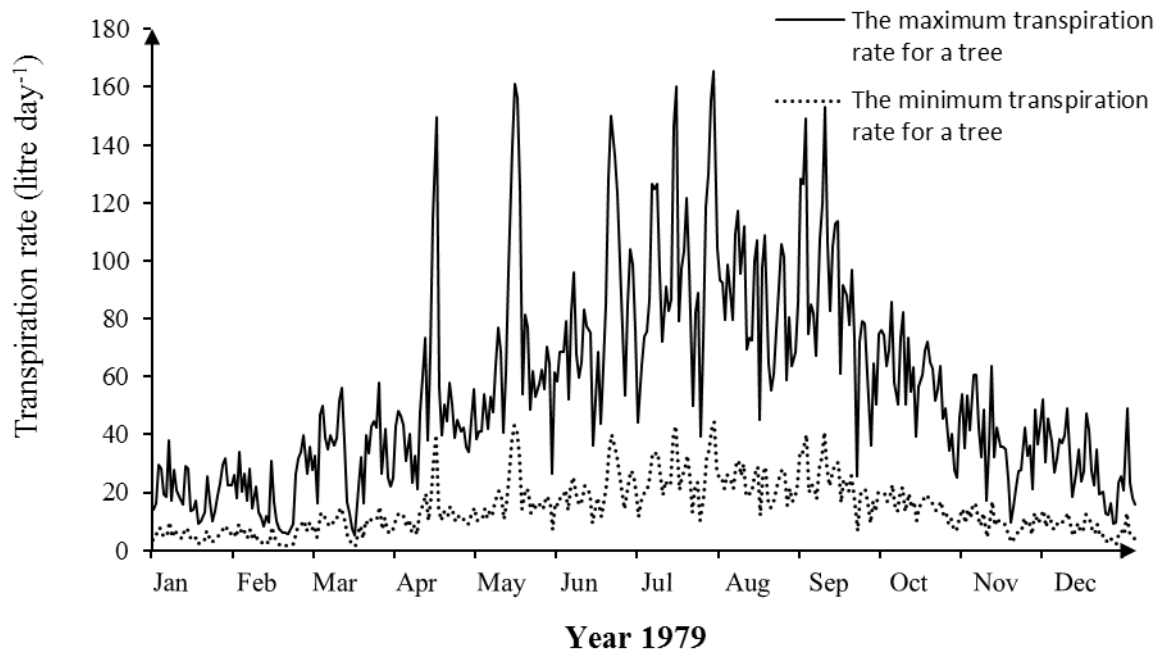


Figure 6. 16    The transpiration rate for a single lime tree

The transpiration rate for a lime tree is based on the assumption of stomatal resistance. Given the importance of these parameter on the results generated, a sensitivity check has been made to ensure the assumptions made were reasonable. To do this, a

maximum transpiration rate of lime tree (55 L/day based on $r_s$ which was assumed 500 s m$^{-1}$) and a minimum transpiration rate of lime tree (15 L/day based on $r_s$ which was assumed 2000 s m$^{-1}$) were considered in Simulation 6-3.

The transpiration rate of a lime tree also can be estimated from the average soil moisture depletion between the moisture profiles at the driest date and soil at field capacity during soil drying period, calculations find this to be approximately 28 L/day. Since the possible range of the transpiration rate for a single tree at the experimental field, based on the PM calculations, is from 15 to 55 L/day, it seems reasonable to take this value of 28 L/day to define the total transpiration rate employed in this simulation. This value was distributed throughout the root-zone via application of the water-uptake model described in Chapter 3. The pressure head dependent reduction factor was assumed to be constant at a value of 1.0 to ensure that optimal water extraction was possible throughout the simulation period.

### 6.2.7   Time Dependent Boundary Conditions

This section considers a simple method of representing time dependent variations in boundary conditions based on daily rainfall patterns. Data from the nearest Meteorological Station to the site under consideration has been used to estimate behaviour at the soil surface.

For this location, Biddle (1998) provided an estimate of the soil moisture deficit (SMD) variation at distances of 1.4 m and 4.9 m from the tree as shown in Figures

6.11 and 6.12 respectively. According to Figure 6.11, the resulting variation in SMD during the season is shown for depths of 0.3 m, 1.0 m and 2.0 m below ground surface level. Overall, the soil profile appears to have undergone a period of drying from August to October in 1979. The data for 0.3 m depth shows some fluctuation. This may indicate a short period of wetting near the surface of the profile during the summer period.



Figure 6. 17    Study Site and Meteorological Office Station, figure reproduced from Bing Maps

Rainfall data is provided by British Atmospheric Data Centre for the nearest weather station to the study site (Stacey Hall, Wolverton, UK). Figure 6.17 shows the location of the nearest station at Bradwell Abbey (Buckinghamshire, UK) which is some 962 m away from the site under consideration.

Figure 6.18 shows the rainfall data recorded at weather station for the period under consideration here (16th April 1979 to 24th October 1979). The SMD data and rainfall data presented above provide a general indication of the seasonal weather patterns and soil moisture variations that took place at the site of the field experiment. The following numerical simulation utilizes some of this information in an attempt to include a more representative surface boundary condition than was previously adopted in the Simulation 6-1. There are two basic forms of boundary condition (fixed or flux) that can be applied in this numerical formulation. Although the flux boundary conditions can provide the advantage of directly controlling the quantity of water flowing in or flowing out the system, these may result in significant numerical instability problems when incorporated within a highly non-linear flow simulation, Therefore, an attempt is made below to approximate surface conditions using fixed boundary conditions only.
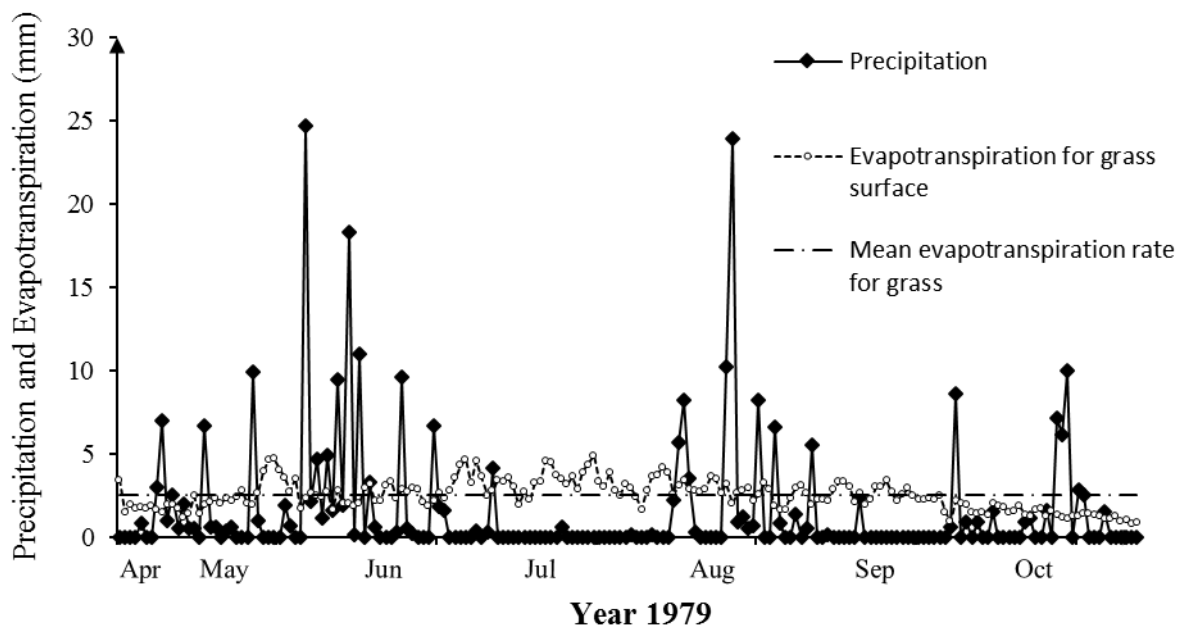


Figure 6. 18    Rainfall Data and Evapotranspiration for grass

Simulation 6-2 employs time varying surface boundary conditions based on the rainfall data given in Figure 6.18. The evapotranspiration for uniform grass cover has been estimated by Penman-Monteith equation and it is approximately 2.5 mm/day (as shown in Figure 6.18). Therefore, it is assumed that the soil surface was saturated during the simulation when the daily rainfall exceeded evapotranspiration demand from the grass. The saturation of the soil surface was simulated via application of a fixed boundary condition of zero capillary potential prescribed at the surface nodes.

The saturated boundary condition was only applied to the surface at times when the rate of the rainfall was found to be more than the evapotranspiration rate of grass as shown in Figure 6.18. Therefore, the simulation is based on an alternating surface boundary that is either fixed at saturation or is unconstrained (free state) depending on this criterion. In particular, the simulated period starts at Day 1 (16th April 1979) and ends at Day 192 (24th October 1979). The process is illustrated in Figure 6.19.
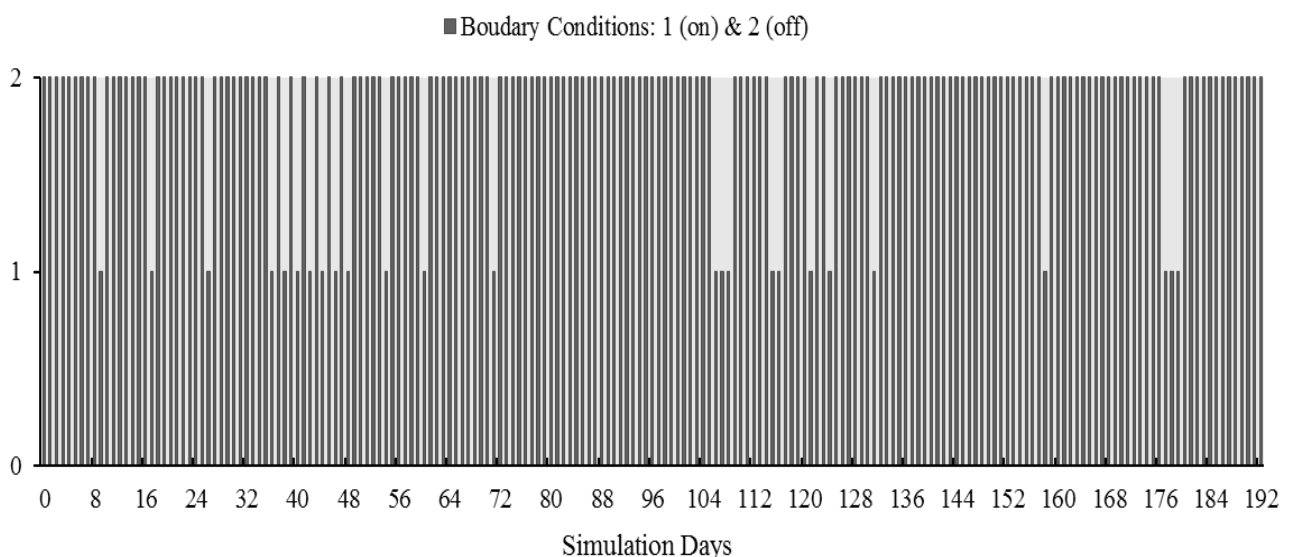


Figure 6. 19    Switch On/Off periods for boundary conditions

6.2.8    Simulation Results

The numerical model is formulated in terms of capillary potential for the reasons discussed previously (see Chapter 3).    However, for ease of interpretation and comparison with field data the raw results have been converted to volumetric moisture content.    This is done employing the water retention curve for boulder clay (i.e. equation 3.1 – employing the parameters given in Table 6.2).

Figures 6.20, 6.21 and 6.22 show the simulated and measured moisture content profiles of simulation 6-1 at a radial distance of 1.4 m from the centre-line of the lime tree for the times of 109 days, 159 days and 192 days respectively.    Although Field data were only available on the specific dates of 02/08/79, 21/09/79 and 24/10/79 respectively, the simulation can serve to display the overall behaviour at this site.    The corresponding moisture content profiles of simulation 6-1 at a distance of 4.9 m from the lime tree are provided from Figures 6.23 to 6.25.    Two typical contour plots are shown in Figures 6.26 and 6.27.    These results from Simulation 6-1 are considered in detail below.

Firstly, considering the simulated moisture content profiles, Figure 6.20 shows the initial measured moisture content alongside the uniform numerical initial condition. The simulated and measured results at 109 days are also presented.    The sink term is active within the depth of the root zone (i.e. the upper 1.3 m of the soil profile) and to a radial extent of 5 m (as described previously).    It is clear that the moisture extraction profile is roughly matching the root distribution of lime tree (as expected by definition) and the moisture content increases to its initial value of 38.2% at

approximately 1.5 m below the ground surface. While the measured data showed small change in moisture content is evident between a depth of 1.5 m and 2.0 m, the results suggest that the real root zone may be a little bigger than the assumption employed here. In general, the figure indicates that a reasonable agreement between the simulated results and the measured moisture profiles has been achieved.

For Simulation 6-1, Figure 6.21 and 6.22 show that a very similar set of results was obtained at 159 days and 192 days respectively. The initial moisture content profile has also been included on this plot since it provides a useful visual reference of the overall moisture content variation. Although the new model may not distribute moisture in exactly same manner as observed in the field, the level of accuracy generated by application of an image based root-density approach appears acceptable for application over a considerable time period. Figures 6.23 to 6.25 show the corresponding set of results achieved remote from the tree. It can be seen that the roots of this lime tree have relatively little effect on the seasonal moisture depletion at a radial distance of 4.9 m. It should also be recognized that the differences of between measured data and simulated results at a radial distance of 4.9 m could be caused by the assumed initial conditions. Further study is needed to consider the impact of non-uniform initial data over the whole domain. Overall, a good agreement between simulated and measured profiles is also achieved at this distance.

Figures 6.26 and 6.27 present the simulated contours of volumetric moisture content (%) generated by Simulation 6-1 at 100 days and 192 days respectively. These figures provide further illustration that the approach adopted has produced an overall moisture pattern is fundamentally determined by the root density and morphology

(see Figure 6.10). Unfortunately, there was no field data available to compare with these results. It is also recognized that further demonstration of the overall moisture pattern simulated may be necessary in practice.

Volumetric Moisture Content
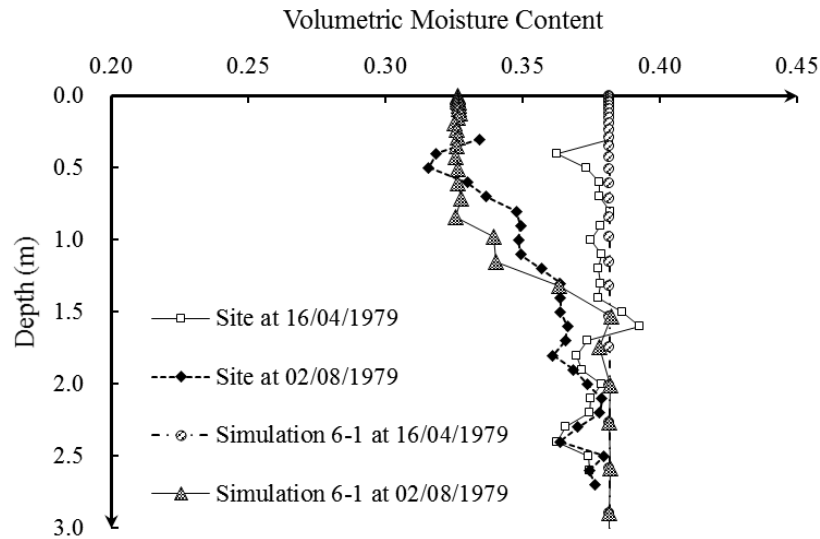
Figure 6. 20    Simulated and Measured Moisture Content Profiles in Simulation 6-1 (Time at 02/08/1979, Radial Distance 1.4 m)

Volumetric Moisture Content
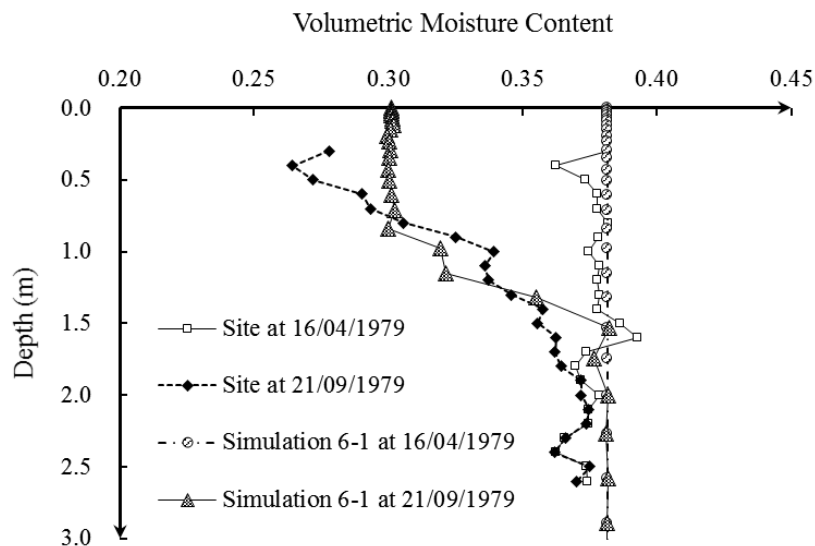
Figure 6. 21    Simulated and Measured Moisture Content Profiles in Simulation 6-1 (Time at 21/09/1979, Radial Distance 1.4 m)
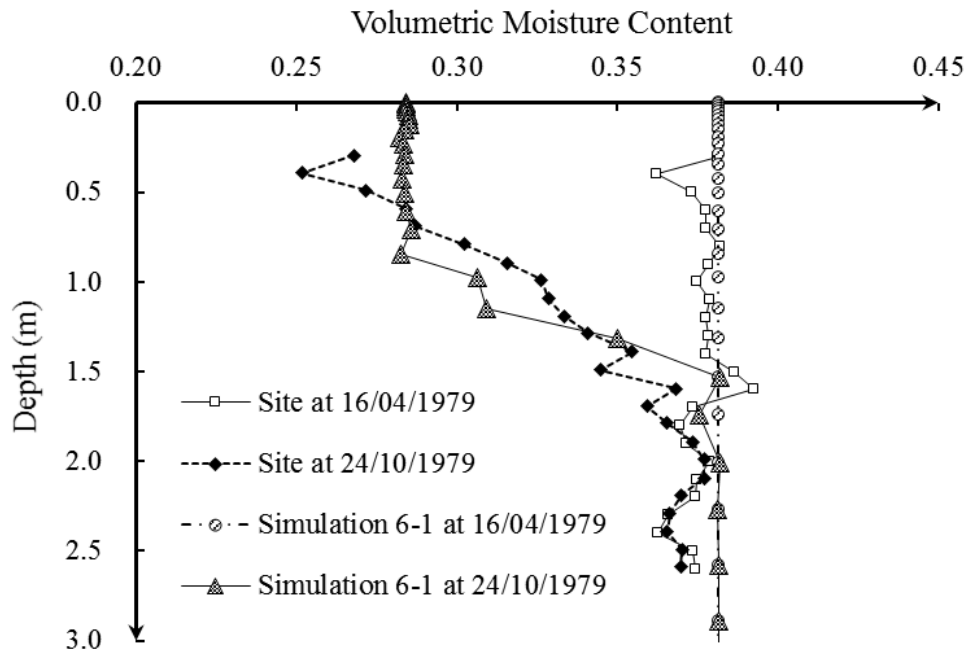
Figure 6. 22    Simulated and Measured Moisture Content Profiles in Simulation 6-1

(Time at 24/10/1979, Radial Distance 1.4 m)
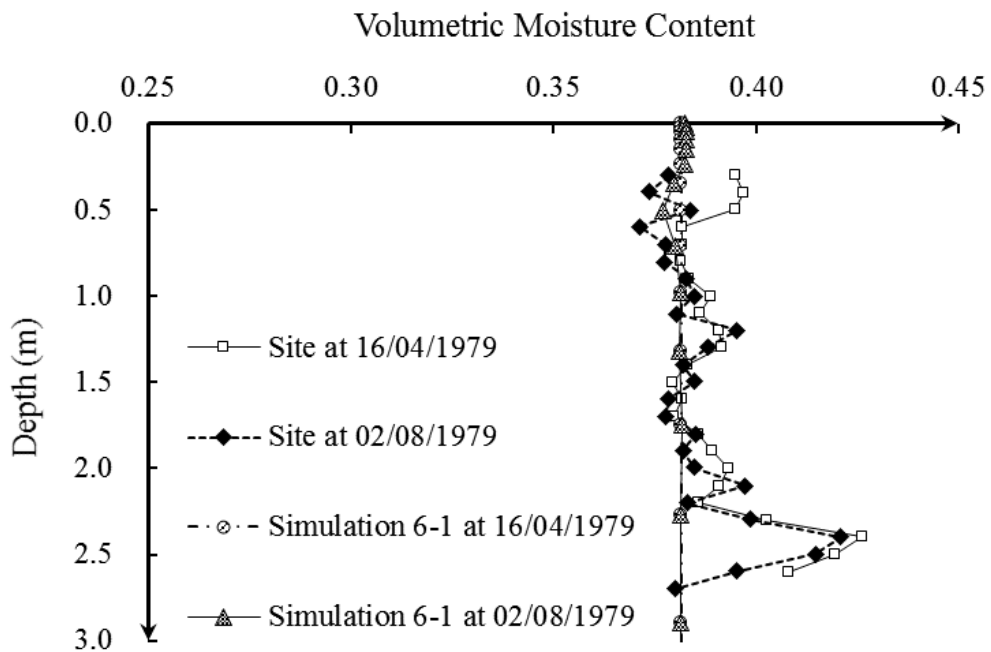


Figure 6. 23    Simulated and Measured Moisture Content Profiles in Simulation 6-1

(Time at 02/08/1979, Radial Distance 4.9 m)
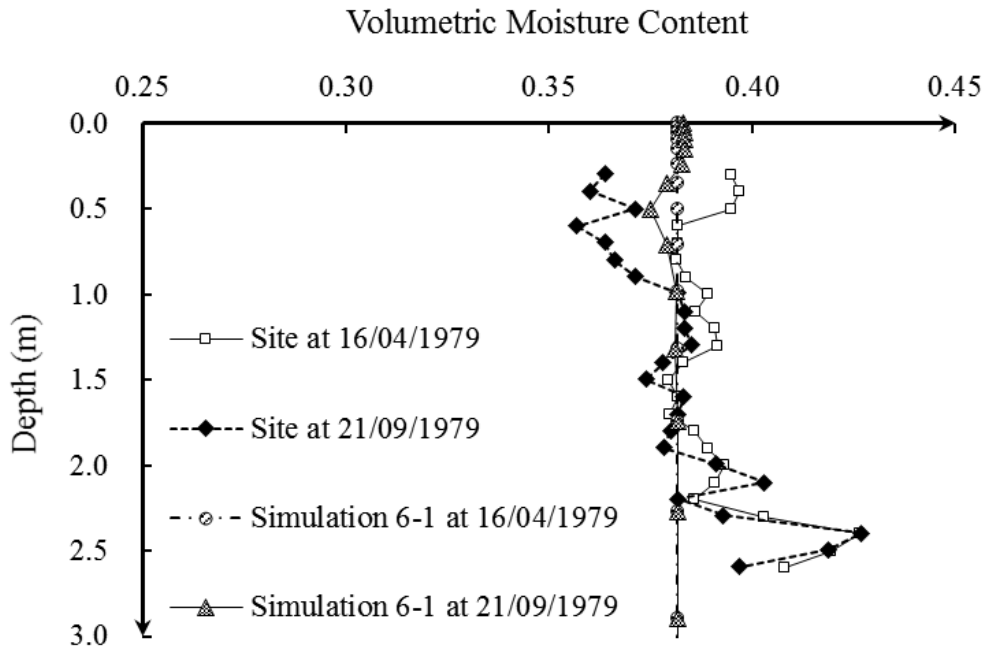
Figure 6. 24    Simulated and Measured Moisture Content Profiles in Simulation 6-1

(Time at 21/09/1979, Radial Distance 4.9 m)
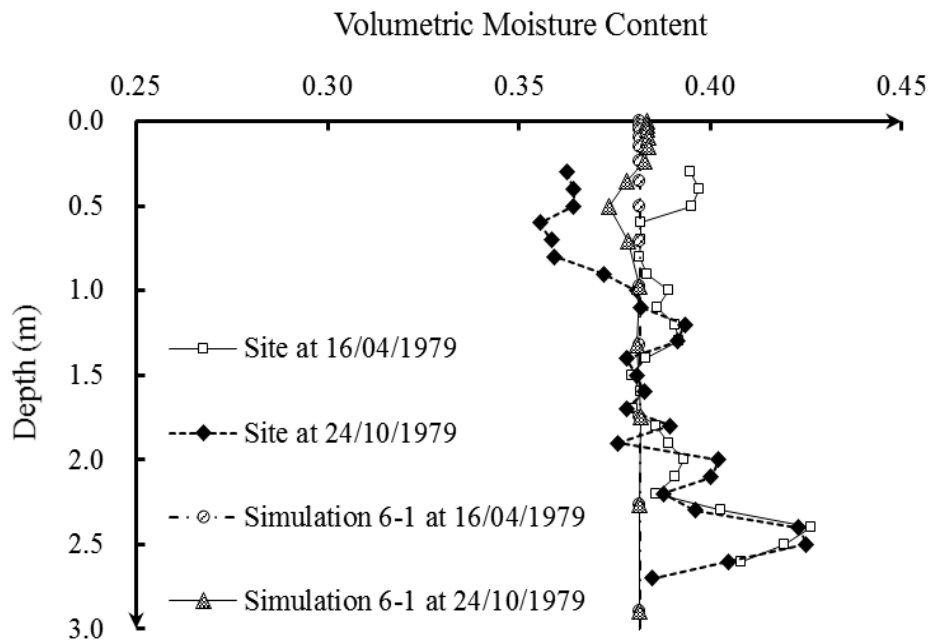


Figure 6. 25    Simulated and Measured Moisture Content Profiles in Simulation 6-1

(Time at 24/10/1979, Radial Distance 4.9 m)
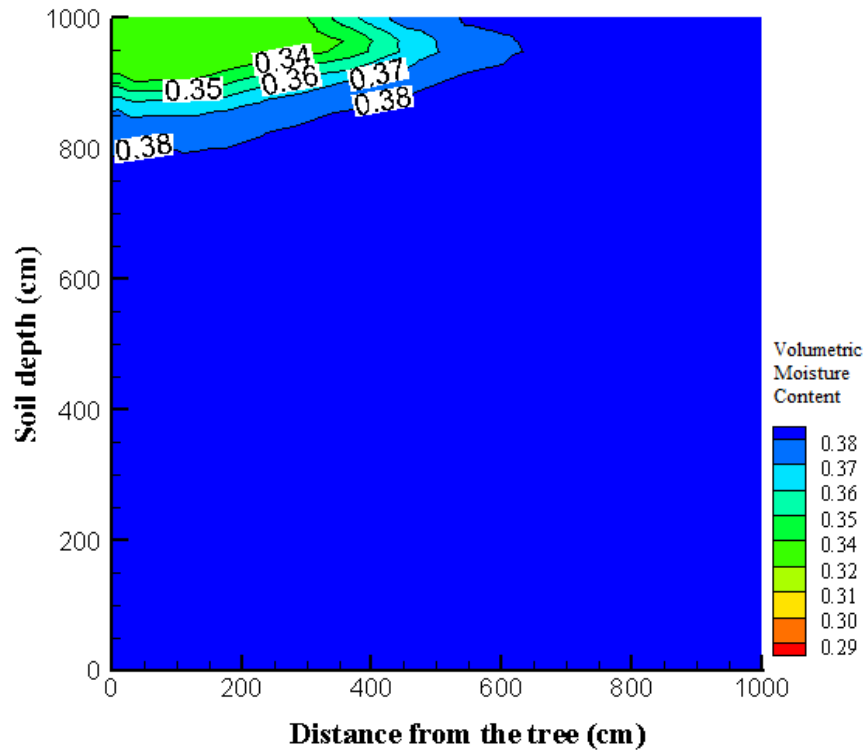
Figure 6. 26   Contour Plots of volumetric moisture content at 100 days in Simulation 6-1
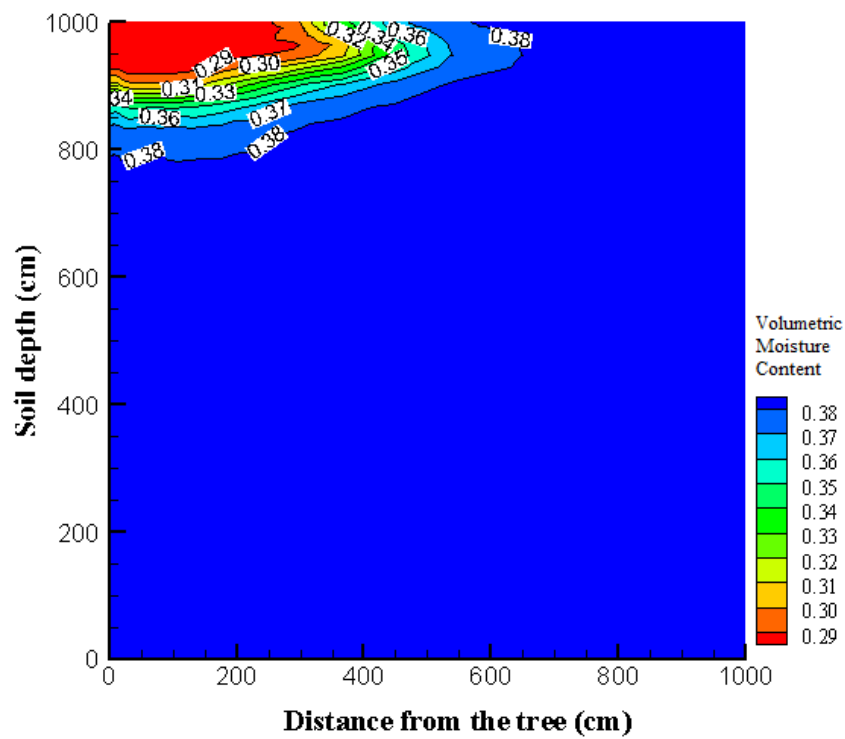


Figure 6. 27   Contour Plots of volumetric moisture content at 192 days in Simulation 6-1

Simulation 6-2 employs time varying surface boundary conditions based on the daily rainfall conditions. The rainfall period was represented by the use of a fixed, saturated, boundary condition applied at the soil surface (i.e. a zero capillary potential was prescribed at the surface nodes). A comparison of simulated and measured moisture content profiles between Simulation 6-1 and Simulation 6-2 is provided in Figure 6.28, 6.29 and 6.30. This comparison, particularly towards the surface where both the observed results and those of simulation 6-2 show an increase in moisture content, indicates that the top layer of the profile can be predicted by Simulation 6-2. Although the field data was insufficiently detailed to compare with these results, this gives an indication of the significance of the inclusion of time varying boundary conditions have on the prediction of water uptake.

Figures 6.31 to 6.33 present the results plotted in terms of moisture content versus time, at depths 0.05 m, 0.3 m, 1.0 m and 2.0 m below the surface and at a radial distance of 1.4 m from the tree. The measured data is simply plotted as discrete data points at the times when measurements were recorded on site. Considering no adequate field measured data available, there was no extrapolation carried out. Numerical results can be output at any number of time intervals hence a continuous variation has been plotted for comparison. The results plotted in Figure 6.33 indicate that relatively little moisture variation occurred at (and below) a depth of 2.0 m. The overall simulated trend appears to be in fair agreement with the measured data. Figures 6.34 to 6.36 represent a corresponding set of results at a radial distance of 4.9 m from the trees. There is very little change in moisture content occurred at this distance from the lime tree. These results serve to show that the root depth and radial assumed in the simulation appears reasonable. It is recognized that the time varying

boundary condition does not aim to reflect the true intricacy of the natural fluctuations that happen. However, the current study attempts to provide an assessment of the developed approach. Further refinement of boundary conditions to simulate a problem with full drying and wetting periods is likely to be necessary for a range of practical applications.
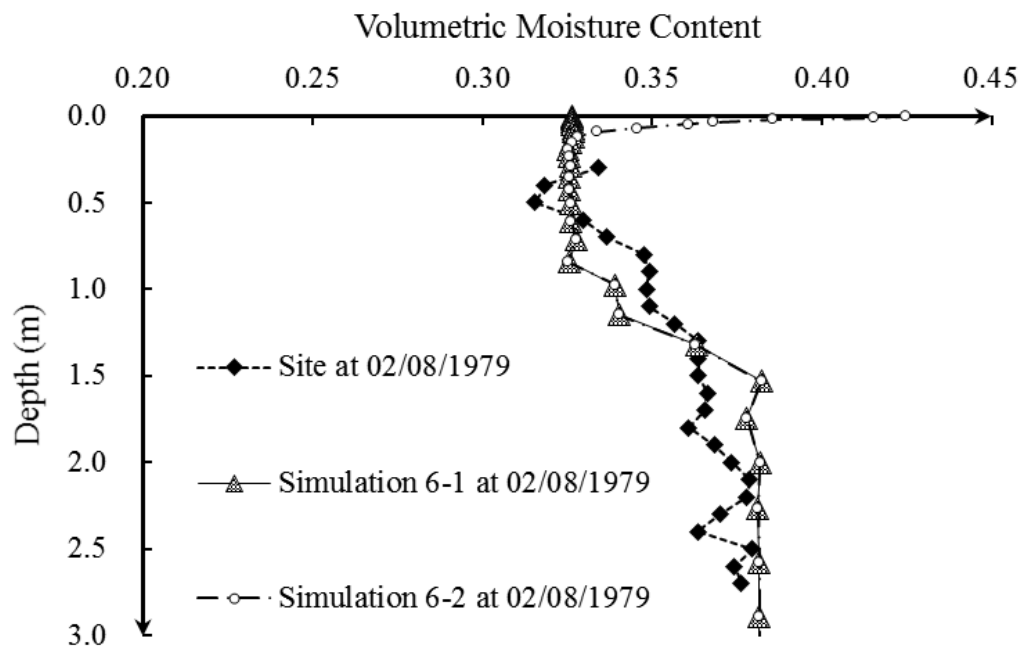
Figure 6. 28    Simulated and Measured Moisture Content Profiles in Simulation 6-2 (Time at 02/08/1979, Radial Distance 1.4 m)
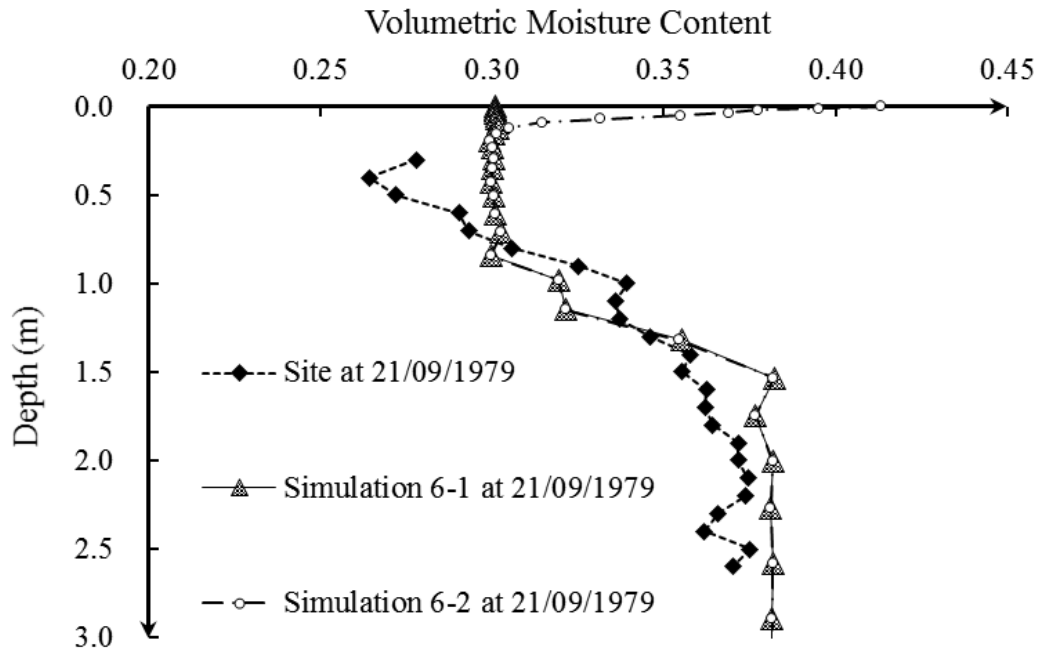
Figure 6. 29    Simulated and Measured Moisture Content Profiles in Simulation 6-2 (Time at 21/09/1979, Radial Distance 1.4 m)
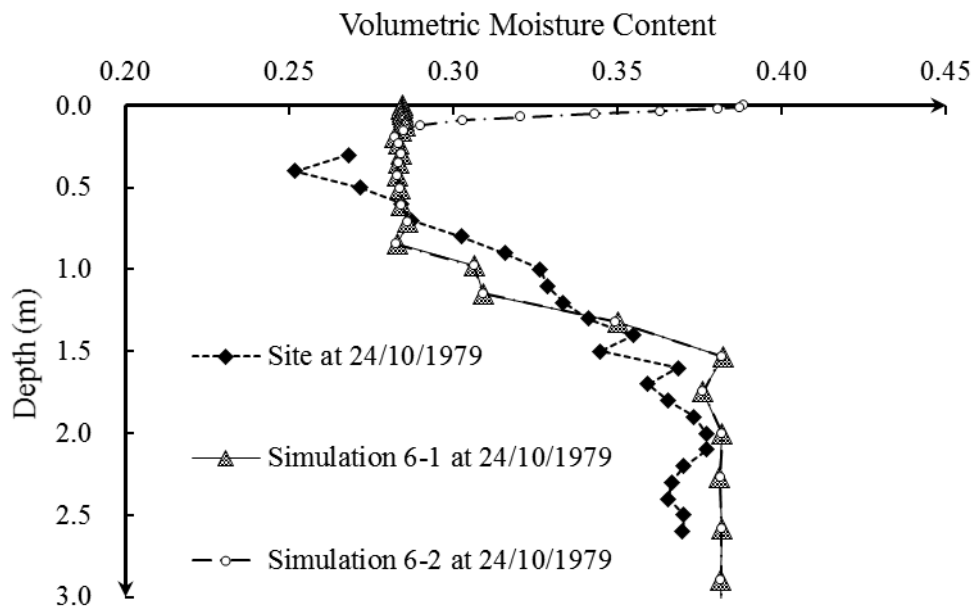


Figure 6. 30    Simulated and Measured Moisture Content Profiles in Simulation 6-2 (Time at 24/10/1979, Radial Distance 1.4 m)
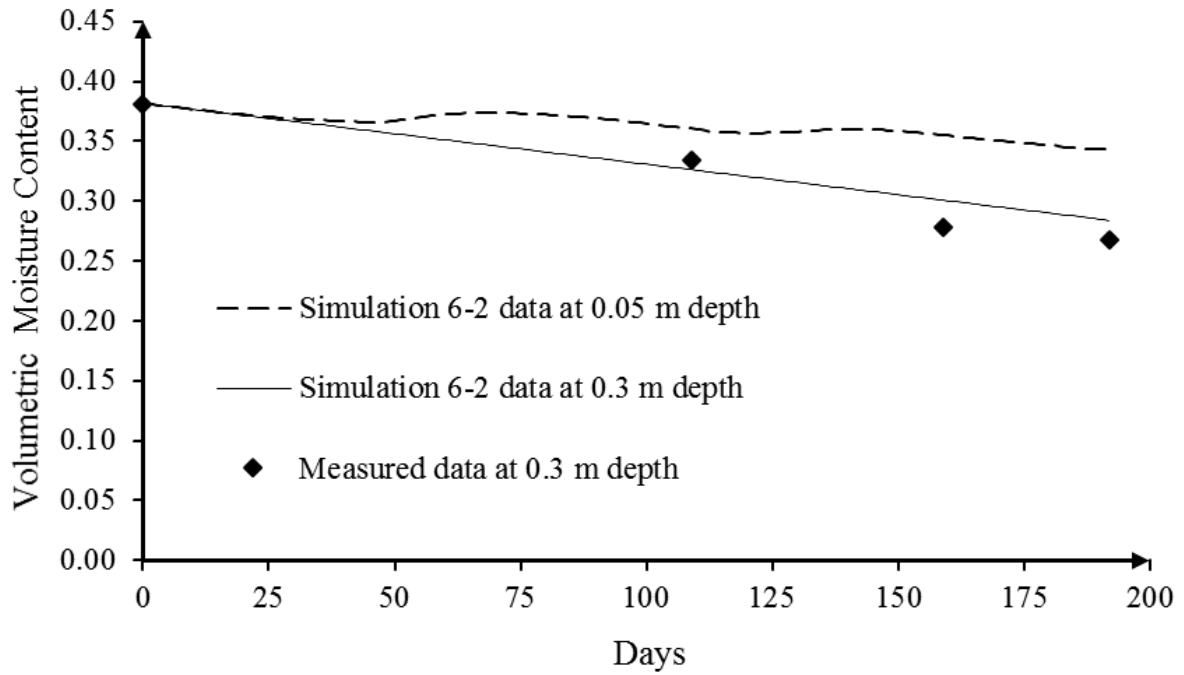
Figure 6. 31    Simulated and Measured Transient Moisture Content Variation in

Simulation 6-2 (Depth 0.05 and 0.3 m, Radial Distance 1.4 m)
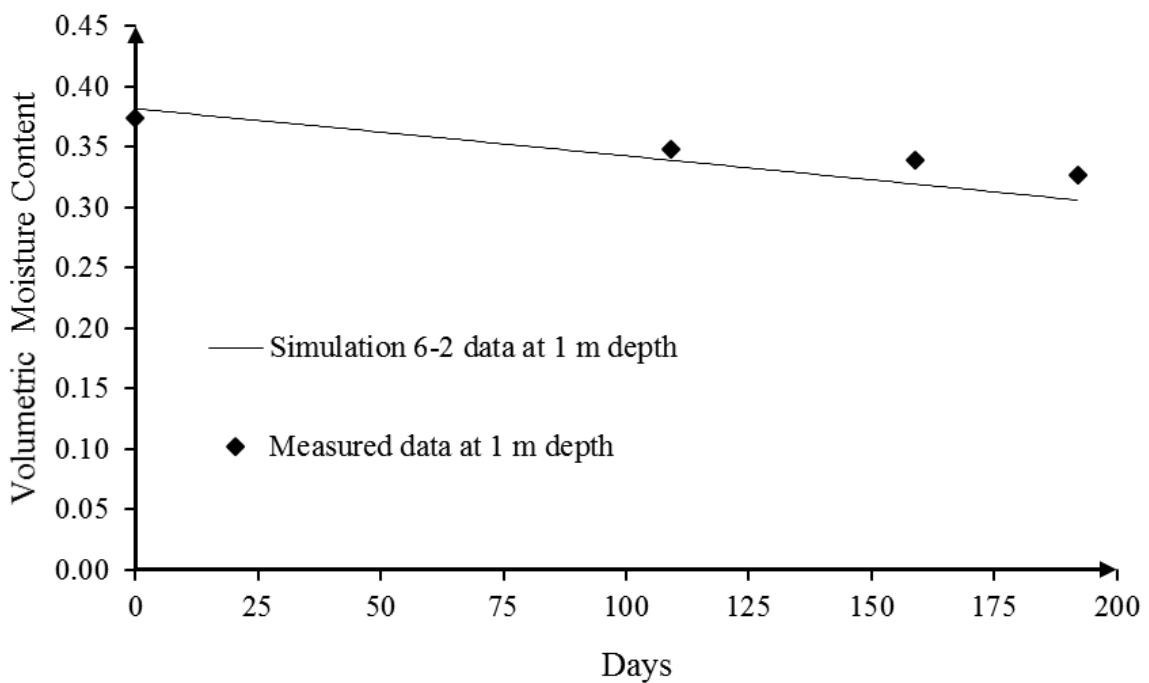


Figure 6. 32    Simulated and Measured Transient Moisture Content Variation in

Simulation 6-2 (Depth 1 m, Radial Distance 1.4 m)
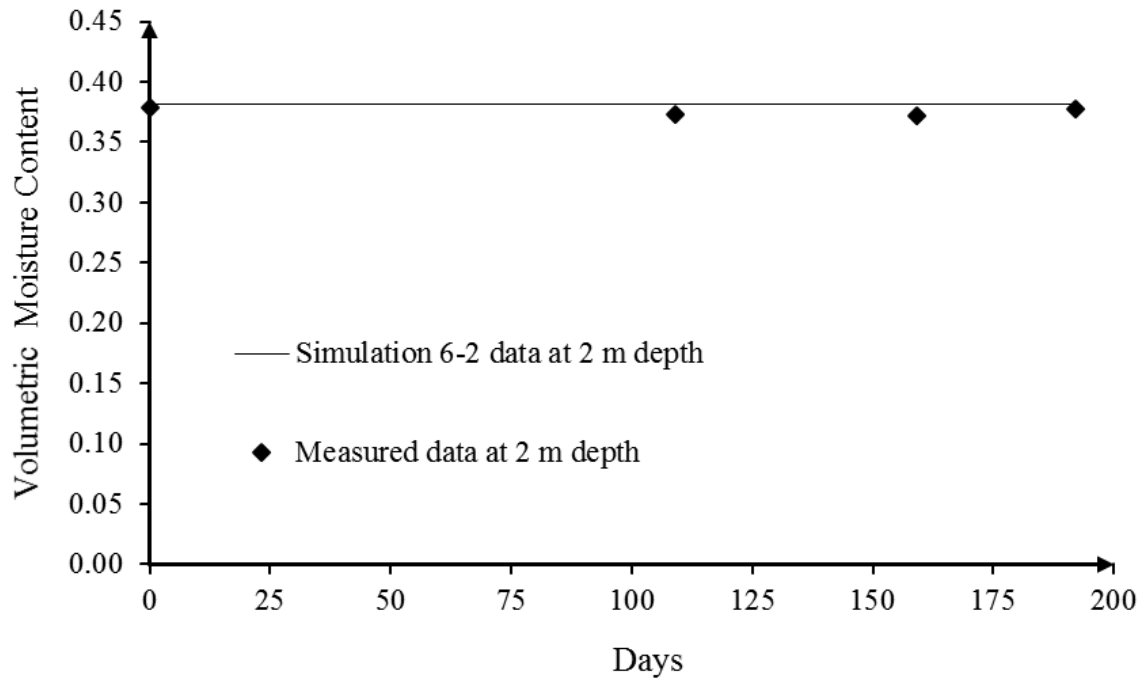
Figure 6. 33    Simulated and Measured Transient Moisture Content Variation in Simulation 6-2 (Depth 2 m, Radial Distance 1.4 m)
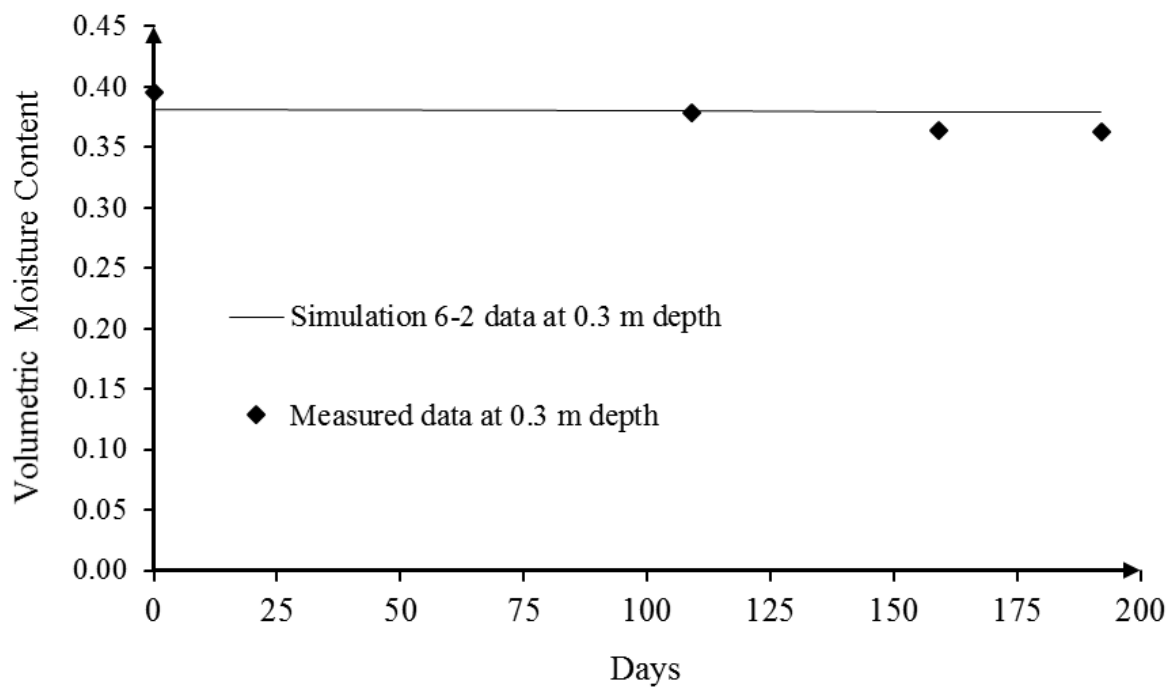


Figure 6. 34    Simulated and Measured Transient Moisture Content Variation in Simulation 6-2 (Depth 0.3 m, Radial Distance 4.9 m)
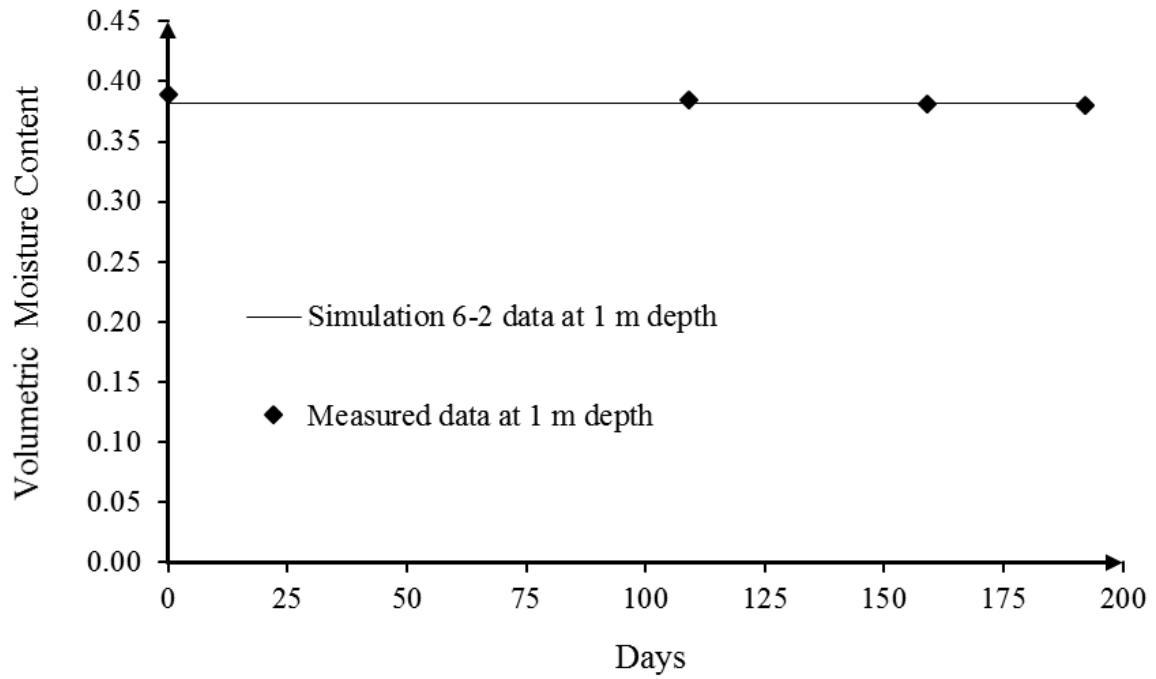
Figure 6. 35    Simulated and Measured Transient Moisture Content Variation in Simulation 6-2 (Depth 1 m, Radial Distance 4.9 m)
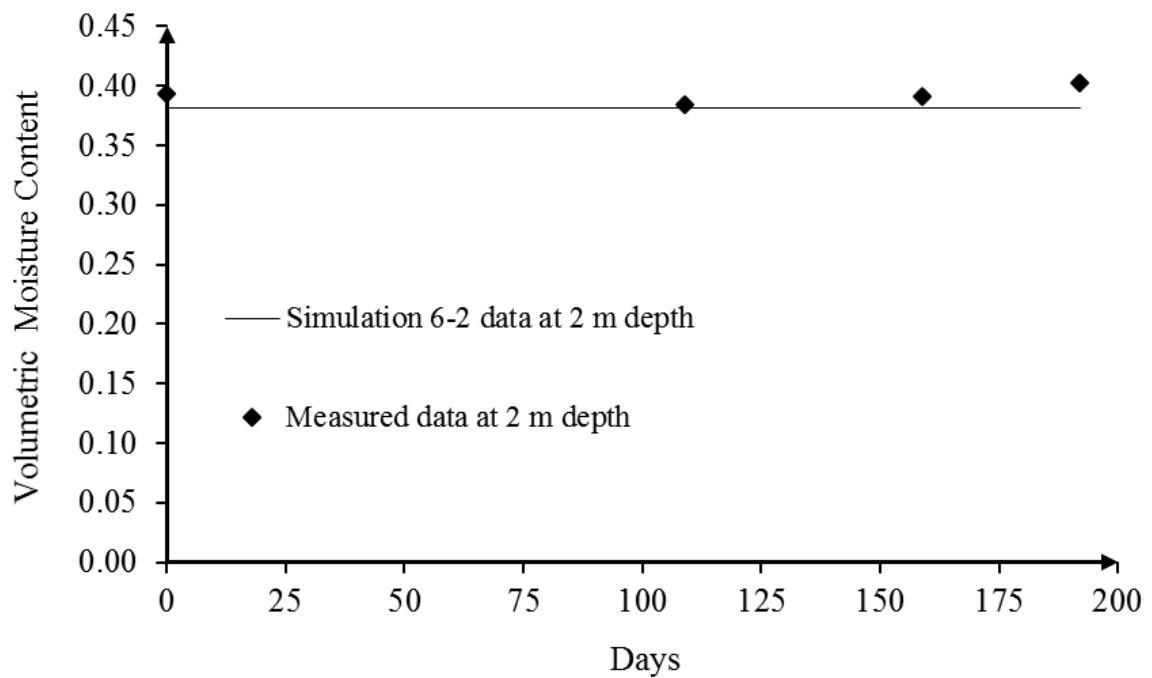


Figure 6. 36    Simulated and Measured Transient Moisture Content Variation in Simulation 6-2 (Depth 2 m, Radial Distance 4.9 m)

Figure 6.37, 6.38 and 6.39 show results from Simulation 6-3 with three simulated moisture profiles at a distance of 1.4 m from the tree (time at 109, 159 and 192 days) when using the three different transpiration rates presented. The maximum and minimum moisture profiles are shown in these figures when comparing the results of Simulation 6-1 based on the initial assumptions with transpiration rate from measured data. These results provide an overall indication of the sensitivity of transpiration rate on the simulation and demonstrate that the transpiration rate (28 L/day) calculated based on the measured data is reasonable and acceptable.
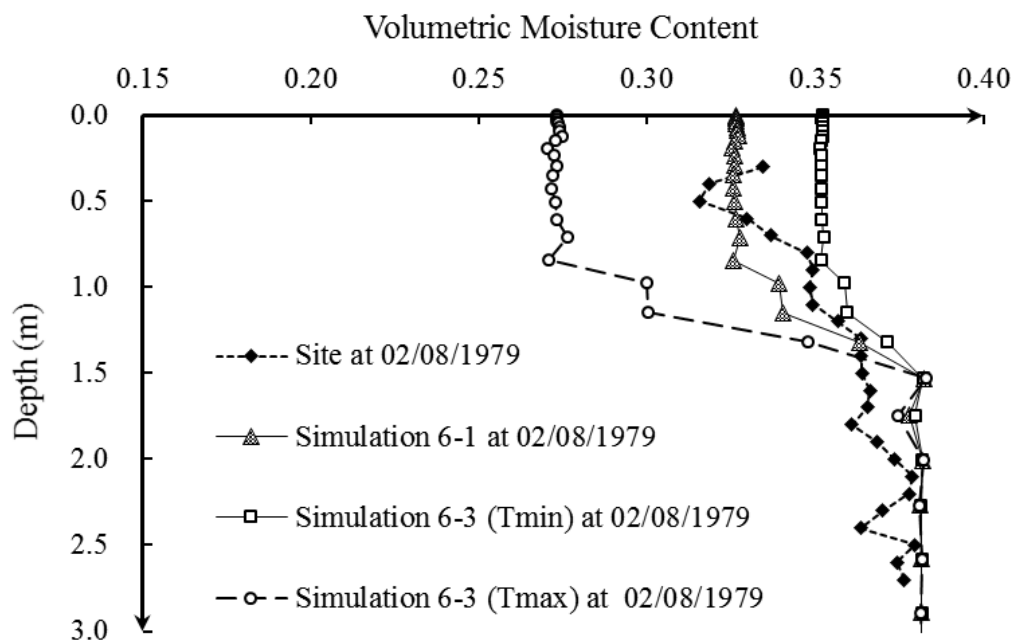


Figure 6. 37    Simulated and Measured Moisture Content Profiles in Simulation 6-3 (Time on 02/08/1979, Radial Distance 1.4 m)
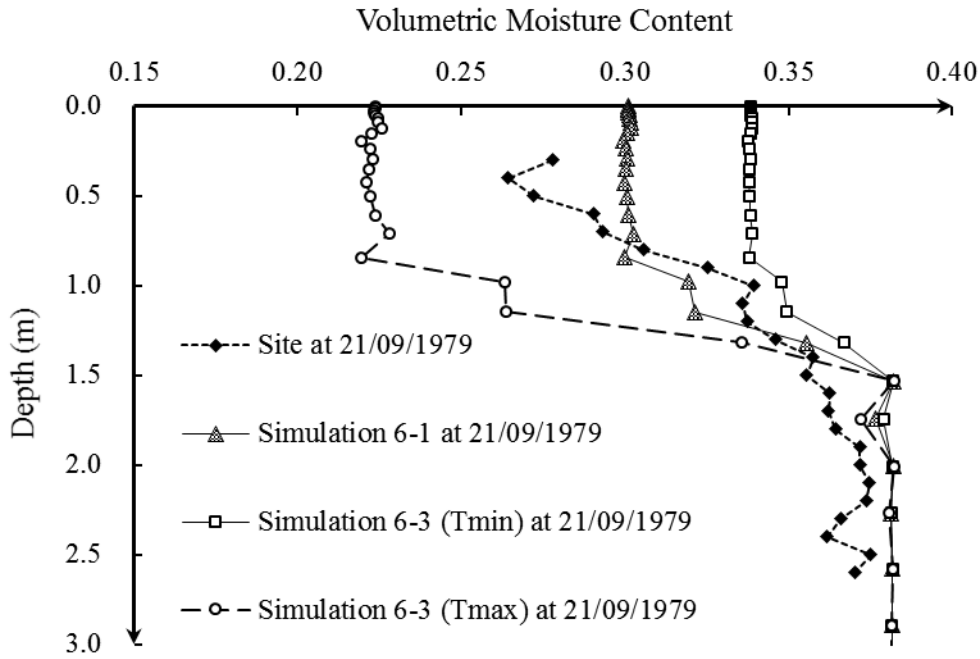
Figure 6. 38    Simulated and Measured Moisture Content Profiles in Simulation 6-3

(Time on 21/09/1979, Radial Distance 1.4 m)
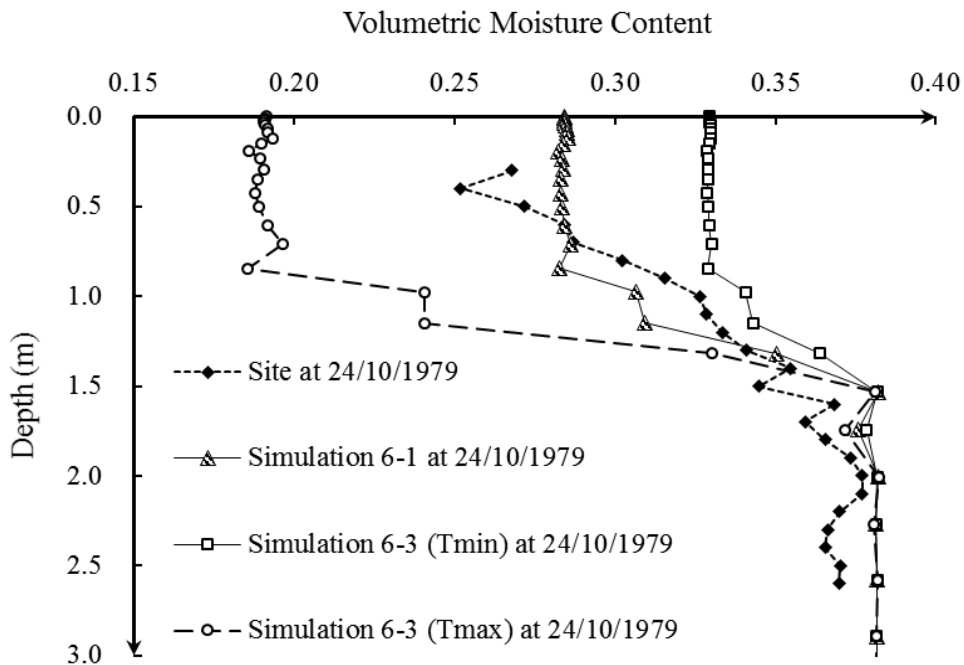


Figure 6. 39    Simulated and Measured Moisture Content Profiles in Simulation 6-3

(Time on 24/10/1979, Radial Distance 1.4 m)

Figures 6.40 to 6.42 present results from Simulation 6-4 which assumes a linear distribution of water extraction rates with both depth and radius after Rees and Ali (2006), for comparison results from Simulation 6-1 are also shown. One apparent disadvantage of the linear model is that the resulting soil moisture content pattern generated can be unrealistically 'linearized'. In the work presented here, Simulation 6-1 is implemented using the new proposed approach. By contrast, it can be seen that the simulated results from the image-based root density approach achieve better quality than the results by the linear approach (Simulation 6-4). In general, good agreement between simulated and measured profiles is achieved by image-based root density approach indicating that this root pattern is closer to the actual field conditions.

The quality of the results achieved is inevitably dependent on the available data about the soil hydraulic properties and the root information employed in the simulation. Overall, the new approach adopted appears capable of providing a reasonable prediction of water uptake in the vicinity of a mature tree. However, it is also recognized that further refinement of the initial and boundary conditions employed may be necessary in practice.
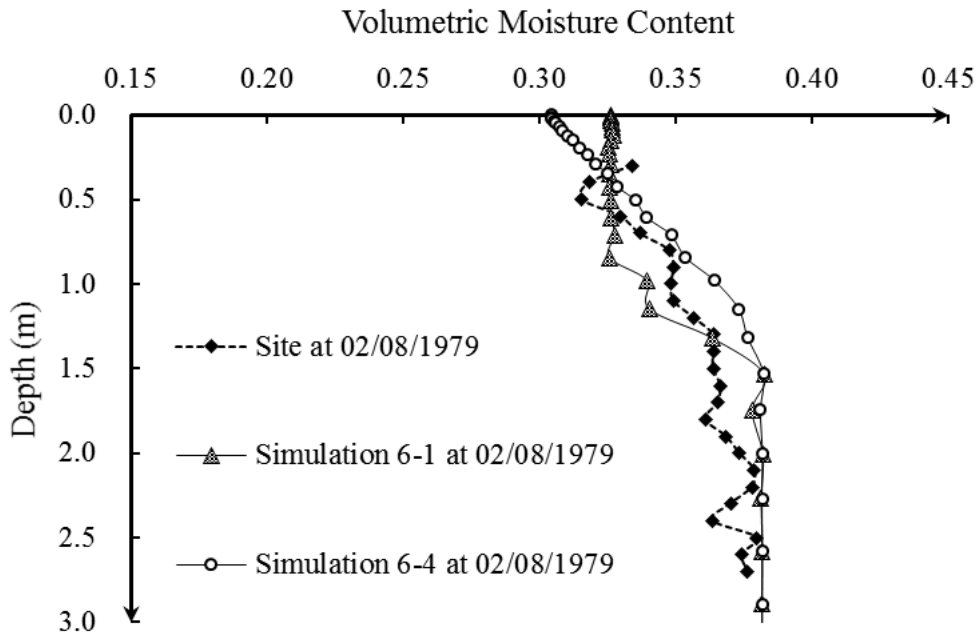
Figure 6. 40    Simulated and Measured Moisture Content Profiles in Simulation 6-4

(Time on 02/08/1979, Radial Distance 1.4 m)
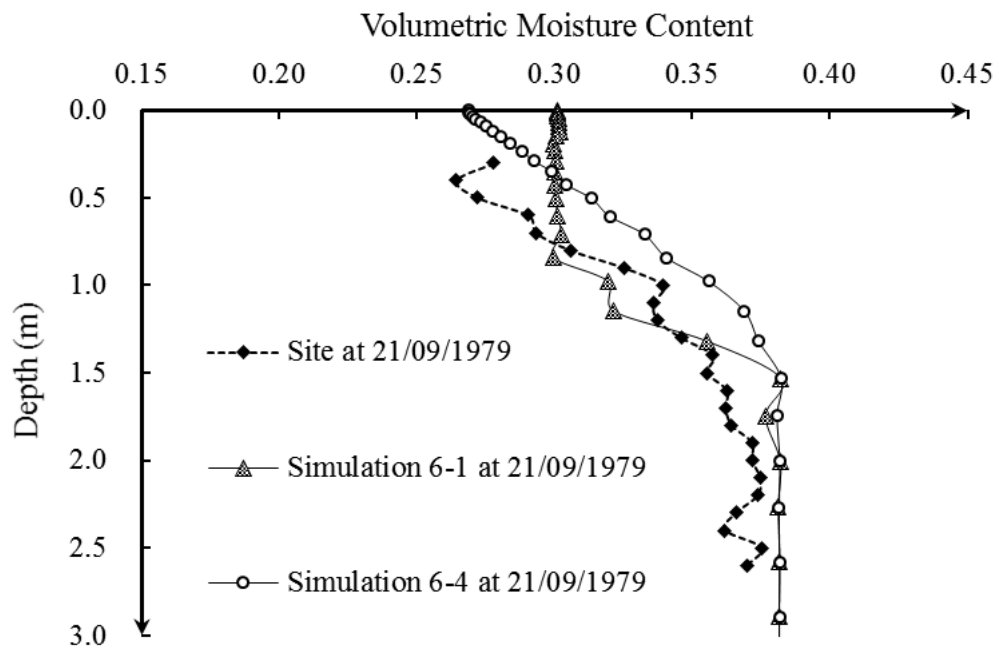


Figure 6. 41    Simulated and Measured Moisture Content Profiles in Simulation 6-4

(Time on 21/09/1979, Radial Distance 1.4 m)
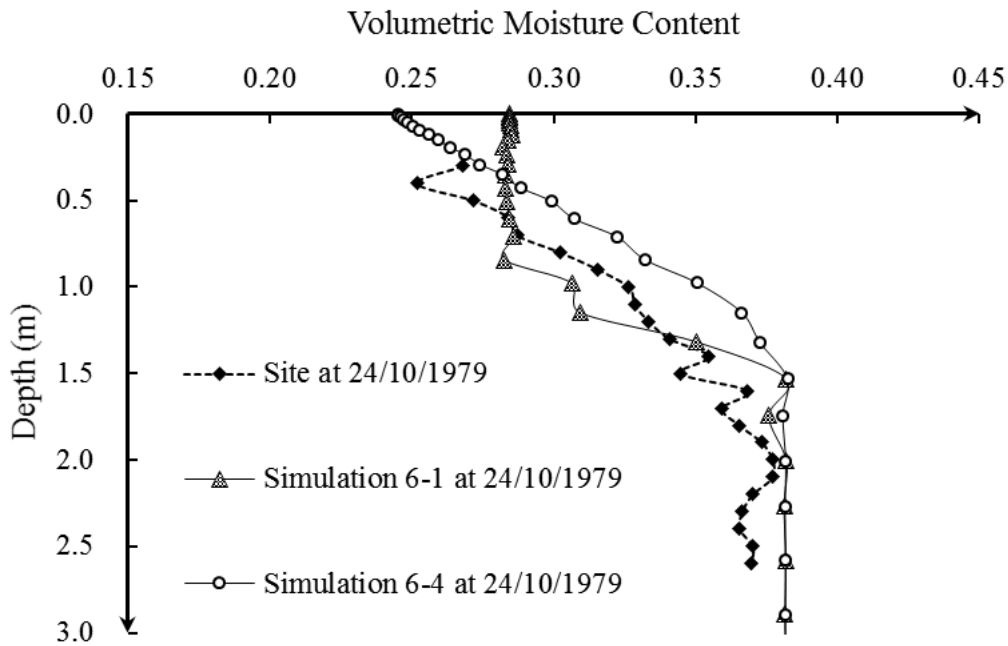
Figure 6. 42    Simulated and Measured Moisture Content Profiles in Simulation 6-4 (Time on 24/10/1979, Radial Distance 1.4 m)

## 6.3    CASE 2: MATURE ALMOND TREE ON SHALLOW GRAVELY LOAM

### 6.3.1    Site Description

The experimental site is located in an almond orchard located 90 km north of Davis, California, in the Sacramento Valley and covers about one quarter of an area wetted by a microsprinkler irrigating a single a 6-year-old almond tree (Koumanov et al. 1997). In the $2.0 \cdot \times 2.0$ m$^2$ monitored area, 25 polyvinyl chloride neutron probe access tubes (diameter 50 mm) were installed in a square grid with a 0.5 m spacing, to a depth of 0.9 m (Figure 6.43). Soil water content was measured at the depth of 0.15, 0.30, 0.45, 0.60, 0.75 and 0.90 m during and after access tube installation. The measurements were carried out from 13 September through 29 September in the

summer of 1995.  The measured soil moisture profile after irrigation, 13th September 1995, was used to define initial condition for the numerical simulations.  The soil surface was maintained free of weeds by periodic herbicide treatment.  The soil of the experimental site had not been tilled since tree planting in 1990 and the surface terrain is irregular and slightly undulated (Koumanov et al. 2006).  The shallow soil contains substantial gravel which, in combination with the high sand content, results in a low water holding capacity (Koumanov et al. 1997).  Additional information on the reported soil layers is presented in Table 6.4.
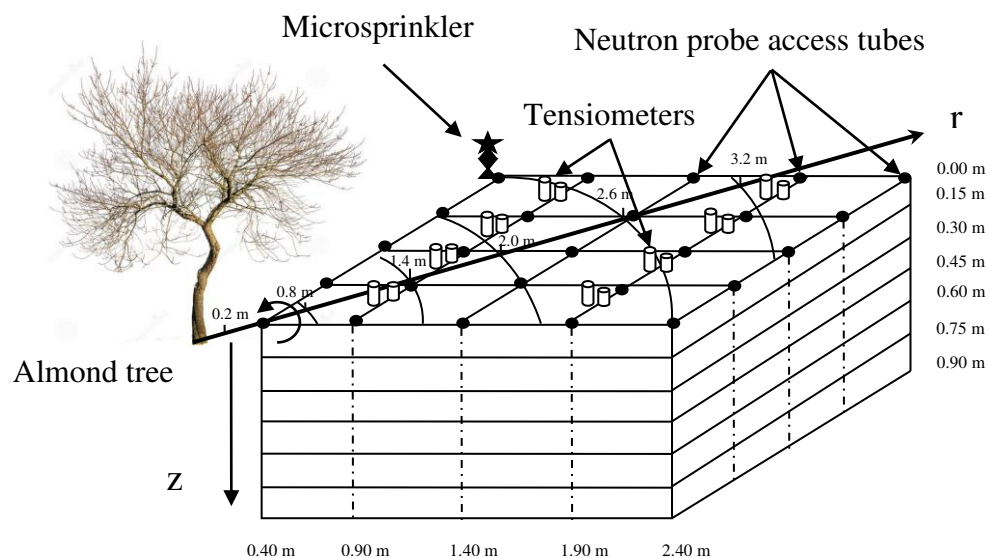


Figure 6. 43    Schematic view of the experimental plot, figure re-drafted after Koumanov et al. (1997) and Vrugt et al. (2001)

The micro-sprinkler system was used to wet the experimental site on 13th September, after which the irrigation was cut off.  From 13th September to 29th September 1995, soil water depletion was monitored during a 16-day period with no irrigation. Neutron probe and tensiometer readings were taken immediately after irrigation at

13:00, 15:00, and 18:00 o'clock on 13th September, then every four hours daily (at 6:00, 10:00, 14:00, and 18:00 o'clock) from 14th September to 17th September, and only one time daily at about 10:00 o'clock from 18th September to 29th September. Therefore, the total observation time is 381 hours.

Table 6. 4    Particle size distribution, bulk density, field capacity, and volumetric gravel content of the various soil layers (adapted from Koumanov et al. 2006)

| Depth (cm) | Soil texture (%, by weight) | | | Volumetric gravel content ($m^3 m^{-3}$) | Bulk density ($kg m^{-3}$) | Soil moisture at field capacity ($m^3 m^{-3}$) |
|---|---|---|---|---|---|---|
| | Sand | Silt | Clay | | | |
| 15 | | | | 0.25 | 1598 | 0.196 |
| 30 | 53.0 | 41.0 | 6.0 | 0.29 | 1610 | 0.185 |
| 45 | | | | 0.29 | 1646 | 0.214 |
| 60 | 58.0 | 32.5 | 9.5 | 0.40 | 1738 | 0.252 |
| 75 | | | | 0.31 | 1807 | 0.272 |
| 90 | 67.0 | 25.0 | 8.0 | 0.30 | 1790 | 0.229 |

6.3.2   Almond Trees

The almond tree (*Prunus amygdalus*) is a deciduous tree, growing 4 to 10 m in height, with a trunk of up to 30 cm in diameter (Micke 1996).  The almond tree can grow almonds after about three years after planting and after about 6 years the tree is mature.  The almond tree starts to bloom between late February and early March.  The harvest time of an almond tree is typically from mid-August through October.  In a cultivated orchard the tree canopies typically covers 60 % of the soil surface, determined by the average area of 30 tree crown vertical projections (Koumanov et al. 2006).

Figure 6. 44    Almond Orchard, figure reproduce from Mullins (2014)

The California Department of Food and Agriculture reports the almond acreage of California is approximately 940,000 acres in 2013 (California Department of Food and Agriculture 2014).  California is the world's largest producer of almonds since 80% of the world's almonds supplies are produced in this area and exporting to nearly 90 countries (Wilkinson 2005; Wells 2013).  Although almond trees prefer hot and dry areas with abundant sunshine, cropping is limited without irrigation. Therefore, most almond producers in California apply irrigation (including furrow irrigation, solid-set sprinklers, micro-sprinklers, and drip irrigation) throughout the growing season (Wells 2013).  Wells (2013) states that the applied water for irrigation of almond trees per year is approximately 10,000-20,000 $m^3$/ha and which is determined by precipitation, evapotranspiration, soil and tree conditions.

Micke (1996) states lateral roots of almond trees may extend to 4 metres in coarse-textured, well-drained soil.  Often 75 % or more of the roots are in the upper soil and

lateral roots extension can tends to be greater in coarse sandy soils than in fine-textured ones (Micke 1996).  The depth of the roots for almond tree may exceed 1.5 to 2.0 m and lateral expansion 2.5 to 4.0 m even when water is applied by drip irrigation (Ben-Asher et al. 1994).

### 6.3.3   Hydraulic Properties of Shallow Gravely Loam

The soil at the experimental site is a shallow gravely loam (Andreu et al. 1997). Figure 6.45 and 6.46 show measured data (volumetric water content/capillary potential) using the multistep outflow method from soil cores taken at a 30 cm depth at a nearby location, and (volumetric water content/hydraulic conductivity) points as obtained using the instantaneous profile method at a nearby location at the 30 cm soil depth (Andreu et al. 1997).  Equations (3.1) and (3.2) have been fitted to this data to yield the water retention curve and the hydraulic conductivity relationship for Shallow Gravely Loam.   The values of $\theta_r$ and $\theta_s$ are approximated from the measured moisture profiles.  A summary of the relevant properties is shown in Table 6.5

Table 6. 5      Assumed soil properties for Shallow Gravely Loam

| Soil Type | $\theta_r$ (cm³/cm³) | $\theta_s$ (cm³/cm³) | $\alpha$ (1/cm) | $n$ | $K_s$ (cm/s) | $l$ | $m$ |
|---|---|---|---|---|---|---|---|
| Shallow gravely loam | 0.05 | 0.3 | 0.094 | 1.99 | 0.00039444 | 3 | 0.4975 |
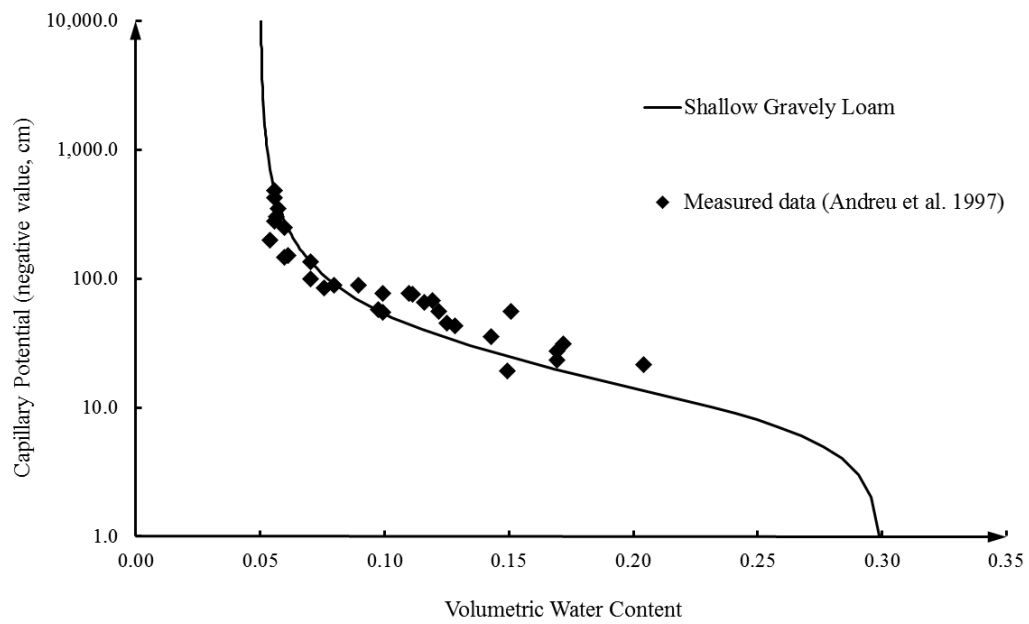
Figure 6. 45    Soil Water Retention Curve for Shallow Gravely Loam (plotted on a

log scale of capillary potential)
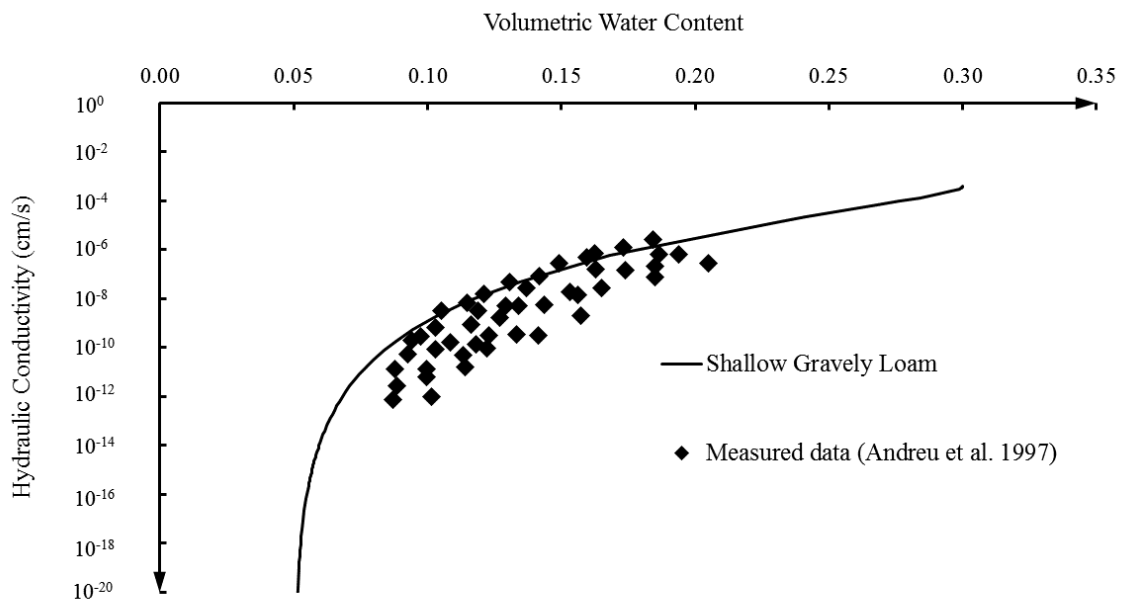


Figure 6. 46    Hydraulic Conductivity Curve for Shallow Gravely Loam (plotted on a

log scale of hydraulic conductivity)

It is noted that when considering this soil Vrugt (2001) fixed the residual water content to zero since some of the measured water content values were smaller than the residual water content values reported by Andreu et al. (1997). However, in this study, the parameters presented in Table 6.5 have been fitted the experimental data - although it may well be having a negative influence on the match between simulated and measured results, this is more appropriate and reasonable than assuming a zero residual water content.

### 6.3.4   Numerical Simulation

For validation of their root water uptake model, Vrugt et al. (2001) transformed the 3-D grid measurements of water content to a 2-D axi-symmetric (r and z) domain. For this Vrugt et al. (2001) assumed that:

- The water uptake by root around the almond tree was axi-symmetrical.
- The measurement volume of neutron probe water content was a sphere (a constant radius of 0.25 m).

Firstly, the rectangular measurement was partitioned into five adjacent 0.6 m wide concentric circular soil strips (Figure 6.43). Secondly, a radial average value of water content was calculated by using weighing factors for each of the five soil areas (0.2-0.8 m, 0.8-1.4 m, 1.4-2.0 m, 2.0-2.6 m, and 2.6-3.2 m). Vrugt et al. (2001) employed 0.6 m wide strips to ensure that enough water content measurements were contained within each of the five soil areas. Therefore, the final 2-D map included 20 average

water content values (four depth intervals: 0 to 0.15 m, 0.15 to 0.3 m, 0.3 to 0.45 m, and 0.45 to 0.6 m; five radial distance increments) at each measurement time during simulated period (Vrugt et al. 2001).
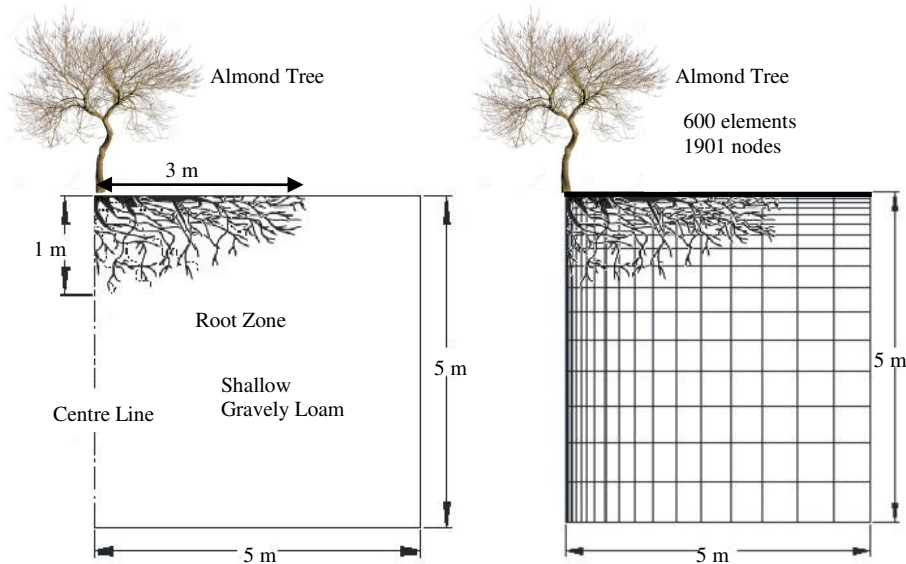


Figure 6. 47    Axi-symmetric Domain and Finite Element Mesh

Based on the field observations provided by Vrugt et al. (2001), the root zone is assumed to extend a depth of 1.0 m and a radial distance of 3.0 m.  Figure 6.47 shows a diagrammatic representation of the tree, the extent of the root zone and the domain size employed.  A similar finite element mesh as used in Case 1 is employed here (see Figure 6.47).  The overall size of the finite element domain is 5 m × 5 m.  The mesh analysed consisted of six hundred, eight-node isoparametric elements with 1901 nodes.  Once again, preliminary numerical tests were conducted to ensure for this domain size, the outer boundaries do not significantly influence the simulated results within the region of interest.  The simulation employs a time-step size of 3600 seconds, which was held constant for the entire period considered.   Again,

preliminary checks were made to ensure that the solution is both time-step and spatially converged. For the reason explained in the Lime Tree case study, the pressure head dependent reduction factor $\alpha(\psi)$ was assumed constant at a value of 1.0.

Almond tree potential evapotranspiration was determined by an appropriate crop coefficient ($K_c = 0.91$) and daily reference evapotranspiration data ($ET_0$) (Snyder and Pruitt 1989, Vrugt et al. 2001). The daily reference evapotranspiration was provided by a nearby weather station of the California Irrigation Management Information System (CIMIS) (Vrugt et al. 2001). Vrugt et al. (2001) employed Ritchie's (1972) equation to estimate soil evaporation ($E_s$). The potential transpiration of almond tree ($T_p$) was obtained by subtracting soil evaporation from almond potential evapotranspiration (Equation 6.1).
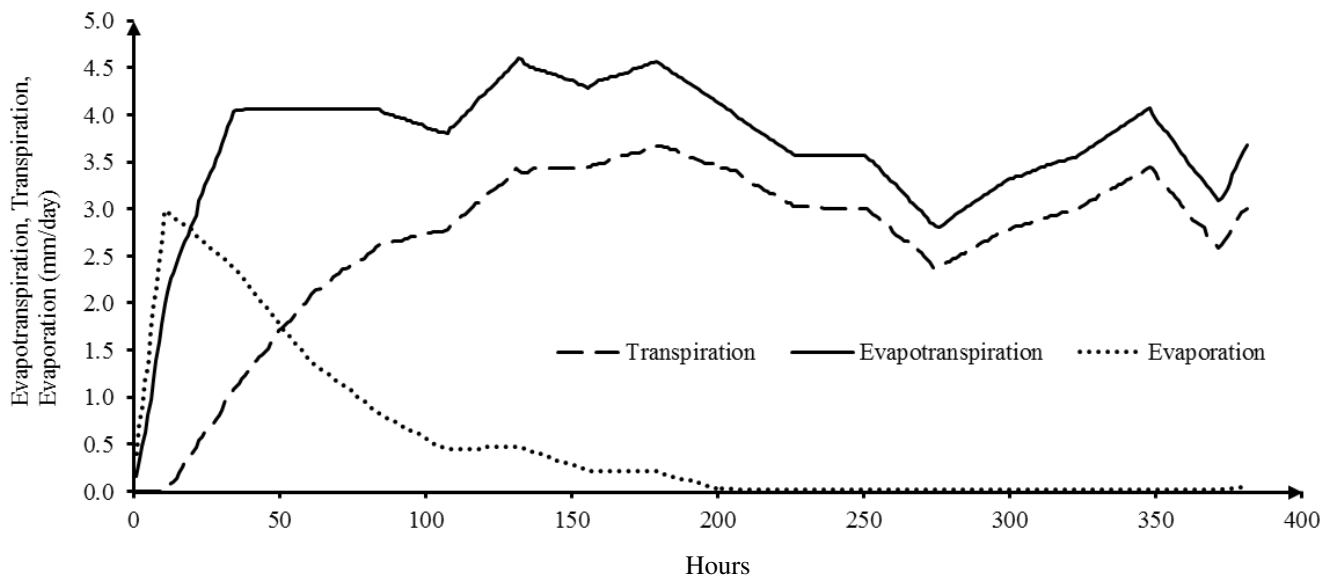


Figure 6. 48 Daily evapotranspiration, evaporation and transpiration for Almond tree (Time 0 corresponds with 13th September 1995), figure re-drafted from Vrugt et al. (2001)

$$T_p = K_c ET_0 - E_s \tag{6.1}$$

Figure 6.48 presents the variation of evapotranspiration and its components, evaporation and transpiration for almond tree throughout the simulated period (from 13th September 1995 to 29th September 1995). The almond tree transpiration is used as the sink term in the numerical model and the soil evaporation is used as the boundary condition at the ground surface. Since no irrigation or rainfall was observed during the experimental period a flux (0.0.53 mm/day) boundary condition is applied at the surface representing soil evaporation. In this study, the simulation employed a time dependent varying transpiration rate throughout the entire simulated period.

The initial conditions employed for the simulation were based on the measured moisture content profile for the start date of the period considered. However, the profile of the start date (at 13:00 on 13th September 1995) lacks enough measured data to define initial conditions for the whole simulated domain. Therefore, a uniform initial value of capillary potential of -12.88 cm (the average value of the measured soil moisture profile at 13:00 on 13th September 1995) was applied throughout the domain, representing an initial volumetric water content of 20.97 % - this corresponds to a degree of saturation of approximately 69.89 %. Due to the lack of flux information, a unit hydraulic gradient as the lower boundary condition (gravity flow) is assumed. The simulated period covered 381 hours (13th September 1995 to 29th September 1995).

Figure 6. 49    A sketch of root system of a mature almond tree, figure reproduced from Micke (1996)
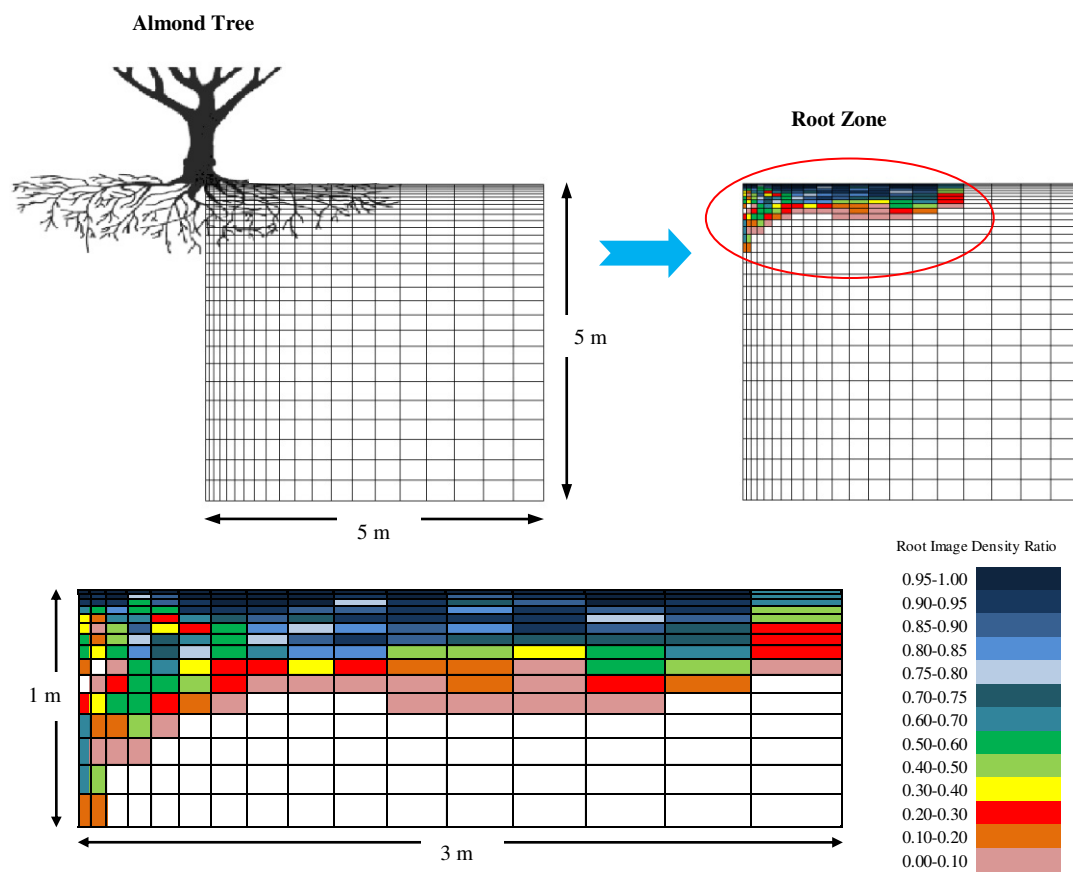


Figure 6. 50    A process diagram of root density based on a graphical (or photographic) representation of the actual root morphology

Figure 6.49 shows a simple graphical representation of a typical mature almond tree root system at depth of 1.0 m below ground and a radial distance of 3.0 m as presented by Micke (1996). This was considered in the simulation utilizing the new graphically based root density distribution approach. The real root system of a mature almond tree and a process diagram of root density based on a graphical (or photographic) representation of the actual root morphology are presented in Figure 6.50.

6.3.5   Simulation Results

Figure 6.51 shows the initial measured moisture content alongside the uniform numerical initial condition. Figures 6.52 to 6.56 show the simulated and measured moisture content profiles at a radial distance of 0.55 m, 1.1 m, 1.7 m, 2.3 m and 2.9 m from the centre-line of the almond tree for the time of 381 hours (at 10:00 o'clock on the 29th September 1995). Although field data were only available at specific depths of 0.075 m, 0.225 m, 0.375 m and 0.525 m respectively, the simulation can serve to display the overall behaviour at this site. The results plotted in terms of moisture content versus time are presented from Figure 6.57 to Figure 6.73. The simulated contours of volumetric moisture content generated at the middle of simulation (189 hours) and end of simulation (381 hours) are shown from Figure 6.74 and Figure 6.75. These from are considered in below.

Firstly, considering the simulated moisture content profiles it can be seen that the sink term is active within the depth of the root zone (i.e. the upper 1 m of the soil profile,

mainly at the upper 0.4 m of the soil profile) and to a radial extent of 3 m (as described previously). It is clear that the moisture extraction profile is roughly matching the root distribution of almond tree (as expected by definition). The figures indicate that a reasonable agreement between the simulated results and the measured moisture profiles has been achieved. Although the new model may not distribute moisture in exactly same manner as observed in the field, the level accuracy generated by application of an image based root-density approach appears acceptable for application over a considerable time period. Figures 6.52 to 6.56 show the corresponding set of results achieved remote from the tree. It can be seen that the majority of water is extracted from within the root zone itself and the majority of the moisture extraction has occurred near the surface – corresponding to the region of highest root density. In the Figure 6.53, the simulated results at the depth of 0.525 m provide a relatively poor match with the measured data - in this case the initial simulated data is underestimated. Further study is needed to explore non-uniform initial data over the whole domain. Moreover, the present model is assumed to be axisymmetric. However, the root water-uptake model is based on only one cross-section, whereas in reality the soil water extraction rate could be caused by a non-uniform root system. In general, a good agreement between simulated and measured profiles is also achieved in the root zone.

Figures 6.57 to 6.73 present the results plotted in terms of moisture content versus time, at depths 0.075 m, 0.225 m, 0.375 m and 0.525 m below the surface and at a radial distance of 0.55 m, 1.1 m, 1.7 m 2.3 m and 2.9 m from the almond tree. The measured data is simply plotted as discrete data points at the times when measurements were recorded on site. Numerical results can be output at any number

of time intervals hence a continuous variation has been plotted for comparison. It is clear that the most of extraction of soil water occurred at the depth of 0.075 m and 0.225 m during 381 hours. Below the soil surface at a depth of 0.075 m, details of the simulated moisture content variation achieved remote from the tree during the simulated period (381 hours) are shown in Figures 6.57, 6.61, 6.65 and 6.69. The soil moisture content at depth of 0.075 m reduced steadily with time until approximately 300 hours, after that relatively little moisture variation occurred due to the soil moisture decreased near to the residual soil water content. It can be seen that the rate of simulated soil water reduction was a little higher than that of measured moisture content depletion at the top layer of soil. Although it is acceptable that this study employed an average value of evaporation rate on the soil surface, a time varying flux on the surface boundary condition may be necessary to reflect conditions when evaporation is dominant in the process of evapotranspiration – perhaps in the first 50 hours in this case. According to the results achieved remote from the tree, it is clear that the soil moisture depletion takes place up to a radial distance of 2.3 m. This indicates that definition of the root system with a radial distance of 3.0 m in this simulation was a reasonable assumption. The results plotted in the figures indicate that relatively little moisture variation occurred at (and below) a depth of 0.525 m. The overall simulated trend appears to be in good agreement with the measured data. These results serve to show that the root depth and radial assumed in the simulation appears reasonable.

Figures 6.74 and 6.75 present the simulated contours of volumetric moisture content (%) generated by the simulation at 189 hours and 381 hours respectively. The Figure 6.75 presents the spatially distributed volumetric moisture content (%), as determined

over the 16-day monitoring period. Clearly, the zone of maximum root water uptake is concentrated in a top soil surface layer (0.25 m). These figures provide further demonstration that the new approach has produced an overall moisture pattern that is fundamentally determined by the assumed tree root morphology and density (see Figure 6.50).

The quality of the simulated results achieved is certainly dependent on the root data and the definition of the hydraulic properties employed. This study shows the proposed model appears capable of providing time varying rates of transpiration to predict soil water variation in the vicinity of a mature almond tree. However, it is also recognized that only one homogenous soil type and uniform initial soil moisture conditions were considered in the present study. Further exploration of a long term modelling, multi-dimensional water uptake by trees and more realistic representation of boundary conditions may be necessary in practice.
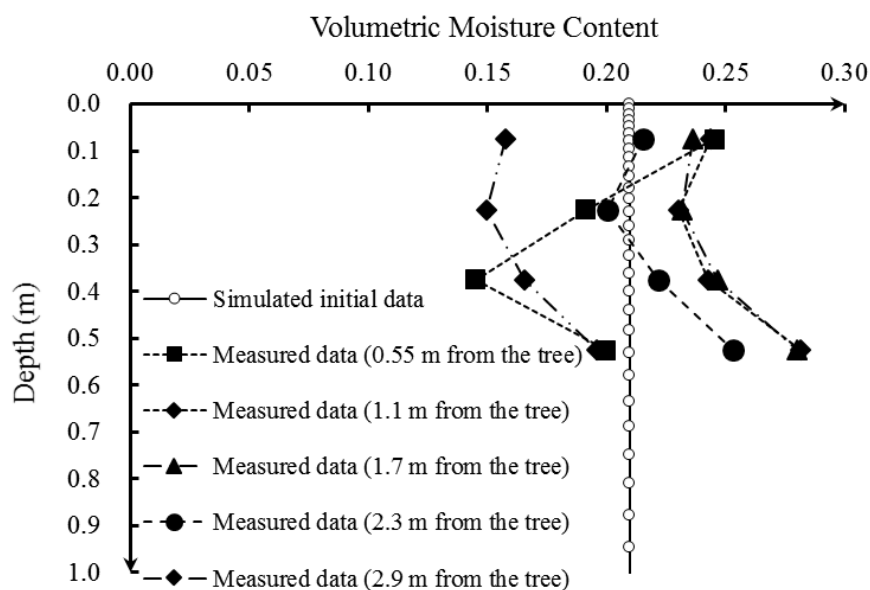


Figure 6. 51    Simulated and Measured Initial Moisture Content Profiles
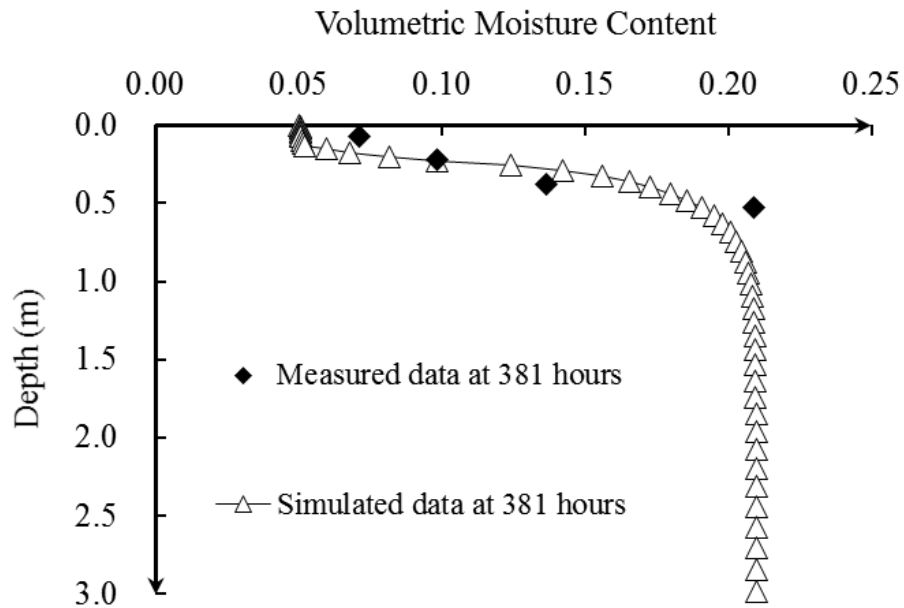
Figure 6. 52   Comparison of Simulated and Measured Moisture Content Profiles

(Time at 381 hours, Radial Distance: 0.55 m from the almond tree)
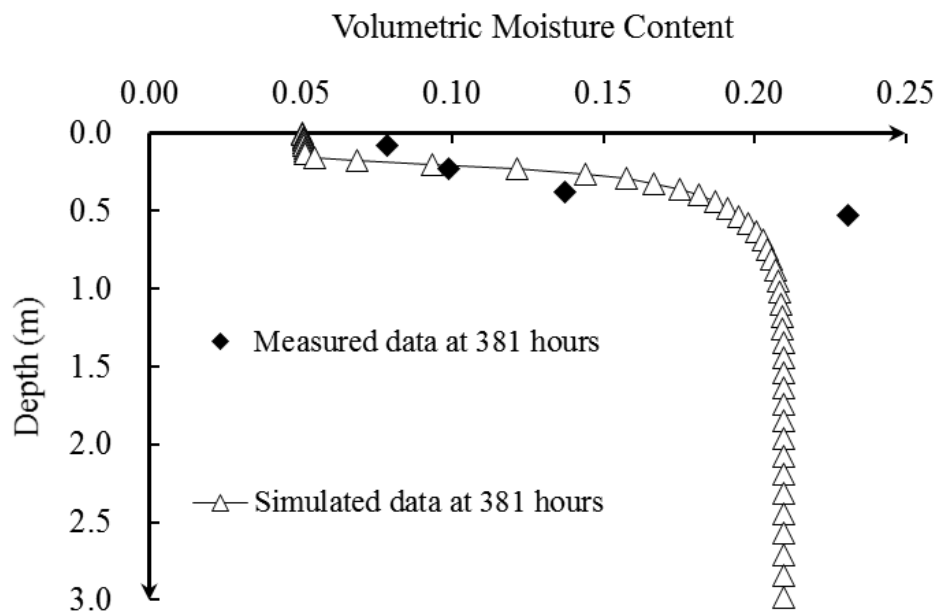


Figure 6. 53   Comparison of Simulated and Measured Moisture Content Profiles

(Time at 381 hours, Radial Distance: 1.1 m from the almond tree)
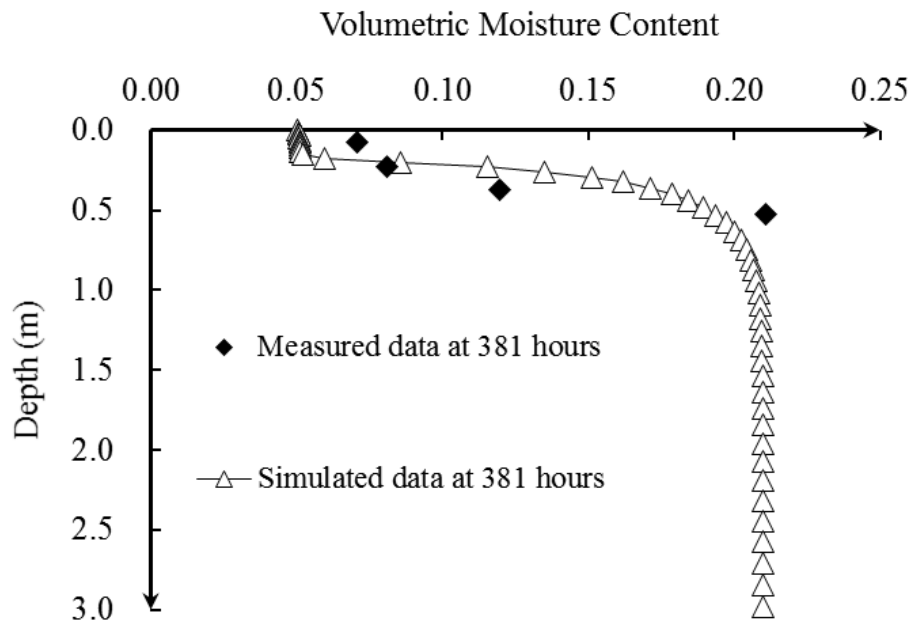
Figure 6. 54 Comparison of Simulated and Measured Moisture Content Profiles (Time at 381 hours, Radial Distance: 1.7 m from the almond tree)
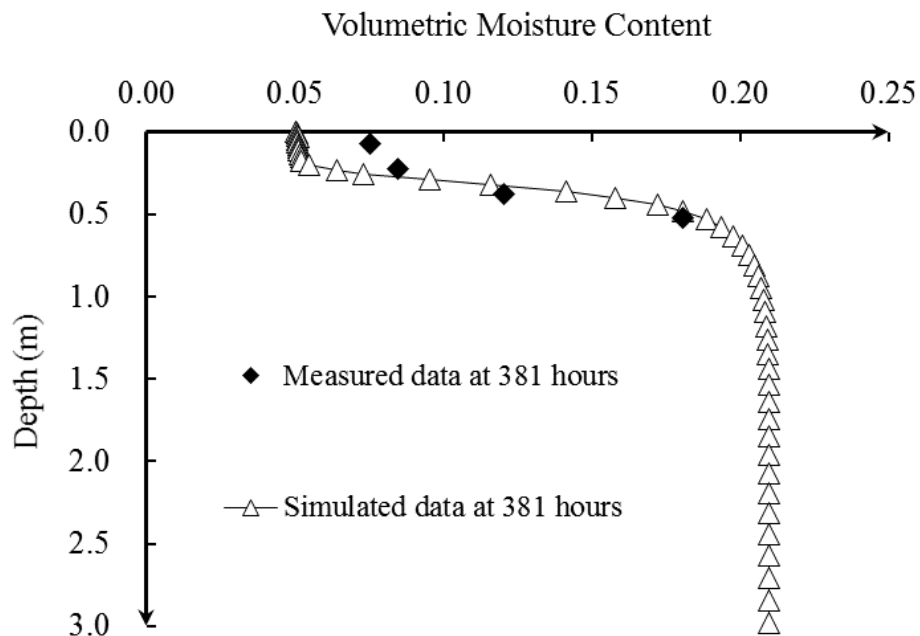


Figure 6. 55 Comparison of Simulated and Measured Moisture Content Profiles (Time at 381 hours, Radial Distance: 2.3 cm from the almond tree)
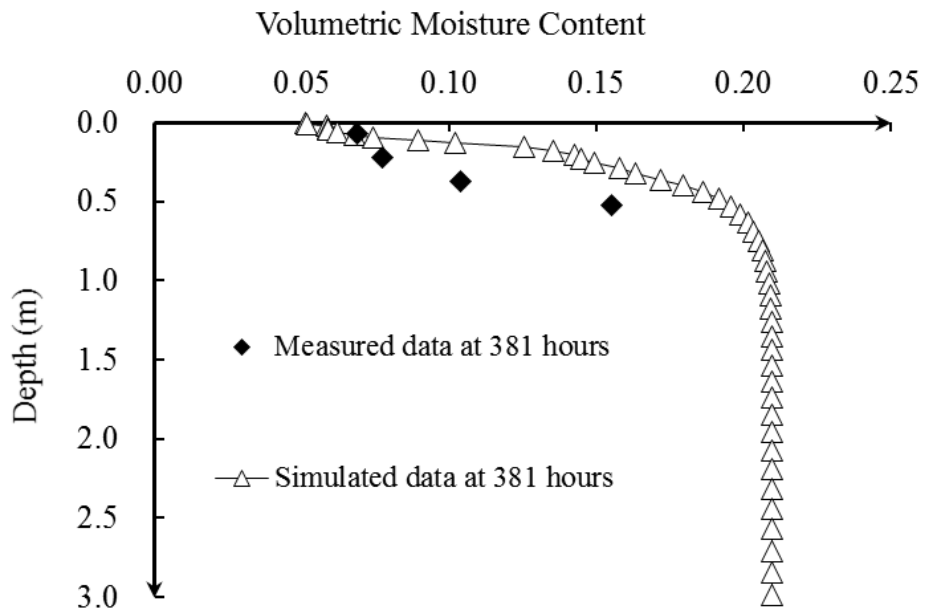
Figure 6. 56   Comparison of Simulated and Measured Moisture Content Profiles

(Time at 381 hours, Radial Distance: 2.9 m from the almond tree)
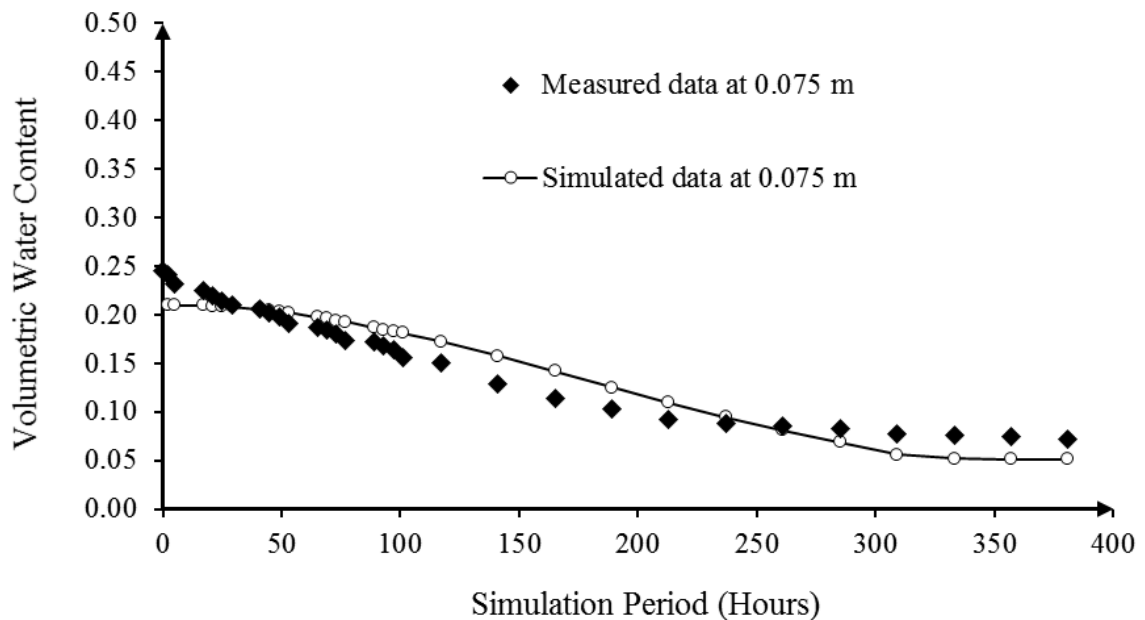


Figure 6. 57   Comparison of Simulated and Measured Transient Moisture Content

Variation (Depth: 0.075 m, Radial Distance: 0.55 m from the almond tree)
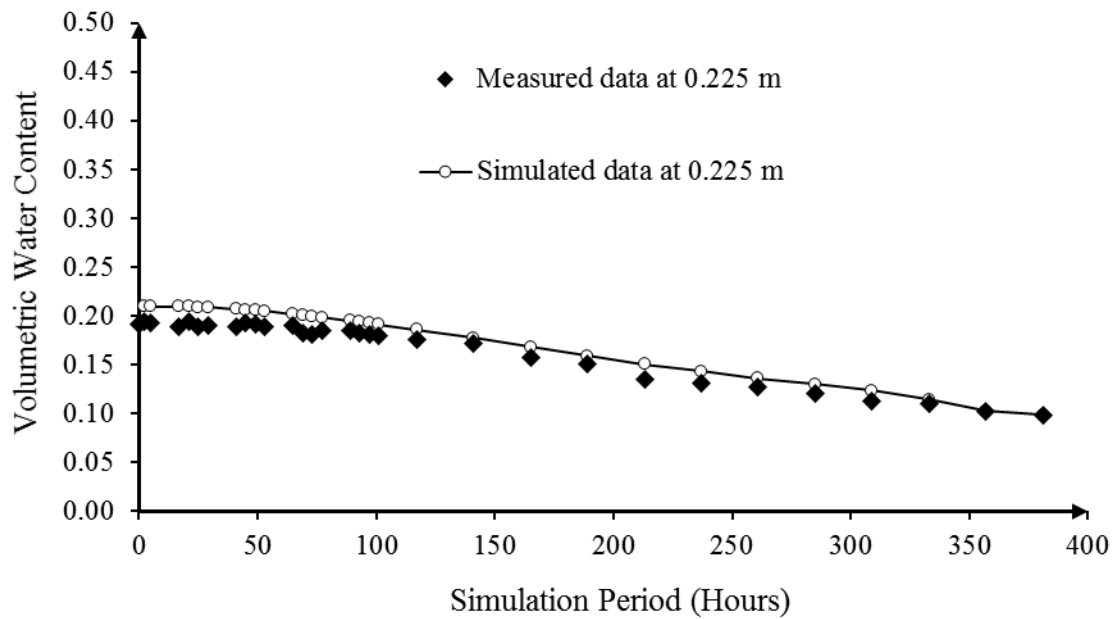
Figure 6. 58    Comparison of Simulated and Measured Transient Moisture Content

Variation (Depth: 0.225 m, Radial Distance: 0.55 m from the almond tree)
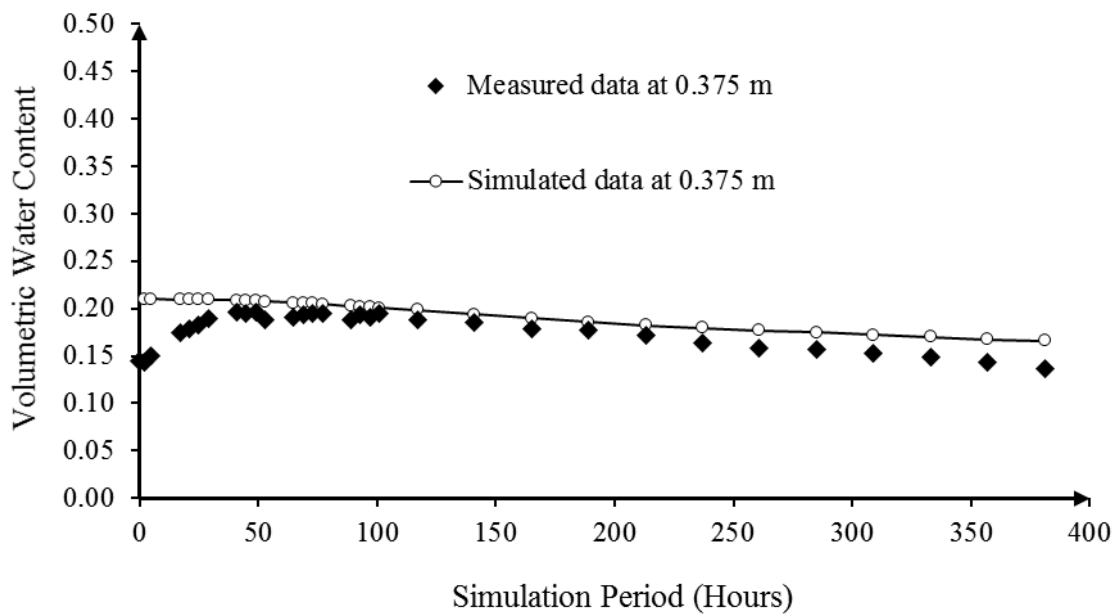


Figure 6. 59    Comparison of Simulated and Measured Transient Moisture Content

Variation (Depth: 0.375 m, Radial Distance: 0.55 m from the almond tree)
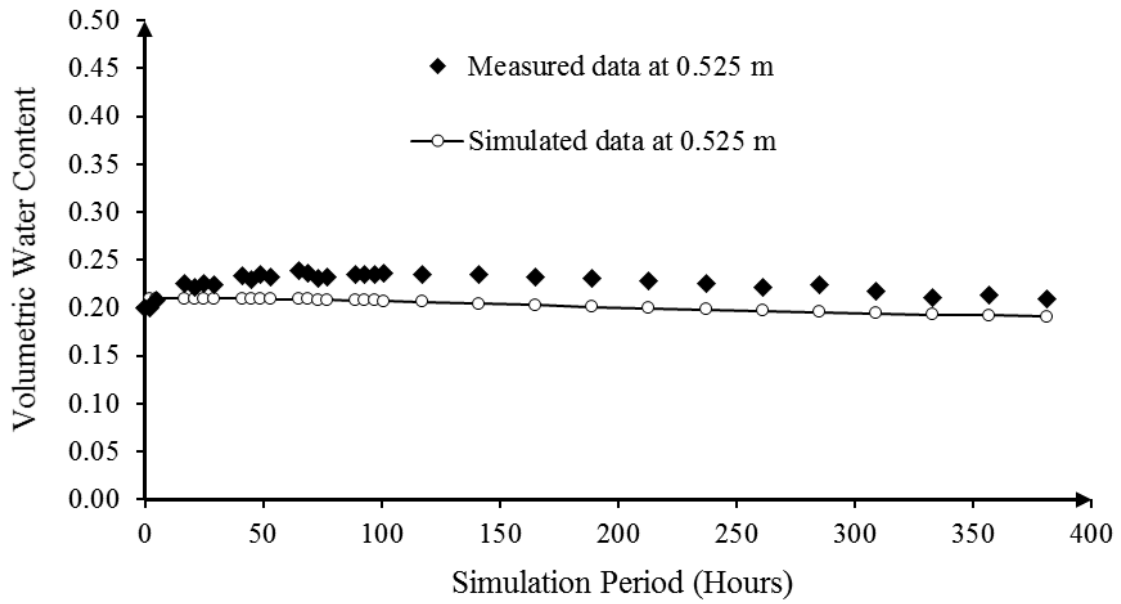
Figure 6. 60   Comparison of Simulated and Measured Transient Moisture Content

Variation (Depth: 0.525 m, Radial Distance: 0.55 m from the almond tree)
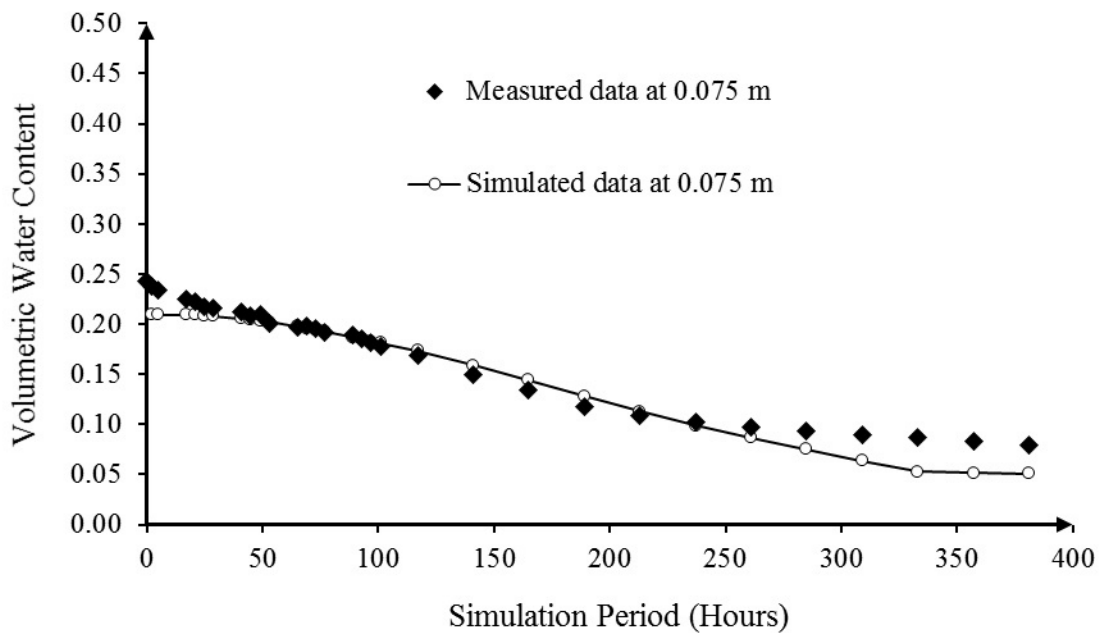


Figure 6. 61   Comparison of Simulated and Measured Transient Moisture Content

Variation (Depth: 0.075 m, Radial Distance: 1.1 m from the almond tree)
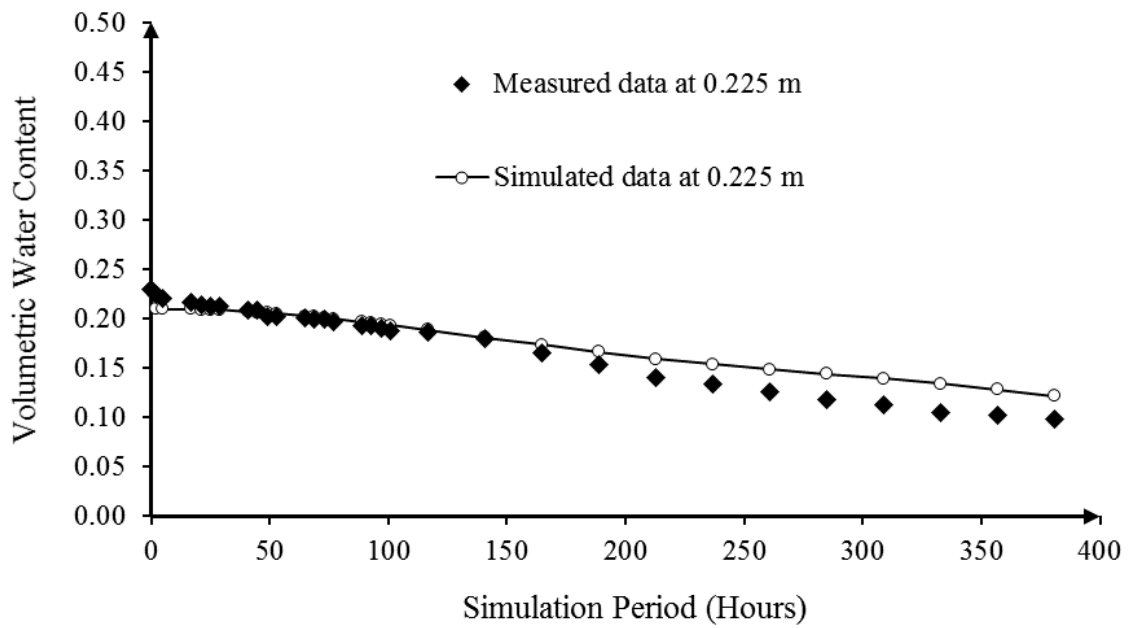
Figure 6. 62    Comparison of Simulated and Measured Transient Moisture Content

Variation (Depth: 0.225 m, Radial Distance: 1.1 m from the almond tree)
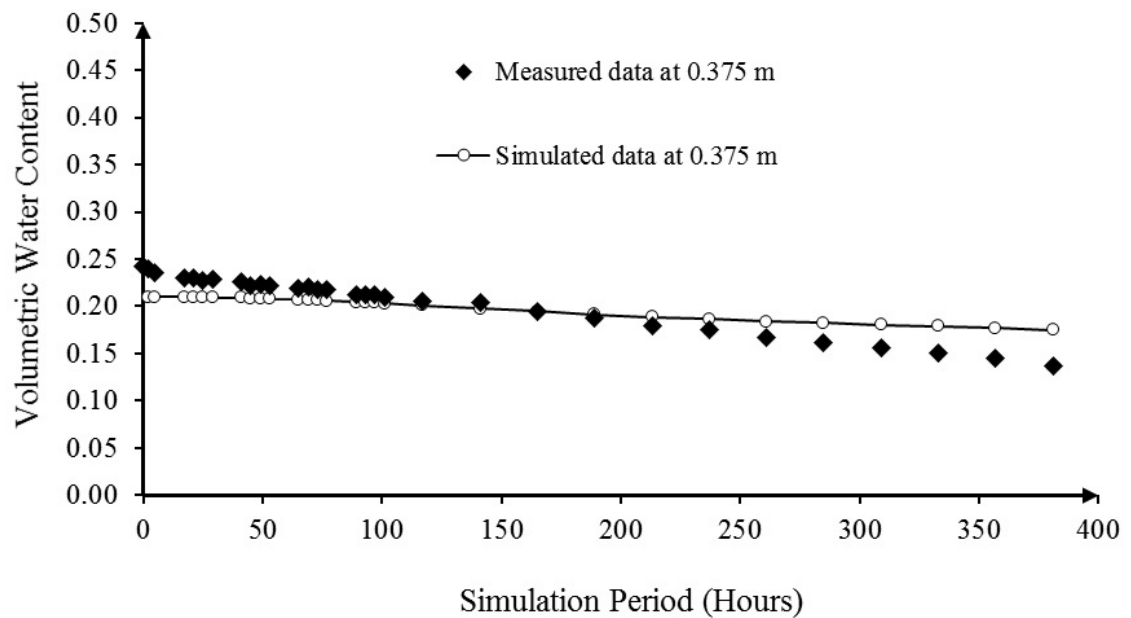


Figure 6. 63    Comparison of Simulated and Measured Transient Moisture Content

Variation (Depth: 0.375 m, Radial Distance: 1.1 m from the almond tree)
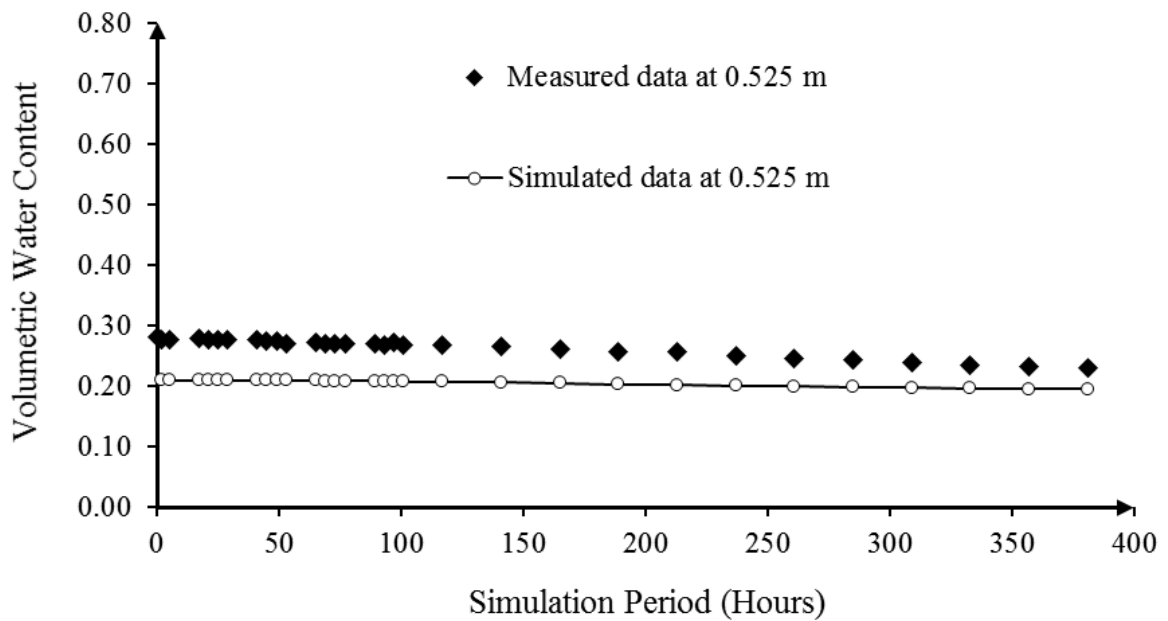
Figure 6. 64   Comparison of Simulated and Measured Transient Moisture Content

Variation (Depth: 0.525 m, Radial Distance: 1.1 m from the almond tree)
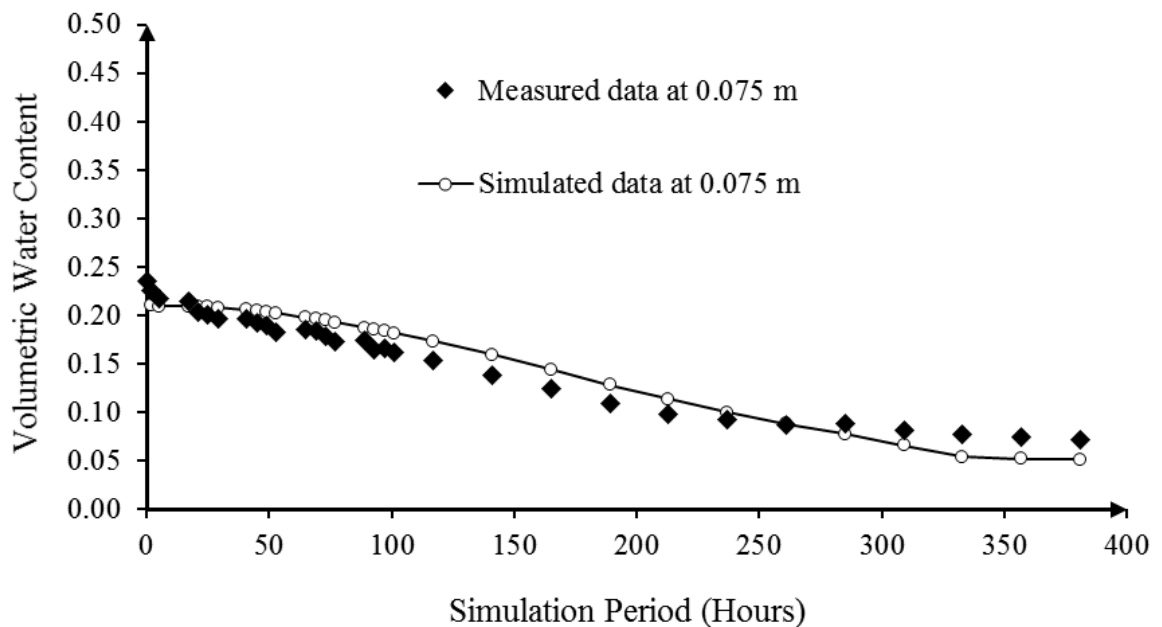


Figure 6. 65   Comparison of Simulated and Measured Transient Moisture Content

Variation (Depth: 0.075 m, Radial Distance: 1.7 m from the almond tree)
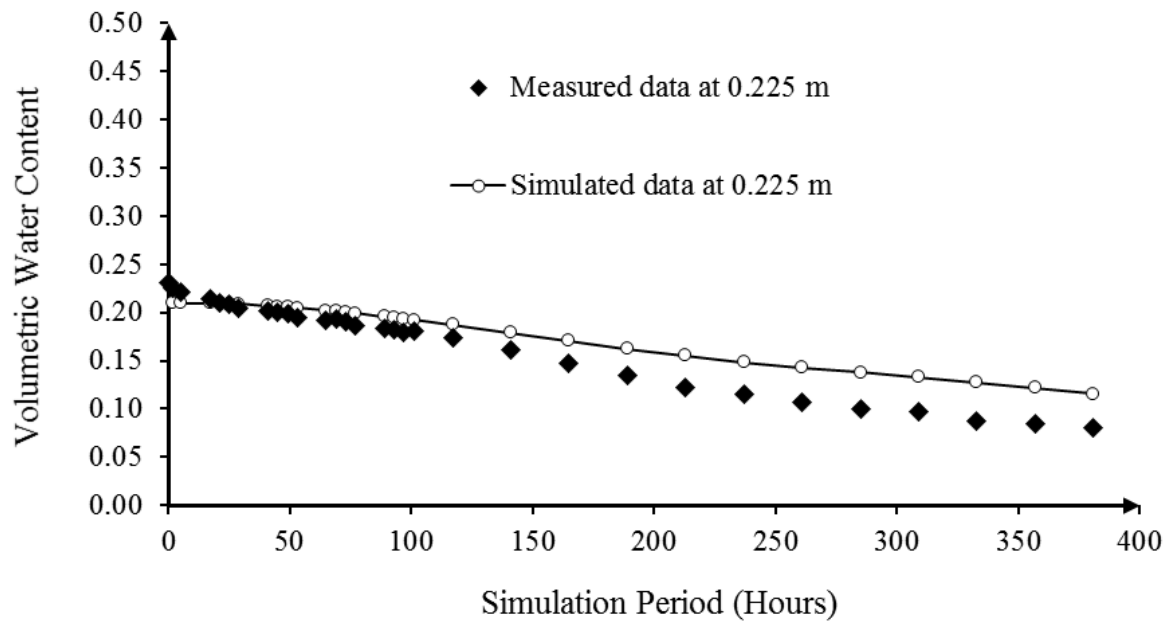
Figure 6. 66   Comparison of Simulated and Measured Transient Moisture Content

Variation (Depth: 0.225 m, Radial Distance: 1.7 m from the almond tree)
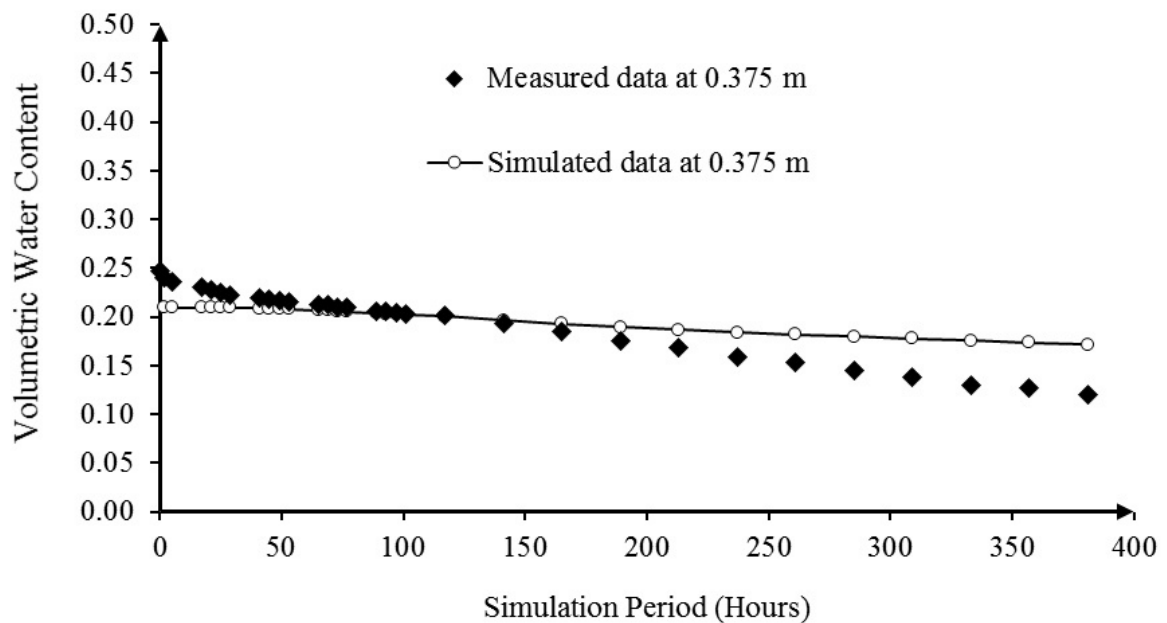


Figure 6. 67   Comparison of Simulated and Measured Transient Moisture Content

Variation (Depth: 0.375 m, Radial Distance: 1.7 m from the almond tree)
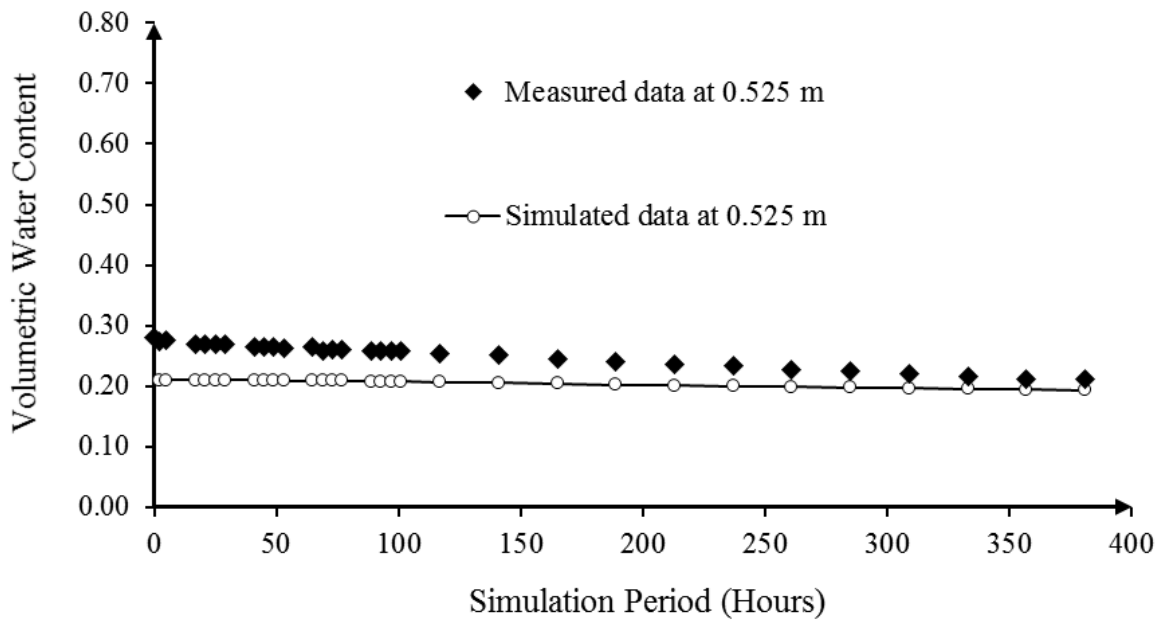
Figure 6. 68    Comparison of Simulated and Measured Transient Moisture Content

Variation (Depth: 0.525 m, Radial Distance: 1.7 m from the almond tree)
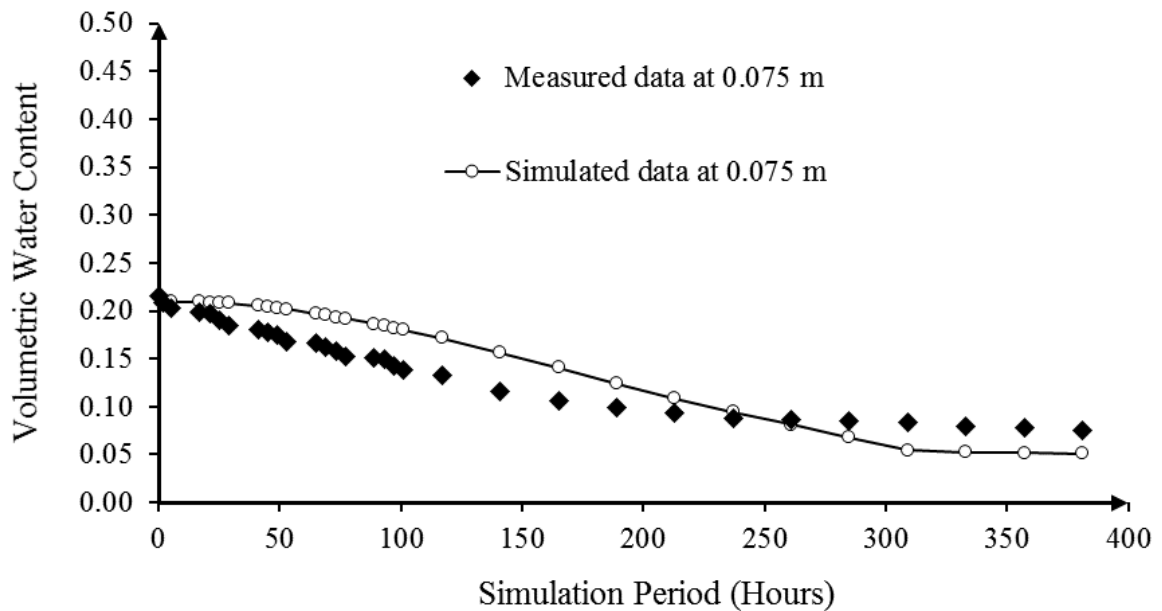


Figure 6. 69    Comparison of Simulated and Measured Transient Moisture Content

Variation (Depth: 0.075 m, Radial Distance: 2.3 m from the almond tree)
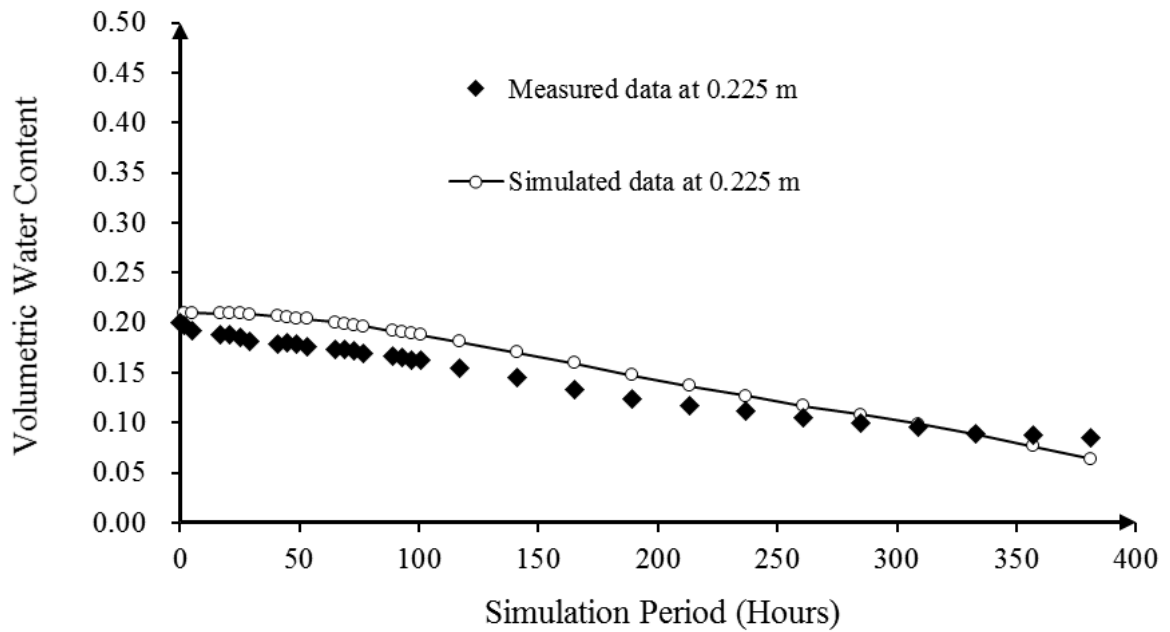
Figure 6. 70    Comparison of Simulated and Measured Transient Moisture Content

Variation (Depth: 0.225 m, Radial Distance: 2.3 m from the almond tree)
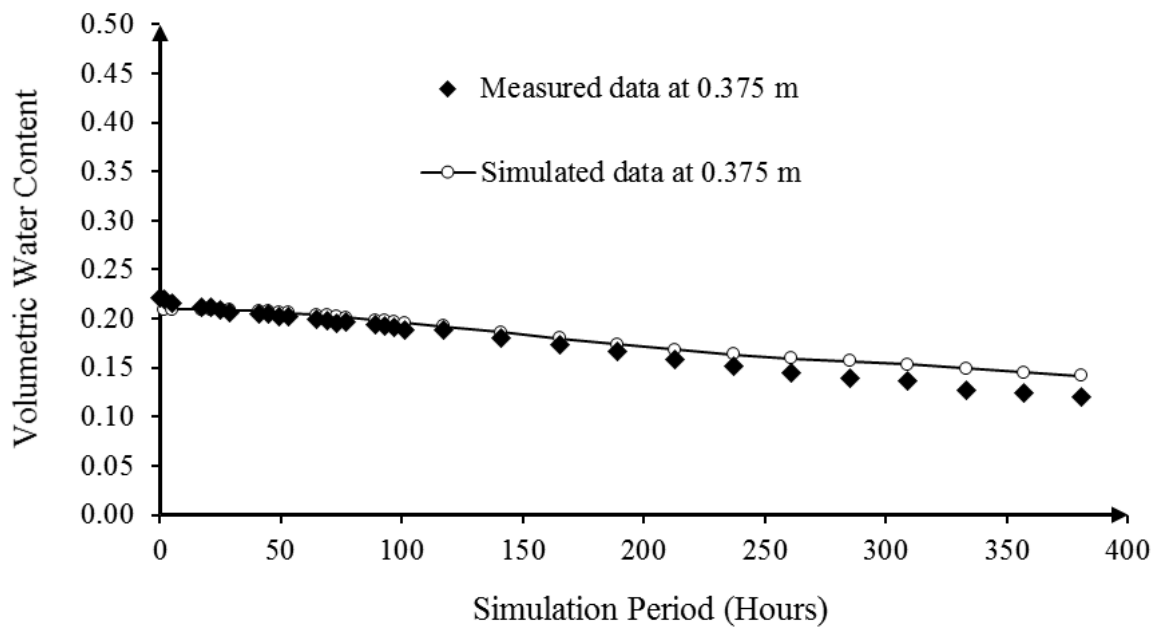


Figure 6. 71    Comparison of Simulated and Measured Transient Moisture Content

Variation (Depth: 0.375 m, Radial Distance: 2.3 m from the almond tree)
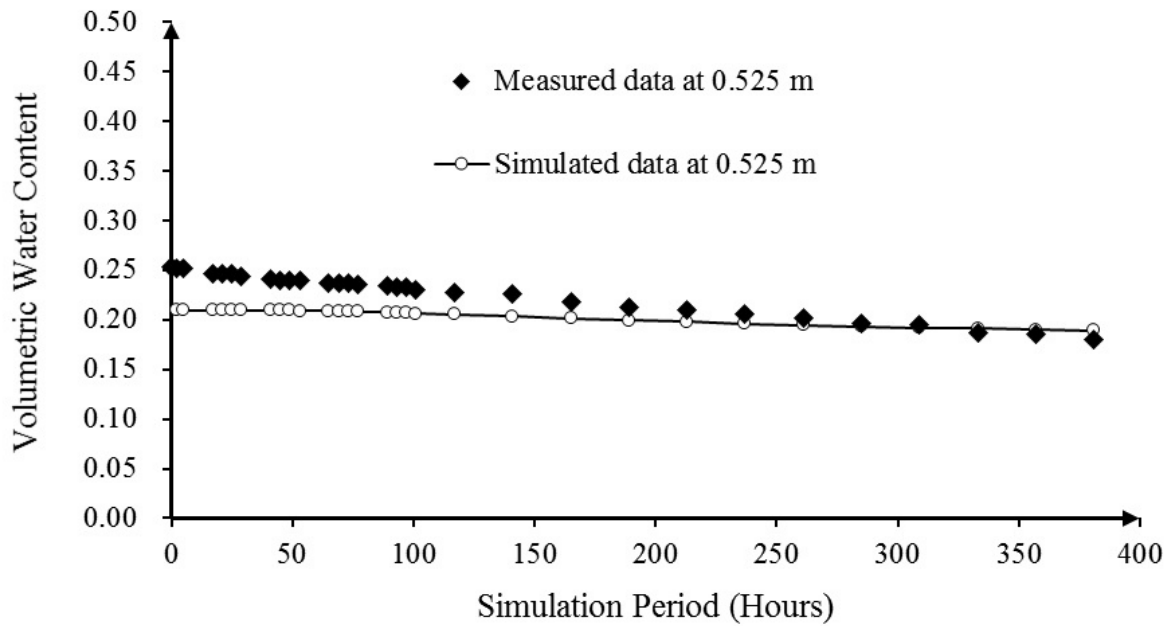
Figure 6. 72   Comparison of Simulated and Measured Transient Moisture Content

Variation (Depth: 0.525 m, Radial Distance: 2.3 m from the almond tree)
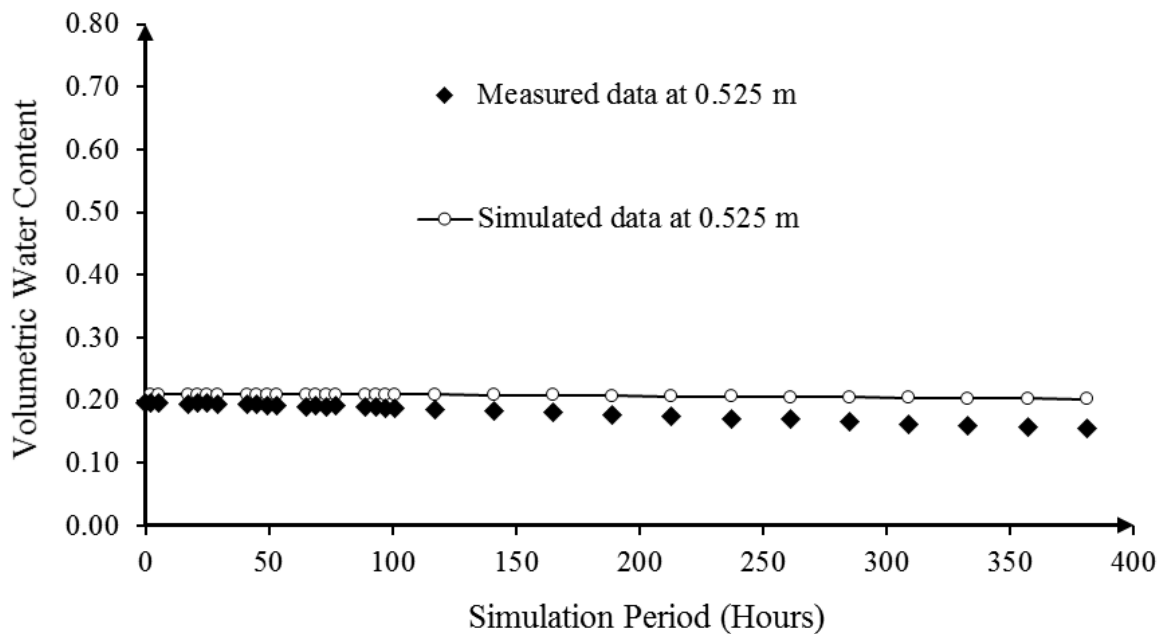


Figure 6. 73   Comparison of Simulated and Measured Transient Moisture Content

Variation (Depth: 0.525 m, Radial Distance: 2.9 m from the almond tree)
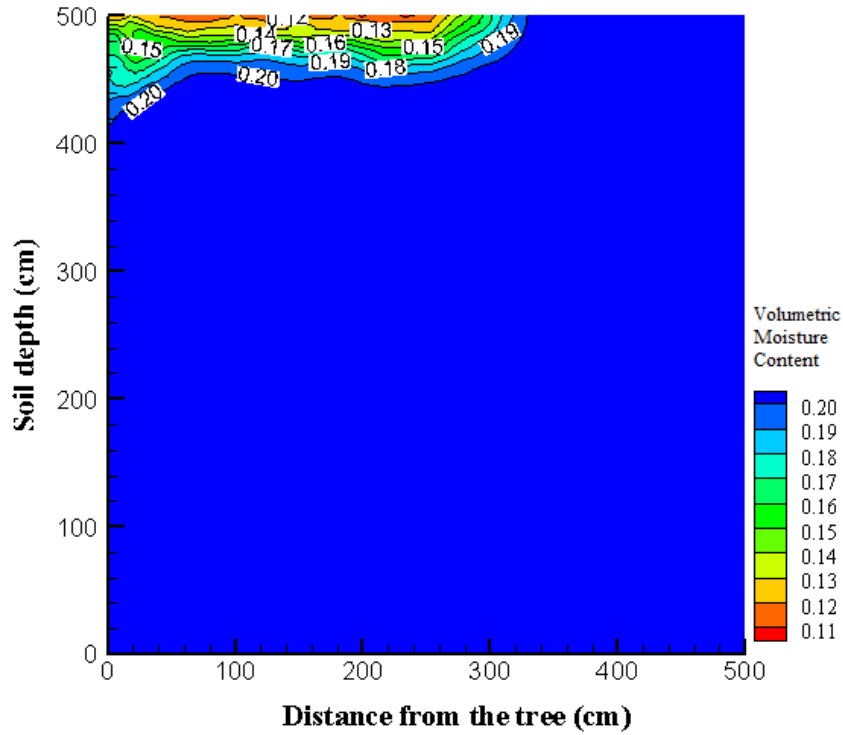
Figure 6. 74    Simulated Contour Plots of Volumetric Moisture Content at 190 Hours
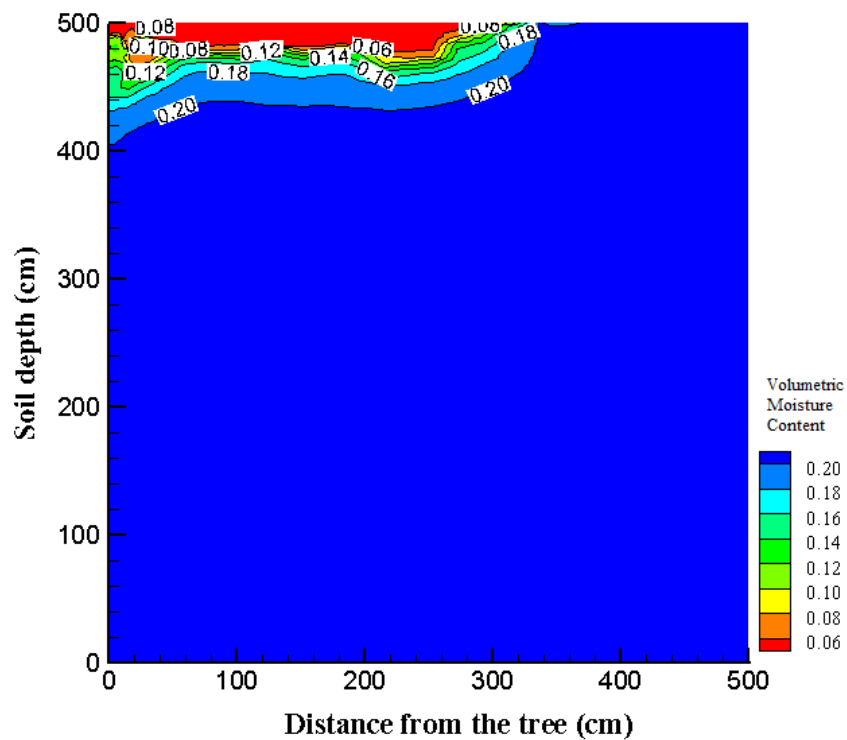


Figure 6. 75    Simulated Contour Plots of Volumetric Moisture Content at 381 Hours

6.4    CONCLUSIONS

The application of the new model for the simulation of moisture migration patterns near trees has been presented in this chapter.  Particular attention is given to the prediction of moisture content variations in the unsaturated zone and in the vicinity of a single mature tree.  The approach proposed utilizes radial symmetry and an image based root density distribution of water extraction rate with both depth and radius.  An approach of estimating transpiration rate for a single tree has been represented in this chapter.

The model has been validated by direct comparison to the field measurements recorded for two cases.  Four simulations have been undertaken to consider a mature lime tree located on boulder clay and explore the behaviour of the new approach.  The problem chosen for consideration covered a period with the tree in full leaf.  As such it is believed to be the first attempt at simulating the behaviour of an established tree over such a timescale.  A method of estimating the total transpiration rate has been explored by using Penman-Monteith equation based on the field conditions in this chapter.

Simulation 6-1 utilizes a graphical representation of the lime tree root morphology to define the distribution of water uptake with depth and radius and a transpiration rate based on field data (Biddle 1998) with free surface boundary conditions.  A good overall correlation between field data and simulated results was achieved in Simulation 6-1.  Time varying boundary conditions has also been considered in the simulation 6-2.  The moisture profiles at key times and at key locations based on site

data have been presented. The majority of the moisture extraction occurred near the surface and depletion reduced significantly when the distance from the tree increased. These served to illustrate that an overall moisture pattern similar to that observed in the field was produced by the proposed approach. The overall simulation strategy also has been successful to provide a simple method for a more realistic representation of boundary conditions at the soil surface.

Simulation 6-3 considers a sensitivity study of transpiration rate based on the results of Penman-Monteith equation. The simulation results demonstrated that the transpiration rate (28 L/day) calculated based on the measured data is reasonable and acceptable. The image-based root density approach achieved better quality than the results by linear approach (Simulation 6-4) and indicates that this root pattern is closer to the real field condition.

To provide further confidence in the implementation of the approach, a second numerical simulation has also been presented to show application of the model for a different tree species and soil type. In this case, a mature almond tree located on a shallow gravely loam soil was analysed overall good agreement with the available field data was also achieved.

## 6.5    REFERENCES

Anderson, C. and Sivakumar, V. 2008. Permeability of Natural Clay Liners: Effect of Accelerated Permeability Testing on Soil Structure. *The 12th International*

*Conference of International Association for Computer Methods and Advances in Geomechanics (IACMAG)*. Goa, India, 1-6 October.

Andreu, L. Hopmans, J. W. Schwankl, L. J. 1997. Spatial and temporal distribution of soil water balance for a drip-irrigated almond tree. *Agric Water Manage*. 35, pp. 123-146.

Aplin, A. C. Fleet, A. J. Macquaker, J. H. S. 1999. *Muds and Mudstones: Physical and Fluid-Flow Properties*. London: The Geological Society.

Bell, J. P. 1987. *Neutron Probe Practice*. Institute of Hydrology.

Ben-Asher, J. Cardon, G. Peters, D. Rolston, D. E. Phene, C. J. Biggar, J. W. Hutmacher, R. B. 1994. Determining almond root zone from surface carbon dioxide fluxes. *Soil Science Society of America Journal*. 58, pp. 930-934.

Biddle, P. G. 1998. *Tree Root Damage to Buildings*. Swindon: Willowmead Publishing Ltd, Wantage.

California Department of Food and Agriculture. 2014. *2013 California Almond Acreage Report*. Available at: http://www.nass.usda.gov/Statistics_by_State/California/Publications/Fruits_and_Nuts/201405almac.pdf [Accessed: 22 August 2015].

Cutler, D. F. and Richardson, I. B. K. 1989. *Tree roots and buildings*. Singapore: Longman Scientific and Technical.

Jarvis, P. G. 1976. The interpretation of the variations in leaf water potential and stomatal conductance found in canopies in the field. *Phil. Trans. R. Soc. Lond. B*. 273, pp. 593-610.

Kelliher, F. M. and Black, T. A. 1986. Estimating the Effects of Understory Removal from a Douglas Fir Forest Using a Two-Layer Canopy Evapotranspiration Model. *Water Resources Research*. 22(13), pp. 1891-1899.

Koumanov, K. S. Hopmans, J. W. Schwankl, L.W. Andreu, L. Tuly, A. 1997. Application efficiency of micro-sprinkler irrigation of almond trees. *Agric Water Manage*. 34, pp. 247-263.

Koumanov, K. S. Hopmans, J. W. Schwankl, L. W. 2006. Spatial and temporal distribution of root water uptake of an almond tree under microsprinkler irrigation. *Irrig Sci.*

Köstler, J. N. Brückner, E. and Bibelriether, H. 1968. *Die Wurzeln der Walbäume*. Hamburg: Parey.

Martin, T. Hinckley, T. M. Meinzer, F. C. and Sprugel, D. G. 1999. Boundary layer conductance, leaf temperature and transpiration of Abies amabilis branches.

*Tree Physiology*. 19, pp. 435-443.

Micke, W. C. 1996. *Almond Production Manual.* University of California: Division of Agriculture and Natural Resources.

Mullins, E. 2014. 10 Things You Probably Didn't Know About Almonds. *Eating bird food*. Available at: http://www.eatingbirdfood.com/10-things-you-probably-didnt-know-about-almonds/

Price, D. G. 2009. *Engineering Geology: Principles and Practice.* In: de Freitas, M. eds. Springer.

Rees, S. W. 1990. *Seasonal Ground Movement Effects on Buried Services*. PhD thesis, University of Wales, Cardiff.

Rees, S. W. and Ali, N. 2006. Seasonal water uptake near trees: a numerical and experimental study. *Geomechanics and Geoengineering: An International Journal*. 1(2), pp. 129-138.

Ritchie, J.T. 1972. Model for predicting evaporation from a row crop with incomplete cover. *Water Resour. Res*. 8, pp. 1204-1212.

SAPS (Science and Plants for Schools). 2007. *Common Lime (Tilia x europaea).* Homerton College, Cambridge UK.

Snyder, R. L. and Pruitt, W. O. 1989. Crop coefficients. P. 67. In: Goldhamer and Snyder eds. *Irrigation scheduling – A guide for efficient on farm water management*. Univer. Of Calf. Div. Agric. Nat. Res. Publ. No. 21454.

Tang, J. Bolstad, P. V. Ewers, B. E. Desai, A. R. Davis, K. J. and Carey, E. V. 2006. Sap flux–upscaled canopy transpiration, stomatal conductance, and water use efficiency in an old growth forest in the Great Lakes region of the United States. *Journal of Geophysical Research*. 111, pp. 1-12.

Vrugt, A. Hopmans, J. W. Simunek, J. 2001. Calibration of a twodimensional root water uptake model. *Soil Sci Soc Amer J*. 65(4), pp. 1027-1037.

Wells, M. L. 2013. Agricultural practices to reduce microbial contamination of nuts. In: Harris, L. J. eds. *Improving the Safety and Quality of Nuts*. Woodhead Publishing Limited, pp. 3-19.

Wilkinson, J. 2005. *Nut Grower's Guide: The Complete Handbook for Producers and Hobbyists*. Australia: Landlink Press.

**CHAPTER SEVEN**

**PRELIMINARY ANALYSIS OF WATER UPTAKE ON SLOPE**

**STABILITY**

7.1    INTRODUCTION

It is clear from previous chapters that vegetation can be beneficial to slope stability not only through mechanical soil reinforcement, but also via water uptake by the roots of vegetation.  From the numerical simulations presented in the preceding chapters it is also clear that significant moisture (and suction) variations may occur in the presence of vegetation.  This chapter aims to explore the influence of root architecture on such moisture content variations within the context of slope stability assessment.

In particular, this chapter presents a study of slope stability that includes an estimate of suction induced shear strength.  This research only considers hydrological effects (i.e. water uptake) at this stage.  The work presented employs a typical slope geometry.  A range of specific locations of a tree (e.g. near the toe, at mid-slope) and

different tree root architectures are also considered to illustrate their influence on calculated factors of safety.

Set against this background, the work presented here must be viewed as a generalised assessment aimed at illustrating the potential value of the new developed water uptake modelling approach and the influence of root architectures on slope stability.

## 7.2   COMBINED WATER-UPTAKE MODELLING AND UNSATURATED SLOPE ANALYSIS

This section attempts to bring together the slope stability approach and the new water-uptake model.  The main theoretical background has been presented in Chapter 3. The factor of safety for an unsaturated slope is evaluated using Equation (3.52). However, the traditional slope stability problem is formulated as a two-dimensional (2-D) plane problem and the previous simulation work presented in Chapter 6 was undertaken within a 2-D axi-symmetric framework.  Therefore, in order to obtain some compatibility between the two formats, the moisture flow simulation undertaken here is also conducted in 2D plane geometry.

Combining the standard two-dimensional Richards equation (Appendix 5 provides the full derivation) and the sink term Equation (3.44) provides the 2D plane form of the water uptake model:

$$C(\psi)\frac{\partial \psi}{\partial t} = \frac{\partial}{\partial x}\left[K(\psi)\frac{\partial \psi}{\partial x}\right] + \frac{\partial}{\partial z}\left[K(\psi)\frac{\partial \psi}{\partial z}\right] + \frac{\partial K(\psi)}{\partial z} - S \qquad (7.1)$$

A solution of Equation (7.1) was obtained via application of the numerical techniques described in Chapter 4. The necessary changes to the numerical formulation are provided in Appendix 6.

## 7.3 CASE STUDY - OAK TREE ON A SOIL SLOPE

The case study presented here is based, in part, on a soil slope that was instrumented and monitored by Southampton University (Smethurst et al. 2006). This work is used to define the soil slope and some of the main soil properties. The case study is then developed by introducing a hypothetical range of scenarios that represent the possible impact of a mature oak tree imposed on this slope. The properties of a typical oak tree are assumed based on the research of others.

### 7.3.1 Site Description (Southampton University: Smethurst et al. 2006)

The slope geometry employed in this study is developed from the original field experiment carried out by Smethurst et al. (2006). The site of the monitored slope is located on the A34 Newbury bypass in Southern England (Figure 7.1). The cross-section of the slope is shown in Figure 7.2. The slope section is 8 m high and 28 m long and the cutting was constructed in 1997, and is located entirely within London Clay. The groundwater regime was considered to be effectively hydrostatic below the slope section. Vegetation on the slope surface was primarily rough grass and herbs with a few small shrubs and mature beech, oak and silver birch trees planted at the top

of the slope. The site was instrumented to monitor seasonal moisture content and pore water pressure changes within the slope. Further detail of the site and the monitoring experiment is described in Smethurst et al. (2006; 2012).



Figure 7. 1    Photograph of slope site, figure reproduced from Google Maps
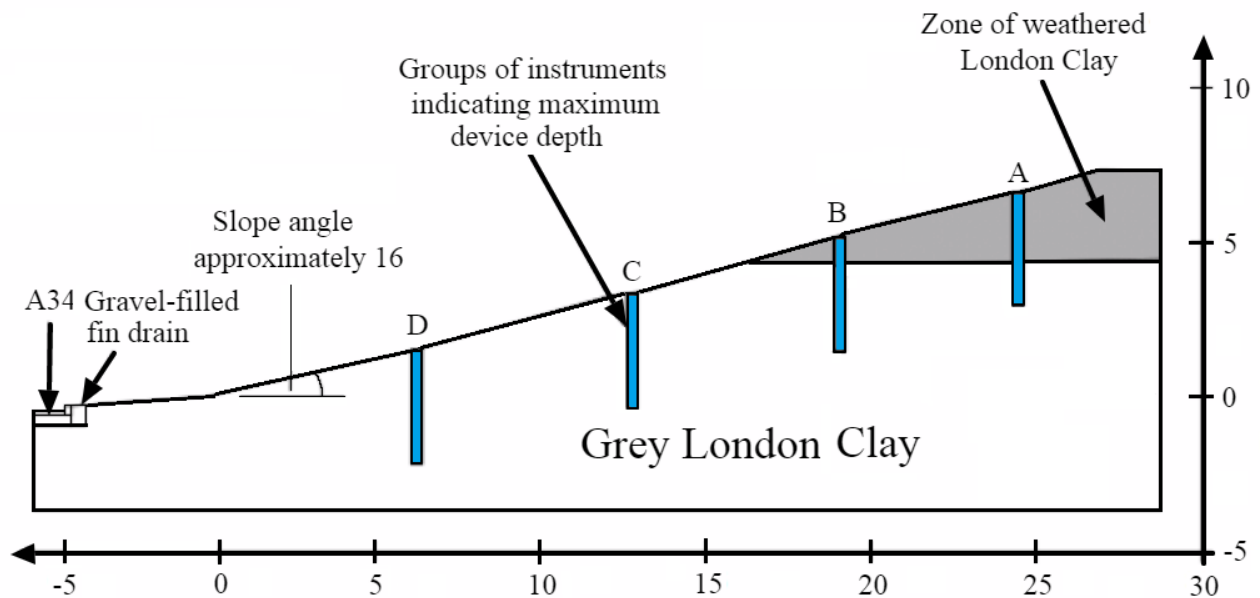


Figure 7. 2    Cross-section through the slope, figure from Smethurst et al. (2012)

7.3.2    Material Properties

The soil type at this site is predominated by a stiff grey London Clay (Smethurst et al. 2006).  The main soil properties are presented in Table 7.1.  The measured value of saturated hydraulic conductivity for the London Clay at the site was determined from field tests in 2003 and the dry unit weight was measured from undisturbed samples obtained from 0.5 m depth for the London Clay (Smethurst et al. 2006).

Table 7. 1    Material parameters for London clay soil (Croney 1977; Smethurst et al. 2006; Smethurst et al. 2012)

| Soil property | Value |
|---|---|
| Dry unit weight $\gamma$ (kN/m$^3$) | 14.60 |
| Saturated soil unit weight $\gamma$ (kN/m$^3$) | 19.21 |
| Cohesion $c'$ (kPa) | 7 |
| Friction angle $\phi'$ (degrees) | 20 |
| Residual volumetric moisture content $\theta_r$ | 0.05 |
| Saturated volumetric moisture content $\theta_s$ | 0.47 |
| van Genutchen parameter $n$ | 1.12 |
| van Genutchen parameter $\alpha$ (cm$^{-1}$) | 0.009 |
| van Genutchen parameter $l$ | 0.5 |
| Saturated hydraulic conductivity $K_s$ (cm/s) | $3.7 \times 10^{-7}$ |

In this study, the soil profile is simplified and it is assumed to comprise a single homogenous layer of London Clay.  The soil water retention relationship for samples of London Clay has been given by Croney (1977).  In the absence of directly measured data, equation (3.1) has again been used to determine the water retention curve based on the data provided by Croney (1977) and equation (3.2) has been used

to estimate the hydraulic conductivity. The resulting water retention and hydraulic conductivity relationships for London Clay, adopted for this study, are shown in Figures 7.3 and 7.4 respectively.
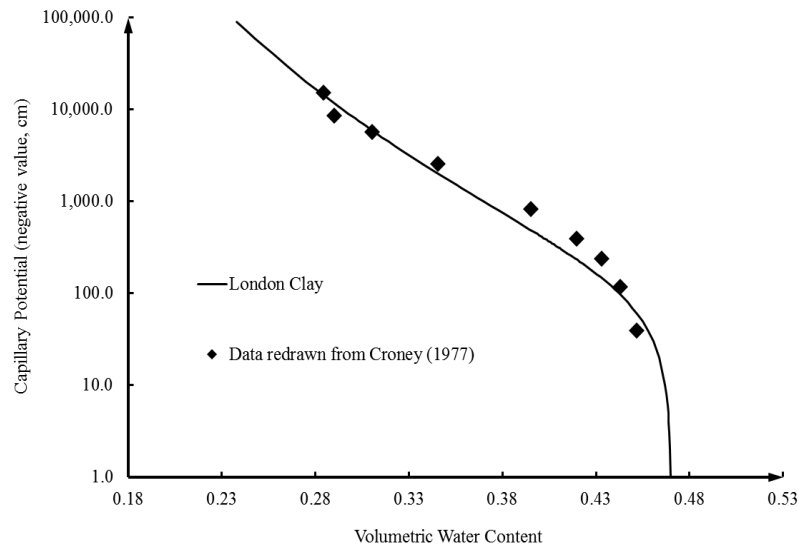


Figure 7. 3    Soil Water Retention Curve for London Clay (plotted on a log scale of capillary potential)
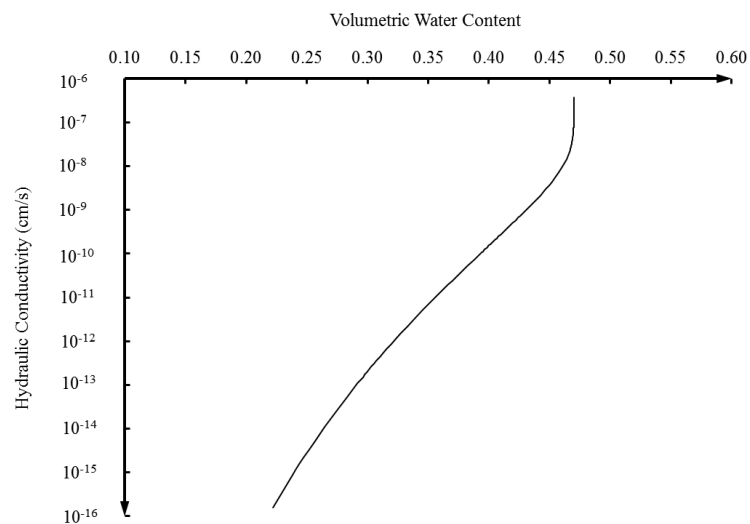


Figure 7. 4    Hydraulic Conductivity Curve for London Clay (plotted on a log scale of hydraulic conductivity), figure redrawn from Croney (1977)

In applying the method of slices, the weight of a slice is determined from the cross sectional area of the slice and the unit weight of the soil. The unit weight is given as:

$$\gamma = \gamma_w \frac{G + Se}{1 + e} \qquad (7.2)$$

where, $\gamma_w$ is the unit weight of water, $G$ is the specific gravity, $S$ is the degree of saturation and $e$ is the void ratio.

For example, if the soil is saturated: $S = 1$, $G = 2.8$, $\gamma_w = 9.81$ kN/m$^3$, $e = 0.6$, and the unit weight is 20.85 kN/m$^3$. Conversely, above the water table where the soil is unsaturated, for a degree of saturation of 80 %, the corresponding the unit weight of soil would reduce to 20.11 kN/m$^3$. This example yields a difference between saturated and unsaturated soil weight of about 3.5 %. Within the context of a slope stability analysis, a 3.5 % difference in the unit weight is not particularly significant. As a result, unit weight of the saturated soil has been used in the calculation of slope stability for this study.

### 7.3.3   Properties of a Typical Oak Tree

The case study aims to explore the behaviour of a typical mature oak tree (15 m in height) situated on a London Clay. The study aims to show the root-architecture that may arise on sloping ground – however there is a distinct lack of good quality data of this kind in the literature. Based on the available data, two white oak trees (*Quercus*

*alba L.*) of different shapes were selected for the case study (see Figure 7.5). Two forms of root-architecture are considered; heartroot and taproot. These are based on measured information from two closely situated white oak trees located on sloping ground provided by Danjon et al. (2008). The root zone for the taproot-architecture is assumed to extend to a depth of 4 m (Hinckley et al. 1981; Urban 2010), the maximum depth of heartroot-architecture is assumed about 3 m and a radial distance of 5 m both left and right of the centre line of the tree root system.



**(a) Heartroot**                                        **(b) Taproot**
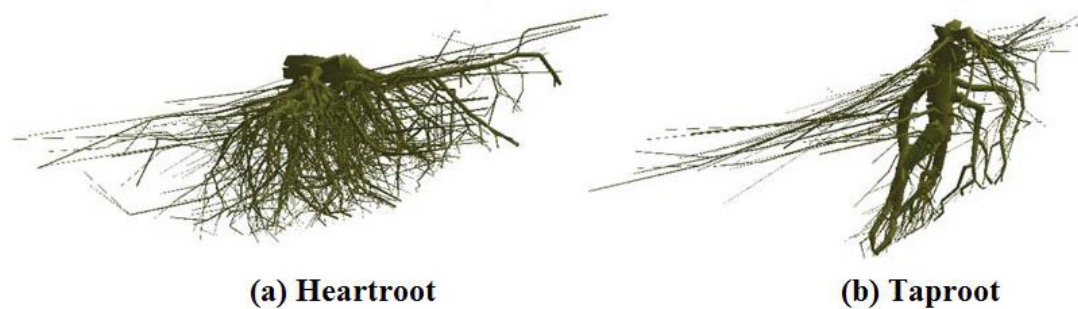
Figure 7. 5     Typical tree root systems on slope, figure reproduced from Danjon et al. (2008)

7.3.4    Numerical Simulation

To simulate the case study, a simplified typical soil slope is considered and the water table is assumed 1 m below the slope section (see Figure 7.6). The slope angle is at 1:3.5 gradient and the slope is assumed to be formed of a single soil type (London Clay). Considering the purpose of this analysis is to explore the influence from vegetation near surface of the slope, an impenetrable layer (bedrock) is introduced

under the London Clay to constrain behaviour to upper regions of the domain. In addition, tension cracks are excluded from the current work.
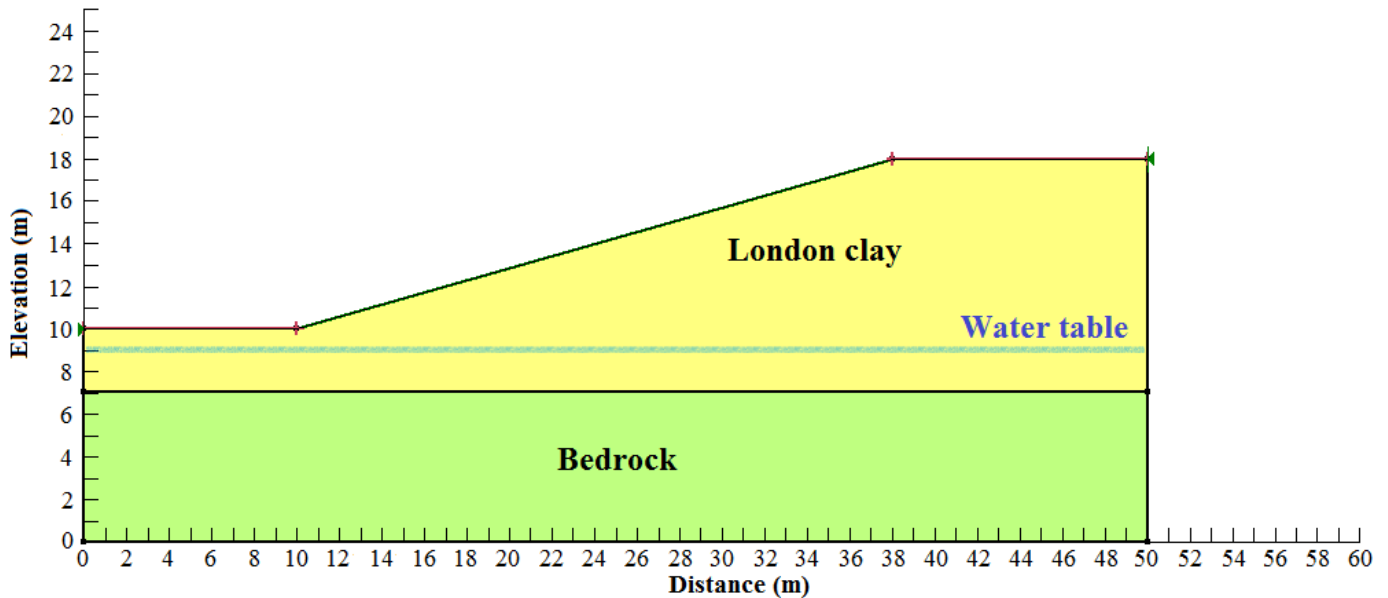


Figure 7. 6    Slope of case study

A series of seven numerical simulations have been undertaken to explore two forms of root architecture (heartroot and taproot) and the influence of their position on the soil slope. The simulations involved a two stage procedure: i) prediction of the water extraction generated by the transpiration demand of the oak tree; and ii) utilisation of this information in subsequent assessment of slope stability. The second step of the procedure has been undertaken by using commercial software SLOPE/W (GeoStudio 2007 Version 7.10). The results from the first stage of the procedure are used to define the pore-water pressures throughout the domain which can be prescribed in SLOPE/W. The seven simulations can be summarized as follows:

- Simulation 1: Considers the behaviour of an unsaturated soil slope in the absence of any trees (see Figure 7.7).

- Simulation 2: Utilizes an image of heartroot-architecture provided by Danjon et al. (2008) positioned at mid-slope (see Figure 7.15).

- Simulation 3: Employs a graphical representation of taproot-morphology (Danjon et al. 2008) positioned at mid-slope (see Figure 7.19).

- Simulation 4: As Simulation 2, but in this case the tree is positioned nearer to the toe of the slope (exact position of tree: coordinate $x = 13.6$ m, $z = 11.0$ m; the coordinates are based on an origin located at lower left corner of the domain.) as shown in Figure 7.23.

- Simulation 5: As Simulation 3, but in this case the tree is again positioned nearer to the toe of the slope (exact position of tree: coordinate $x = 14.6$ m, $z = 11.4$ m) as represented in Figure 7.27.

- Simulation 6: As Simulation 4 but the tree (heartroot- morphology) is located closer to the toe of the slope (exact position of tree: coordinate $x = 12.0$ m, $z = 10.6$ m).

- Simulation 7: As Simulation 5 but the tree (taproot-morphology is located closer to the toe of the slope (exact position of tree: coordinate $x = 11.5$ m, $z = 10.4$ m).

For each simulation, spatial discretization was achieved using a finite-element mesh which comprises of 1400 eight-node isoparametric elements with 4361 nodes. The mesh was designed to offer some refinement within the root zone area since this is the region where the main variations of moisture content were expected to occur. The simulation employs a time-step size of 21600 seconds, which was held constant for the entire period considered. Again, a check has been made to ensure that the solution is both spatially and time-step converged.

In all of the simulations (except simulation 1 where there is no root system), a transpiration rate of approximately 400 litres per day (for a large oak tree) has been converted to a per metre run basis (Perlman 2016). The water-uptake simulations are undertaken using the new root image density approach. In effect the transpiration rate is therefore distributed in proportion to root density through the root zone via use of the sink term. In each simulation, water uptake is evaluated for a soil-drying period of 270 days. A zero flux boundary condition is specified on all external boundaries of the domain. In the present study, a gravitational condition has been applied. The water table is assumed 1 m below the slope section as an initial condition and it is not maintained during the simulations.

Since, the problem considered is a typical drying period caused by transpiration from a single tree, the same approach described in Chapter 6 is again employed here. Several minor modifications to the numerical code were implemented to ensure correct control over location and geometry of the root system. The resulting code ensures that the water uptake model functions correctly when the root system is positioned anywhere along the slope surface.

Figure 7.7 shows a diagrammatic representation of the soil slope, in the absence of any trees, and the finite element domain (as described above) used. A slope with an initially hydrostatic pore-water pressure head distribution was assumed - as shown in Figure 7.8. The resulting hydrostatic state is used to define initial conditions in all of the following simulations.
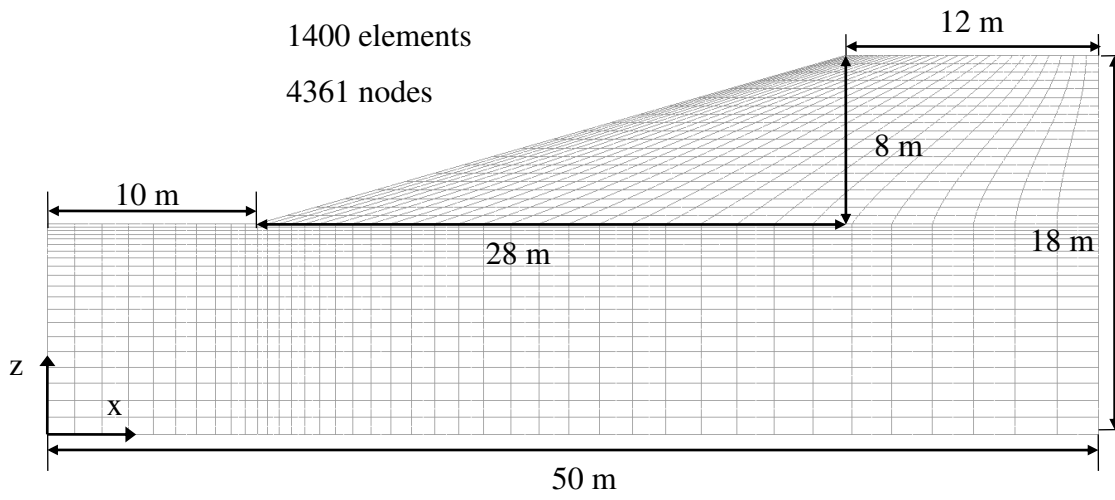
Figure 7. 7    Simulation 1:  Slope in the absence of any trees
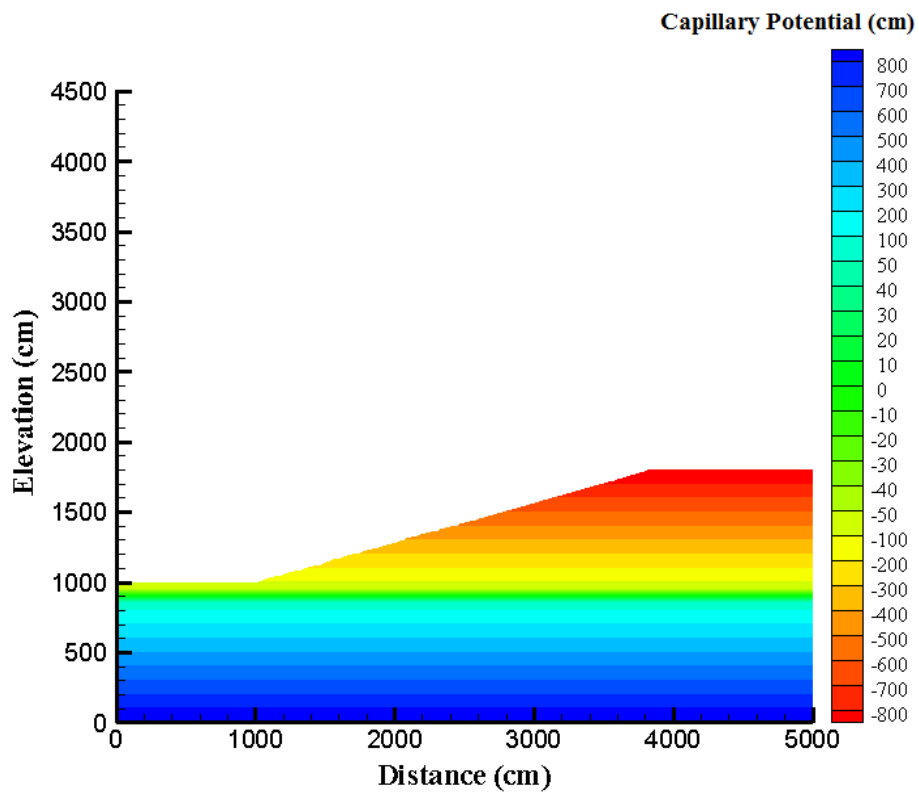


Figure 7. 8    Contour plots of pore-water pressure head (cm) at 0 day

7.3.5    Results

**Simulation 1**
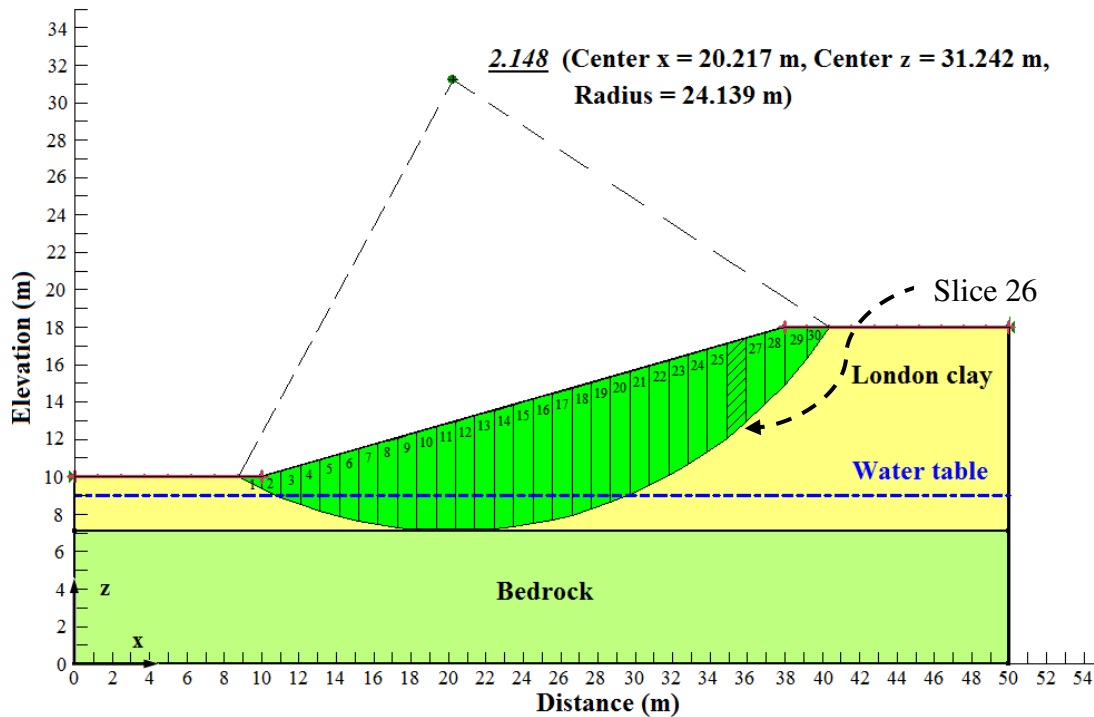


Figure 7. 9    Simulation 1:    Identification of the Critical Slip Surface, using SLOPEW (2007)

For simulation 1 no prediction of the water extraction generated by the transpiration demand of the oak tree is required and so the hydrostatic conditions shown in Figure 7.8 can be used in the second stage of the analysis procedure.  The results of the corresponding stability analysis are summarized in Figure 7.9.  To find the critical circular slip surface, 1089 possible failure surfaces were examined.  To implement equation (3.52), the mass of soil bounded by the critical slip surface was then divided into 30 slices.  More detailed manual calculations of each slice are summarised in Appendix 7.  As a result, a minimum factor of safety of 2.148 for Simulation 1 was

calculated. This corresponded to a slip surface of radius 24.139 m and of origin $x = 20.217$ m, $y = 31.242$ m. As a check on the process, a comparison between the results from the software and a manual/hand calculation was found to be 0.02 %. Therefore, it was concluded that the implementation of the current procedure has been successfully undertaken. The lowest factor of safety for Simulation 1 (2.148) is used as reference to compute the change in factor of safety for the subsequent simulations.

For this first simulation only, a more detailed illustration of the stresses developed at the base of a typical slice is presented. In particular, the pore-water pressure, shear strength and mobilized shear strength at the base of each slice of the critical slip surface in Simulation 1 are given in Figure 7.10 and 7.11, respectively. Figure 7.12 and 7.13 then show the details for a 'typical' slice (No. 26, Fig 7.9) based on the two methods of calculating shear strength considered. In the comparison, Fredlund's equation (Fredlund et al. 1978) gives an increase of unsaturated shear strength related to a constant value of $\phi^b$, a typical value of 15° was used here based on the work of Fredlund and Rahardjo (1993). The second approach was based on Vanapalli's equation (Vanapalli et al. 1996) as described previously in section 3.51, Chapter 3. It is clear that there is a little difference between the methods for this example slice. The overall factor of safety for Simulation 1, calculated using these two shear strength equations are compared in Table 7.2.

Figure 7.14 presents the comparison of the suction related shear strength contribution produced by Fredlund's approach versus Vanapalli's model for Simulation 1. It can be seen that a more significant difference occurs when the base of slice is located above the position of the water table.
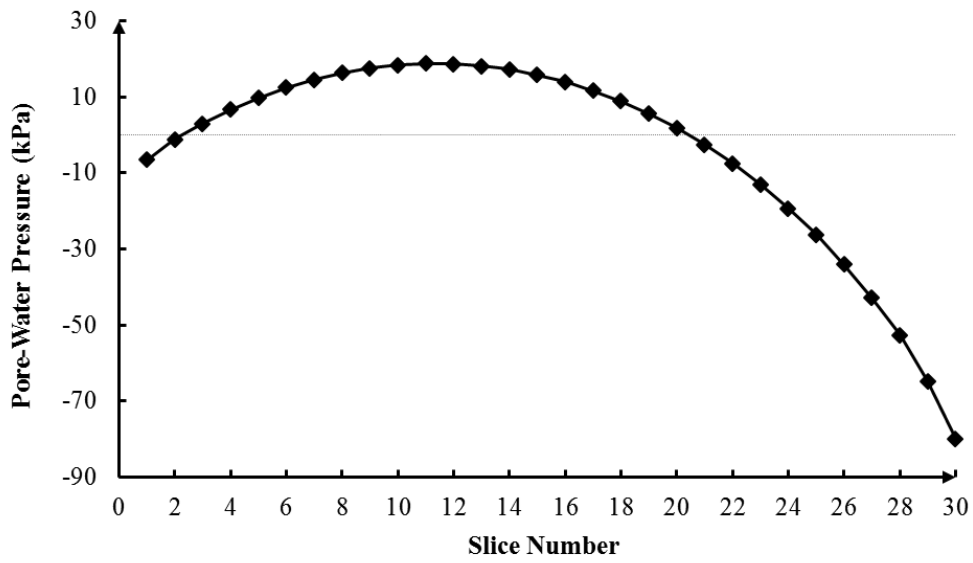
Figure 7. 10    Simulation 1:  Pore-water pressure (kPa) versus slice number
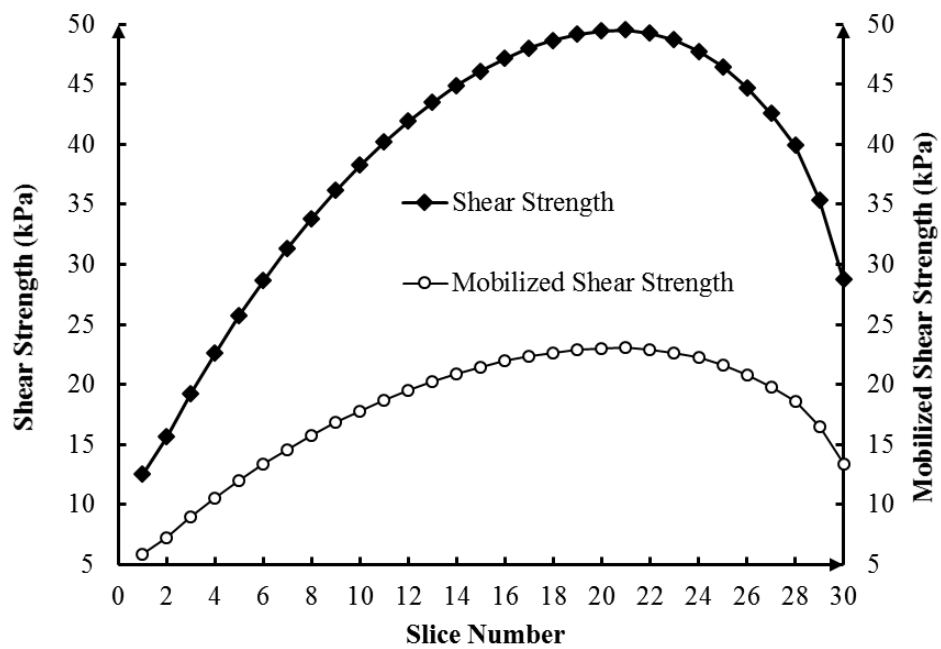


Figure 7. 11    Simulation 1:  Shear strength and mobilized shear strength versus slice

number

**Slice 26 - Bishop Method with Fredlund's shear strength equation**

Slice Width: 1.037 m

Slice Mid-Height: 4.7659 m

Slice Base Angle: 39.015 °

Slice Base Length: 1.3347 m

Weight (kN) 94.944

Interslice Normal Force (kN) 100.49

Interslice Normal Force (kN) 60.829

Pore-Water Pressure: -34.089 kPa

27.299 Base Shear Mobilized Force (kN)

100.08 Base Normal Force (kN)

Base Shear Mobilized Force (kN)

Base Normal Force (kN)

Weight (kN)

Interslice Normal Force (kN)
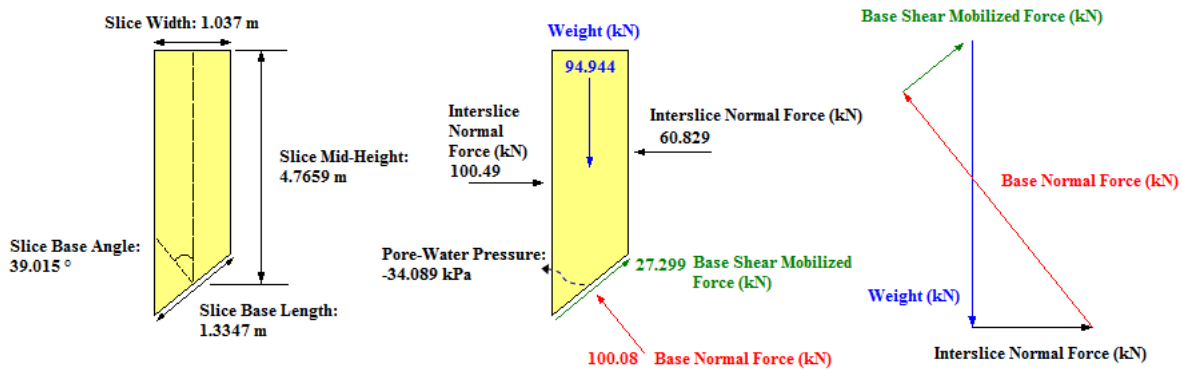
Figure 7. 12    Simulation 1:    The detailed information about slope stability calculation of Slice 26 using Fredlund's equation (Fredlund et al. 1978)

**Slice 26 - Bishop Method with Vanapalli's shear strength equation**

Slice Width: 1.037 m

Slice Mid-Height: 4.7659 m

Slice Base Angle: 39.015 °

Slice Base Length: 1.3347 m

Weight (kN) 94.944

Interslice Normal Force (kN) 95.917

Interslice Normal Force (kN) 56.855

Pore-Water Pressure: -34.089 kPa

27.791 Base Shear Mobilized Force (kN)

99.679 Base Normal Force (kN)

Base Shear Mobilized Force (kN)

Base Normal Force (kN)

Weight (kN)

Interslice Normal Force (kN)
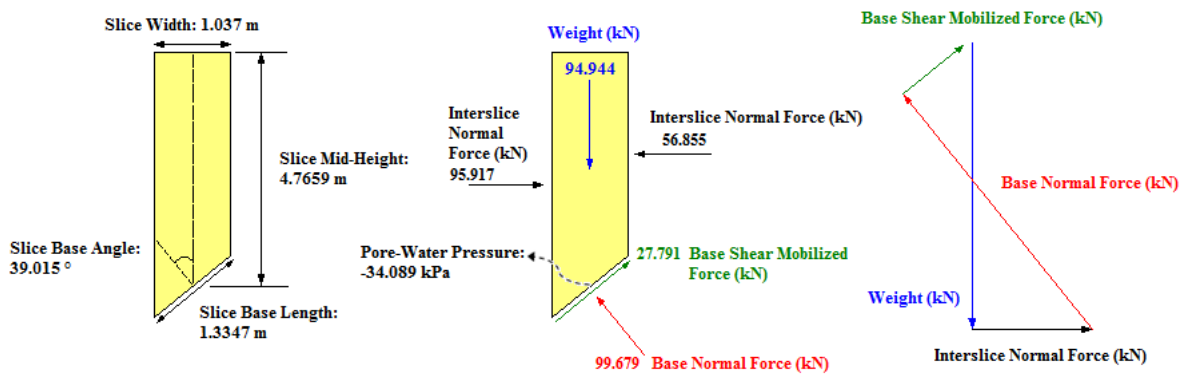
Figure 7. 13    Simulation 1:    The detailed information about slope stability calculation of Slice 26 using Vanapalli's equation (Vanapalli et al. 1996)

Table 7. 2 Comparison of factor of safety calculation based on two shear strength models

| Shear Strength Method | Lowest of $F$ for Simulation 1 | Stresses at the base of Slice 26, Simulation 1 | | |
|---|---|---|---|---|
| | | Normal Stress (kPa) | Shear Strength (kPa) | Shear Mobilized (kPa) |
| Fredlund et al.(1978) shear strength equation | 2.123 | 74.983 | 43.426 | 20.453 |
| Vanapalli et al. (1996) shear strength equation | 2.148 | 74.683 | 44.735 | 20.822 |
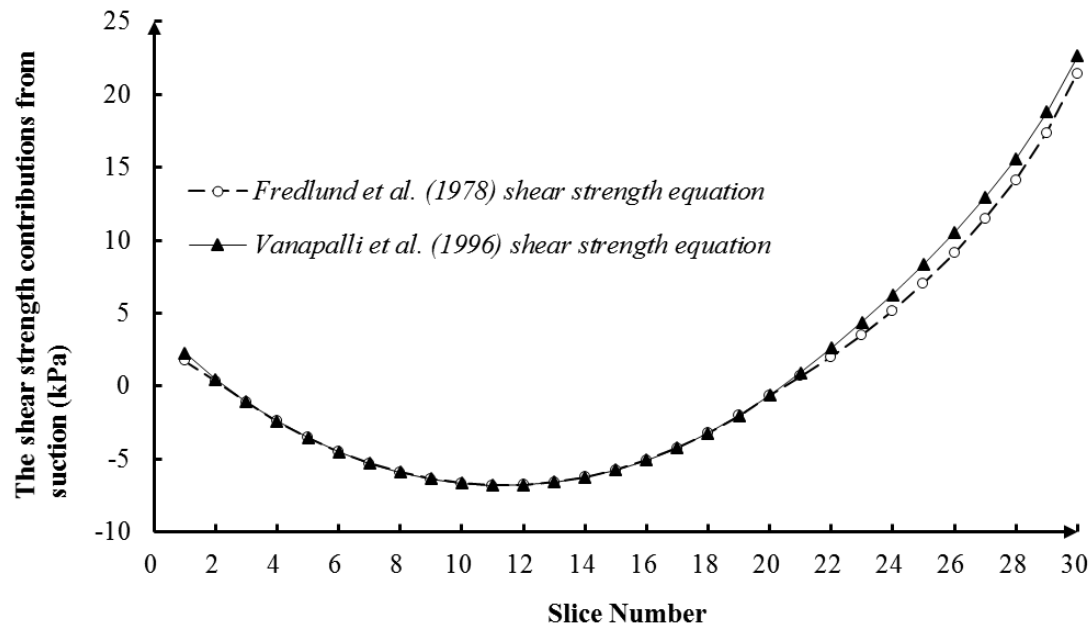
Figure 7. 14    Comparison of the shear strength contributions from suction between two shear strength methods

**Simulation 2**

A diagrammatic representation of the heartroot configuration located at mid-slope for Simulation 2 is shown in the Figure 7.15 and the corresponding image density ratio for this problem can be seen in the Figure 7.16. Figure 7.17 presents a contour plot of simulated pore water pressure head at 270 days for the heartroot-morphology at mid-slope. This figure shows a maximum pore-water pressure head of -100000 cm near the soil surface within the slope. In absolute terms this value may appear quite high with respect to a transpiration rate of 400 litres per day and the relatively low value of soil hydraulic conductivity and no rainfall infiltration considered in the simulated period. The magnitude of pore-water pressure results is determined by the shape of the soil-water-retention curve (Figure 7.3). In this study, the estimated hydraulic

properties have been found to be in good agreement with measured data for this type of soil. The shape of the affected area is the same as the root geometry. This figure also means that clear variations in moisture content have taken place within the slope. The largest change moisture content (16.5 %) occurs at the location in the slope where the root density is at its maximum.

The information available therefore provides a means for predicting the pore-water pressure change generated by the drying process with the scenario of Simulation 2 which can be employed in the slope stability analysis. Figure 7.18 shows a minimum factor of safety of 2.148 was calculated for Simulation 2. This corresponded to a slip surface of radius 24.139 m and of origin $x = 20.217$ m, $z = 31.242$ m which is the same as that of Simulation 1. It indicates that the oak tree with heartroot-morphology located at mid-slope does not have any effect on the slope stability in terms of its impact on hydraulic factors.
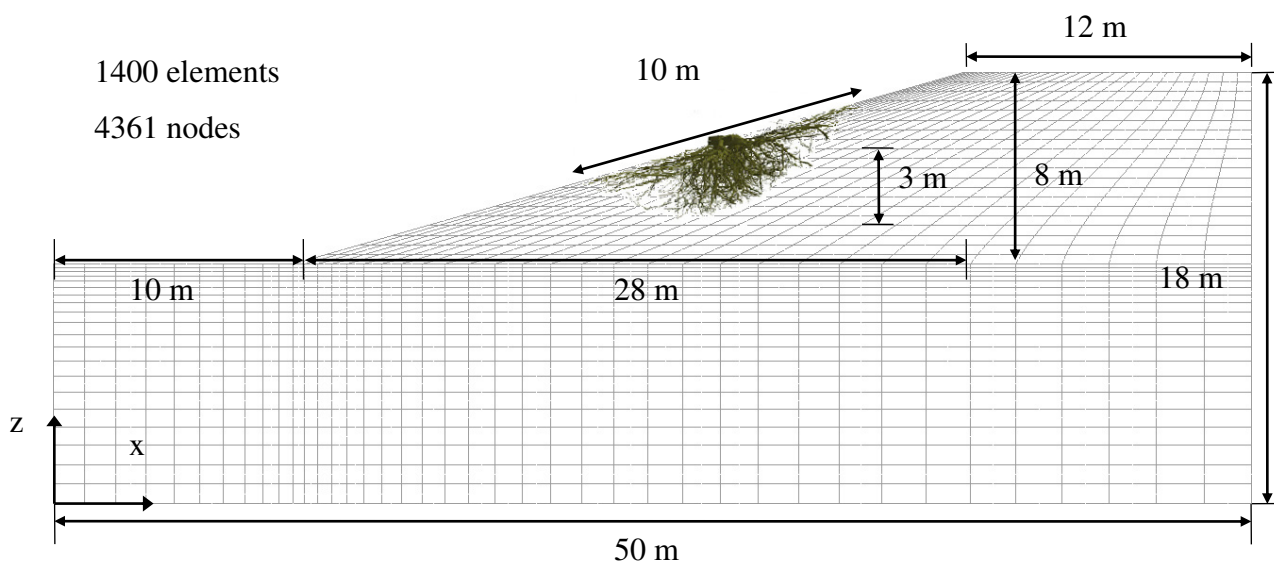


Figure 7. 15    Simulation 2:  Oak tree with heartroot-morphology at mid-slope
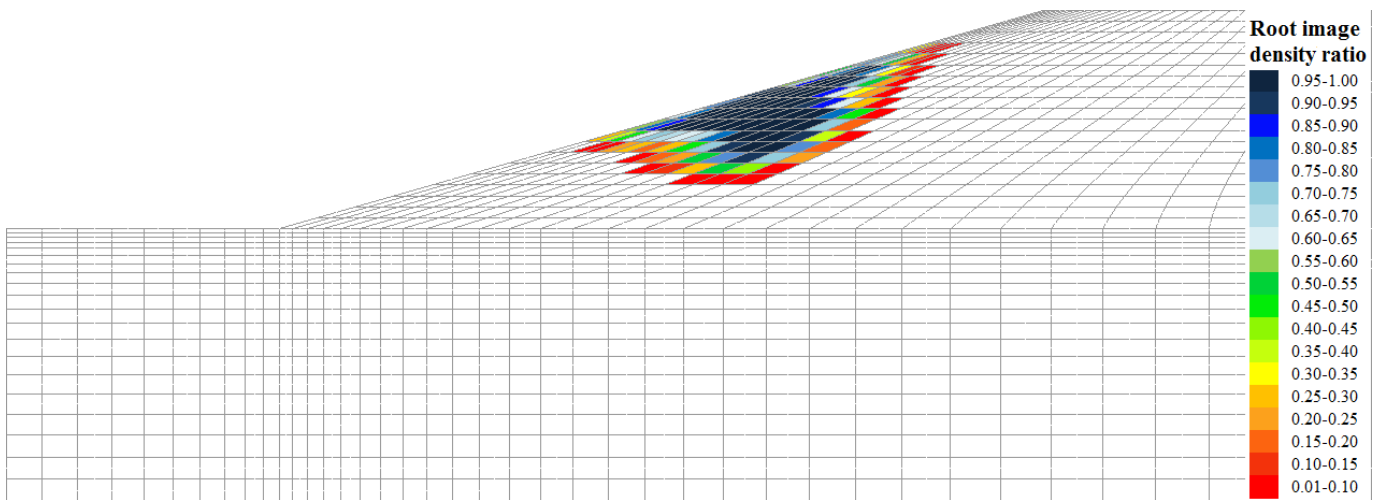
Figure 7. 16    Simulation 2:  Root image density ratio
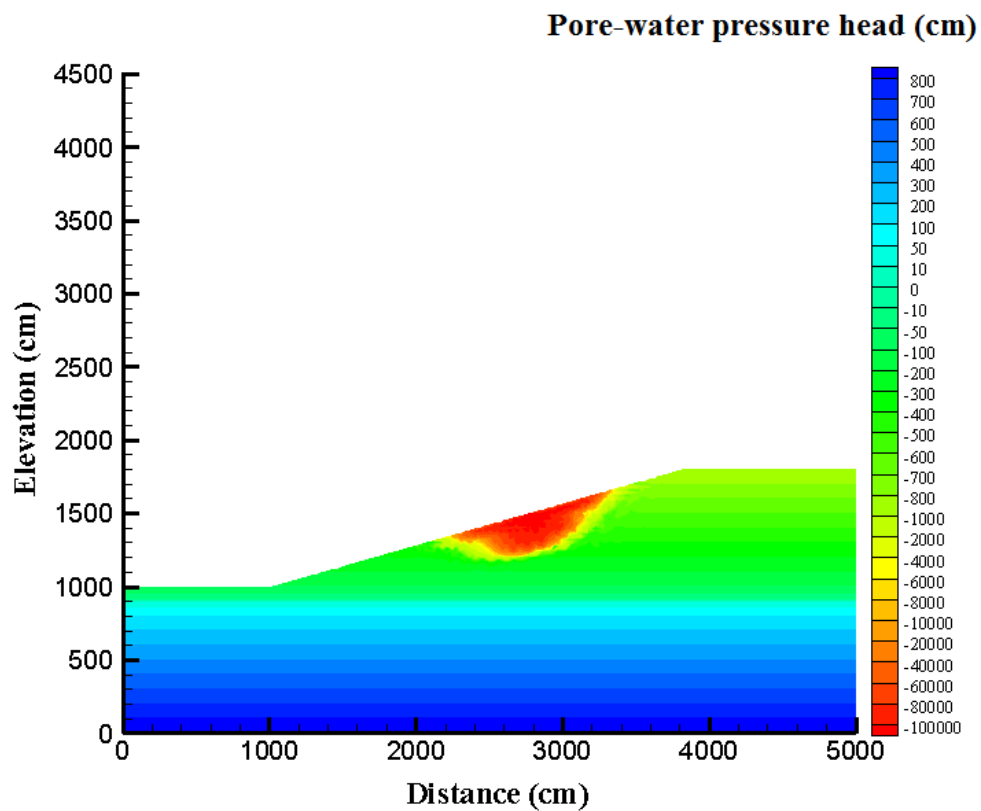


Figure 7. 17    Simulation 2:  Contour plots of pore-water pressure head (cm) at 270 days
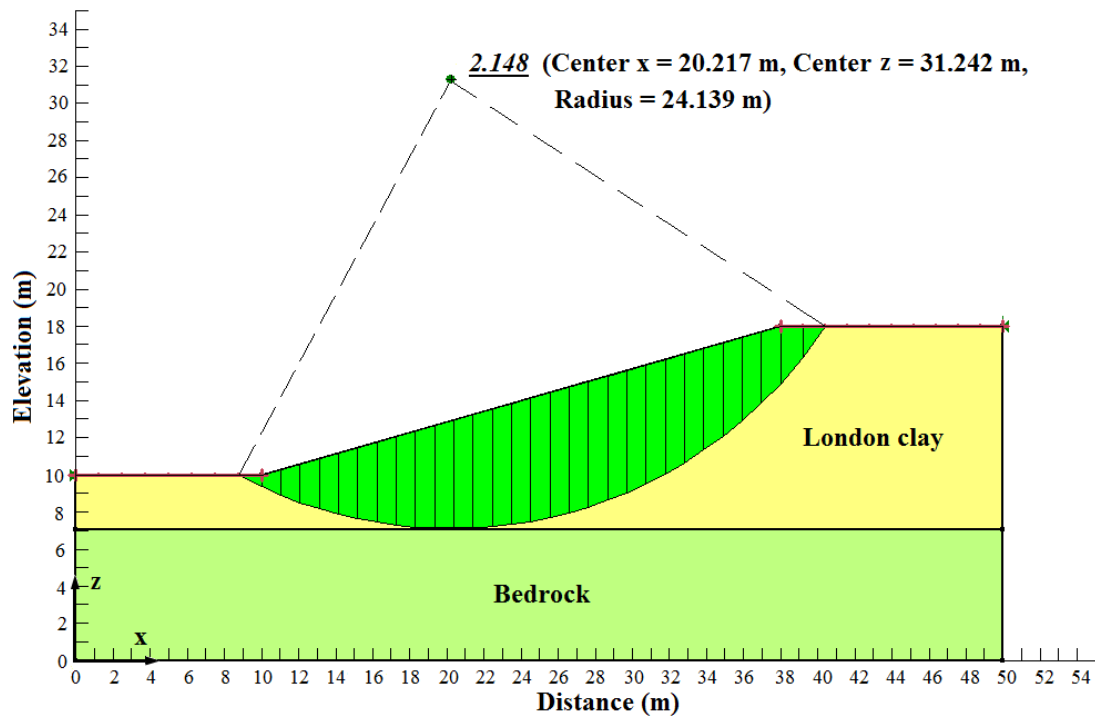
Figure 7. 18    Simulation 2:  Identification of the critical slip surface

**Simulation 3**

A graphical representation of taproot-morphology applied at mid-slope is shown in Figure 7.19.  The corresponding image density ratio is presented in Figure 7.20.  The simulated results at 270 days from the first stage of the procedure for Simulation 3 presented in contour plots is shown in Figure 7.21.  This figure presents a maximum pore-water pressure head of -180000 cm near the soil surface within the slope, where the root image density ratio is at its maximum.  By comparing Figure 7.20 with Figure 7.21, it is clear that the geometry of the affected pore-water pressure area by the process of transpiration is quite similar as the taproot-morphology.  The largest change moisture content (17.6%) is generated by the tree with taproot-morphology at the mid-slope.  At this location the volumetric moisture content reduced from an initial value of 41.6% to 24.0% after 270 days of transpiration.

278

The critical slip surface is presented in Figure 7.22 with a minimum factor of safety of 2.217 calculated.  This corresponded to a slip surface of radius 24.168 m and of origin $x$ = 18.994 m, $z$ = 31.260 m.  For comparison a factor of safety of 2.275 is calculated for the critical slip surface of Simulation 1 ($x$ = 20.217 m, $z$ = 31.242 m and radius = 24.139 m).  It can be found out that the taproot-morphology of oak tree presented at mid-slope could change the location of the critical slip surface for the soil slope and slightly increase the stability of slope.
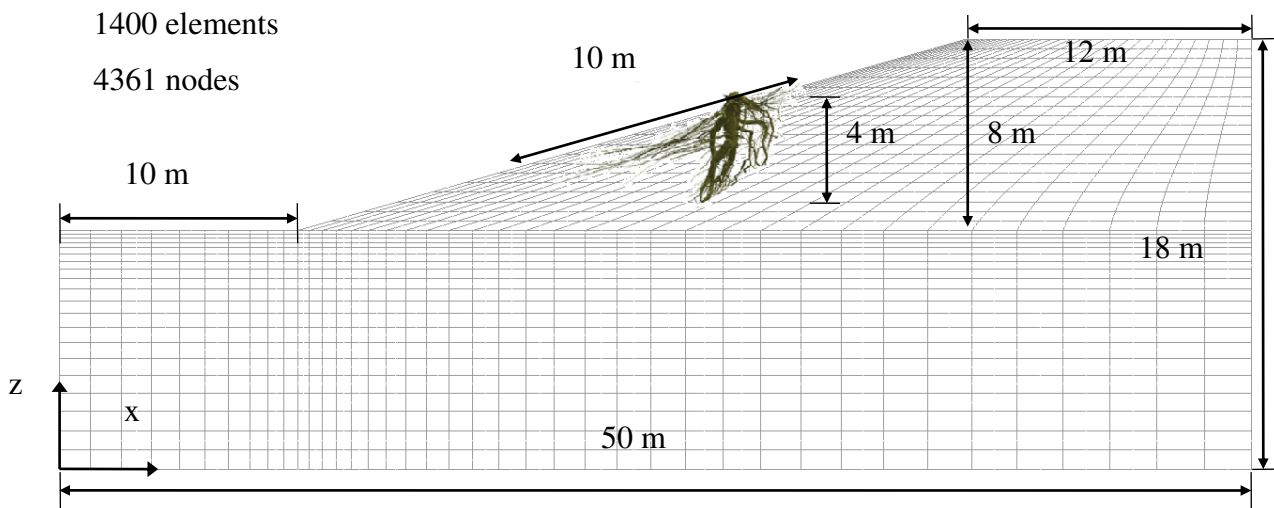
Figure 7. 19    Simulation 3:  Oak tree with taproot-morphology at mid-slope
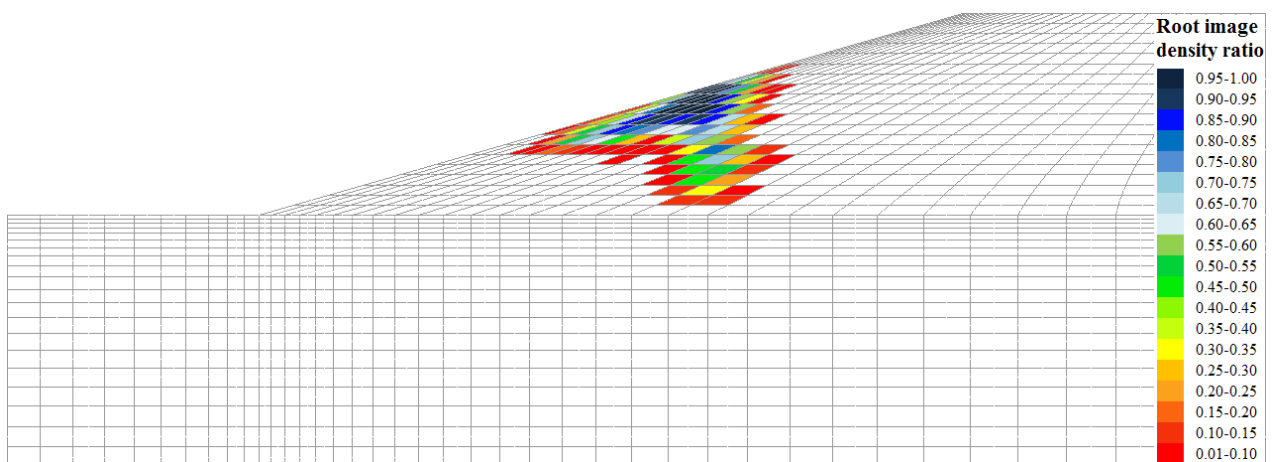
Figure 7. 20    Simulation 3:  Root image density ratio
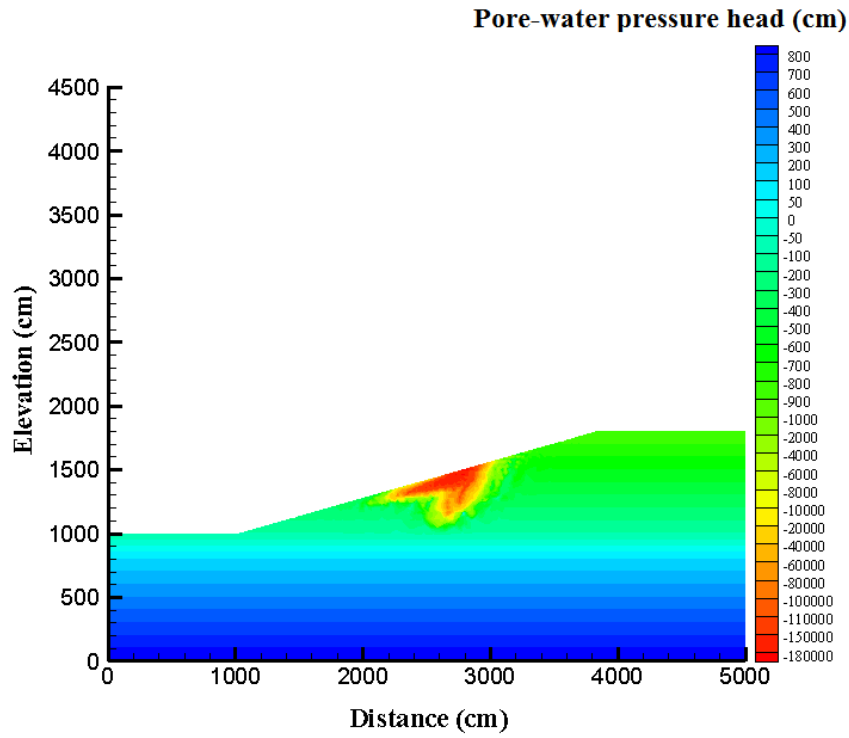
Figure 7. 21    Simulation 3:  Contour plots of pore-water pressure head (cm) at 270

days
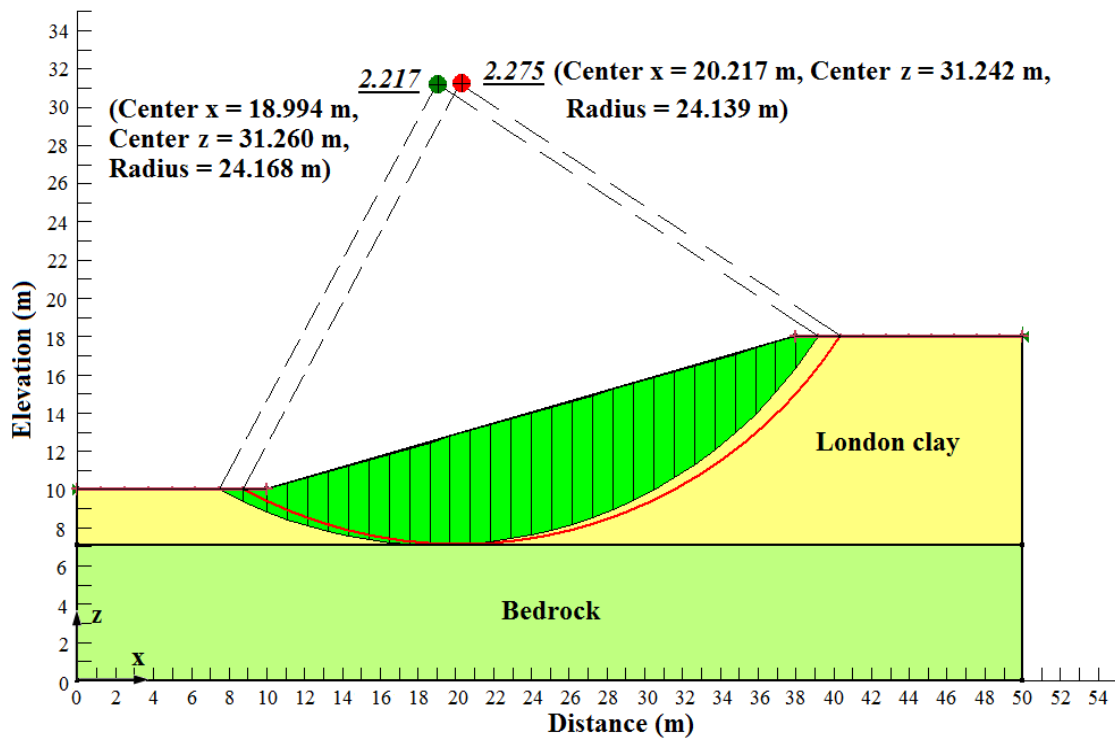


Figure 7. 22    Simulation 3:  Identification of the critical slip surface

**Simulation 4**

Figure 7.23 shows a diagrammatic representation of the heartroot configuration positioned nearer the toe of the slope. Figure 7.24 presents root image density ratios calculated based on the root pattern from Simulation 4. Contour plots of pore-water pressure head produced at 270 days for simulation 4 is shown in Figure 7.25. It is clear that the variations in moisture content/pore-water pressure are exactly similar to the configuration of root system. This figure presents a maximum pore-water pressure head of -90000 cm within the slope, where the root image density ratio is at its maximum. By comparing the Figure 7.24 and 7.25, it can again be seen that the pattern of the influenced pore-water pressure area by the drying process is much the same as the heartroot-morphology. A clear variation of water table occurred under the influenced pore-water area. The response of water table indicates that the soil water is extracted towards the tree root from regions outside of root zone. In this simulation, the largest change of the soil moisture content is about 22.8%, where the volumetric moisture content decreased from an initial value of 47.0% (fully saturated) to 24.2% after 270 days of transpiration.

Figure 7.26 shows the slope stability analysis results of Simulation 4 – with a minimum factor of safety of 2.218 that corresponds to a slip surface of radius 31.468 m and of origin $x = 17.901$ m, $z = 38.702$ m. Figure 7.26 also presents a factor of safety of 4.281 that corresponds a slip surface which is the same as the critical slip surface of Simulation 1. It is clear that simply comparing this value with that of Simulation 1 the factor of safety increases by 99.3 % (from 2.148 to 4.281). The results indicated that for Simulation 4, the failure surface has been changed with

respect Simulation 1 and the lowest factor of safety of the slope increases to 2.218 with an increase of 3.26 %. However, it should be noticed that the improvement in the lowest factor of safety of the slope shown here is not significant.
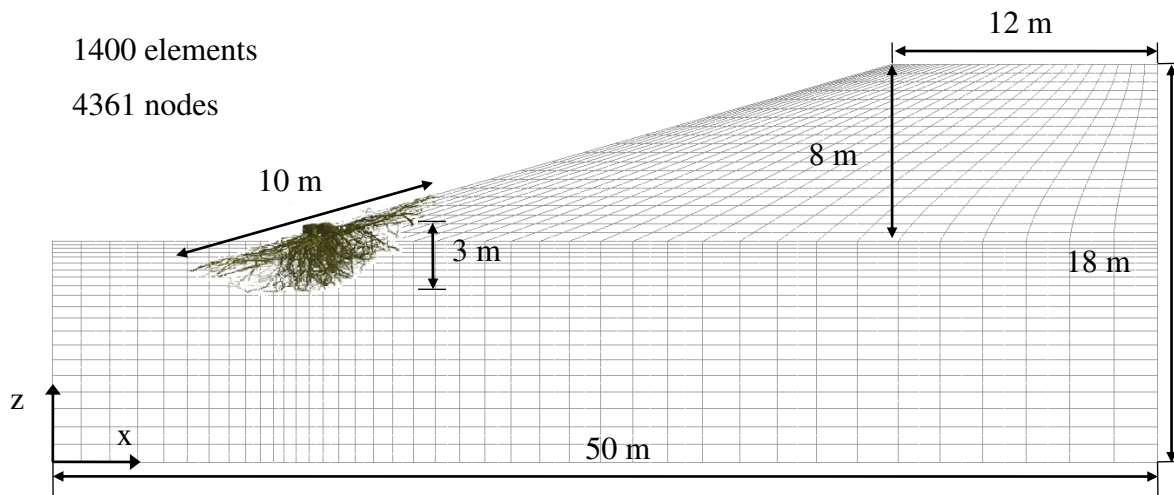


Figure 7. 23    Simulation 4 and 6:  Oak tree with heartroot-morphology nearer to the toe of slope
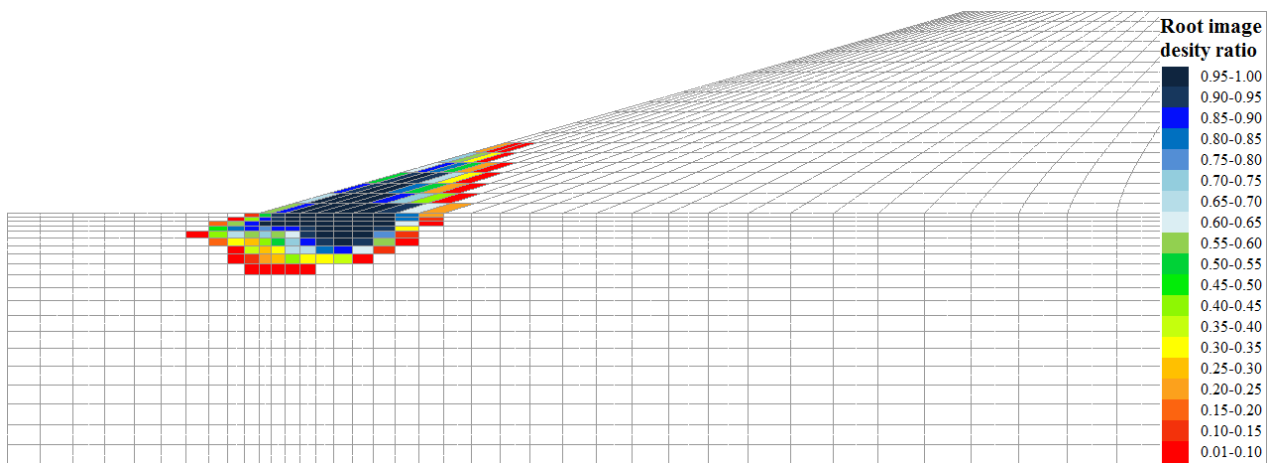


Figure 7. 24    Simulation 4:  Root image density ratio
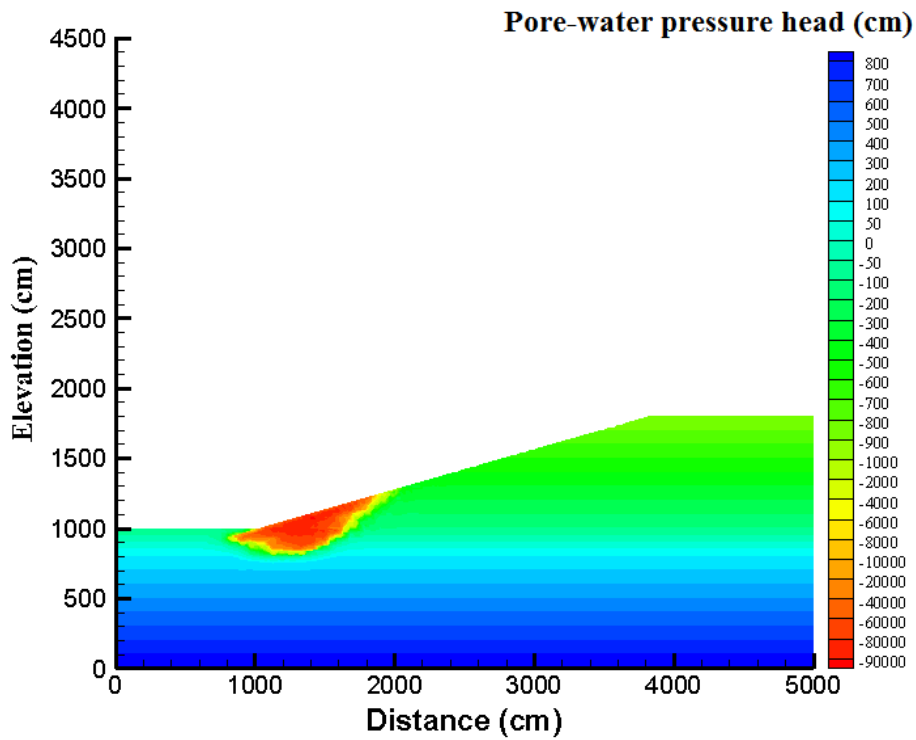
Figure 7. 25    Simulation 4:   Contour plots of pore-water pressure head (cm) at 270

days
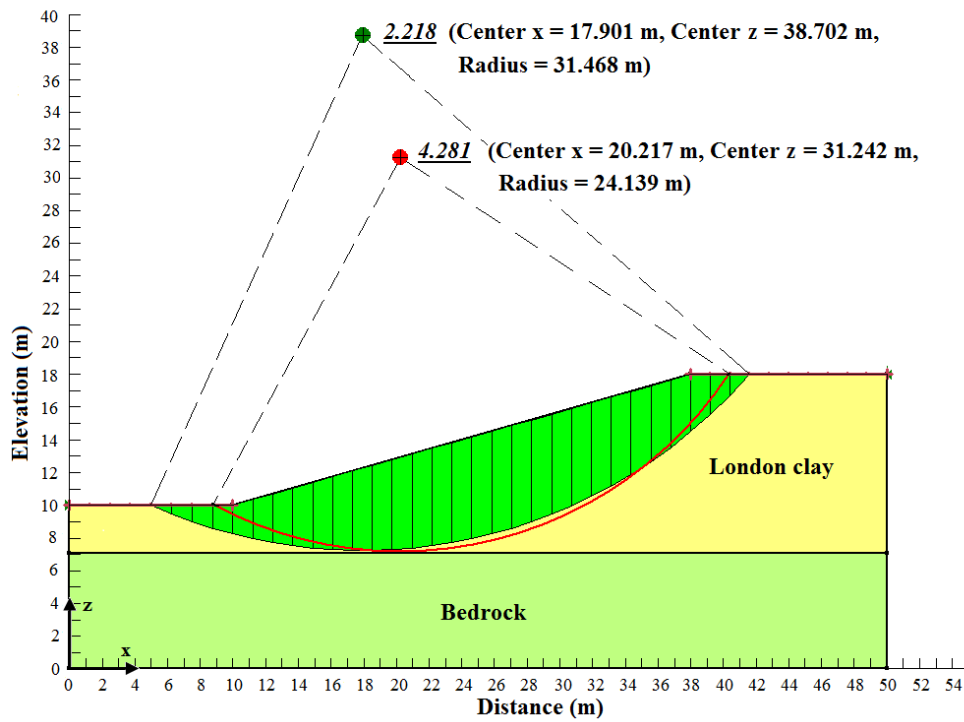


Figure 7. 26    Simulation 4:  Identification of the Critical Slip Surface

**Simulation 5**

A graphical representation of taproot-morphology positioned nearer the toe of the slope is shown in Figure 7.27 and the corresponding image density ratio is presented in Figure 7.28. Figure 7.29 presents the simulated contour plots of pore water pressure head generated at the end of the simulation 5 (at 270 days). This figure shows a maximum pore-water pressure head of -130000 cm within the slope that correspond the root image density ratio is at its maximum. It is clear that the profile of pore-water pressure changed region within the slope is the same as the configuration of root zone. A little variation in the water table occurred under the influenced pore-water area, which indicates that the soil water is extracted towards the tree root from regions outside of root zone. In this simulation, the largest change of soil moisture content is about 23.5 %. At this position, the volumetric moisture content reduced from an initial value of 47.0 % to 23.5 % after 270 days of transpiration.

The results of the slope stability analysis are shown in Figure 7.30 with a lowest factor of safety of 2.302 corresponding to a slip surface of radius 30.695 m and of origin $x = 16.029$ m, $z = 38.132$ m. It has an increase of 7.17 % with respect to Simulation 1 after 270 days of water-uptake by the oak tree in Simulation 5. Figure 7.30 also indicates a factor of safety of 5.209 relates to a slip surface where at the same location of critical slip surface in Simulation 1. It is clear that the factor of safety increases of 142.5 % (from 2.148 to 5.209) for that slip surface. The results indicate that the factor of safety against failure surface of the bare slope increased

significantly as the soil water reduction and consequently the shear strength increased in the soil.
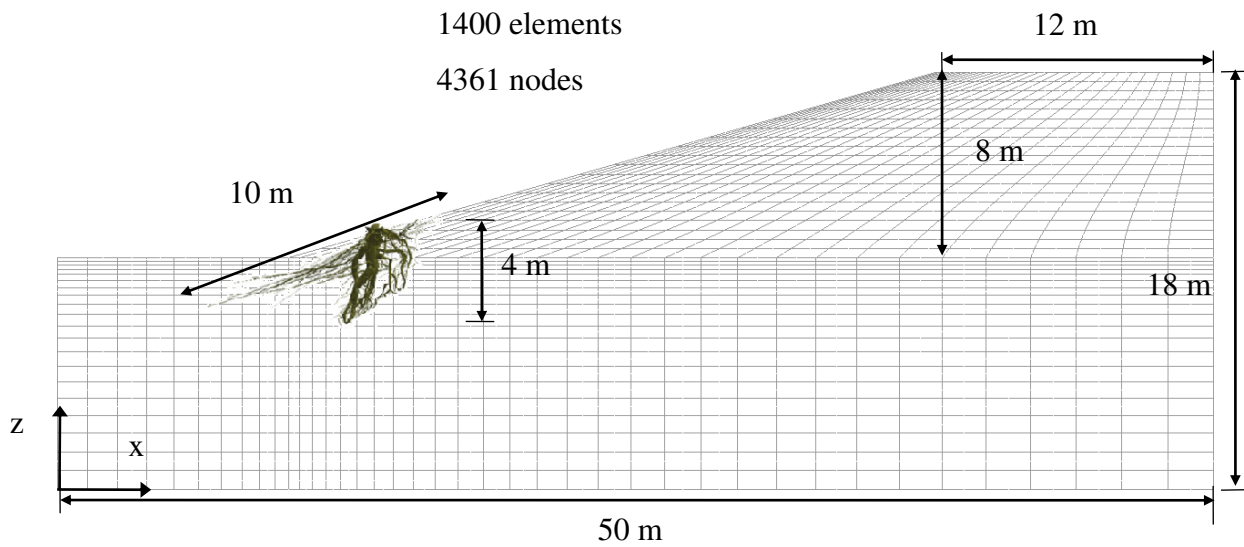


Figure 7. 27    Simulation 5 and 7:   Oak tree with taproot-morphology nearer to the toe of slope
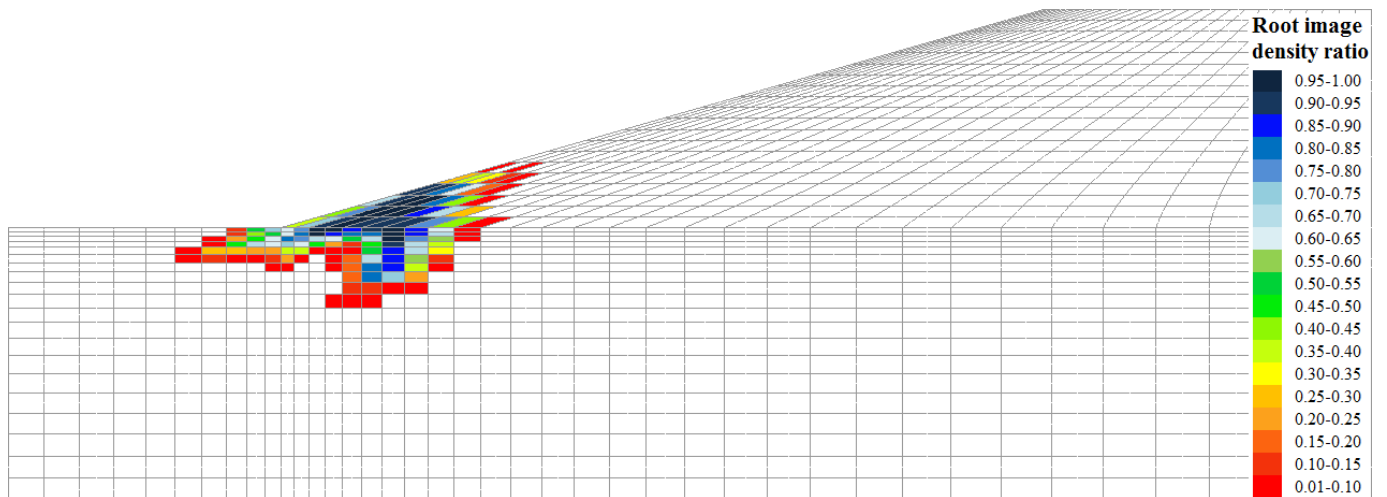


Figure 7. 28    Simulation 5:  Root image density ratio
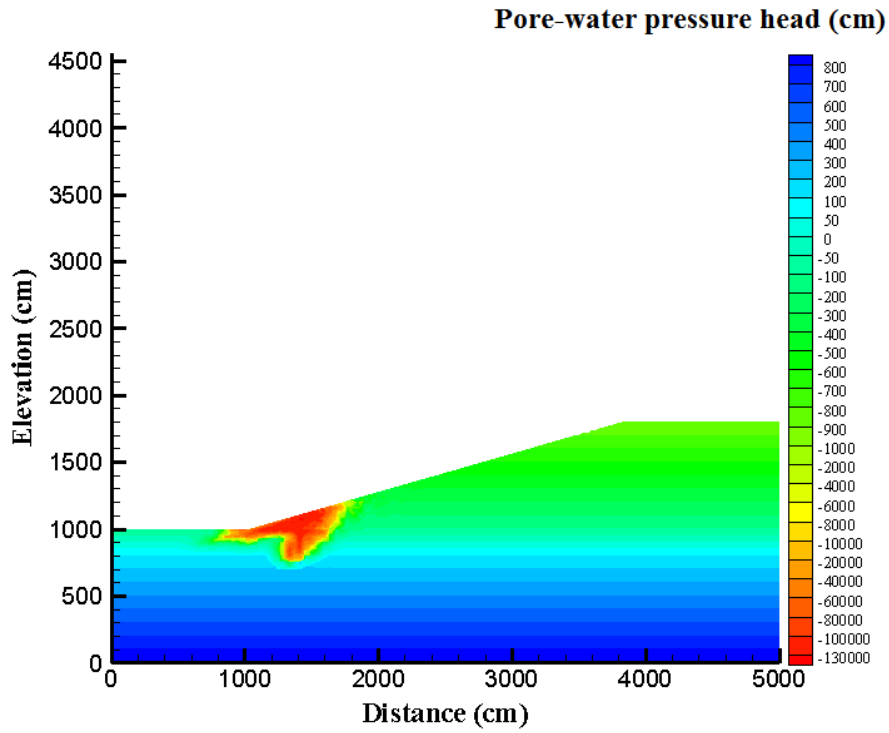
Figure 7. 29    Simulation 5:  Contour plots of pore-water pressure head (cm) at 270

days
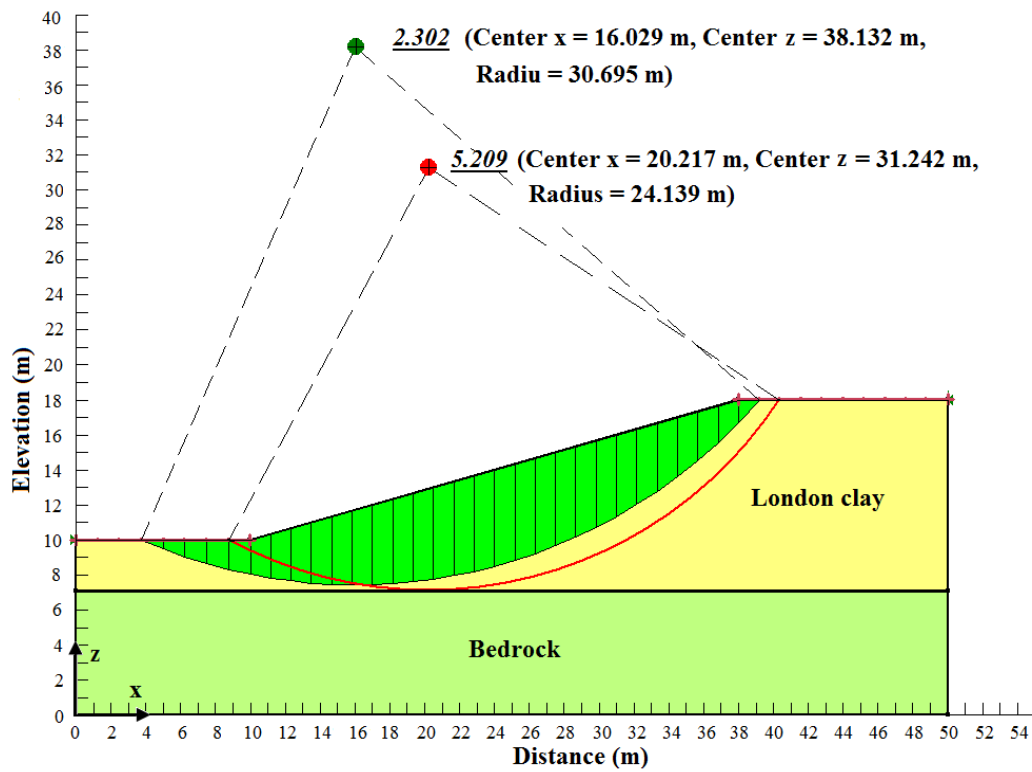


Figure 7. 30    Simulation 5:  Identification of the Critical Slip Surface

**Simulation 6**

For Simulation 6, a diagrammatic representation of the heartroot configuration positioned much nearer the toe of the slope than Simulation 4 and the corresponding image density ratio is presented in Figure 7.31. The simulated results (at 270 days) from the first stage of the procedure presented as contour plots are shown in Figure 7.32. This figure presents a maximum capillary potential of -80000 cm within the slope, where the root image density ratio is at its maximum. It can be seen that the shape of the affected pore-water pressure area by the process of transpiration is quite similar as the configuration of root zone employed in Simulation 6. In Figure 7.32, a clear variation of water table has been shown under the influenced pore-water area. The response of water table indicates that the water is extracted and depleted by the process of transpiration. The largest change moisture content (22.7%) generated by the tree located nearer the toe of the slope. At this location the volumetric moisture content reduced from an initial value of 47.0% to 24.3% after 270 days of transpiration.

Figure 7.33 shows a minimum factor of safety of 2.286 for Simulation 6 after considering 1089 possible failure surfaces. It is clear that the critical slip surface for Simulation 1 (no tree water uptake) has been changed to a failure slip surface of radius 31.502 m and of origin $x$ = 16.678 m, $z$ = 38.727 m at the end of simulated period and the factor of safety increases of 261.7 % (from 2.148 to 7.770) at that slip surface. Again the results indicate that the factor of safety against the failure slip surface of the bare slope increased significantly as the soil water reduction and consequently the suction increased in the soil. From these results it can be seen that

the lowest factor of safety in Simulation 6 has an increase of 6.42 % in comparison to the results of Simulation 1 (from 2.148 to 2.286).
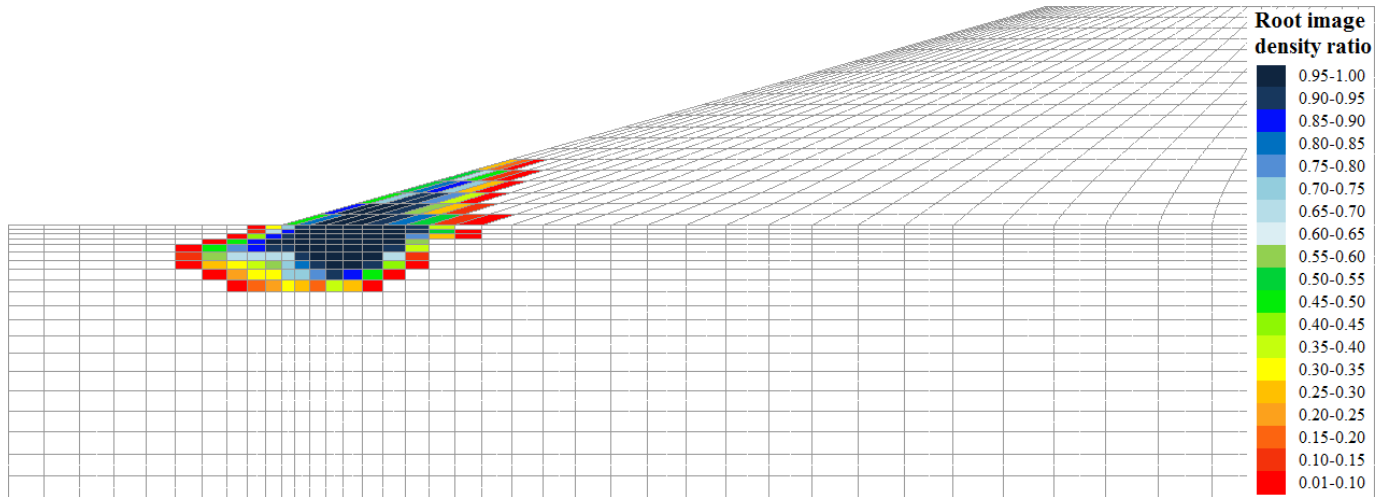


Figure 7. 31    Simulation 6:  Root image density ratio
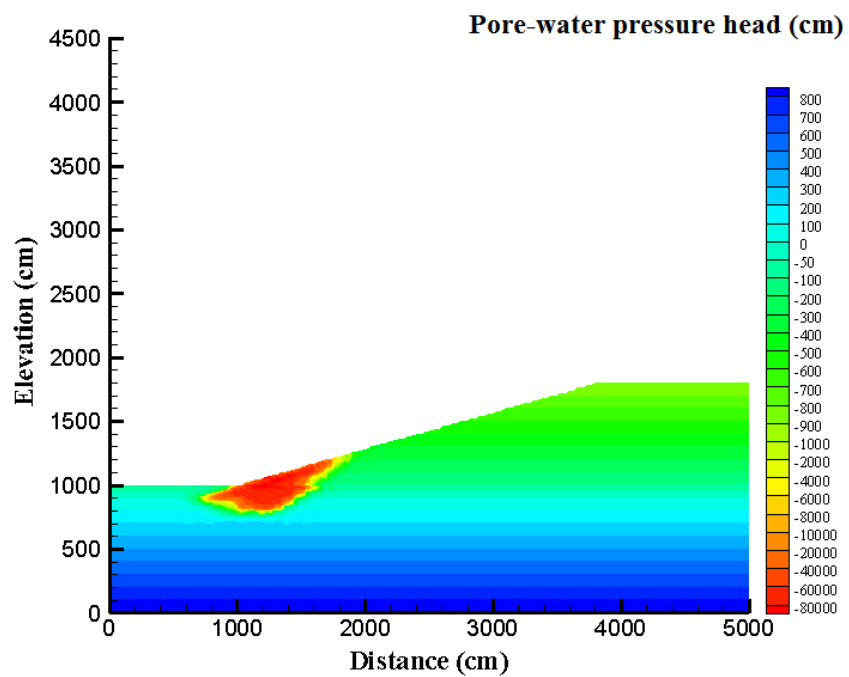


Figure 7. 32    Simulation 6:  Contour plots of pore-water pressure head (cm) at 270 days
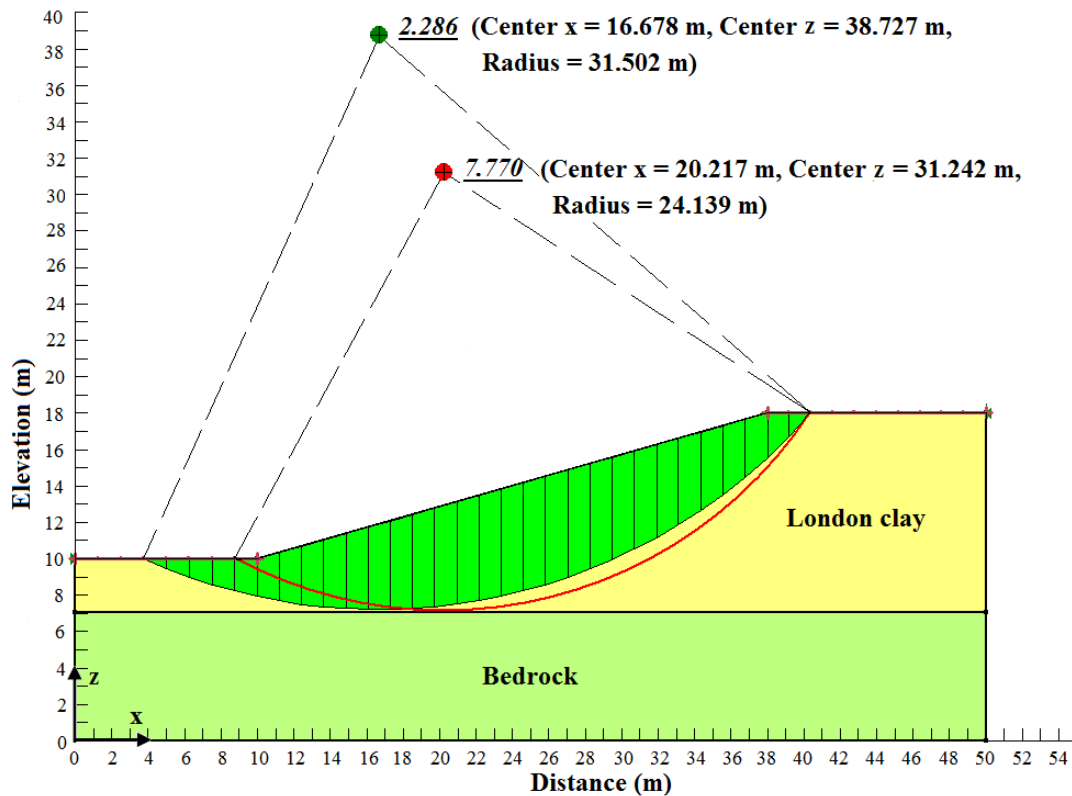
Figure 7. 33    Simulation 6:  Identification of the Critical Slip Surface

## Simulation 7

For Simulation 7, the root image density ratio based on the taproot-morphology and location on the simulated domain is presented in Figure 7.34.  The simulated results from the first stage of the procedure presented as contour plots of pore-water pressure head at 270 days are shown in Figure 7.35.  It shows a maximum pore-water pressure head of -140000 cm within the slope, where the root image density ratio is at its maximum.  The largest change moisture content (23.9%) generated by the tree at the mid-slope.  At this location the volumetric moisture content reduced from an initial value of 47.0% to 23.1% after 270 days of transpiration.  By comparing with the previous simulations, it can be seen that Simulation 7 has contributed the most

significant change of water content, at the deepest location of the slope in relation to the configuration of root zone.  It is also clear that the fluctuation of water table takes place within the slope and reflects the water is draw and depleted by the tree during the process of transpiration.
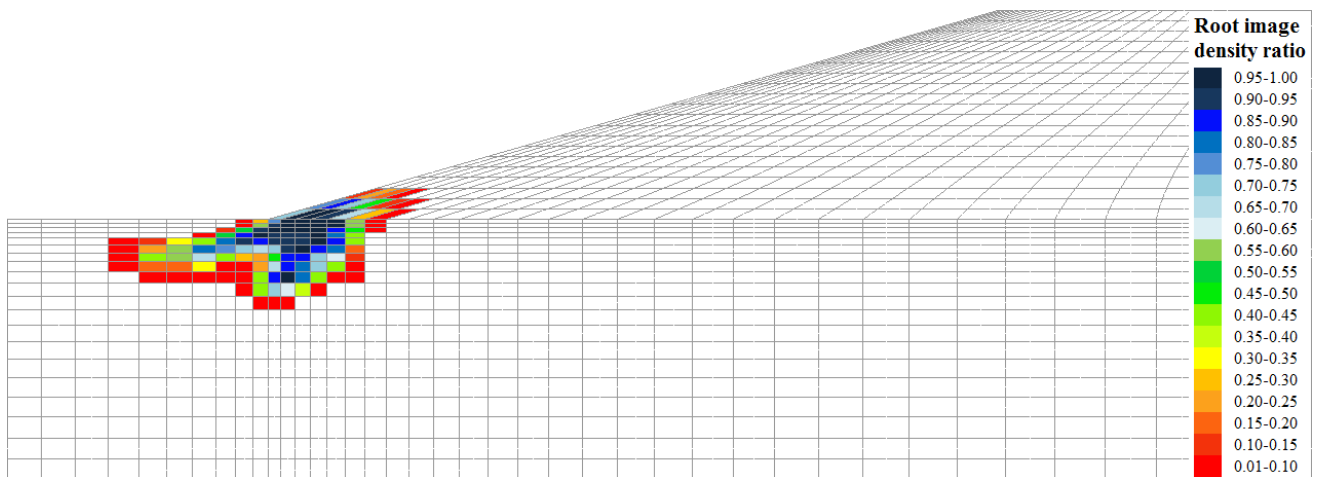


Figure 7. 34    Simulation 7:  Root image density ratio
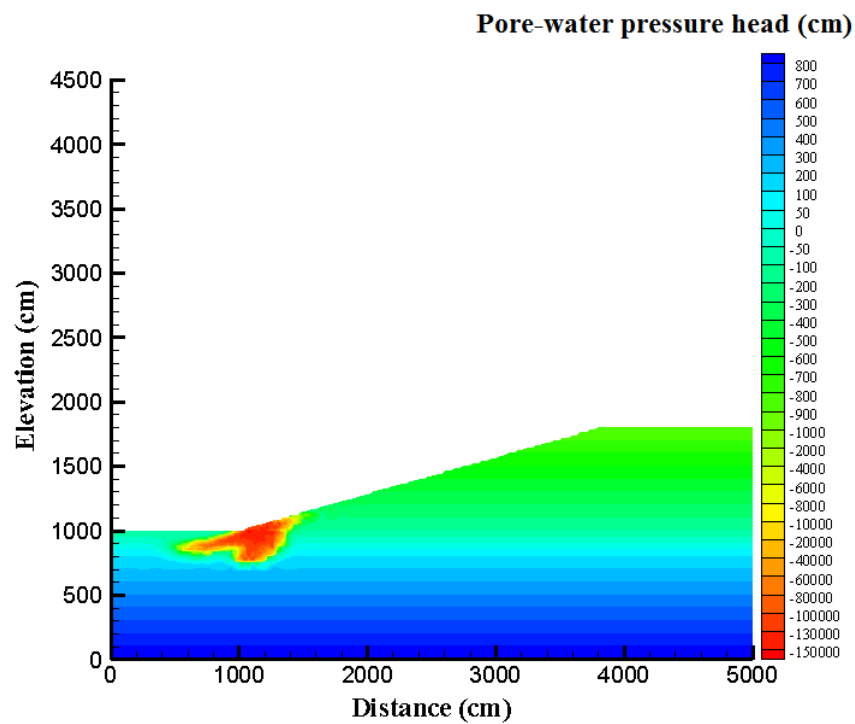


Figure 7. 35    Contour plots of pore-water pressure head (cm) at 270 days in Simulation 7

In Figure 7.36, the factor of safety for a slip surface (red colour) with respect to Simulation 1 has been increased, compared to the reference value (2.148), by 340.18 %. It is clear that the most significant variation in the minimum factor of safety occurred in Simulation 7, when an oak tree with taproot-morphology located nearer the toe of the slope – generating an increase of 80.63 % (from 2.148 to 3.880). It is clear that the radius of the most critical slip surface has been increased by 94.05 % and it indicates that the possibility of slope failure has been reduced.
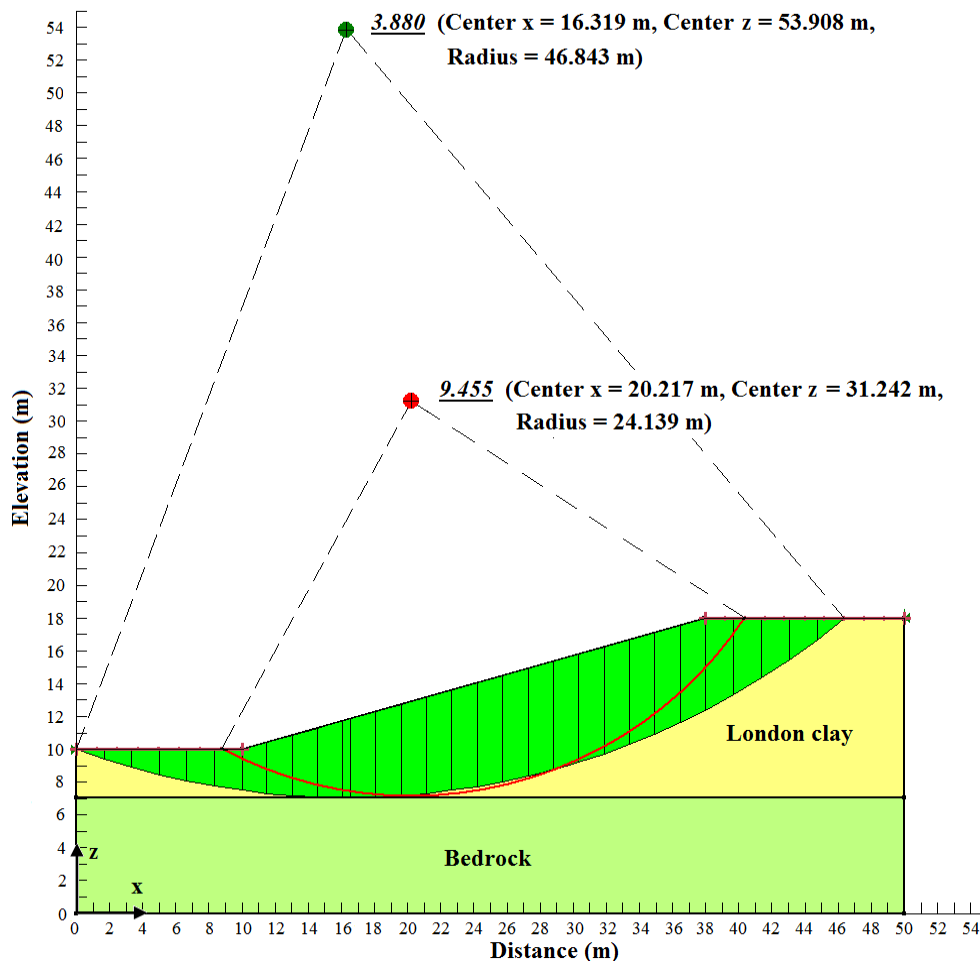


Figure 7. 36    Identification of the Critical Slip Surface for Simulation 7

In the present study, the results of water-uptake model, in terms of pore-water pressures, were used to study the effect of the vegetation on the stability of the slope.

The application of the sink term in the water uptake model applies within the root zone and soil water is free to migrate towards the tree from regions outside of this zone. Therefore some drying of the slope can be expected from these scenarios. However, the simulated results showed little variation of the groundwater table due to the low soil permeability in this case study. It is also recognized that further refinement of the boundary conditions employed to deal with more complex positions of groundwater table within the slope may be necessary in practice. A reduction factor for the potential transpiration rate is not considered in this study. Slope failure is often triggered by the rainfall which infiltrated into the soil slope and decreases soil suction, as the result of the shear strength of the soil. Therefore, it is recognized that further study would be necessary to consider the effect of rainfall on the soil slope. Some hydrological other parameters such as evaporation, grass cover, surface runoff can also affect the distribution of pore-water pressure within a vegetated slope and the overall slope stability. The contributions of these factors are excluded in this study but may be considered in the future.

7.3.6   Summary of Factor of Safety Variations

In Table 7.3, a comparison of the factors of safety for each simulation and the percentage difference when compared to a typical slope in the absence of any trees is provided. It shows the various conditions considered, the types of tree root architecture, the position of tree in terms of coordinates, the values of the factor of safety and the position of the critical slip surface.

The comparisons of factor of safety for the critical slip surface have been made according to the presence of a tree (taproot or heartroot-architecture) at various locations on the slope. During the root water uptake, the variation in pore-water pressure distributions has a marked change between the bare slope and the vegetated slope. According to Simulation 2, it is clear that the influences of heartroot-morphology positioned at mid-slope on slope stability are negligible. The results also indicate the factor of safety against slip failure increases by 3.21 % from 2.148 to 2.217 when the tree with taproot-architecture located at mid-slope. Based on the performance of the two types of root architecture located at mid-slope, it can be found that different root architectures show little difference when the tree presented at mid-slope.

Table 7. 3     Comparison of Factor of Safety at Various Conditions

| CONDINTIONS | DESCRIPTION | Factor of Safety | PERCENTAGE DIFFERENCE (%) | CRITICAL SLIP SURFACE |
|---|---|---|---|---|
| Unsaturated slope | S1-slope with no tree water uptake | 2.148 | 0.00% | $x = 20.217$ m, $z = 31.242$ m, radius $= 24.139$ m |
| Tree at centre of slope | S2-tree with heartroot, position of tree: coordinate $x = 27.5$ m, $z = 15.0$ m | 2.148 | 0.00% | $x = 20.217$ m, $z = 31.242$ m, radius $= 24.139$ m |
| | S3-tree with taproot, position of tree: coordinate $x = 27.5$ m, $z = 15.0$ m | 2.217 | 3.21% | $x = 18.994$ m, $z = 31.260$ m, radius $= 24.168$ m |
| Tree near the toe of slope | S4-tree with heartroot, position of tree: coordinate $x = 13.6$ m, $z = 11.0$ m | 2.218 | 3.26% | $x = 17.901$ m, $z = 38.702$ m, radius $= 31.468$ m |
| | S5-tree with taproot, position of tree: coordinate $x = 14.6$ m, $z = 11.4$ m | 2.302 | 7.17% | $x = 16.029$ m, $z = 38.132$ m, radius $= 30.695$ m |
| | S6-tree with heartroot, position of tree: coordinate $x = 12.0$ m, $z = 10.6$ m | 2.286 | 6.42% | $x = 16.678$ m, $z = 38.727$ m, radius $= 31.502$ m |
| | S7-tree with taproot, position of tree: coordinate $x = 11.5$ m, $z = 10.4$ m | 3.880 | 80.63% | $x = 16.319$ m, $z = 53.908$ m, radius $= 46.843$ m |

*The factor of safety for Simulation is 2.148 which is used as reference to compute the percentage difference of factor of safety for other conditions.

Further factor of safety comparisons have been made according to the presence of a tree nearer to the toe of slope. It is clear that the most significant variation in the factor of safety occurred when the tree is nearer to the toe of slope. From these results

it can be seen that taproot architecture water uptake nearer to the toe of slope can increase the lowest factor of safety in the range from 7.17 % to 80.63 %, since the location of tree in Simulation 7 is much nearer to the toe of slope than that in Simulation 5. Among the two types of root architectures, it is clear that the taproot-morphology located nearer to the toe (Simulation 7) shows the most significant improvement on slope stability. This is due to the fact that the majority of pore-water pressure change induced by taproot occurs at the deepest location of the slope. For a given transpiration rate, inside the root zone, the deeper the root depth, the deeper position of the variation of the pore-water distributions induced in the soil. The results from Simulation 7 also indicated that the factor of safety against failure surface of the bare slope increased significantly – 340.18 % as the suction increased in the soil. The deeper roots of tree would be more beneficial from the point of view that roots recover water storage capacity by drying the soil zone containing roots substantially. It may conclude that tree species with taproot architecture should be chosen for the purposes of lowering pore-water pressure and increasing shear strength of soil to prevent failure in the slope.

## 7.4    CONCLUSIONS

The chapter provided a generalised assessment of the significance of water content (and therefore suction) changes on the stability of unsaturated soil slopes. Two typical root architectures were considered to investigate the influence of root architecture on slope stability. In particular, effects of root architecture were emphasized.

Considering typical slope geometry, a range of tree root architectures (heartroot and taproot) and two locations of a tree on the slope have been considered. These were, i) a tree located at mid-slope and ii) a tree located nearer to the toe of the slope. The numerical results in terms of pore-water pressure head have been presented. It is therefore, clear that exact variations in moisture content/pore-water pressure are highly dependent on the architecture of root system.

A comparison of the factor of safety for different tree root architectures and locations was also made. The percentage change in factor of safety was shown to depend, to some extent, on the root architecture of the tree and the precise position of the tree. The results illustrated that for all simulations, the factor of safety significantly increased due to the reduction of water content in a vegetated soil slope. For example, the factor of safety from Simulation 7 against failure surface of the bare slope increased significantly – 340.18 % (from 2.148 to 9.455) due to drying of the soil slope caused by the tree. The study indicated that the suction generated by a tree with taproot-architecture much nearer to the toe of slope may significantly increase the lowest factor safety up to 80.63 %. It can be concluded that the deeper root system would be more beneficial on improving slope stability.

This is viewed as a significant contribution in the overall assessment of the influence of root architectures on the stability of slopes – but is the result of soil moisture variations driven by transpiration only. It is recognised that the results studied here only serve to provide an indication of the significance of this aspect of the problem. Clearly further research would be required to focus on more wide areas (more complicated vegetation, soil properties and slope geometry).

7.5    REFERENCES

Croney, D. 1977. *The design and performance of road pavements*. London: Her Majesty's Stationery Office.

Danjon, F. Barker, D. H. Drexhage, M. and Stokes, A. 2008. Using Three-dimensional Plant Root Architecture in Models of Shallow-slope Stability. *Annals of Botany*. 101, pp. 1281-1293.

Fredlund, D. G. Morgenstern, N. R. and Widger, R. A. 1978. The shear strength of unsaturated soils. *Canadian Geotechnical Journal*. 15, pp. 313-321.

Fredlund, D. G. and Rahardjo, H. 1993. *Soil Mechanics of Unsaturated Soils*. New York: John Wiley & Sons.

Hinckley, T. M. Teskey, R. O. Duhme, F. and Richter, H. 1981. Temperate Hardwood Forests. In: Kozlowski, T. T. eds. *WATER DEFICITS AND PLANT GROWTH*. 1981. London: Academic Press, pp. 154-197.

Smethurst, J. A. Clarke, D. and Powrie, W. 2006. Seasonal changes in pore water pressure in a grass-covered cut slope in London Clay. *Géotechnique*. 56 (8), pp. 523-537.

Smethurst, J. A. Clarke, D. and Powrie, W. 2012. Factors controlling the seasonal variation in soil water content and pore water pressures within a lightly

vegetated clay slope. *Géotechnique.* 40, pp. 643-660.

Urban, J. 2010. *How Deep Do Tree Roots Grow?* [Online]. Available at: http://www.deeproot.com/blog/blog-entries/how-deep-do-tree-roots-grow [Accessed: 18 October 2014].

Vanapalli, S. K. Fredlund, D. G. and Clifton, A. W. 1996. Model for the prediction of shear strength with respect to soil suction. *Canadian Geotechnical Journal.* 33, pp. 379-392.

# CHAPTER EIGHT

# CONCLUSIONS

## 8.1   OVERALL CONCLUSIONS

The overall objectives and limitations of the current research were described in Chapter 1.   It is claimed that the overall objectives have been successfully accomplished.

In this research, the main aim was to develop a new root density based approach to modelling water uptake by plants.  To this end, the proposed image-based approach avoids imposition of an artificial root zone geometry that is common in alternative methods.  The theoretical basis development of an image based root-density approach utilized a digitized image of the root zone to determine an 'effective root density ratio' that is subsequently employed to yield a spatially variable root water extraction over the active root zone.  It therefore offers the potential to include natural root

morphology within the modelling process. A series of case studies have demonstrated that the proposed model is capable of representing field behaviour of water uptake by crops and a single tree. The model has been validated by direct comparison to published field measurements. Overall, a good correlation between field data and simulated results has been achieved. It is believed that the image-based root density approach achieves better quality results than those from a simple linear approach and maintains a root pattern that is closer to the real field condition. Therefore, the implementation of the water-uptake model and the associated sink term with a newly proposed image-based root density approach has been successfully undertaken. This approach can be extended for application to a wide range of geotechnical problems.

The new water-uptake model was combined with slope stability analysis to investigate how suctions generated by a tree may contribute to the overall stability. It was also found that the influence of root-architecture and the locations of trees can have a significant influence on the stability of unsaturated soil slopes. Specifically, the study illustrated that suctions generated by a tree with clear taproots positioned near to the toe of slope had the largest improvement on stability of slope.

In conclusion, this study has provided a useful contribution on modelling the water-uptake process and on the overall assessment of slope stability.

## 8.2    FUTURE RESEARCH

The current approach has been presented to be capable of generating reasonable results for the range of problems considered.  However, some suggestions of the further development and refinement of the current approach arise if application to a wider range of problems should be considered.

The image based model described here has been shown operating in 1D, 2D, and 2D-axisymetic applications.  However, development of a three-dimensional model form of the model is feasible.  This requires re-casting the moisture transfer model in 3D form and developing the corresponding 3D FE numerical solution.  The image-based distribution of transpiration would also require further work to extend it to full 3D mode.  This is an achievable but not insignificant task.  Furthermore, validation of the resulting model will be challenging because of a distinct lack of experimental/field data.

The current work was established for potential application to a wide range of geo-engineering problems as described in Chapter 1.  The application of the approach requires some form of image of the root zone that can be digitized to determine a spatially variable 'effective root density ratio'.  However, it is recognized that the ultimate success of this approach is dependent on the quality of available root image data and this is clearly an area that would benefit from further research.

In addition, the new approach has been applied using radial symmetry which assumes that root density of plant has uniformity in the radial direction.  In reality the root

density of most plants will exhibit some variation radially and with depth. This apparent limitation of the current model appears to be 'averaged' out to the extent that it does not appear to significantly affect the overall water extract patterns around the root zone. However, it is thought that this area should be considered in further detail and some further refinement of the current approach may be necessary.

Since the current work was focused on the behaviour of crops for short time period and established mature trees, the vegetation was considered of astatic nature in the current model. The inclusion of root growth functions in the current model may prove a useful for future applications of taking into account the root decay, root regrowth after harvesting, temporal nature of root dynamics and trait expression.

All of the current modelling work assumed homogenous soil profiles. However, it is clear that the field conditions may often include a variation with depth of soil properties. Although in the cases considered here this did not appear to be particularly significant, in other applications more detailed consideration of this assumption may be necessary.

The results presented here were based on the assumption of a constant volume (no deformation) soil model. However, it is known that in some cases seasonal variations in water content result in shrinkage and swelling of the soil – where there is a clear link between moisture content change and volume change. Some examples where a coupled flow and deformation approach would be useful include; i) the assessment of the influence of trees in relation to foundation movements, which can damage

domestic buildings, or ii) disturbance to rail track geometry resulting in train speed restrictions for the rail industry.

The slope stability work presented in the Chapter 7 maintained the traditional 2D-plane simplification of the slope based on an assumption that a line-source of moisture extraction applied. It aims to provide some indication of the influence of vegetation on stability, although it is also clear that a much more complex moisture migration may exist in a number of field problems.

In the analysis of water uptake on slope stability, the groundwater table was assumed 1 m below the section of slope. Future applications could be considered to explore conditions with variable groundwater table position. In addition, the current work has been limited to the assessment of slope stability considering a single tree on the slope with no other vegetation (grass or more trees) included in the framework. Although this study aimed to provide some indication of the influence of tree locations and tree root architectures on stability, further study of transpiration rate (different trees), more complex soil properties and slope geometry would be appear necessary.

The stability calculations presented in this research only considered hydrological effects related to soil moisture variations driven by transpiration. Mechanical effects that arise from the tensile strength of roots and the weight of vegetation were excluded here. Therefore, it is clear that the inclusion of both hydrological and mechanical effects would become necessary in the further research of influence of the presence of trees on slope safety.

In the future, more applications may need to consider an annual climate conditions, particularly in a changing climate, within the assessment of stability in addition to the presence of trees and/or other vegetation. It may also help with the condition assessment and maintenance prioritisation of railway/road embankments and cuttings – especially where planting or removal of vegetation is involved.

**APPENDIX 1**



**ROOT DENSITY RATIO CALCULATION**

The numerical evaluation of the root density ratio was coded in Matlab. The resulting values were then used to define the spatial variation of the sink term within the finite element code. The relevant Matlab code is as follows:

```
function result=dataread(rowsize1,colsize1,rowsize2,colsize2,bar,xmin,xmax,ymin,ymax,dist)
for ElementNo=1:1400
I=load('C:\Users\KS\Documents\MATLAB\node.txt');
n1=I(ElementNo,1);
n2=I(ElementNo,2);
n3=I(ElementNo,3);
n4=I(ElementNo,4);
n5=I(ElementNo,5);
n6=I(ElementNo,6);
n7=I(ElementNo,7);
n8=I(ElementNo,8);
M=load('C:\Users\KS\Documents\MATLAB\meshdata.txt');
x1mesh=M(n1,1);
y1mesh=M(n1,2);
x2mesh=M(n2,1);
y2mesh=M(n2,2);
x3mesh=M(n3,1);
y3mesh=M(n3,2);
x4mesh=M(n4,1);
y4mesh=M(n4,2);
x5mesh=M(n5,1);
y5mesh=M(n5,2);
x6mesh=M(n6,1);
y6mesh=M(n6,2);
x7mesh=M(n7,1);
y7mesh=M(n7,2);
x8mesh=M(n8,1);
y8mesh=M(n8,2);
x=[x1mesh,x2mesh,x3mesh,x4mesh,x5mesh,x6mesh,x7mesh,x8mesh];
y=[y1mesh,y2mesh,y3mesh,y4mesh,y5mesh,y6mesh,y7mesh,y8mesh];
fill(x,y,'k');
axis([xmin xmax ymin ymax]);
set(gca,'position',[0 0 1 1]);
set(gca,'xtick',[],'ytick',[]);
saveas(gcf,'C:\Users\KS\Documents\MATLAB\sp1.jpg');
densityinmesh=rootinmesh(rowsize1,colsize1,rowsize2,colsize2,bar,dist)/meshpoint(rowsize1
,colsize1);
result=[ElementNo,densityinmesh];
save('C:\Users\KS\Documents\MATLAB\re.txt','result','-ascii','-double','-append');
end
end

function result = rootinmesh(rowsize1,colsize1,rowsize2,colsize2,bar,dist)
```

```
A=imread('C:\Users\KS\Documents\MATLAB\sp1.jpg');
I=rgb2gray(A);
B=imresize(I,[rowsize1,colsize1]);
for i=1:rowsize1
   for j=1:colsize1
     if B(i,j)==255
        B(i,j)=0;
     else B(i,j)=1;
      end
   end
end

P=imread('C:\Users\KS\Documents\MATLAB\sp2.jpg');
C=rgb2gray(P);
for i=1:rowsize2
   for j=1:colsize2
     if C(i,j)> bar
        C(i,j)=0;
     else C(i,j)=1;
      end
   end
end
F=zeros(rowsize2,dist);
G=zeros(rowsize2,colsize1-colsize2-dist);
H=zeros(rowsize1-rowsize2,colsize1);
J=[F,C,G;H];
E=B.*J;

result=sum(sum(E));

function s=meshpoint(rowsize1,colsize1)
a=imread('C:\Users\KS\Documents\MATLAB\sp1.jpg');
b=rgb2gray(a);
c=imresize(b,[rowsize1,colsize1]);

for i=1:rowsize1
   for j=1:colsize1
     if c(i,j)==255
        c(i,j)=0;
     else c(i,j)=1;
      end
   end
end
s=sum(sum(c));
```

**APPENDIX 2**

**EXAMPLE CALCULATION
FOR MATERIAL PROPERTY NON-LINEARITY**

The numerical solution algorithm incorporates material property non-linearity. In the code, this is achieved by adopting an average calculation based on the models of van Genuchten (1980) and Mualem (1976).

For example: if $\psi = -100cm$ and the soil properties defined as the below table, the average calculation is as follows:

Table A2-1    Parameters    defining    the    water    retention    curve    and    hydraulic conductivity for sandy loam soil

| $\theta_r$ | $\theta_s$ | $K_s$ (cm/s) | $\alpha$ (cm$^{-1}$) | $n$ | $l$ | $m$ |
|---|---|---|---|---|---|---|
| 0.039 | 0.440 | 0.00009693626 | 0.027 | 1.449 | -0.861 | 0.310 |

An estimate of the hydraulic conductivity function for the soil is determined utilizing the water retention curve obtained from the model of van Genuchten (1980) and the pore size distribution model provided by Mualem (1976):

$$K(\psi) = K_s \frac{\left[\left(1 + |\alpha\psi|^n\right)^m - |\alpha\psi|^{n-1}\right]^2}{\left(1 + |\alpha\psi|^n\right)^{m(l+2)}}$$

$$K(\psi) = 0.00009694 \frac{\left[\left(1 + |0.027(-100)|^{1.45}\right)^{0.31} - |0.027(-100)|^{1.45-1}\right]^2}{\left(1 + |0.027(-100)|^{1.45}\right)^{0.31(-0.86+2)}} = 0.0000006299188(cm/s)$$

The water retention curve is defined by van Genuchten's (1980) method:

$$\theta(\psi) = \theta_r + \frac{\theta_s - \theta_r}{\left(1 + |\alpha\psi|^n\right)^m}$$

$$\theta_1 = 0.039 + \frac{0.44 - 0.039}{\left(1 + |0.027(100 + 1)|^{1.45}\right)^{0.31}} = 0.2796068$$

$$\theta_2 = 0.039 + \frac{0.44 - 0.039}{\left(1 + |0.027(100 - 1)|^{1.45}\right)^{0.31}} = 0.2813527$$

The specific moisture capacity $C(\psi)$ is determined numerically as $C(\psi) = \frac{\theta_2 - \theta_1}{\Delta\psi}$,

thus:

$$C(\psi) = \frac{\theta_2 - \theta_1}{2} = \frac{0.2813527 - 0.2796068}{2} = 0.00087295$$

**APPENDIX 3**

**A PHOTOGRAPHIC SURVEY OF SEASONAL CANOPY CHANGES FOR LIME TREES**
(***Tilia x europaea***)

*Note. The following photographs of Lime trees (Tilia x europaea) were taken at Pontcanna Fields, Cardiff during the period March to November in 2014.*

Figure A3-1.   Lime tree - *Tilia x europaea* (Tree No. 2)

Figure A3-2.   Lime tree - *Tilia x europaea* (Tree No. 3)

Figure A3-3.   Lime tree - *Tilia x europaea* (Tree No. 4)

Figure A3-4.   Lime tree - *Tilia x europaea* (Tree No. 5)

March | April | May
June | July | August
September | October | November
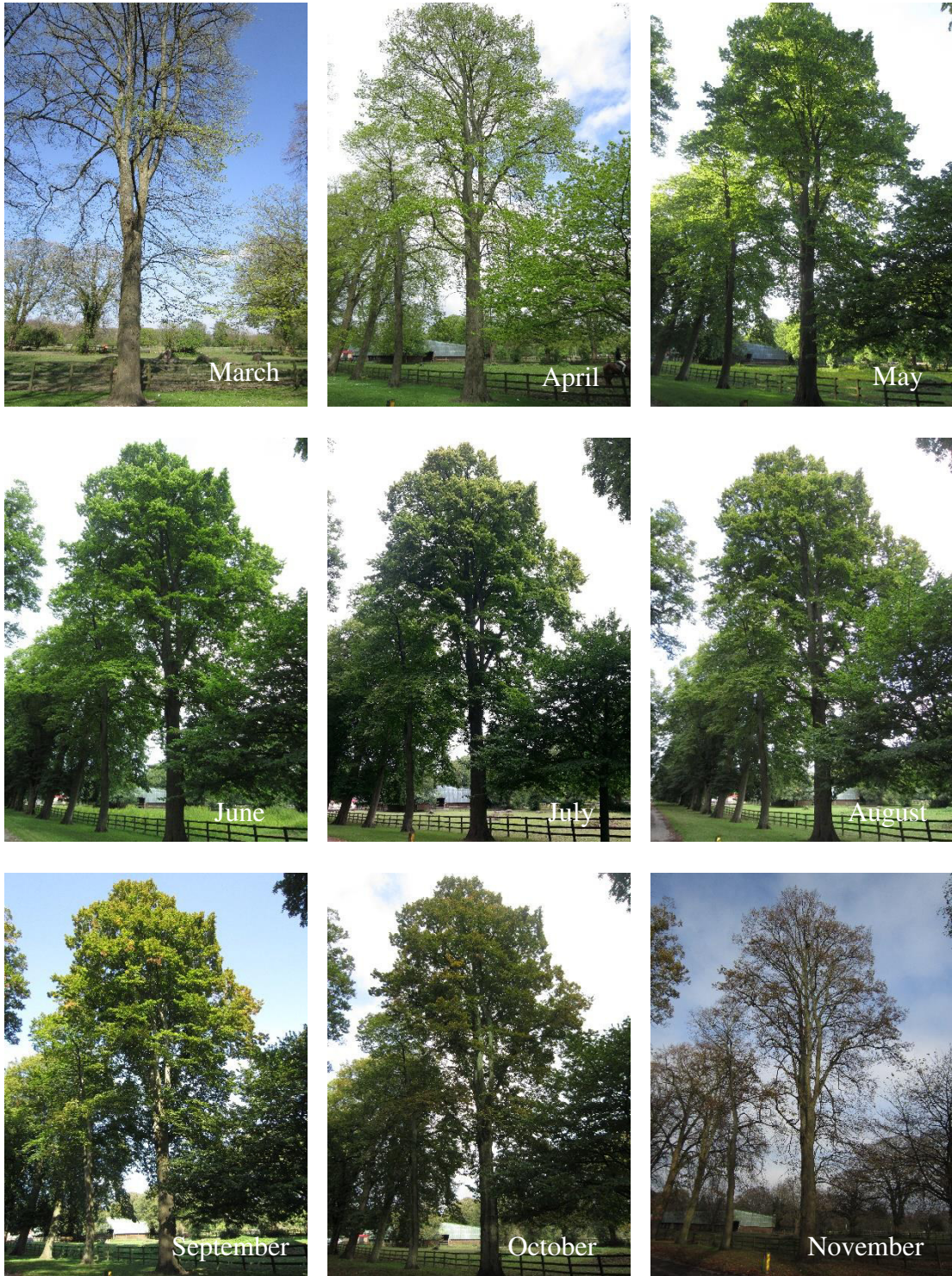
Figure A3-5.   Lime tree - *Tilia x europaea* (Tree No. 6)

Figure A3-6.   Lime tree - *Tilia x europaea* (Tree No. 7)

Figure A3-7.   Lime tree - *Tilia x europaea* (Tree No. 8)

Figure A3-8.   Tree No. 1 (Canopy change from March to November in 2014)

Figure A3-9.   Tree No. 2 (Canopy change from March to November in 2014)

Figure A3-10. Tree No. 3 (Canopy change from March to November in 2014)

Figure A3-11. Tree No. 4 (Canopy change from March to November in 2014)

Figure A3-12. Tree No. 5 (Canopy change from March to November in 2014)

Figure A3-13. Tree No. 6 (Canopy change from March to November in 2014)

Figure A3-14. Tree No. 7 (Canopy change from March to November in 2014)

Figure A3-15. Tree No. 8 (Canopy change from March to November in 2014)

# APPENDIX 4

## EXAMPLE CALCULATION
## FOR ESTIMATING TRANSPIRATION RATE

*Note. The purpose of this appendix is to provide the background information that has been employed elsewhere in the thesis for the determination of transpiration rates. Since much of this related to the long established Penman-Monteith approach it was thought that this material was better placed in an appendix.*

## Estimating Transpiration Rate

The Penman-Monteith (PM) equation for transpiration from a single hypostomatous leaf (the stomata are present only on the lower surface of the leaves) can be written as (Thorpe, 1978):

$$\lambda E_{leaf} = \frac{\Delta R_{n,leaf} + 0.93 \rho_a c_p \frac{(e_s - e_a)}{r_a}}{\Delta + 0.93 \gamma (2 + r_s / r_a)} \qquad (A4\text{-}1)$$

Where, $E_{leaf}$ is the transpiration rate per unit leaf area (kg m$^{-2}$ day$^{-1}$), $R_{n,leaf}$ is the net radiation flux density absorbed by the leaf, $(e_s - e_a)$ represents the vapour pressure deficit of the air; $\rho_a$ is the mean air density at constant pressure; $c_p$ is the specific heat of the air; $\Delta$ represents the slope of the saturation vapour pressure temperature relationship; $\gamma$ is the psychrometric constant; $r_s$ is the surface resistance which describes the resistance of vapour flow through stomata openings, total leaf area and soil surface; $r_a$ is the aerodynamic resistance which describes the resistance from the vegetation upward and involves friction from air flowing over vegetative surfaces. $\lambda$ is known as the latent heat of vaporization and is a function of the water temperature. For example, at 20°C, $\lambda$ is approximately 2.45 MJ kg$^{-1}$. In other words, 2.45 MJ are needed to vaporize 1 kg or 0.001 m$^3$ of water. Hence, an energy input of 2.45 MJ per m$^2$ is able to vaporize 0.001 m or 1 mm of water, and therefore 1 mm of water is equivalent to 2.45 MJ m$^{-2}$.

In Equation A4-1, the factor 0.93 represents the ratio between the boundary layer conductance for water vapor and for sensible heat (Thorpe 1978, Monteith and

Unsworth 1990, Green 1993, Caspari et al. 1993), but rounding it to unity (Green and McNaughton 1997, Green et al. 2003a, b) makes little difference in practical terms because of the many uncertainties introduced in the parameterization of the other variables, as described in the sequence.

The factor 2 on the bottom of Equation (A4-1) arises because leaves are hypostomatous, with heat loss occurring from both sides of the leaf and transpiration occurring from just one side ((Butler 1976, Thorpe 1978, Green 1993, Caspari et al. 1993, Edwards and Warwick 1984, Green et al. 2003a, b, Green and McNaughton 1997, Zhang et al. 1997, Pereira et al. 2006).

The transpiration rate for a whole tree can be found by summing Equation (A4-1) over the population of leaves on the trees (Jones et al. 1988, Green 1993, Caspari et al. 1993, Zhang et al. 1997). For an approximation, hypostomatous leaves exposed to air with a uniform saturation deficit, the equation can be written as the sum of the fluxes from all of the leaves so that:

$$\lambda E_{tree} = L \frac{\Delta R_{n,tree} + 0.93 \rho_a c_p \dfrac{(e_s - e_a)}{r_a}}{\Delta + 0.93 \gamma (2 + \overline{r_s}/r_a)} \qquad \text{(A4-2)}$$

Where $L$ is the total leaf area of the tree canopy, $\overline{r}_s$ is the measured mean stomatal resistance within the tree canopy, $R_{n,tree}$ is the net radiation absorbed per unit leaf area, and $E_{tree}$ is the transpiration rate for a whole tree (kg day$^{-1}$ or litre day$^{-1}$). The total

leaf area of the common lime tree (*Tilia x europaea*) canopy is 132.65 m$^2$ (Rogers et al. 2012).

There are only a few cases where the net radiation absorbed by leaves of single trees has been measured (Butler 1976, Thorpe 1978, Jones et al. 1988, McNaughton et al. 1992, Green 1993).  In these studies, the regression coefficient between the average net radiation absorbed per unit leaf area and the net radiation per unit land area above the trees ranged from 0.33 to 0.75 for a range of tree sizes.  Equation (A4-3) was assumed to estimate radiation absorbed by per unit leaf area of the trees (Butler 1976, Thorpe 1978, Jones et al. 1988, Zhang et al. 1997) because no direct measurements were available for absorption by the tree canopy:

$$R_{n,tree} = 0.5R_n \qquad\qquad\qquad\qquad\qquad\qquad\qquad\qquad \text{(A4-3)}$$

Where, $R_n$ is the net radiation above the grass.  The error introduced by this approximation is likely to be small because the radiation term contributes less than 30% to total transpiration (Thorpe 1978, Green 1993, Zhang 1997).

Leaf boundary resistance can be calculated from an empirical relation derived by Landsberg and Powell (1973), which accounts for the mutual sheltering of clustered leaves as:

$$r_a = 58P^{0.56}(d/u)^{0.5} \qquad\qquad\qquad\qquad\qquad\qquad\qquad \text{(A4-4)}$$

Where, *d* is a characteristic leaf dimension (leaf width, m). In this case, the leaves of lime tree are 6–12 cm broad. *u* is the mean wind speed (m s$^{-1}$) across the leaf surface, if the (average) daily wind speed (m s$^{-1}$) measured is not available, the wind speed could be assumed at 2 m s$^{-1}$ in the current case. *P* is a measure of foliage density to wind given by the ratio of total leaf plan area (38 m$^2$) to the area of the foliage projected onto a vertical plane (42 m$^2$).

Table A4-1. Meteorological data required by Penman-Monteith equation for daily calculations (Allen et al. 2006).

| | |
|---|---|
| ***Location*** | Altitude above sea level (m) and latitude (degrees north or south) of the location should be specified. |
| ***Temperature*** | The (average) daily maximum and minimum air temperatures in degrees Celsius (°C) are required. |
| ***Humidity*** | The actual vapor pressure is required. If it is not available, can be derived from the maximum and minimum relative humidity (%), psychrometric data (dry and wet bulb temperatures in °C) or dewpoint temperature (°C) according to the procedures outlined in the below. |
| ***Radiation*** | The daily net radiation (MJ m$^{-2}$ day$^{-1}$) is required. These data are not commonly available but can be derived from the shortwave radiation measured with a pyranometer. The calculation procedures are outlined in the below. |
| ***Wind speed*** | The (average) daily wind speed (m s$^{-1}$) measured is required. If it is not available, the wind speed can be simply assumed at 2 m s$^{-1}$. |
| ***Missing climatic data*** | Radiation data can be derived from the air temperature difference, or, along with wind speed and humidity data, can be imported from a nearby weather station. Humidity data can also be estimated from daily minimum air temperature. |

Therefore, it is clear that the methods for calculating transpiration from meteorological data require various climatological and physical parameters. Some of the data are measured directly in weather stations. Others are related to commonly

measured data and can be derived with the help of a direct or empirical relationship. Table A4-1 provide some further information.

The atmospheric pressure (*P*) is the pressure exerted by the weight of the earth's atmosphere. A simplification of the ideal gas law, assuming 20°C for a standard atmosphere, can be employed to calculate *P*:

$$P = 101.3 \left( \frac{293 - 0.0065z}{293} \right)^{5.26} \tag{A4-5}$$

Where, *P* atmospheric pressure (kPa), *z* elevation above sea level (m). In this study, the site of lime tree is located at Stacey Hall, Wolverton, UK and the elevation above sea level is 92 m.

The psychrometric constant $\gamma$, is given by:

$$\gamma = \frac{c_p P}{\varepsilon \lambda} = 0.665 \times 10^{-3} P \tag{A4-6}$$

Where, $\gamma$ is the psychrometric constant (kPa°C$^{-1}$), $\lambda$ latent heat of vaporization, 2.45 (MJ kg$^{-1}$), $c_p$ is the specific heat at constant pressure, 1.013×10$^{-3}$ (MJ kg$^{-1}$ °C$^{-1}$), $\varepsilon$ is the ratio molecular weight of water vapour/dry air (0.622), the atmospheric pressure (*P*) is calculated by Equation (A4-5).

Equation (A4-6) can be rearranged:

$$c_p = \frac{\gamma \varepsilon \lambda}{P} \tag{A4-7}$$

And considering the ideal gas law for $\rho_a$ :

$$\rho_a = \frac{P}{T_{Kv}R} \tag{A4-8}$$

Where, $T_{Kv}$ is the virtual temperature, which may be substituted by:

$$T_{Kv} = 1.01(T + 273) \tag{A4-9}$$

Results in: $c_p \rho_a = \dfrac{\gamma \varepsilon \lambda}{1.01(T + 273)R}$ $\tag{A4-10}$

Where, $c_p$ is the specific heat at constant pressure (MJ kg$^{-1}$ °C), $\rho_a$ is the mean air density at constant pressure (kg m$^{-3}$), $R$ is the specific gas constant (0.287 kJ kg$^{-1}$ K$^{-1}$).

As saturation vapour pressure is related to air temperature, it can be calculated from the air temperature. The relationship is expressed by:

$$e^0(T) = 0.6108 \exp\left[\frac{17.27T}{T + 237.3}\right] \tag{A4-11}$$

Where, $e^0(T)$ is the saturation vapor pressure at the air temperature $T$ (kpa), $T$ is air temperature (°C).

From the above equation, the mean saturation vapor pressure ($e_s$) could be calculated as the mean between the saturation vapour pressure at the mean daily maximum and minimum air temperatures for a day, week, month or decade:

$$e_s = \frac{e^0(T_{max}) + e^0(T_{min})}{2} \qquad \text{(A4-12)}$$
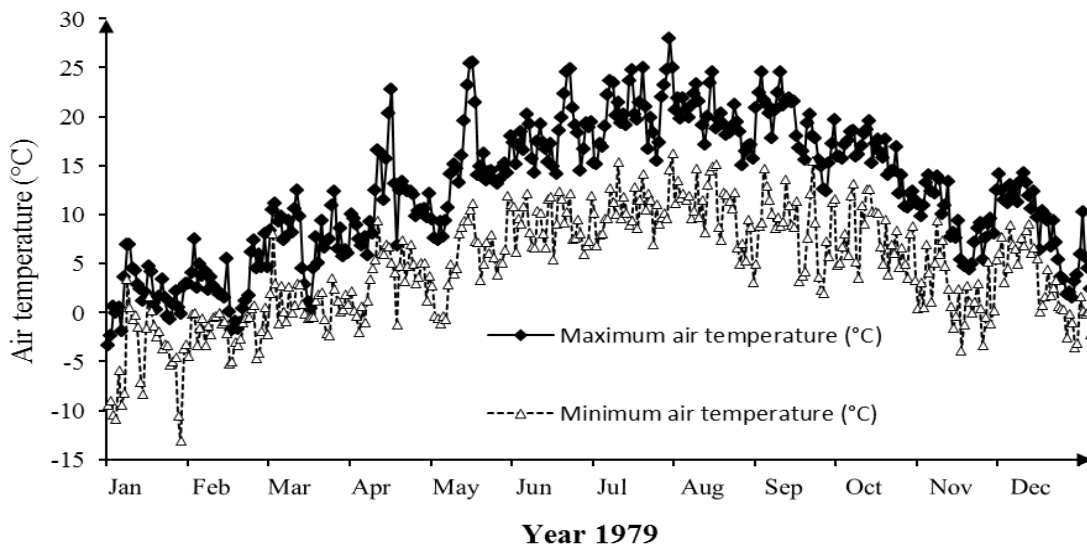


Figure A4-1. Measured maximum and minimum air temperature of the weather station (British Atmospheric Data Centre).

The measured maximum and minimum air temperature provided by the British Atmospheric Data Centre has been acquired for the nearest weather station to the site (Grendon Underwood, Buckinghamshire, UK). Figure A4-1 shows the temperature data recorded at Grendon Underwood for the year of 1979 under consideration here.
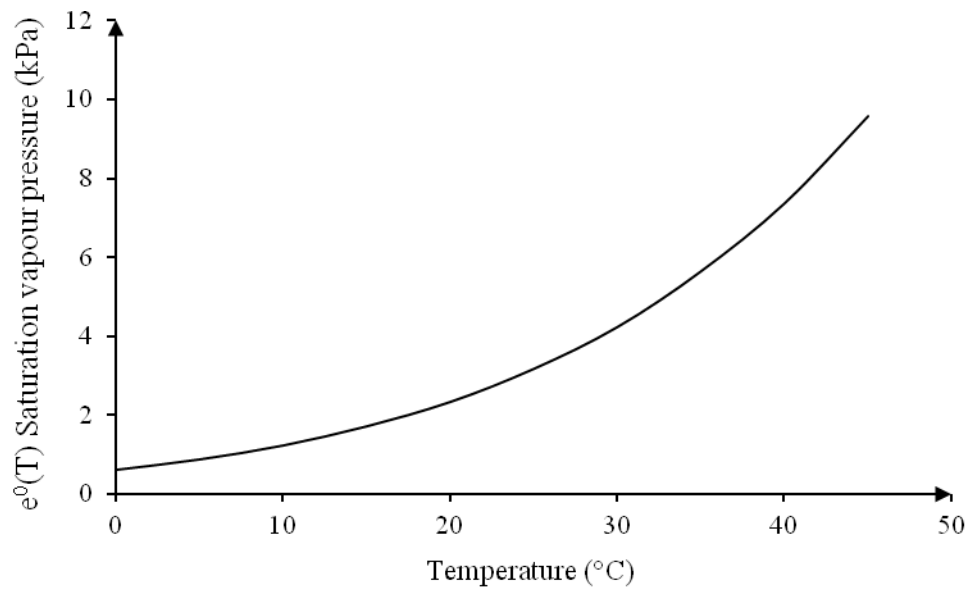
Figure A4-2.   Saturation vapour pressure shown as a function of temperature: $e^0(T)$ curve (Allen et al. 2006).

For the calculation of transpiration, the slope of the relationship between saturation vapour pressure and temperature ($\Delta$) is required (see Figure A4-2). The slope of the curve at a given temperature is given by:

$$\Delta = \frac{4098 \left[ 0.6108 \exp\left( \dfrac{17.27T}{T + 237.3} \right) \right]}{(T + 237.3)^2} \tag{A4-13}$$

Where, $\Delta$ is the slope of saturation vapour pressure curve at air temperature $T$ (kPa°C$^{-1}$) calculated using mean air temperature.

It is not possible to directly measure the actual vapour pressure ($e_a$) but it can be obtained in terms of the dew-point temperature given by:

$$e_a = e^0(T_{dew}) = 0.6108\exp\left[\frac{17.27T_{dew}}{T_{dew}+237.3}\right] \tag{A4-14}$$

The actual vapor pressure can also be calculated from the relative humidity. The choice of approach depends on the availability of the humidity data.

$$e_a = \frac{e^0(T_{min})\left[\dfrac{RH_{max}}{100}\right] + e^0(T_{max})\left[\dfrac{RH_{min}}{100}\right]}{2} \tag{A4-15}$$

Where, $e_a$ is actual vapour pressure (kPa), $e^0(T_{min})$ saturation vapour pressure at daily minimum temperature (kPa), $e^0(T_{max})$ saturation vapour pressure at daily maximum temperature (kPa), $RH_{max}$ maximum relative humidity (%), $RH_{min}$ minimum relative humidity (%).

Where humidity data are lacking or are of questionable quality, an estimate of actual vapour pressure can be obtained by assuming that the dewpoint temperature ($T_{dew}$) is near the daily minimum temperature ($T_{min}$). This statement implicitly assumes that the air is nearly saturated with water vapour and the relative humidity is nearly 100% when the air temperature is close to $T_{min}$ (Allen et al. 2006). If $T_{min}$ is used to represent $T_{dew}$ then:

$$e_a = e^0(T_{min}) = 0.6108\exp\left[\frac{17.27T_{min}}{T_{min}+237.3}\right] \tag{A4-16}$$

Therefore, the vapor pressure deficit $(e_s - e_a)$ is the difference between the saturation and an actual vapor pressure for a given time period and it can be calculated by the above equations.
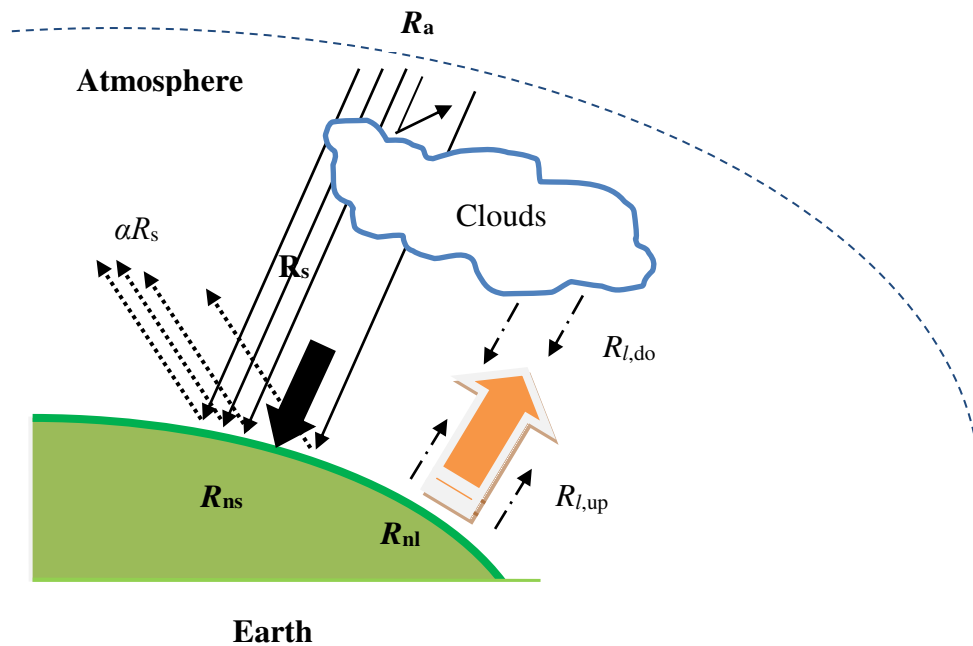


Figure A4-3.   Various components of radiation (after Allen et al. 2006)

The solar radiation received at the top of the earth's atmosphere on a horizontal surface is termed the extraterrestrial radiation ($R_a$) (Allen et al. 2006).  Some of the radiation is scattered, reflected or absorbed by the atmospheric gases, clouds and dust when the radiation penetrates the atmosphere.  The remaining amount of radiation is known as the solar radiation or shortwave radiation ($R_s$).  The solar radiation is roughly 75% of extraterrestrial radiation under a cloudless day while about 25% of that may still reach the earth's surface even with extremely dense cloud cover (Allen et al. 2006).  Some solar radiation is absorbed by the earth and converted to heat

energy. Then the earth starts to lose this heat energy and emits longwave radiation. The net longwave radiation ($R_{nl}$) means the difference between the incoming net shortwave and the net outgoing longwave and represents an energy loss from the earth's surface due to outgoing longwave radiation is almost always greater than the incoming longwave radiation (Allen et al. 2006). The net radiation ($R_n$) is the balance between the energy absorbed, reflected and emitted by the earth's surface and the difference between incoming and outgoing radiation of both short and long wavelengths (Allen et al. 2006). Those various components of radiation are illustrated in Figure A4-3.

Common units used to express energy received on a unit surface per unit time, and conversion factors are summarized in Table A4-2.

Table A4-2. Conversion factors for radiation

|  | MJ m$^{-2}$ day$^{-1}$ | J cm$^{-2}$ day$^{-1}$ | cal cm$^{-2}$ day$^{-1}$ | W m$^{-2}$ | mm day$^{-1}$ |
|---|---|---|---|---|---|
| 1 MJ m$^{-2}$ day$^{-1}$ | 1 | 100 | 23.9 | 11.6 | 0.408 |
| 1 cal cm$^{-2}$ day$^{-1}$ | $4.1868 \times 10^{-2}$ | 4.1868 | 1 | 0.485 | 0.0171 |
| 1 W m$^{-2}$ | 0.0864 | 8.64 | 2.06 | 1 | 0.035 |
| 1 mm day$^{-1}$ | 2.45 | 245 | 58.5 | 28.4 | 1 |

The extraterrestrial radiation ($R_a$) for different latitudes can be estimated from the solar constant, the solar declination and the time of the year by:

$$R_a = \frac{24(60)}{\pi} G_{sc} d_r [\varpi_s \sin(\varphi)\sin(\delta) + \cos(\varphi)\cos(\delta)\sin(\varpi_s)] \qquad \text{(A4-17)}$$

Where, $R_a$ is the extraterrestrial radiation (MJ m$^{-2}$ day$^{-1}$), $G_{sc}$ is the solar constant which is equal to 0.082 MJ m$^{-2}$ min$^{-1}$, $d_r$ is the inverse relative distance Earth-Sun (Euquation A4-18), $\varpi_s$ is the sunset hour angle (Equation A4-20) and the unit is radian, $\varphi$ is the latitude (radian), $\delta$ is solar declination (Equation A4-19) and the unit is radian. The latitude of lime tree site (Stacey Hall, Wolverton, UK) is 52°3N.

The conversion from decimal degrees to radians is given by:

The inverse relative distance Earth-Sun $d_r$, and the solar declination, $\delta$, are given by:

$$d_r = 1 + 0.033\cos\left(\frac{2\pi}{365}J\right) \tag{A4-18}$$

$$\delta = 0.409\sin\left(\frac{2\pi}{365}J - 1.39\right) \tag{A4-19}$$

Where, $J$ is the number of the day in the year between 1 (1 January) and 365 (31 December).

The sunset hour angle $\varpi_s$ is given by:

$$\varpi_s = \arccos\left[-\tan(\varphi)\tan(\delta)\right] \tag{A4-20}$$

The data of solar radiation ($R_s$) provided by the British Atmospheric Data Centre has been acquired for the nearest weather station to the site (Rothamsted, Hertfordshire).

Figure A4-4 shows the solar radiation data recorded at Rothamsted for the year of 1979 under consideration here.
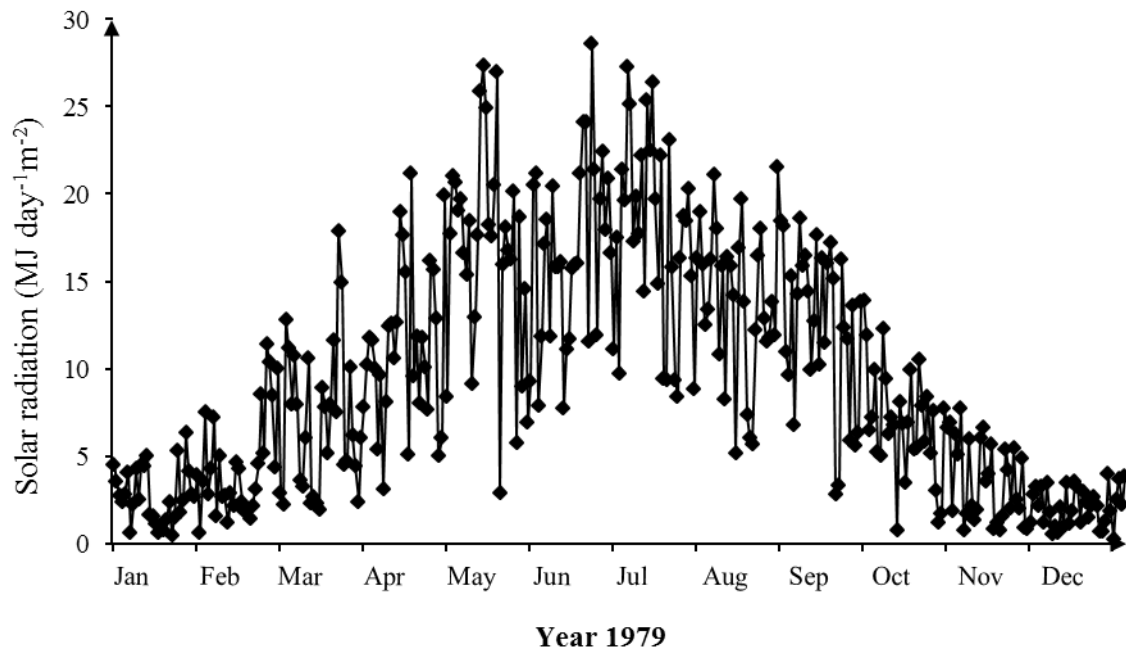


Figure A4-4. The measured solar radiation at the nearest weather station (British Atmospheric Data Centre)

The calculation of the clear-sky radiation is given by:

$$R_{so} = \left(0.75 + 2 \times 10^{-5} z\right) R_a \qquad \text{(A4-21)}$$

Where, z is the elevation above sea level of the site (92 m).

The net shortwave radiation resulting from the balance between incoming and reflected solar radiation is given by:

$$R_{ns} = (1 - \alpha)R_s \tag{A4-22}$$

Where, $R_{ns}$ is the net solar or shortwave radiation (MJ m$^{-2}$ day$^{-1}$), $\alpha$ is albedo or canopy reflection coefficient, which is 0.23 for the hypothetical grass reference crop (Allen et al. 2006).

The net outgoing longwave radiation equation can be written as (Allen et al. 2006):

$$R_{nl} = \sigma \left[ \frac{T_{max,K}^4 + T_{min,K}^4}{2} \right] \left( 0.34 - 0.14\sqrt{e_a} \right) \left( 1.35 \frac{R_s}{R_{so}} - 0.35 \right) \tag{A4-23}$$

Where, $R_{nl}$ is the net outgoing longwave radiation (MJ m$^{-2}$ day$^{-1}$), $\sigma$ is the Stefan-Boltzmann constant ($4.903 \times 10^{-9}$ MJ K$^{-4}$ m$^{-2}$ day$^{-1}$), $T_{max,K}$ maximum absolute temperature during the 24-hour period [K = °C + 273.16], $T_{min,K}$ minimum absolute temperature during the 24-hour period [K = °C + 273.16], $e_a$ actual vapour pressure [kPa], $R_s/R_{so}$ relative shortwave radiation (limited to ≤ 1.0). In Equation (A4-23), the term $\left( 0.34 - 0.14\sqrt{e_a} \right)$ expresses the correction for air humidity, and will be smaller if the humidity increases. The effect of cloudiness is expressed by $\left( 1.35 \frac{R_s}{R_{so}} - 0.35 \right)$.

The net radiation ($R_n$) is the difference between the incoming net shortwave radiation ($R_{ns}$) and the outgoing net longwave radiation ($R_{nl}$):

$$R_n = R_{ns} - R_{nl} \tag{A4-24}$$

The net radiation for a tree can be calculated by the Equation (A4-3) and the results are shown in Figure A4-5.
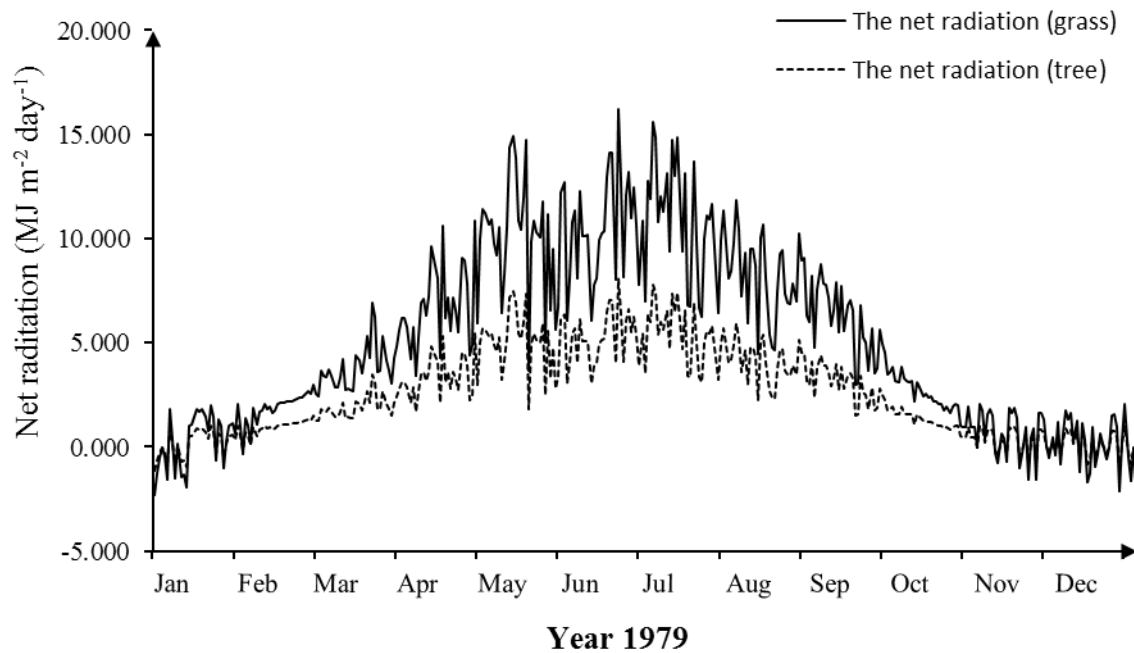


Figure A4-5.   The net radiation data

Since the average daily measured mean stomatal resistance ($r_s$) within the tree canopy is from 500 s m$^{-1}$ to 2000 s m$^{-1}$ (Tang et al. 2009, Martin et al. 1999, Jarvis 1976, Kelliher and Blacek 1986).

*Resulting Calculation of Transpiration:*

According to the above calculations and parameters data, the transpiration rate for a whole tree can be estimated. Figure A4-6 shows the resulting variation of maximum and minimum transpiration, for the entire leaf period of a deciduous tree at a site located at Stacey Hall, Wolverton, UK.
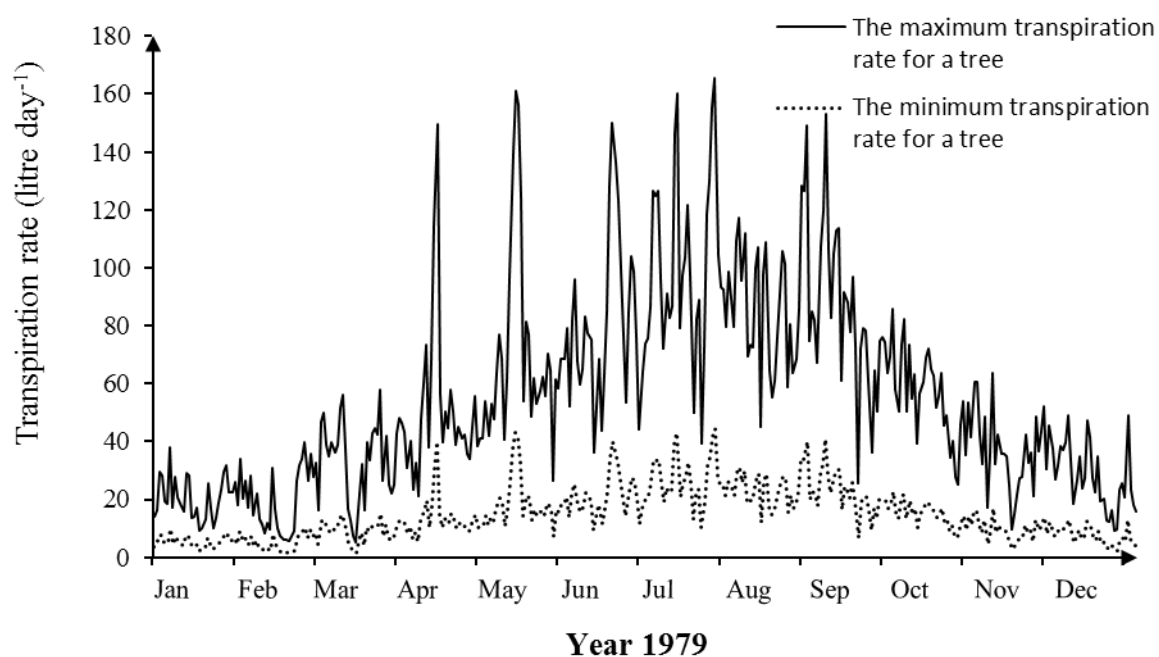


Figure A4-6.   The transpiration rate for a single lime tree

References:

Allen, R. G. Pereira, L. S. Raes, D. and Simth, M. 2006. *Crop Evapotranspiration (guidelines for computing crop water requirements).* FAO Irrigation and Drainage Paper No. 56.

Butler, D. R. 1976. Estimation of the transpiration rate in an apple orchard from net radiation and vapour pressure deficit measurements. *Agric. For. Meteorol*. 16, pp. 277-289.

Caspari, H. W. Green, S. R., Edwards, W. R. N. 1993. Transpiration of well-watered and water-stressed Asian pear trees as determined by lysimetry, heat-pulse, and estimated by a Penman-Monteith model. *Agric. For. Meteorol*. 67, pp. 13-27.

Edwards, W. R. N. Warwick, N. W. M. 1984. Transpiration from a kiwifruit vine as estimated by the heat-pulse technique and the Penman–Monteith equation. *NZ J. Agric. Res*. 27, pp. 537–543.

Green, S. R. 1993. Radiation balance, transpiration and photosynthesis of an isolated tree. *Agric. For. Meteorol*. 64, pp. 201-221.

Green, S. R. and McNaughton, K. G. 1997. Modelling effective stomatal resistance for calculating transpiration from an apple tree. *Agric. For. Meteorol*. 83, pp. 1–26.

Green, S. R. Clothier, B. Jardine, B. 2003a. Theory and practical application of heat-pulse to measure sap flow. *Agron. J*. 95, pp. 1371–1379.

Green, S. R. McNaughton, K. G. Wüsche, J. N. Clothier, B. 2003b. Modeling light interception and transpiration of apple tree canopies. *Agron. J*. 95, 1380–1387.

Jarvis, P. G. 1976. The interpretation of the variations in leaf water potential and stomatal conductance found in canopies in the field. *Phil. Trans. R. Soc. Lond. B*. 273, pp. 593-610.

Jones, H. G. Hamer, P. J. C. Higgs, K. H. 1988. Evaluation of various heat-pulse methods for estimation of sap flow in orchard trees: comparison with micrometeorological estimates of evaporation. *Trees: Structure and Function* 2, pp. 250-260.

Kelliher, F. M. and Black, T. A. 1986. Estimating the Effects of Understory Removal from a Douglas Fir Forest Using a Two-Layer Canopy Evapotranspiration Model. *Water Resources Research*. 22(13), pp. 1891-1899.

Landsberg, J. J. Powell, D. B. B. 1973. Surface exchange characteristics of leaves subject to mutual interference. *Agric. For. Meteorol*. 13, pp. 169-184.

Martin, T. Hinckley, T. M. Meinzer, F. C. and Sprugel, D. G. 1999. Boundary layer conductance, leaf temperature and transpiration of Abies amabilis branches. *Tree Physiology*. 19, pp. 435-443.

Monteith, J. L. and Unsworth, M. H. 1990. *Principles of Environmental Physics*. 2nd ed. Edward Arnold, London.

Pereira, A. R. Green, S. Nova, N. A. V. 2006. Penman–Monteith reference evapotranspiration adapted to estimate irrigated tree transpiration. *Agricultural Water Management* 83, pp. 153-161.

Rogers, K. Jaluzot, A. Neilan, C. 2012. *Green Benefits in Victoria Business Improvement District*. London: Victoria Business Improvement District.

Tang, J. Bolstad, P. V. Ewers, B. E. Desai, A. R. Davis, K. J. and Carey, E. V. 2006. Sap flux–upscaled canopy transpiration, stomatal conductance, and water use efficiency in an old growth forest in the Great Lakes region of the United States. *Journal of Geophysical Research*. 111, pp. 1-12.

Thorpe, M.R. 1978. Net radiation and transpiration of apple trees in rows. *Agric. For. Meteorol*. 19, pp. 41-57.

Zhang, H. Simmonds, L. P. Morison, J. I. L. Payne, D. 1997. Estimation of transpiration by single trees: comparison of sap flow measurements with a combination equation. *Agricultural and Forest Meteorology* 87, pp. 155-169.

**APPENDIX 5**

**DERIVATION OF
RICHARDS EQUATION FOR TWO DIMENSIONAL CONDITIONS**

## Governing Differential Equation Describing Isothermal Moisture Flow

Figure A5-1 illustrates a typical control element with inflow and outflow occurring in three dimensions $x$, $y$ and $z$.
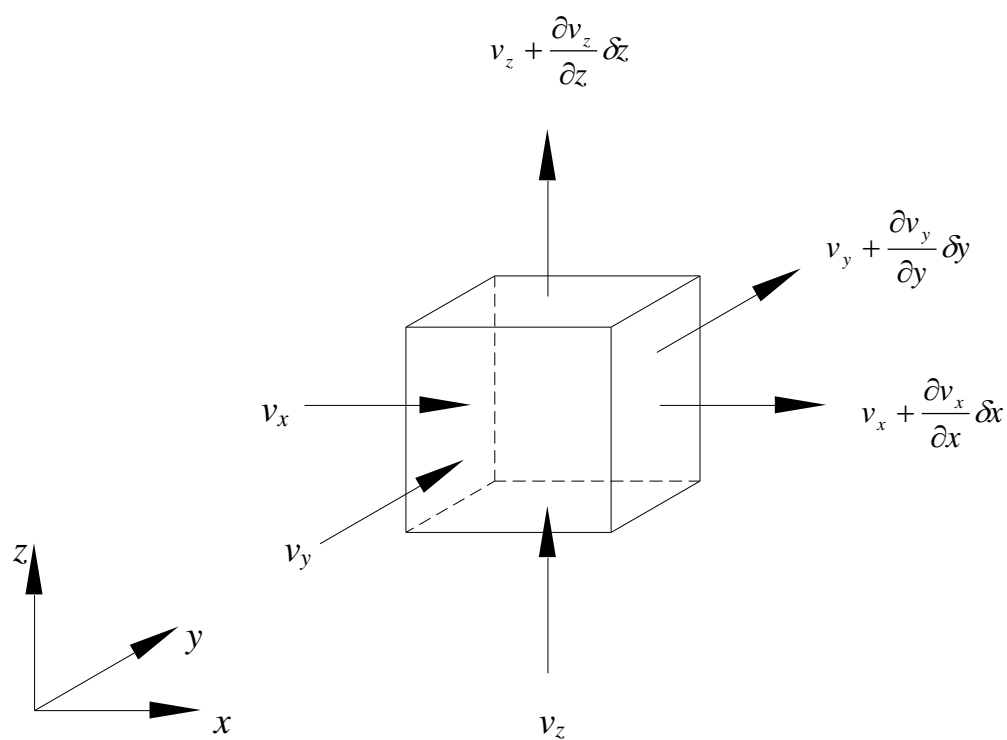


Figure A5-1.   3D Flow through a typical control element, modified after Yong and Warkentin (1974)

Considering first the flow of the moisture in the $x$ direction only.  The volume of water entering the system per unit time in the $x$ direction is given by

$$V_{Input} = v_x \delta z \delta y \tag{A5-1}$$

Where, $v_x$ is the velocity of water flow in the $x$ direction. Similarly the volume of water leaving the system per unit time is given by

$$V_{Output} = \left( v_x + \frac{\partial v_x}{\partial x} \delta x \right) \delta z \delta y \tag{A5-2}$$

The change in the volume of water stored in the control element per unit time is therefore given by difference between inflow and outflow i.e.

$$V_{Input} - V_{Output} = -\frac{\partial v_x}{\partial x} \delta x \delta z \delta y \tag{A5-3}$$

By symmetry the change in volume of water stored under three-dimensional conditions is given by

$$V_{Input} - V_{Output} = -\left( \frac{\partial v_x}{\partial x} + \frac{\partial v_y}{\partial y} + \frac{\partial v_z}{\partial z} \right) \delta x \delta y \delta z \tag{A5-4}$$

For the cases of flow through a saturated soil, assuming steady conditions exist, the change in storage of water in the control element must be equal to zero i.e.

$$\left( \frac{\partial v_x}{\partial x} + \frac{\partial v_y}{\partial y} + \frac{\partial v_z}{\partial z} \right) \delta x \delta y \delta z = 0 \tag{A5-5}$$

And since $\delta x \delta y \delta z \neq 0$ then

$$\left(\frac{\partial v_x}{\partial x} + \frac{\partial v_y}{\partial y} + \frac{\partial v_z}{\partial z}\right) = 0 \tag{A5-6}$$

Alternatively, for an unsaturated soil the net excess flow is equated to the change in the volume of water in the control element per unit time, thus

$$\left(\frac{\partial v_x}{\partial x} + \frac{\partial v_y}{\partial y} + \frac{\partial v_z}{\partial z}\right)\delta x \delta y \delta z = -\frac{\partial \theta}{\partial t}\delta x \delta y \delta z \tag{A5-7}$$

Where, $\theta$ is the volumetric moisture content. Equation (A5-7) may be abbreviated to

$$-\frac{\partial \theta}{\partial t} = \nabla v \tag{A5-8}$$

Equation (A5-8) can be expressed as follows for two-dimensional flow only,

$$-\frac{\partial \theta}{\partial t} = \frac{\partial v_x}{\partial x} + \frac{\partial v_z}{\partial z} \tag{A5-9}$$

Introducing Darcy's Law expressed for fluid flow in a partially saturated soil yields,

$$\frac{\partial \theta}{\partial t} = \frac{\partial}{\partial x}\left[K_x(\phi)\frac{\partial \phi}{\partial x}\right] + \frac{\partial}{\partial z}\left[K_z(\phi)\frac{\partial \phi}{\partial z}\right] \tag{A5-10}$$

The total potential for moisture flow is taken as the sum of the pressure or capillary potential and gravitational potential i.e.

$$\phi = \psi + z \tag{A5-11}$$

Therefore, substituting Equation (A5-11) into Equation (A5-10) gives,

$$\frac{\partial \theta}{\partial t} = \frac{\partial}{\partial x}\left[K_x(\psi)\frac{\partial \psi}{\partial x}\right] + \frac{\partial}{\partial z}\left[K_z(\psi)\frac{\partial \psi}{\partial z}\right] + \frac{\partial K_z(\psi)}{\partial z} \tag{A5-12}$$

Assuming that the soil is isotropic and restating the left hand side of Equation (A5-12) in terms of capillary potential yields,

$$\frac{\partial \theta}{\partial \psi}\frac{\partial \psi}{\partial t} = \frac{\partial}{\partial x}\left[K(\psi)\frac{\partial \psi}{\partial x}\right] + \frac{\partial}{\partial z}\left[K(\psi)\frac{\partial \psi}{\partial z}\right] + \frac{\partial K(\psi)}{\partial z} \tag{A5-13}$$

The term $\partial\theta/\partial\psi$ is called the specific moisture capacity of the soil and is denoted as $C(\psi)$.

$$C(\psi)\frac{\partial \psi}{\partial t} = \frac{\partial}{\partial x}\left[K(\psi)\frac{\partial \psi}{\partial x}\right] + \frac{\partial}{\partial z}\left[K(\psi)\frac{\partial \psi}{\partial z}\right] + \frac{\partial K(\psi)}{\partial z} \tag{A5-14}$$

Equation (A5-14) is often referred to as two-dimensional Richards equations (Richards 1931).

References:

Richards, L. A. 1931. Capillary conduction of liquids in porous media. *Physics*. 1, pp. 318 - 333.

Yong, R. N. and Warkentin, B. P. 1974. *Soil properties and behaviour*. Elsevier Publishing Company, Amsterdam.

**APPENDIX 6**

**DISCRETISATION OF STANDARD
TWO-DIMENSIONAL MOISTURE TRANSFER**

Two-dimensional moisture transfer in an unsaturated soil is derived by combining standard two-dimensional Richards equation and sink term equation:

$$C(\psi)\frac{\partial \psi}{\partial t} = \frac{\partial}{\partial x}\left[K(\psi)\frac{\partial \psi}{\partial x}\right] + \frac{\partial}{\partial z}\left[K(\psi)\frac{\partial \psi}{\partial z}\right] + \frac{\partial K(\psi)}{\partial z} - S \qquad \text{(A6-1)}$$

A solution of equation (A6-1) is obtained via a finite element spatial discretisation procedure and a finite difference time-stepping scheme. In particular, adopting a Galerkin weighted residual approach yields:

$$\int_{\Omega^e} N_r \begin{bmatrix} \dfrac{\partial}{\partial x}\left[K\left(\hat{\psi}\right)\dfrac{\partial \hat{\psi}}{\partial x}\right] + \dfrac{\partial}{\partial z}\left[K\left(\hat{\psi}\right)\dfrac{\partial \hat{\psi}}{\partial z}\right] \\ + \dfrac{\partial K\left(\hat{\psi}\right)}{\partial z} - S\left(\hat{\psi}\right) - C\left(\hat{\psi}\right)\dfrac{\partial \hat{\psi}}{\partial t} \end{bmatrix} \partial\Omega = 0 \qquad \text{(A6-2)}$$

Using, Green's formula and introducing boundary terms leads to the final disctretised form:

$$-\int_{\Omega^e} K \frac{\partial N_s}{\partial x}\frac{\partial N_r}{\partial x}\psi_s \partial\Omega^e - \int_{\Omega^e} K \frac{\partial N_r}{\partial z}\frac{\partial N_s}{\partial z}\psi_s \partial\Omega^e - \int_{\Omega^e} N_r \frac{\partial K}{\partial z}\partial\Omega^e$$
$$+\int_{\Gamma} N_r \lambda \partial\Gamma - \int_{\Omega^e} N_r S \partial\Omega^e - \int_{\Omega^e} N_r N_s C \frac{\partial \psi_s}{\partial t}\partial\Omega^e = 0 \qquad \text{(A6-3)}$$

Summing for all elements and re-casting equation (A6-3) into concise matrix notation yields;

$$K\psi_s + C\frac{\psi_s}{\partial t} + J + S = 0 \tag{A6-4}$$

Where

$$K = \sum_{e=1}^{m} \int_{\Omega^e} \left[ K \frac{\partial N_s}{\partial x} \cdot \frac{\partial N_x}{\partial x} + K \frac{\partial N_s}{\partial z} \cdot \frac{\partial N_x}{\partial z} \right] \partial \Omega^e \tag{A6-5}$$

$$C = \sum_{e=1}^{m} \int_{\Omega^e} [N_x N_s C] \partial \Omega^e \tag{A6-6}$$

$$J = \sum_{e=1}^{m} \int_{\Omega^e} r \left[ K \frac{\partial N_x}{\partial x} \right] \partial \Omega^e - \sum_{e=1}^{m} \int_{\Gamma^e} r [N_x \lambda] \partial \Gamma^e \tag{A6-7}$$

$$S = \sum_{e=1}^{m} \int_{\Omega^e} [N_x S] \partial \Omega^e \tag{A6-8}$$

The time dependent nature of equation (A6-4) is dealt with via a mid-interval backward difference technique, yielding:

$$K^{n+1/2}\psi^{n+1} + C^{n+1/2} \left[ \frac{\psi^{n+1} - \psi^{n}}{\Delta t} \right] + J^{n+1/2} + S^{n+1/2} = 0 \tag{A6-9}$$

**APPENDIX 7**

**SLOPE STABILITY ANALYSIS CALCULATIONS**

**SLOPE STABILITY ANALYSIS CALCULATIONS – Bishop Simplified Method**

Detailed manual calculations are summarised as below. This was undertaken as a basic check on solution procedures. The difference between the program and manual calculation by hand is 0.02 %.  It is recognised that the above comparison is of limited value.   However, it is thought that this approach yields some confidence in the implementation of the current procedure.

Table A7-1     Shear strength parameters for London clay soil (Smethurst et al. 2006; Smethurst et al. 2012)

| $c'(kPa)$ | $\phi'(^{o})$ | $\gamma(kN/m^{3})$ |
|---|---|---|
| 7 | 20 | 19.21 |

Table A7-2     Hydraulic parameters for London clay soil (Croney 1977)

| Soil Type | $\theta_r$ $(cm^{3}/cm^{3})$ | $\theta_s$ $(cm^{3}/cm^{3})$ | $\alpha$ $(kPa)$ | $n$ | $K_s$ $(cm/s)$ | $l$ | $m$ |
|---|---|---|---|---|---|---|---|
| Grey London Clay | 0.05 | 0.47 | 10.90 | 1.12 | 3.70E-07 | 0.50 | 0.11 |

Vanapalli et al. (1996) nonlinear shear strength equation:

$$\tau = c' + \left(\sigma_n - u_a\right)\tan\phi' + \left(u_a - u_w\right)\left[\left(\frac{\theta_w - \theta_r}{\theta_s - \theta_r}\right)\tan\phi'\right] \tag{A7-1}$$

The factor of safety for an unsaturated slope is evaluated using:

$$F = \frac{\sum\left[\dfrac{c'l + \dfrac{W\tan\phi'}{\cos\alpha} - u_w\left(\dfrac{\theta_w - \theta_r}{\theta_s - \theta_r}\right)\tan\phi'l}{1 + \dfrac{\tan\phi'\sin\alpha}{F}}\right]}{\sum W\sin\alpha} \tag{A7-2}$$

Table A7-3    Slope Stability Analysis Manual Calculations using Vanapalli's equation (Vanapalli et al. 1996)

| Slice No. | Height (m) | b (m) | W (kN) | α(°) | sinα | Wsinα (kN) | l (m) | ψ (kPa) | tanφ' | $(\theta_w-\theta_r)/(\theta_s-\theta_r)$ tanφ' | c'l (kN) | sinα tanφ' | cos α + tanφ' sin α / F | c'l sinα | ψ l $((\theta_w-\theta_r)/(\theta_s-\theta_r)$ tanφ') sinα | (c'l sinα-ψ l $((\theta_w-\theta_r)/(\theta_s-\theta_r)$ tanφ') sinα)/F | ψ l $((\theta_w-\theta_r)/(\theta_s-\theta_r)$ tanφ') |
|---|---|---|---|---|---|---|---|---|---|---|---|---|---|---|---|---|---|
| 1 | 0.31 | 1.25 | 7.55 | -26.70 | -0.45 | -3.39 | 1.40 | -6.55 | 0.36 | 0.35 | 9.79 | -0.16 | 0.82 | -4.40 | 1.43 | -2.71 | -3.18 |
| 2 | 1.00 | 1.04 | 20.01 | -23.70 | -0.40 | -8.04 | 1.13 | -1.24 | 0.36 | 0.36 | 7.93 | -0.15 | 0.85 | -3.19 | 0.20 | -1.58 | -0.51 |
| 3 | 1.73 | 1.04 | 34.42 | -21.03 | -0.36 | -12.35 | 1.11 | 2.95 | 0.36 | 0.36 | 7.78 | -0.13 | 0.87 | -2.79 | -0.43 | -1.10 | 1.19 |
| 4 | 2.40 | 1.04 | 47.73 | -18.42 | -0.32 | -15.08 | 1.09 | 6.60 | 0.36 | 0.36 | 7.65 | -0.11 | 0.90 | -2.42 | -0.83 | -0.74 | 2.62 |
| 5 | 3.01 | 1.04 | 60.00 | -15.84 | -0.27 | -16.38 | 1.08 | 9.73 | 0.36 | 0.36 | 7.55 | -0.10 | 0.92 | -2.06 | -1.04 | -0.47 | 3.82 |
| 6 | 3.58 | 1.04 | 71.28 | -13.30 | -0.23 | -16.39 | 1.07 | 12.38 | 0.36 | 0.36 | 7.46 | -0.08 | 0.93 | -1.72 | -1.10 | -0.28 | 4.80 |
| 7 | 4.10 | 1.04 | 81.59 | -10.78 | -0.19 | -15.26 | 1.06 | 14.55 | 0.36 | 0.36 | 7.39 | -0.07 | 0.95 | -1.38 | -1.05 | -0.16 | 5.59 |
| 8 | 4.57 | 1.04 | 90.96 | -8.28 | -0.14 | -13.10 | 1.05 | 16.25 | 0.36 | 0.36 | 7.34 | -0.05 | 0.97 | -1.06 | -0.89 | -0.08 | 6.20 |
| 9 | 4.99 | 1.04 | 99.41 | -5.80 | -0.10 | -10.05 | 1.04 | 17.51 | 0.36 | 0.36 | 7.30 | -0.04 | 0.98 | -0.74 | -0.67 | -0.03 | 6.64 |
| 10 | 5.37 | 1.04 | 106.97 | -3.33 | -0.06 | -6.21 | 1.04 | 18.32 | 0.36 | 0.36 | 7.27 | -0.02 | 0.99 | -0.42 | -0.40 | -0.01 | 6.93 |
| 11 | 5.70 | 1.04 | 113.63 | -0.87 | -0.02 | -1.72 | 1.04 | 18.70 | 0.36 | 0.36 | 7.26 | -0.01 | 1.00 | -0.11 | -0.11 | 0.00 | 7.06 |
| 12 | 5.99 | 1.04 | 119.40 | 1.60 | 0.03 | 3.32 | 1.04 | 18.63 | 0.36 | 0.36 | 7.26 | 0.01 | 1.00 | 0.20 | 0.20 | 0.00 | 7.03 |
| 13 | 6.24 | 1.04 | 124.28 | 4.06 | 0.07 | 8.80 | 1.04 | 18.13 | 0.36 | 0.36 | 7.28 | 0.03 | 1.01 | 0.52 | 0.49 | 0.01 | 6.86 |
| 14 | 6.44 | 1.04 | 128.26 | 6.53 | 0.11 | 14.59 | 1.04 | 17.19 | 0.36 | 0.36 | 7.31 | 0.04 | 1.01 | 0.83 | 0.74 | 0.04 | 6.53 |
| 15 | 6.59 | 1.04 | 131.34 | 9.02 | 0.16 | 20.59 | 1.05 | 15.80 | 0.36 | 0.36 | 7.35 | 0.06 | 1.01 | 1.15 | 0.95 | 0.10 | 6.04 |
| 16 | 6.70 | 1.04 | 133.50 | 11.52 | 0.20 | 26.66 | 1.06 | 13.95 | 0.36 | 0.36 | 7.41 | 0.07 | 1.01 | 1.48 | 1.07 | 0.19 | 5.37 |
| 17 | 6.76 | 1.04 | 134.71 | 14.05 | 0.24 | 32.70 | 1.07 | 11.64 | 0.36 | 0.36 | 7.48 | 0.09 | 1.01 | 1.82 | 1.10 | 0.33 | 4.53 |
| 18 | 6.77 | 1.04 | 134.95 | 16.60 | 0.29 | 38.55 | 1.08 | 8.86 | 0.36 | 0.36 | 7.57 | 0.10 | 1.01 | 2.16 | 1.00 | 0.54 | 3.49 |
| 19 | 6.74 | 1.04 | 134.18 | 19.19 | 0.33 | 44.10 | 1.10 | 5.57 | 0.36 | 0.36 | 7.69 | 0.12 | 1.00 | 2.53 | 0.73 | 0.84 | 2.23 |
| 20 | 6.64 | 1.04 | 132.36 | 21.82 | 0.37 | 49.19 | 1.12 | 1.76 | 0.36 | 0.36 | 7.82 | 0.14 | 0.99 | 2.91 | 0.27 | 1.23 | 0.72 |
| 21 | 6.50 | 1.04 | 129.42 | 24.49 | 0.41 | 53.66 | 1.14 | -2.59 | 0.36 | 0.36 | 7.98 | 0.15 | 0.98 | 3.31 | -0.44 | 1.74 | -1.05 |
| 22 | 6.29 | 1.04 | 125.30 | 27.23 | 0.46 | 57.33 | 1.17 | -7.52 | 0.36 | 0.34 | 8.16 | 0.17 | 0.97 | 3.74 | -1.38 | 2.38 | -3.02 |
| 23 | 6.02 | 1.04 | 119.91 | 30.04 | 0.50 | 60.02 | 1.20 | -13.08 | 0.36 | 0.33 | 8.39 | 0.18 | 0.95 | 4.20 | -2.62 | 3.17 | -5.23 |
| 24 | 5.68 | 1.04 | 113.15 | 32.93 | 0.54 | 61.50 | 1.24 | -19.31 | 0.36 | 0.32 | 8.65 | 0.20 | 0.93 | 4.70 | -4.21 | 4.15 | -7.75 |
| 25 | 5.27 | 1.04 | 104.89 | 35.91 | 0.59 | 61.52 | 1.28 | -26.29 | 0.36 | 0.32 | 8.96 | 0.21 | 0.91 | 5.26 | -6.25 | 5.36 | -10.65 |
| 26 | 4.77 | 1.04 | 94.94 | 39.02 | 0.63 | 59.77 | 1.33 | -34.09 | 0.36 | 0.31 | 9.34 | 0.23 | 0.88 | 5.88 | -8.86 | 6.86 | -14.07 |
| 27 | 4.17 | 1.04 | 83.09 | 42.26 | 0.67 | 55.88 | 1.40 | -42.83 | 0.36 | 0.30 | 9.81 | 0.24 | 0.85 | 6.60 | -12.21 | 8.75 | -18.15 |
| 28 | 3.46 | 1.04 | 69.02 | 45.69 | 0.72 | 49.39 | 1.48 | -52.66 | 0.36 | 0.30 | 10.39 | 0.26 | 0.82 | 7.44 | -16.57 | 11.17 | -23.16 |
| 29 | 2.38 | 1.20 | 54.76 | 49.65 | 0.76 | 41.74 | 1.85 | -64.79 | 0.36 | 0.29 | 12.97 | 0.28 | 0.78 | 9.89 | -26.53 | 16.95 | -34.81 |
| 30 | 0.83 | 1.20 | 19.24 | 54.29 | 0.81 | 15.62 | 2.06 | -79.91 | 0.36 | 0.28 | 14.39 | 0.30 | 0.72 | 11.69 | -37.81 | 23.04 | -46.57 |
| **Total** | | | | | Σ | 636.9703 | | | | Σ | 250.92 | | | | | Σ | -80.51 |

Table A7-4    Slope Stability Analysis Manual Calculations using Vanapalli's equation (Vanapalli et al. 1996)

| Slice No. | N (kN) | T (kN) | $\tau_f l$ (kN) | N tanφ' (kN) | $\theta_w$ | $\|\psi/a\|^n$ | $(1+\|\psi/a\|^n)^m$ | $\theta_s - \theta_r$ | 1+tanφ'tan α/F | tanα | Wtanφ'/cosα | $(-u_w)l ((\theta_w-\theta_r)/(\theta_s-\theta_r) tan\phi')$ | $(c'l +Wtan\phi'/cos\alpha+(-u_w)l ((\theta_w-\theta_r)/(\theta_s-\theta_r) tan\phi'))/(1+tan\phi'tan\alpha/F)$ | Base Normal Stress (kPa) | Base Shear Resistance Stress (kPa) |
|---|---|---|---|---|---|---|---|---|---|---|---|---|---|---|---|
| 1 | 12.56 | 8.17 | 17.55 | 4.57 | 0.45 | 0.57 | 1.05 | 0.42 | 0.91 | -0.50 | 3.08 | 3.18 | 17.55 | 8.97 | 12.54 |
| 2 | 25.47 | 8.24 | 17.70 | 9.27 | 0.47 | 0.09 | 1.01 | 0.42 | 0.93 | -0.44 | 7.95 | 0.51 | 17.70 | 22.49 | 15.63 |
| 3 | 40.70 | 9.96 | 21.40 | 14.81 | 0.47 | 0.23 | 1.02 | 0.42 | 0.93 | -0.38 | 13.42 | -1.19 | 21.40 | 36.63 | 19.26 |
| 4 | 54.14 | 11.51 | 24.73 | 19.71 | 0.47 | 0.57 | 1.05 | 0.42 | 0.94 | -0.33 | 18.31 | -2.62 | 24.73 | 49.53 | 22.63 |
| 5 | 66.04 | 12.92 | 27.76 | 24.04 | 0.47 | 0.88 | 1.07 | 0.42 | 0.95 | -0.28 | 22.70 | -3.82 | 27.76 | 61.26 | 25.75 |
| 6 | 76.60 | 14.21 | 30.54 | 27.88 | 0.47 | 1.15 | 1.09 | 0.42 | 0.96 | -0.24 | 26.66 | -4.80 | 30.54 | 71.88 | 28.66 |
| 7 | 85.98 | 15.40 | 33.10 | 31.30 | 0.47 | 1.38 | 1.10 | 0.42 | 0.97 | -0.19 | 30.23 | -5.59 | 33.10 | 81.45 | 31.35 |
| 8 | 94.32 | 16.51 | 35.47 | 34.33 | 0.47 | 1.56 | 1.11 | 0.42 | 0.98 | -0.15 | 33.45 | -6.20 | 35.47 | 90.00 | 33.84 |
| 9 | 101.71 | 17.53 | 37.67 | 37.02 | 0.47 | 1.70 | 1.11 | 0.42 | 0.98 | -0.10 | 36.37 | -6.64 | 37.67 | 97.57 | 36.14 |
| 10 | 108.22 | 18.49 | 39.73 | 39.39 | 0.47 | 1.79 | 1.12 | 0.42 | 0.99 | -0.06 | 39.00 | -6.93 | 39.73 | 104.18 | 38.25 |
| 11 | 113.93 | 19.40 | 41.67 | 41.47 | 0.47 | 1.83 | 1.12 | 0.42 | 1.00 | -0.02 | 41.36 | -7.06 | 41.67 | 109.85 | 40.18 |
| 12 | 118.88 | 20.24 | 43.50 | 43.27 | 0.47 | 1.82 | 1.12 | 0.42 | 1.00 | 0.03 | 43.47 | -7.03 | 43.50 | 114.59 | 41.93 |
| 13 | 123.10 | 21.05 | 45.22 | 44.80 | 0.47 | 1.77 | 1.12 | 0.42 | 1.01 | 0.07 | 45.35 | -6.86 | 45.22 | 118.41 | 43.50 |
| 14 | 126.60 | 21.81 | 46.86 | 46.08 | 0.47 | 1.67 | 1.11 | 0.42 | 1.02 | 0.11 | 46.99 | -6.53 | 46.86 | 121.29 | 44.89 |
| 15 | 129.41 | 22.53 | 48.42 | 47.10 | 0.47 | 1.52 | 1.10 | 0.42 | 1.03 | 0.16 | 48.40 | -6.04 | 48.42 | 123.25 | 46.11 |
| 16 | 131.51 | 23.23 | 49.90 | 47.87 | 0.47 | 1.32 | 1.09 | 0.42 | 1.03 | 0.20 | 49.59 | -5.37 | 49.90 | 124.26 | 47.15 |
| 17 | 132.89 | 23.89 | 51.32 | 48.37 | 0.47 | 1.08 | 1.08 | 0.42 | 1.04 | 0.25 | 50.54 | -4.53 | 51.32 | 124.31 | 48.01 |
| 18 | 133.51 | 24.52 | 52.68 | 48.59 | 0.47 | 0.79 | 1.06 | 0.42 | 1.05 | 0.30 | 51.25 | -3.49 | 52.68 | 123.38 | 48.68 |
| 19 | 133.33 | 25.13 | 53.99 | 48.53 | 0.47 | 0.47 | 1.04 | 0.42 | 1.06 | 0.35 | 51.71 | -2.23 | 53.99 | 121.43 | 49.17 |
| 20 | 132.27 | 25.71 | 55.24 | 48.14 | 0.47 | 0.13 | 1.01 | 0.42 | 1.07 | 0.40 | 51.89 | -0.72 | 55.24 | 118.42 | 49.46 |
| 21 | 130.25 | 26.27 | 56.44 | 47.41 | 0.46 | 0.20 | 1.02 | 0.42 | 1.08 | 0.46 | 51.76 | 1.05 | 56.44 | 114.29 | 49.52 |
| 22 | 127.15 | 26.75 | 57.47 | 46.28 | 0.45 | 0.66 | 1.06 | 0.42 | 1.09 | 0.51 | 51.29 | 3.02 | 57.47 | 109.02 | 49.27 |
| 23 | 122.82 | 27.15 | 58.32 | 44.70 | 0.44 | 1.23 | 1.09 | 0.42 | 1.10 | 0.58 | 50.42 | 5.23 | 58.32 | 102.53 | 48.69 |
| 24 | 117.03 | 27.46 | 58.99 | 42.59 | 0.42 | 1.90 | 1.12 | 0.42 | 1.11 | 0.65 | 49.07 | 7.75 | 58.99 | 94.72 | 47.75 |
| 25 | 109.46 | 27.67 | 59.46 | 39.84 | 0.42 | 2.68 | 1.15 | 0.42 | 1.12 | 0.72 | 47.13 | 10.65 | 59.46 | 85.49 | 46.44 |
| 26 | 99.68 | 27.78 | 59.69 | 36.28 | 0.41 | 3.59 | 1.18 | 0.42 | 1.14 | 0.81 | 44.47 | 14.07 | 59.69 | 74.68 | 44.72 |
| 27 | 87.04 | 27.76 | 59.64 | 31.68 | 0.40 | 4.63 | 1.20 | 0.42 | 1.15 | 0.91 | 40.86 | 18.15 | 59.64 | 62.12 | 42.56 |
| 28 | 70.57 | 27.57 | 59.23 | 25.68 | 0.39 | 5.84 | 1.23 | 0.42 | 1.17 | 1.02 | 35.96 | 23.16 | 59.23 | 47.54 | 39.90 |
| 29 | 48.69 | 30.49 | 65.51 | 17.72 | 0.38 | 7.36 | 1.26 | 0.42 | 1.20 | 1.18 | 30.79 | 34.81 | 65.51 | 26.27 | 35.35 |
| 30 | -5.26 | 27.48 | 59.04 | -1.92 | 0.38 | 9.31 | 1.28 | 0.42 | 1.24 | 1.39 | 12.00 | 46.57 | 59.04 | -2.56 | 28.72 |
| Total | | | Σ | 1036.81 | | | | | | | | Σ | 1368.24 | | |

*F* of *S* = 1368.24/636.97 = 2.14804

Table A7-5    Shear strength parameters for London clay soil (Smethurst et al. 2006;

Smethurst et al. 2012; Fredlund and Rahardjo (1993))

| $c'(kPa)$ | $\phi'(^o)$ | $\phi^b\,(^o)$ | $\gamma(kN/m^3)$ |
|---|---|---|---|
| 7 | 20 | 15 | 19.21 |

Fredlund et al.(1978) linear shear strength equation:

$$\tau = c' + \left(\sigma_n - u_a\right)\tan\phi' + \left(u_a - u_w\right)\tan\phi^b \tag{A7-3}$$

$$F = \frac{\sum\left[c'l + N\tan\phi' - u_w l\tan\phi^b\right]}{\sum W\sin\alpha} \tag{A7-4}$$

Table A7-6    Slope Stability Analysis Manual Calculations using Fredlund's equation (Fredlund et al. 1978)

| Slice No. | Height (m) | b (m) | W (kN) | α(°) | sinα | Wsinα (kN) | l (m) | ψ (kPa) | tanφ' | tanφ^b | c'l (kN) | sinα tanφ' | cos α + tanφ' sin α / F | c'l sinα | ψ l tanφ^b sinα | (c'l sinα-ψ l tanφ^b sinα)/F | ψ l tanφ^b | N (kN) | T (kN) | τ_f l (kN) | N tanφ' (kN) |
|---|---|---|---|---|---|---|---|---|---|---|---|---|---|---|---|---|---|---|---|---|---|
| 1 | 0.31 | 1.25 | 7.55 | -26.70 | -0.45 | -3.39 | 1.40 | -6.55 | 0.36 | 0.27 | 9.79 | -0.16 | 0.82 | -4.40 | 1.10 | -2.59 | -2.46 | 12.42 | 7.90 | 16.77 | 4.52 |
| 2 | 1.00 | 1.04 | 20.01 | -23.70 | -0.40 | -8.04 | 1.13 | -1.24 | 0.36 | 0.27 | 7.93 | -0.15 | 0.85 | -3.19 | 0.15 | -1.57 | -0.38 | 25.48 | 8.28 | 17.58 | 9.28 |
| 3 | 1.73 | 1.04 | 34.42 | -21.03 | -0.36 | -12.35 | 1.11 | 2.95 | 0.36 | 0.36 | 7.78 | -0.13 | 0.87 | -2.79 | -0.43 | -1.11 | 1.19 | 40.75 | 10.09 | 21.42 | 14.83 |
| 4 | 2.40 | 1.04 | 47.73 | -18.42 | -0.32 | -15.08 | 1.09 | 6.60 | 0.36 | 0.36 | 7.65 | -0.11 | 0.89 | -2.42 | -0.83 | -0.75 | 2.62 | 54.19 | 11.66 | 24.75 | 19.72 |
| 5 | 3.01 | 1.04 | 60.00 | -15.84 | -0.27 | -16.38 | 1.08 | 9.73 | 0.36 | 0.36 | 7.55 | -0.10 | 0.92 | -2.06 | -1.04 | -0.48 | 3.82 | 66.08 | 13.09 | 27.78 | 24.05 |
| 6 | 3.58 | 1.04 | 71.28 | -13.30 | -0.23 | -16.39 | 1.07 | 12.38 | 0.36 | 0.36 | 7.46 | -0.08 | 0.93 | -1.72 | -1.10 | -0.29 | 4.80 | 76.64 | 14.39 | 30.55 | 27.89 |
| 7 | 4.10 | 1.04 | 81.59 | -10.78 | -0.19 | -15.26 | 1.06 | 14.55 | 0.36 | 0.36 | 7.39 | -0.07 | 0.95 | -1.38 | -1.05 | -0.16 | 5.59 | 86.02 | 15.60 | 33.11 | 31.31 |
| 8 | 4.57 | 1.04 | 90.96 | -8.28 | -0.14 | -13.10 | 1.05 | 16.25 | 0.36 | 0.36 | 7.34 | -0.05 | 0.96 | -1.06 | -0.89 | -0.08 | 6.20 | 94.35 | 16.71 | 35.48 | 34.34 |
| 9 | 4.99 | 1.04 | 99.41 | -5.80 | -0.10 | -10.05 | 1.04 | 17.51 | 0.36 | 0.36 | 7.30 | -0.04 | 0.98 | -0.74 | -0.67 | -0.03 | 6.64 | 101.73 | 17.75 | 37.68 | 37.03 |
| 10 | 5.37 | 1.04 | 106.97 | -3.33 | -0.06 | -6.21 | 1.04 | 18.32 | 0.36 | 0.36 | 7.27 | -0.02 | 0.99 | -0.42 | -0.40 | -0.01 | 6.93 | 108.24 | 18.72 | 39.74 | 39.39 |
| 11 | 5.70 | 1.04 | 113.63 | -0.87 | -0.02 | -1.72 | 1.04 | 18.70 | 0.36 | 0.36 | 7.26 | -0.01 | 1.00 | -0.11 | -0.11 | 0.00 | 7.06 | 113.94 | 19.63 | 41.67 | 41.47 |
| 12 | 5.99 | 1.04 | 119.40 | 1.60 | 0.03 | 3.32 | 1.04 | 18.63 | 0.36 | 0.36 | 7.26 | 0.01 | 1.00 | 0.20 | 0.20 | 0.00 | 7.03 | 118.87 | 20.49 | 43.49 | 43.27 |
| 13 | 6.24 | 1.04 | 124.28 | 4.06 | 0.07 | 8.80 | 1.04 | 18.13 | 0.36 | 0.36 | 7.28 | 0.03 | 1.01 | 0.52 | 0.49 | 0.01 | 6.86 | 123.08 | 21.30 | 45.21 | 44.80 |
| 14 | 6.44 | 1.04 | 128.26 | 6.53 | 0.11 | 14.59 | 1.04 | 17.19 | 0.36 | 0.36 | 7.31 | 0.04 | 1.01 | 0.83 | 0.74 | 0.04 | 6.53 | 126.58 | 22.07 | 46.85 | 46.07 |
| 15 | 6.59 | 1.04 | 131.34 | 9.02 | 0.16 | 20.59 | 1.05 | 15.80 | 0.36 | 0.36 | 7.35 | 0.06 | 1.01 | 1.15 | 0.95 | 0.10 | 6.04 | 129.37 | 22.80 | 48.40 | 47.09 |
| 16 | 6.70 | 1.04 | 133.50 | 11.52 | 0.20 | 26.66 | 1.06 | 13.95 | 0.36 | 0.36 | 7.41 | 0.07 | 1.01 | 1.48 | 1.07 | 0.19 | 5.37 | 131.46 | 23.50 | 49.88 | 47.85 |
| 17 | 6.76 | 1.04 | 134.71 | 14.05 | 0.24 | 32.70 | 1.07 | 11.64 | 0.36 | 0.36 | 7.48 | 0.09 | 1.01 | 1.82 | 1.10 | 0.34 | 4.53 | 132.82 | 24.16 | 51.30 | 48.34 |
| 18 | 6.77 | 1.04 | 134.95 | 16.60 | 0.29 | 38.55 | 1.08 | 8.86 | 0.36 | 0.36 | 7.57 | 0.10 | 1.01 | 2.16 | 1.00 | 0.55 | 3.49 | 133.43 | 24.80 | 52.65 | 48.56 |
| 19 | 6.74 | 1.04 | 134.18 | 19.19 | 0.33 | 44.10 | 1.10 | 5.57 | 0.36 | 0.36 | 7.69 | 0.12 | 1.00 | 2.53 | 0.73 | 0.85 | 2.23 | 133.23 | 25.41 | 53.95 | 48.49 |
| 20 | 6.64 | 1.04 | 132.36 | 21.82 | 0.37 | 49.19 | 1.12 | 1.76 | 0.36 | 0.36 | 7.82 | 0.14 | 0.99 | 2.91 | 0.27 | 1.24 | 0.72 | 132.16 | 26.00 | 55.20 | 48.10 |
| 21 | 6.50 | 1.04 | 129.42 | 24.49 | 0.41 | 53.66 | 1.14 | -2.59 | 0.36 | 0.27 | 7.98 | 0.15 | 0.98 | 3.31 | -0.33 | 1.71 | -0.79 | 130.17 | 26.45 | 56.14 | 47.38 |
| 22 | 6.29 | 1.04 | 125.30 | 27.23 | 0.46 | 57.33 | 1.17 | -7.52 | 0.36 | 0.27 | 8.16 | 0.17 | 0.97 | 3.74 | -1.08 | 2.27 | -2.35 | 127.15 | 26.75 | 56.79 | 46.28 |
| 23 | 6.02 | 1.04 | 119.91 | 30.04 | 0.50 | 60.02 | 1.20 | -13.08 | 0.36 | 0.27 | 8.39 | 0.18 | 0.95 | 4.20 | -2.10 | 2.97 | -4.20 | 122.90 | 27.00 | 57.32 | 44.73 |
| 24 | 5.68 | 1.04 | 113.15 | 32.93 | 0.54 | 61.50 | 1.24 | -19.31 | 0.36 | 0.27 | 8.65 | 0.20 | 0.93 | 4.70 | -3.47 | 3.85 | -6.39 | 117.21 | 27.18 | 57.70 | 42.66 |
| 25 | 5.27 | 1.04 | 104.89 | 35.91 | 0.59 | 61.52 | 1.28 | -26.29 | 0.36 | 0.27 | 8.96 | 0.21 | 0.91 | 5.26 | -5.29 | 4.97 | -9.02 | 109.74 | 27.28 | 57.92 | 39.94 |
| 26 | 4.77 | 1.04 | 94.94 | 39.02 | 0.63 | 59.77 | 1.33 | -34.09 | 0.36 | 0.27 | 9.34 | 0.23 | 0.88 | 5.88 | -7.67 | 6.39 | -12.19 | 100.07 | 27.30 | 57.96 | 36.42 |
| 27 | 4.17 | 1.04 | 83.09 | 42.26 | 0.67 | 55.88 | 1.40 | -42.83 | 0.36 | 0.27 | 9.81 | 0.24 | 0.86 | 6.60 | -10.82 | 8.20 | -16.08 | 87.55 | 27.20 | 57.76 | 31.86 |
| 28 | 3.46 | 1.04 | 69.02 | 45.69 | 0.72 | 49.39 | 1.48 | -52.66 | 0.36 | 0.27 | 10.39 | 0.26 | 0.82 | 7.44 | -14.99 | 10.56 | -20.95 | 71.19 | 26.97 | 57.25 | 25.91 |
| 29 | 2.38 | 1.20 | 54.76 | 49.65 | 0.76 | 41.74 | 1.85 | -64.79 | 0.36 | 0.27 | 12.97 | 0.28 | 0.78 | 9.89 | -24.52 | 16.21 | -32.18 | 49.55 | 29.76 | 63.19 | 18.04 |
| 30 | 0.83 | 1.20 | 19.24 | 54.29 | 0.81 | 15.62 | 2.06 | -79.91 | 0.36 | 0.27 | 14.39 | 0.30 | 0.72 | 11.69 | -35.74 | 22.34 | -44.02 | -4.29 | 26.78 | 56.85 | -1.56 |
| Total | | | | | Σ | 636.97 | | | Σ | 250.92 | | | | | | | -63.35 | | | Σ | 1038.07 |

**F** of **S** = (250.92+1038.07+63.35)/636.97 = 2.1230

References:

Croney, D. 1977. *The design and performance of road pavements*. London: Her
   Majesty's Stationery Office.

Fredlund, D. G. Morgenstern, N. R. and Widger, R. A. 1978. The shear strength of
   unsaturated soils. *Canadian Geotechnical Journal*. 15(3), pp. 313-321.

Fredlund, D. G. and Rahardjo, H. 1993. *Soil Mechanics of Unsaturated Soils*. New
   York: John Wiley & Sons.

Smethurst, J. A. Clarke, D. and Powrie, W. 2006. Seasonal changes in pore water
   pressure in a grass-covered cut slope in London Clay. *Géotechnique*. 56 (8), pp.
   523-537.

Smethurst, J. A. Clarke, D. and Powrie, W. 2012. Factors controlling the seasonal
   variation in soil water content and pore water pressures within a lightly vegetated
   clay slope. *Géotechnique*. 40, pp. 643-660.

Vanapalli, S. K. Fredlund, D. G. Pufahl, D. E. and Clifton, A. W. 1996. Model for
   the prediction of shear strength with respect to soil suction. *Canadian
   Geotechnical Journal*. 33(3), pp. 379-392.